# BEHAVIOUR AND MODELLING OF FRP-CONFINED HOLLOW AND CONCRETE-FILLED STEEL TUBULAR COLUMNS

YUE-MING HU

Ph.D

The Hong Kong Polytechnic University

2011

# BEHAVIOUR AND MODELLING OF FRP-CONFINED HOLLOW AND CONCRETE-FILLED STEEL TUBULAR COLUMNS

**By**

**YUE-MING HU**

**BEng**

**A Thesis Submitted in Partial Fulfilment of the Requirements for the Degree of Doctor of Philosophy**

**The Hong Kong Polytechnic University**

**Department of Civil and Structural Engineering**

**September 2010**

# CERTIFICATE OF ORIGINALITY

I hereby declare that this thesis is my own work and that, to the best of my knowledge and belief, it reproduces no material previously published or written, nor material that has been accepted for the award of any other degree or diploma, except where due acknowledgement has been made in the text.

______________________ (Signed)

YUE-MING HU (Name of Student)

# ABSTRACT

Hollow and concrete-filled steel tubes are widely used as columns in many structural systems and a common failure mode of such tubular columns when subjected to axial compression alone or in combination with monotonic/cyclic lateral loading is local buckling near a column end. The use of FRP jackets for the suppression of such local buckling has recently been proposed and has been proven by limited test results to possess great potential in both retrofit/strengthening and new construction. Against this background, this thesis presents a combined experimental and theoretical study aimed at the development of a good understanding of the structural behaviour of and reliable theoretical models for FRP-confined hollow steel tubes and FRP-confined concrete-filled steel tubes (CCFTs).

The first part of the PhD thesis is on FRP-confined hollow steel tubes. A series of axial compression tests is first presented which confirms the effectiveness of FRP confinement of hollow steel tubes whose ductility is otherwise limited by the development of the elephant's foot buckling mode. A finite element (FE) model for predicting the behaviour of these FRP-confined tubes is then described and verified with the test results. The FE model was also used to explore the use of FRP jackets to strengthen thin steel cylindrical shells (e.g. tanks and silos) against local elephant's foot buckling failure at the base and the numerical results presented in the thesis indicate that the FRP jacketing technique leads to significant increases in the strength of such thin shells.

An examination of the behaviour and modelling of CCFTs under monotonic and cyclic axial compression forms the next part of the thesis. The experimental work presented in this part of the thesis includes three series of monotonic axial compression tests and two series of cyclic axial compression tests, where the main test parameters examined were the thickness of the steel tube and the stiffness of the FRP jacket. The test results revealed that the FRP jacket was very effective in improving both the monotonic and the cyclic axial compressive behaviour of CCFTs in terms of both strength and ductility, as it substantially delayed or in some cases completely suppressed local buckling in the steel tube; the behaviour of the concrete was also significantly enhanced due to the additional confinement from the FRP jacket. An analysis-oriented stress-strain model was also developed for CCFTs under monotonic axial compression. The analysis-oriented model considers explicitly interactions between the three components (i.e. concrete, steel tube and FRP jacket) in a CCFT and is shown to provide reasonably accurate predictions of the test results. A cyclic stress-strain model is then presented for the confined concrete in CCFTs. This cyclic stress-strain model was revised from an existing cyclic stress-strain model for FRP-confined concrete by incorporating the new analysis-oriented model developed in the present study for the prediction of the envelope stress-strain curve.

The final part of the PhD thesis presents a series of large-scale tests on CCFTs subjected to combined constant axial compression and monotonic or cyclic lateral loading. The FRP jacket provided near the column end is shown to effectively delay or completely suppress local buckling failure at the end of a cantilevered CCFT. In CCFTs with a relatively thick FRP jacket, the buckling deformation may be forced by the FRP jacket to appear above the jacketed region. Both the flexural strength of the section and the lateral load-carrying capacity of the column can be significantly enhanced due to FRP confinement.

# LIST OF PUBLICATIONS

## REFEREED JOURNAL PAPERS

Teng, J.G., and Hu, Y.M. (2007). "Behaviour of FRP-jacketed circular steel tubes and cylindrical shells under axial compression." *Construction and Building Materials*, 21(4), 827-838.

Hu, Y.M., Yu, T., and Teng, J.G. (2010). "FRP-confined circular concrete-filled thin steel tubes under axial compression." submitted

**CONFERENCE PAPERS**

Teng, J.G., and Hu, Y.M. (2004) "Suppression of local buckling in steel tubes by FRP jacketing." *Proceedings, Second International Conference on FRP Composites in Civil Engineering*, Adelaide, Australia, 8-10 December.

Teng, J.G. and Hu, Y.M. (2005). “Enhancement of seismic resistance of steel tubular columns by FRP jacketing”. *Proceedings, Third International Conference on Composites in Construction*, Lyon, France, 11-13 July, 307-314.

Teng, J.G., and Hu, Y.M. (2006). "Theoretical model for FRP-confined circular concrete-filled steel tubes under axial compression." *Proceedings, Third International Conference on FRP Composites in Civil Engineering,* Miami, Florida, USA, 13-15 December, 503-506.

Teng, J.G., Yu, T., Hu, Y.M. and Wong, Y.L. (2007). “Hybrid FRP-concrete-steel columns”, *Proceedings, Advanced Composites in Construction Conference,* April 2-4, University of Bath, Bath, UK.

Hu, Y.M., Yu, T., and Teng, J.G. (2009). "Axial compression tests on FRP-jacketed circular concrete-filled thin steel tubes." *Proceedings, Sixth International Conference on Advances in Steel Structures*, Hong Kong, China, 16-18 December.

Li, S.Q., Chen, J.F., Bisby, L., Hu, Y.M., and Teng, J.G. (2010). "Effect of geometric discontinuous on FRP strain efficiency in FRP-confined circular concrete-filled steel tubes." *Proceedings, Fifth International Conference on FRP Composites in Civil Engineering*, Beijing, China, 27-29 September.

# ACKNOWLEDGEMENT

The author would like to take this opportunity to express his sincere thanks to his supervisor, Prof. Jin-Guang Teng, and his co-supervisor, Dr. Tao Yu, for their continuous guidance, support and encouragement throughout his research study. Prof. Teng and Dr. Yu's passion for their work, rigorous approach to academic research, breadth and depth of knowledge in structural engineering, and creative and unique insight into many academic problems have demonstrated the essential qualities that a good researcher should possess. The author has been working in a consultant company for nearly one year and has found that all these qualities have greatly benefited him in developing his career.

The author is grateful to The Hong Kong Polytechnic University for providing all the facilities and the financial support for the study.

This PhD research project included a series of experimental studies on 28 columns with different characteristics (excluding the trial specimens). The author is very thankful to the technical staff of the Heavy Structures Laboratory of the Department of Civil and Structural Engineering of The Hong Kong Polytechnic University, in particular, Messrs K.H. Wong, W.C. Chan, K. Tam, M.C. Ng, C.F. Cheung, T.T. Wai, K.H. Kwan, Y.H. Yiu and C.S. Liu for their valuable advice and assistance during the experimental programme.

Special thanks go to the author's friends and fellow students in the Department of Civil and Structural Engineering of The Hong Kong Polytechnic University, in particular, Drs Tao Jiang, Lei Zhang, Guang-Ming Chen, Jin-Yu Lu, Messrs. Shi-Shun Zhang, Dilum Fernando, Qiong-Guan Xiao, Bing Zhang, Yu-Bo Cao, Wing-Keung Ho, Bo Li, Man Fong and Si-Wei Liu not only for their constructive discussions but also for their encouragement in times of difficulty during the course of study.

The author has been away from his home town for nearly 10 year and has been unable to fulfill his duty of looking after his parents over this long period of time. It is his sister and brother-in-law who have willingly shouldered this tremendous responsibility over these years. Hence, the author is greatly indebted to his parents, his sister, Yue-Lai Hu, his brother-in-law, Ya-Ning Li, and his two lovely nieces for their constant understanding, continuous support and encouragement, and everlasting love.

Last but certainly not least, the author would like to thank his girlfriend, Miss Yi-Wen Lu and her parents for their understanding and continuous support. Miss Lu has been so considerate, patient and supportive throughout the author's PhD candidature. It is she who shared the most difficult time with the author. This thesis is dedicated to her with the author's everlasting love.

# CONTENTS

**CHAPTER 5 MODELLING OF FRP-CONFINED CIRCULAR CONCRETE-FILLED STEEL TUBULAR COLUMNS UNDER AXIAL COMPRESSION 120**

# LIST OF FIGURES

# LIST OF TABLES

# NOTATION

| | |
|---|---|
| $A \quad B \quad C$ | coefficients of quadratic equation for determining steel stress state on yield surface |
| $A_2, \ B_2 \ \ C_2$ | coefficients of quadratic equation for determining return envelope strain |
| $A_c$ | cross sectional area of concrete |
| $A_s$ | cross sectional area of steel tube |
| $a \ b \ c$ | coefficients for determining concrete unloading path |
| $c_\Phi$ | a coefficient in lateral strain equation |
| $D_c$ | diameter of concrete core |
| $D_{outer}$ | outer diameter of steel tube |
| $D'$ | horizontal distance between the tips of the two transducers |
| $E_c$ | concrete elastic modulus |
| $E_{el}$ | absorbed elastic energy |
| $E_{frp}$ | elastic modulus of FRP jacket |
| $E_{\mathrm{int}e}$ | absorbed energy at an internal examined point |
| $E_{total}$ | total absorbed energy |
| $E_{re}$ | slope of reloading path |

| | |
|---|---|
| $E_{ret,env}$ | slope at $\varepsilon_{ret,env}$ |
| $E_s$ | elastic modulus of steel |
| $E_{un,0}$ | slope of unloading path at zero stress |
| $f'_{cc}$ | peak strength of confined concrete |
| $f'^{*}_{cc}$ | axial peak strength of concrete under a specific constant confining pressure |
| $f'_{cc,cft}$ | peak concrete strength in CFTs |
| $f'_{co}$ | compressive strength of concrete cylinder |
| $f'_{cu}$ | confined concrete strength at the ultimate state of CFT or CCFT |
| $f_{cu}$ | concrete cube strength |
| $f_y$ | yield strength of steel |
| $f_u$ | tensile strength of steel |
| $H_{adj}$ | adjusted lateral load |
| $H_j$ | lateral load at $j^{\text{th}}$ cycle |
| $H_{\text{mod}}$ | lateral load difference which considers the different second-order effects in different columns |
| $H_{ori}$ | original lateral load |
| $H_{peak}$ | peak lateral load |
| $H_y$ | lateral load at yield displacement |
| $h_{frp}$ | height of FRP jacket |
| $i$ | number of increments |

| | |
|---|---|
| $j$ | number of cycles |
| $K_0$ | initial flexural stiffness |
| $K_{\text{int}e}$ | flexural stiffness at an internal examined point |
| $K_u$ | ultimate flexural stiffness |
| $k_\varepsilon$ | FRP efficiency factor |
| $k_{\varepsilon 1}$ | ratio of the average hoop strain to the maximum hoop strain of FRP jacket |
| $k_{\varepsilon 2}$ | ratio of the maximum hoop strain in an FRP jacket at the ultimate state to the ultimate tensile strain from flat coupon tests |
| $L_0$ | column length between two hinged ends |
| $l_{col}$ | length of column |
| $l_{cr}$ | critical wave length of imperfection in the meridional direction of hollow steel tube |
| $l_{seg}$ | length of segment |
| $l_w$ | half-wave length of imperfection in the meridional direction of hollow steel tube |
| $M_{co}$ | peak moment of CFT column |
| $N_{35}$ | axial load which is 35% of squash load |
| $N_{app}$ | applied axial load |
| $N_{peak}$ | peak axial load |
| $N_{peak,cft}$ | peak axial load of CFT |
| $N_{sq}$ | squash load |
| $N_{sq,cft}$ | squash load of CFT |

| | |
|---|---|
| $N_u$ | axial load at ultimate state |
| $N_y$ | yield load defined as the yield stress of steel from tensile coupon tests times the cross-sectional area of the steel hollow tube |
| $n$ | number of loading/unloading cycles |
| $n_e$ | number of effective cycles |
| $n_\theta$ | number of circumferential waves of the imperfection of hollow steel tube |
| $p_r$ | internal pressure |
| $R_s$ | radius of tube middle surface of steel hollow tube |
| $r$ | parameter accounting for the brittleness of concrete |
| $t_{frp}$ | thickness of FRP jacket |
| $t_s$ | thickness of steel tube |
| $w_0$ | maximum amplitude of the imperfection of hollow steel tube |
| $y$ | axial coordinate from one end of the tube |
| $\alpha_u$ | ultimate rotation |
| $\alpha_y$ | yield rotation |
| $\beta_e$ | constant for taking account of strength deterioration |
| $\beta_{un,n}$ | partial unloading factor of $n^{th}$ cycle |
| $\gamma_{re,n}$ | partial reloading factor of $n^{th}$ cycle |
| $\Delta$ | axial shortening |
| $\Delta_1$ | LVDT readings on western side |
| $\Delta_2$ | LVDT readings on eastern side |

| | |
|---|---|
| $\Delta_{peak,chst}$ | axial shortening of confined hollow steel tube at peak load |
| $\Delta_{peak,bhst}$ | axial shortening of bare hollow steel tube at peak load |
| $\Delta_{u}$ | axial shortening at ultimate state |
| $\Delta_{u,cft}$ | axial shortening of CFT at ultimate state |
| $\Delta_{u,pre}$ | predicted axial shortening |
| $\delta$ | lateral displacement |
| $\delta_{\mathrm{int}e}$ | lateral displacement at an internal examined point |
| $\delta_{j}$ | lateral displacement at $j^{\mathrm{th}}$ cycle |
| $\delta_{u}$ | lateral displacement at ultimate state |
| $\delta_{y}$ | yield lateral displacement |
| $\theta$ | circumferential angle (radian) |
| $\varepsilon_{cc}^{*}$ | axial strain at the peak axial strength of concrete under a specific constant confining pressure |
| $\varepsilon_{co}$ | axial strain at the peak compressive strength of unconfined concrete |
| $\varepsilon_{pl,n}$ | plastic strain of $n^{\mathrm{th}}$ cycle |
| $\varepsilon_{pl,\exp}$ | experimental plastic strain |
| $\varepsilon_{pl,pre}$ | predicted plastic strain |
| $\varepsilon_{re}$ | reloading strain |
| $\varepsilon_{ref,n}$ | reference strain of $n^{\mathrm{th}}$ cycle |
| $\varepsilon_{ret,env}$ | strain where reloading path intersects unloading curve |
| $\varepsilon_{rupt}$ | FRP rupture strain |

| | |
|---|---|
| $\varepsilon_{rupt,\max}$ | maximum strain in FRP jacket at rupture |
| $\varepsilon_{u}$ | concrete axial strain at the ultimate state |
| $\varepsilon_{un}$ | unloading strain |
| $\varepsilon_{u,cft}$ | concrete axial strain at the ultimate state of CFTs |
| $\varepsilon_{un,env}$ | envelope unloading strain |
| $\varepsilon_{x}$ | axial strain |
| $\varepsilon_{x,c}$ | axial strain of concrete |
| $\varepsilon_{x,s}$ | axial strain of steel |
| $\varepsilon_{\theta}$ | hoop strain |
| $\varepsilon_{\theta,c}$ | hoop strain of concrete |
| $\varepsilon_{\theta,frp}$ | hoop strain of FRP jacket |
| $\varepsilon_{\theta,s}$ | hoop strain of steel |
| $\Delta\varepsilon_{x}$ | a small axial strain difference |
| $d\varepsilon_{x}$ | axial strain increment |
| $d\varepsilon_{\theta}$ | hoop strain increment |
| $\mu_{comb}$ | combined index in terms of both displacement and energy |
| $\mu_{e,cumu}$ | cumulative index based on energy |
| $\mu_{e,nonc}$ | non-cumulative index based on energy |
| $\mu_{K}$ | flexural damage ratio based on stiffness |
| $\mu_{K,\mathrm{mod}}$ | modified flexural damage ratio based on stiffness |

| | |
|---|---|
| $\mu_{\alpha}$ | ductility factor based on rotation |
| $\mu_{\delta}$ | ductility factor based on displacement |
| $\mu_{\phi}$ | ductility factor based on curvature |
| $\nu$ | steel Poisson's ratio |
| $\zeta$ | a positive number between zero and unity for determining steel stress state on yield surface |
| $\sigma_c$ | axial stress of concrete |
| $\sigma_{new,\exp}$ | experimental concrete new stress at the reference strain |
| $\sigma_{new,n}$ | concrete new stress at the reference strain of $n^{\text{th}}$ cycle |
| $\sigma_{new,pre}$ | predicted concrete new stress at the reference strain |
| $\sigma_r$ | total confining pressure |
| $\sigma_{r.frp}$ | confining pressure provided by FRP jacket |
| $\sigma_{r.s}$ | confining pressure provided by steel tube |
| $\sigma_{re}$ | concrete reloading stress |
| $\sigma_{ref,n}$ | concrete reference stress of $n^{\text{th}}$ cycle |
| $\sigma_{ret,env}$ | stress at $\varepsilon_{ret,env}$ |
| $\sigma_{un,n}$ | unloading stress of $n^{\text{th}}$ cycle |
| $\sigma_{un,env}$ | unloading stress at envelope curve |
| $\sigma_{x,s}$ | steel axial stress |
| $\sigma_{x,s,y}$ $\sigma_{\theta,s,y}$ | steel stress state on yield surface |
| $\sigma_{\theta,s}$ | steel hoop stress |

$\varphi_n$ stress deterioration ratio of $n^{\text{th}}$ cycle

$\varphi_{n,ful}$ stress deterioration ratio specially for the case of $\beta_{un} = 1$

$\phi_u$ ultimate curvature

$\phi_y$ yield curvature

$\phi_\Delta$ average curvature of the segment based on LVDT readings

$\omega_n$ strain recovery ratio of $n^{\text{th}}$ cycle

$\omega_{n,ful}$ strain recovery ratio specially for the case of $\gamma_{re,n-1} = 1$

# CHAPTER 1

# INTRODUCTION

## 1.1 BACKGROUND

### 1.1.1 Local Buckling in Steel Tubular Columns

Hollow and concrete-filled steel tubes are widely used as columns in many structural systems (Oehlers and Bradford 1995; Uy 1998; Hajjar 2000) and local buckling can occur when they are subject to axial compression alone or in combination with monotonic/cyclic lateral loading. For example, hollow steel tubes are often used as bridge piers and such bridge piers suffered extensive damage and even collapses during the 1995 Hyogoken-nanbu earthquake (Kitada et al. 2002). Figure 1.1a shows a local buckling failure mode at the base of a steel bridge pier and the subsequent repair of the pier by the addition of welded vertical stiffeners. Such local buckling is often referred to as elephants' foot buckling. In typical circular tubular structures, elephant's foot buckling appears after yielding and the appearance of this inelastic local buckling mode normally signifies the exhaustion of the load-carrying capacity and the end of ductile response. The latter is of particular importance in seismic design, as the ductility and energy absorption capacity of the column dictates its seismic resistance.

The elephant's foot buckling mode is not only the critical failure mode in commonly used hollow steel tubes under axial compression and/or bending; it also occurs in much thinner cylindrical shells in steel storage silos and tanks under combined axial compression and internal pressure (Figure 1.1b) as has been commonly observed in earthquakes (Manos and Clough 1985) and under static loading (Rotter 1990). In rectangular (including square) steel tubes, a similar failure mode can occur. Here, the buckling deformation is normally outwards on the flanges and inwards on the webs.

In concrete-filled tubes (CFT), the concrete and the steel tube interact in a beneficial manner: the steel tube confines the concrete and the concrete delays the occurrence of local buckling in the steel tube. CFTs are thus an economic form of structural members, mainly as columns for buildings and bridges, and research on CFTs is abundant (Uy 1998; Hajjar 2000; Han et al. 2004). Nevertheless, although inward buckling deformations of the tube are prevented by the concrete, local outward buckling deformations of the steel tube might still occur and lead to degradation in the confinement to the concrete provided by the steel tube, and hence the overall strength and ductility of the column. When CFTs are used as columns, being subjected to combined axial and lateral loads, the critical regions for the local buckling of the steel tube are near the ends of the column where the moments are the largest. These critical regions are regions where plastic hinges are expected (i.e. plastic hinge regions). Under seismic loading, large plastic rotations within these regions without significant degradation in stiffness and strength are needed to ensure good seismic performance.

### 1.1.2 Traditional Column Retrofit Techniques

A number of methods have been proposed for the seismic retrofit of hollow steel tubes as bridge piers where enhancement of ductility without a significant strength increase is preferred. These techniques include: 1) filling of the steel tube with concrete in the critical region (Kitada et al. 2002) and ; 2) addition of stiffeners or stiffening sub-structures of various forms generally inside the tube for practical and aesthetical reasons (Hsu and Chang 2001; Kitada et al. 2002; Yamao et al. 2002); 3) the creation of an energy absorption segment in the column by leaving a small vertical gap in the filling of the steel tube with concrete (Kitada et al. 2002); and 4) the use of an outer circular tube segment with a clearance between the existing column and the retrofitting segment to provide confinement to the existing steel tube after the development of deformations in the elephant's foot buckling mode (Nishikawa et al. 1998). Method 1) can lead to a significantly higher ultimate strength that may endanger the foundation which is costly and often extremely difficult to strengthen, while Method 2) is costly and inconvenient and may also lead to undesirable strength enhancements. In Method 3), the hollow part needs to be very short to delay local buckling, although local buckling can still occur with outward deformations. Method 4) is expected to be able to successfully enhance ductility without any significant enhancement in strength, but the tests by Nishikawa et al. (1998) did not reveal the full potential of the method as the clearance was arbitrarily set.

For the seismic retrofit CFT columns, several methods developed for the seismic retrofit of reinforced concrete (RC) bridge columns can be directly used. The column might be retrofitted by: 1) the confinement of plastic hinges with steel jackets (Priestley et al. 1992; Chai et al. 1994; Mao and Xiao 2006); 2) the confinement of plastic hinge regions using reinforced concrete jackets (Chapman and Park 1991); and 3) the addition of a reinforced concrete infill wall between two columns (Haroun et al. 2002). In Method 1), axial stresses are likely to develop in the steel jacket due to strain compatibility, which might lead to buckling of steel jackets and hence degradation of the confinement effect. Methods 2) and 3) lead to substantial increases in column stiffness which may attract greater seismic forces to the column (Elsanadedy 2002); these two techniques are thus undesirable in terms of the seismic retrofit.

### 1.1.3 The FRP Jacketing Technique

FRP composites are formed by embedding continuous fibres in a polymeric resin matrix. There are two commonly used FRP systems, namely glass FRP (referred to as GFRP hereafter) system and carbon FRP (referred to as CFRP hereafter) system. FRP composites have a high strength-to-weight ratio and excellent corrosion resistance. Due to these advantages and their ease in site handling derived from their lightweight nature and the use of the adhesive bonding technique, FRP composites have become increasingly popular in civil engineering. Nowadays, various forms of FRP products, including bars, sheets, plates and profiles are commercially available. These products have been used in construction in many different ways: from new construction to the retrofit of existing structures and from internal reinforcing to external strengthening. Among the various possible applications, the most popular one is the external bonding of FRP composites for the strengthening/retrofit of concrete structures (Teng et al. 2002; Teng et al. 2003; Teng and Lam 2004). In particular, the use of confining FRP jackets for the strengthening/retrofit of concrete columns has been very popular (Teng and Lam 2004).

FRP jackets offer many advantages over steel jackets, including their excellent corrosion resistance, very high strength-to-weight ratio and flexibility in shape. The latter two characteristics lead to greatly reduced labor cost and construction time and hence reduced disturbance to services provided by the structure. An additional advantage of an FRP jacket over a steel jacket is that while steel is an isotropic material with the same strength and stiffness in all directions so that a steel jacket may buckle under axial compression, an FRP jacket can be formed with fibres mainly or only in the hoop direction to offer confinement without attracting significant axial stresses. Due to these advantages, FRP jacketing is now the method of choice for the seismic retrofit of RC columns in many projects.

Xiao (2004) recently proposed a novel form of columns, named by him as confined CFT (CCFT) columns in which the column end portions are confined with steel tube segments or FRP jackets. Here, by providing an FRP or steel jacket, the through-tube is prevented from deforming inwards by the concrete core and outwards by the jacket, so both the ductility and strength of CCFTs can be greatly enhanced in the end regions. His initial tests verified the many expected advantages of the CCFT system (Xiao et al. 2005). It may be noted that the CCFT system and the tube confinement retrofit method proposed by Nishikawa et al. (1998) are based on the same principle.

The use of FRP jackets for the suppression of local buckling in circular hollow steel tubes and shells was first explored at The Hong Kong Polytechnic University (Teng and Hu 2004) as an extension of Xiao’s (2004) concept for the FRP confinement of CFT columns. The method was also independently explored by Nishino and Furukawa (2004) in Japan. Shaat and Fam (2004) explored the use of FRP jackets for the strengthening of square hollow steel tubes where both confinement with horizontal fibres and direct load resistance with vertical fibres were considered with the aim being the enhancement of strength and stiffness. FRP wrapping was shown to lead to 10-20% strength increases by Shaat and Fam (2004) in their tests.

The above discussion illustrates clearly the potential of FRP jacketing of hollow steel tubes and CFTs in both retrofit/strengthening and new construction. In the retrofit/strengthening of hollow steel tubes and CFTs, FRP jacketing provides a simple and effective method like FRP jacketing of RC columns, which is now widely used throughout the world for enhancement of both strength and ductility. In new construction, FRP jacketing of critical regions to enhance strength and ductility of hollow steel tubes and CFTs can lead to more economic and/or more ductile structures (Xiao 2004). Indeed, for new columns, the use of local FRP confinement can lead to a substantial reduction in the through-tube thickness as the thickness of a conventional steel tube is dictated by the requirement of the critical regions because thickness variations along the length are generally costly to achieve in practice.

## 1.2 RESEARCH OBJECTIVES

This thesis reports research carried out by the candidate over the last few years aimed at developing an improved understanding of the structural behaviour of steel tubular columns confined using FRP jackets. The work has been carried out with both static and seismic applications in mind, so enhancements in both strength and ductility are considered. The work has also been carried out with both strengthening/retrofit and new construction in mind, so the results are applicable to both the strengthening/retrofit of steel tubular columns with FRP jackets and the design of FRP-confined steel tubular columns in new structures.

For columns, the compressive behaviour is obviously the most important as it underpins studies into their behaviour under other loading conditions. In addition, columns are normally also subjected to bending due to load eccentricity or lateral loads. This thesis therefore first discusses the pure axial compressive behaviour of both hollow steel tubes and CFTs confined with FRP jackets. The behaviour of CFTs subjected to combined axial compression and lateral loading is dealt with as the next subject. More specifically, the research work presented in this PhD thesis was carried out with the following objectives:

1. To obtain a good understanding of the axial compressive behaviour of hollow steel tubes confined with FRP jackets through both experimental and finite element investigations;
2. To clarify the mechanism of confinement from both the FRP jacket and the steel tube to the concrete core in CCFT columns through experimental work;
3. To investigate the behaviour of CFT columns with FRP confinement of the critical region through experimental work; and
4. To develop a simple one-dimensional stress-strain model for confined concrete in CCFTs subjected to monotonic or cyclic axial compression for predicting the behaviour of CCFTs.

## 1.3 LAYOUT OF THE THESIS

The thesis comprises eight chapters. Chapter 1 provides background information on the needs and objectives of the research project. Chapters 2 to 7 present a series of experimental and theoretical studies on various aspects on the behaviour of steel hollow tubes and CFTs confined with FRP jackets. Details of these chapters are summarized below.

Chapter 2 presents a review of the existing literature covering topics related to the present study. The behaviour of hollow steel tubes and CFT columns are discussed first, with particular attention to the elephants' foot buckling mode under pure axial compression or combined bending and axial compression. Some common column retrofit methods are then reviewed and compared in order to highlight the advantage of the method of FRP jacketing. The stress-strain models for confined concrete, which are important in theoretical analysis, as well as relevant existing research, are also examined.

Chapter 3 presents the results of a study in which the benefit of FRP confinement of hollow steel tubular columns under axial compression was examined. Axial compression tests on FRP-confined steel tubes are described first. Finite element modelling of these tests is next discussed. Both the test and the numerical results show that FRP jacketing is a promising technique for the retrofit and strengthening of circular hollow steel tubular columns. In addition, finite element results for FRP-jacketed thin cylindrical shells under combined axial compression and internal pressure are presented to show that FRP jacketing is also an effective strengthening method for such shells failing by elephant's foot buckling near the base.

In Chapter 4, the benefit of FRP confinement of CFTs with a thin steel tube under pure axial compression is examined through an experimental study. Steel tubes of three large diameter-to-thickness ratios were employed in the study to highlight the importance of local buckling and the benefit of FRP confinement. A brief introduction to the test programme is first presented. The parameters of interest are the diameter-to-thickness ratio of the steel tube and the hoop stiffness of the FRP jacket. The procedure of specimen preparation is then described, including the fabrication of thin steel tubes and the wet layup process of forming FRP jackets. The test setup and instrumentation are also reported, followed by the presentation of experimental results and discussions. In particular, based on the flow theory of plasticity for the steel tube, the behaviour of the steel tube is explicitly isolated from that of the confined concrete so that the mechanism in a CCFT is clarified. The test results clearly indicate that FRP jacketing is a promising technique for the retrofit and strengthening of circular CFT columns with a thin steel tube.

Chapter 5 is concerned with the modelling of the monotonic axial compressive behaviour of confined concrete in CCFTs. A theoretical model is proposed and its concept and detailed analysis process are presented. The proposed model is initially based on the active-confinement model proposed by Jiang and Teng (2007) and the lateral equation proposed by Teng et al. (2007). Comparisons of theoretical predictions from this initial proposal with the test results presented in Chapter 4 indicate that the lateral equation proposed by Teng et al. (2007) based on test results of FRP-confined concrete and actively-confined concrete is incapable of accurate simulation of the lateral dilation behaviour of concrete in CCFTs. On the contrary, the active-confinement model proposed by Jiang and Teng (2007) may still be regarded as applicable to the confined concrete in CCFTs. The lateral strain equation is subsequently revised using a simple and direct method. With this modification, the proposed model is capable of accurate prediction of not only the test results of Chapter 4 but also available test results reported by other researchers.

Chapter 6 presents a study on the behaviour of CCFTs under axial cyclic compression. Results from a series of axial cyclic compression tests of CCFTs are first presented and discussed, followed by the development of a cyclic stress-strain model for the confined concrete in such columns.

In Chapter 7, an experimental study on large-scale CFT and CCFT columns is presented. A brief introduction to the test programme is first presented. The parameters of interest are the stiffness of the FRP jacket as well as the loading scheme. The procedure of specimen preparation is then described. The issue of eliminating the horizontal frictional force in the testing frame is next presented; this friction force, which is a deficiency of the testing machine, was large enough to influence the reliability of the test results. The test setup and instrumentation are also reported, followed by the presentation of the experimental results and discussions.

The performance of a CFT column when the column is subjected to both constant axial compression and cyclic lateral loading can be significantly improved by the FRP jacketing.

The thesis closes with Chapter 8, where the conclusions drawn from the previous chapters are reviewed, and areas that are in need of further research are highlighted.


(a) Failure near the base of a steel tube

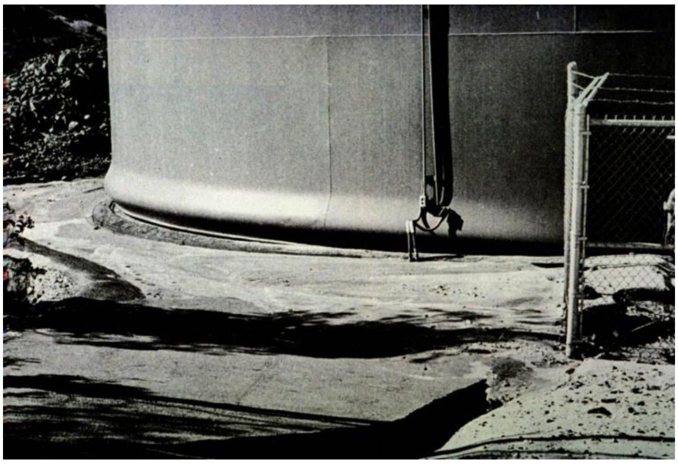

(b) Failure at the base of a liquid storage tank

Figure 1.1 Elephant’s foot buckling in a steel tube or shell

(Courtesy of Dr. H.B. Ge, Nagoya University & Prof. J.M. Rotter, Edinburgh University)

# CHAPTER 2

# LITERATURE REVIEW

## 2.1 INTRODUCTION

This chapter presents a review of existing knowledge related to the current study. The behaviour of hollow steel tubes and concrete filled steel tubes is discussed first, with particular attention to the local buckling failure mode under combined bending and axial compression. Some common column retrofit methods are then reviewed and compared in order to highlight the advantage of the method of FRP jacketing which is regarded as a promising new retrofit method. The stress-strain models for confined concrete and steel are important in the theoretical analysis of steel tubular columns and are thus also examined. Last but not least, the existing methods for theoretical analysis of columns are also briefly reviewed.

## 2.2 BEHAVIOUR OF CIRCULAR HOLLOW STEEL TUBULAR COLUMNS

Circular hollow steel tubes are widely used as columns in many structural systems and a common failure mode of such tubes when subjected to axial compression and bending is local buckling near a column end. For example, hollow steel tubes are often used as bridge piers and such bridge piers suffered extensive damage and even collapses during the 1995 Hyogoken-nanbu earthquake (Kitada et al. 2002). Figure 1.1a shows a local buckling failure mode at the base of a steel bridge pier and the repair of the pier by the addition of welded vertical stiffeners. Such local buckling is often referred to as elephant’s foot buckling. In typical circular tubular members, elephant’s foot buckling appears after yielding and the appearance of this inelastic local buckling mode normally signifies the exhaustion of the load carrying capacity and/or the end of ductile response. The latter is of particular importance in seismic design, as the ductility and energy absorption capacity of the column dictates its seismic resistance.

The elephant’s foot buckling mode is not only the critical failure mode in commonly used circular steel tubular columns under axial compression and/or bending but also a common failure mode in much thinner cylindrical shells in steel storage silos and tanks under combined axial compression and internal pressure (Figure 1.1b) as has been commonly observed in earthquakes (Manos and Clough 1985) and under static loading (Rotter 1990).

## 2.3 BEHAVIOUR OF CIRCULAR CONCRETE-FILLED STEEL TUBULAR COLUMNS

Concrete filled steel tubes (CFTs) have been widely used as columns in moment-resisting frame structures (Shams and Saadeghvaziri 1997; Roeder 1998; Hajjar 2000; Shanmugam and Lakshmi 2001). Their use has ranged from compression members in low-rise buildings to large diameter members used as the primary lateral resistance columns in multi-story frames. For example, concrete-filled box columns, fabricated from four welded steel plates, and concrete-filled steel circular pipe columns have been used in some of the tallest structures (Roeder 1998). In addition, CFT columns have been commonly used as bridge piers throughout Japan (Kitada 1998).

CFT structural members have a number of distinct advantages over equivalent steel or reinforced concrete members: (1) in CFT columns, the concrete and the steel tube interact in a beneficial manner: the steel tube confines the concrete and the concrete delays the occurrence of local buckling in the steel tube, leading to enhanced axial and flexural capacities; (2) the steel tube confines the entire concrete core in the circumferential direction which leads to an excellent energy absorption capacity; (3) CFT members are more economical than steel members due to the reduced usage of steel; and (4) the steel tube can be used as formwork for casting concrete, leading to cost savings in the construction process.

In the past several decades, steady progress has been made in understanding the behaviour of CFT structural members through not only experimental but also theoretical studies (Gardner and Jacobson 1967; Knowles and Park 1969; O'Shea and Bridge 1997; Schneider 1998; O'Shea and Bridge 1999; Gourley et al. 2001; Johansson and Gylltoft 2002; Sakino et al. 2004; Romero et al. 2005; Chung et al. 2009; Hong and Varma 2009; Dai and Lam 2010; Song et al. 2010; Xiao and Choi 2010). The main parameters of interest in understanding the behaviour of CFT columns include: (1) the cross-sectional shape [i.e. circular, square, rectangular or more recently elliptical (Dai and Lam 2010)]; (2) the slenderness ratio; (3) the strength of the in-filled concrete; (4) the yield stress of the steel tube; (5) the manner of loading application (i.e. loading the entire section, the steel section only or the concrete core only); and (6) the loading condition (i.e. concentric or eccentric axial compression, pure bending etc.). In addition, some researchers have investigated the behaviour of concrete-filled double-skin tubular stub columns which consist of two concentric steel tubes and an concrete infill between them (Wei et al. 1995; Tao et al. 2004; Han et al. 2006; Yu et al. 2009; Lu et al. 2010).

The present review is focussed on the behaviour of CFT columns with a circular section as it has been widely recognised that FRP confinement of circular sections is much more effective than rectangular sections (Schneider 1998; Shanmugam and Lakshmi 2001; Inai et al. 2004; Romero et al. 2005).

### 2.3.1 CFT Short Columns

Extensive experimental studies have been conducted on short CFTs under axial compression with relatively low diameter-to-thickness ratios (e.g. $D_{outer} / t_s$

ratios <100) (Gardner and Jacobson 1967; Knowles and Park 1969; Schneider 1998; Johansson and Gylltoft 2002; Fam et al. 2004; Giakoumelis and Lam 2004; Sakino et al. 2004; De Nardin and El Debs 2007). On the contrary, research on CFTs with a thin steel tube (e.g. with $D_{outer}/t_s$ ratios > 100) are much more limited. Indeed, precise definitions of thin-walled CFTs and thick-walled CFTs in terms of the diameter-to-thickness ratio do not exist in the published literature (Prion and Boehme 1994; O'Shea and Bridge 1997; O'Shea and Bridge 1999; Sakino et al. 2004).

The interaction mechanism of a CFT short column (i.e. the interaction between the steel tube and the concrete core) can be summarized as follows based on the existing research (Shams and Saadeghvaziri 1999; Johansson 2002; Johansson and Gylltoft 2002). When concentric axial compression is applied to the steel tube and the concrete core of a CFT simultaneously, the steel tube expands more in the lateral direction than the concrete core in the early stage of loading due to it’s the larger Poisson’s ratio of steel. Therefore, no confinement from the steel tube to the concrete core can be expected during this stage. As a result, provided the bond between the steel tube and the concrete core does not break, the initial hoop stress in the steel tube is compressive while the concrete is initially subjected to hoop tension due to tensile radial stresses from the steel tube. As the axial strain increases, the lateral expansion of concrete becomes greater than that of steel, leading to the development of radial compressive stresses between the steel tube and the concrete. As soon as radial compression appears, the steel tube acts to confine the concrete core. From this moment onwards, the concrete core is subjected to tri-axial compression while the steel tube is subjected to axial compression and hoop tension, provided local buckling of the steel tube has not occurred.

As the applied loading increases further, failure of thick-walled CFTs is likely to involve a combination of local buckling of the steel tube after yielding and crushing of the concrete. The corresponding load-shortening curve is usually of the hardening type, showing good ductility because of the excellent confinement from the steel tube (Schneider 1998). However, the failure mode of thin-walled CFTs tends to be heavily dominated by local buckling of the steel tube, with associated shear failure of the concrete core (Prion and Boehme 1994). Consequently, the design specifications throughout the world concerning CFTs (EC 4 2004; ACI 318 2008) generally specify limits for the steel yield strength, the concrete strength as well as the $D_{outer} / t_s$ ratio (Table 2.1) so as to ensure that some ductile yielding of the steel generally occurs prior to the local buckling of the steel tube or to the crushing of the concrete core.

In particular, the limiting $D_{outer} / t_s$ ratios defined in ACI 318 (2008) and EC 4 (2004) for circular steel tubes in CFT columns are all below 100 with a steel yield stress of 235 MPa aiming to prevent buckling of a hollow steel tube prior to its longitudinal yielding (Boyd et al. 1995). Hence, these limits are simply specified to be close to the limiting $D_{outer} / t_s$ ratios for hollow steel tubes under axial compression [see Table 2.1; (AS 4100 1998; BS 5950 2000; AISC 360 2005)]. However, these limits in design standards might not be necessary if the steel tube is primarily provided to offer confinement to the concrete core. Xiao (2004) recently proposed an innovative column form (CCFT) in which the critical regions are confined. This idea would allow the reduction of the steel tube thickness outside the critical region of the column. That is, for CCFTs, thin steel tubes (e.g. with $D_{outer} / t_s$ ratios > 100) are expected to be a more economical option.

The confinement action in CFTs plays a very important role in their structural behaviour. The confinement can be influenced not only by the manner of loading (Knowles and Park 1969; O'Shea and Bridge 1997; Johansson and Gylltoft 2002; Fam et al. 2004; Romero et al. 2005) but also by the local buckling of the steel tube (O'Shea and Bridge 1999). There are three manners of loading for CFT columns: (1) the load acts on the concrete but not the steel tube; (2) the load acts on the steel but not the concrete core; and (3) the load acts on both the concrete core and the steel tube simultaneously. In cases (1) and (2), axial stresses can only be transferred between the steel tube and the concrete core via interfacial friction and the axial stress in the component not directly loaded is much smaller than when both the concrete and the steel tube are simultaneously loaded [case (3)]. Consequently, the steel tube functions mainly as a confining device in case (1). Since the axial compressive stress in a steel tube has a negative effect on the circumferential hoop stress, the confinement to the concrete core is smaller in case (3) than in case (1). When only the steel tube is loaded, the steel tube confinement does not exist at all as the natural interfacial bond strength is insufficient to redistribute the axial force from the steel tube into the concrete core. In addition, the local buckling load of the steel tube is not enhanced by the in-filled concrete due to the lack of normal interfacial contact. In case (3), strong steel tube confinement will nevertheless be developed when a sufficient amount of load is applied. Therefore, the increase in concrete strength due to steel tube confinement is the greatest when only the concrete is loaded and the extra concrete strength enhancement provided by the steel tube confinement when only the concrete is loaded can fully compensate for the loss in the axial load-carrying capacity due to the absence of direct resistance from the steel tube (O'Shea and Bridge 1999).

The local buckling of a steel tube in CFTs can occur either at or away from the end of the tube. The local wall buckling in the middle region is due to the radial expansion of the tube (Furlong 1967; Schneider 1998), while the local buckling at the end is due to the fixed boundary condition similar to the situation in a hollow steel tube. Schneider (1998) highlighted the occurrence of local buckling in the load-deformation curves; it was shown that the occurrence of local buckling did not necessarily correspond to the peak axial load in such thick-walled concrete-filled steel tubes ( $D_{outer} / t_s$ =47 and 22). In particular, Sham and Saadeghvaziri (1999) concluded that local buckling of steel tube only occurred at the peak load in columns with a $D_{outer} / t_s$ ratio of more than 95 through their numerical modelling. O'shea and Bridge (1999) conducted a series of tests on thin-walled CFTs (with $D_{outer} / t_s$ ratios up to 221) and found that the ultimate load of such CFTs with the occurrence of local buckling was greater than that of their counterparts in which local buckling was prevented by the bond between the concrete and the steel tube. They also explained that the large plastic deformation in the local buckled region was associated with a reduction in the axial load carried by the steel tube. The reduction in the axial stress in the steel tube allowed the development of a greater circumferential tensile stress and hence greater confinement to the concrete core.

Relative few tests have been conducted to study the cyclic behaviour of axially loaded CFT specimens (Kawano and Matsui 1988; Liu and Goel 1988; Zhao et al. 1999; Broderick et al. 2005). Among these studies, only Kawano and Matsui (1988) tested circular concrete filled steel tubes. All the researchers focused on the supporting function of the concrete infill to the steel tube. They showed that that the participation of the concrete infill delayed the local buckling of the steel tube and forced the tube to buckle outward. In addition, the concrete tended to spread the local buckling deformation of the tube over a larger region, mitigating severe strain concentrations. As a result, the participation of concrete increased the number of cycles to failure and hence the amount of energy dissipated. Wei et al. (1995) tested several concrete-filled double-skin steel tubular columns under cyclic axial compression in which both skins were circular steel tubes. They observed that cyclic loading did not have any detrimental effect on the overall load-strain behaviour.

### 2.3.2 CFT Beams and Beam-Columns

Only a limited amount of testing has been performed on circular CFTs under monotonic pure bending (Prion and Boehme 1994; Elchalakani et al. 2001; Wheeler and Bridge 2002) since their primary application is as columns. Particularly, Elchalakani et al. (2001) focused on enhancement in flexural ductility and strength due to in-filled concrete. In addition, they proposed a $D_{outer} / t_s$ limit of 112 for circular CFT beams to achieve their plastic flexural strength. Table 2.1 lists the limits specified in different standards for a steel tube under flexural loading (AS 4100 1998; BS 5950 2000; AISC 360 2005).

The monotonic behaviour of circular CFT beam-columns was investigated by

Furlong (1967). When a circular CFT member is subjected to an axial force and a bending moment, a strain gradient exists over the CFT cross-section, indicating that the CFT section may be subjected to both compressive and tensile stresses at the same time. On the compression side, the concrete and the steel tube work together in resisting compression, while only the steel tube resists tension. As a result, the neutral axis position plays a very important role in determining the flexural strength of the section. Lu and Kennedy (1994) conducted a series of experiments on square and rectangular CFT beam-columns. In their study, they traced the movement of the neutral axis throughout the whole loading process, which should be similar to that in their circular counterparts. When a very small moment is applied without an associated axial load, the section is in the elastic range and the neutral axis is at the mid-height of the section. After the cracking of concrete, the neutral axis moves upward rapidly in order to achieve force equilibrium. Subsequently, the neutral axis continues to shift upwards until the flexural strength is reached together with the yielding of the steel tube on both sides, as well as the spread of plasticity in the concrete and the buckling of steel tube on the compression side. Finally, the loss of resistance of the concrete in compression makes the neutral axis move downwards, leading to degradation in the flexural resistance of the section. During this particular period, severe steel tube buckling together with concrete crushing can be found on the compression side. On the tension side, steel yielding or even fracture can be found. Based on the above mechanism, it can be concluded that enhancement in the flexural strength is closely related to the extent of the upward movement of the neutral axis.

Extensive studies have been conducted on circular CFT beams under cyclic loading (Prion and Boehme 1994; Toshiyuki et al. 1996; Elchalakani et al. 2004; Chitawadagi and Narasimhan 2009; Arivalagan and Kandasamy 2010; Tokgoz and Dundar 2010) and circular CFT beam-columns under cyclic loading (Ichinohe et al. 1991; Sugano and Nagashima 1992; Prion and Boehme 1994; Boyd et al. 1995; Toshiyuki et al. 1996; Elremaily and Azizinamini 2002; Fam et al. 2004; Inai et al. 2004; Han and Yang 2005; Lee 2007; Lu et al. 2009; Valipour and

Foster 2010). Several key parameters which influence the behaviour of beam-columns were investigated by these researchers, namely 1) the $D_{outer} / t_s$ ratio; 2) the axial load ratio which is normally defined as $N_{app} / (A_s f_y + A_c f'_{co})$ in which, $N_{app}$ is the applied axial load, $A_s$ and $A_c$ are the area of steel and concrete sections respectively, $f_y$ is the yield strength of steel, and $f'_{co}$ is the cylinder compressive strength of concrete and 3) the length-to-diameter ($L_0 / D_{outer}$) ratio, where $L_0$ is the column length between two hinged ends.

The $D_{outer} / t_s$ ratio influences directly the section behaviour. A steel tube with a smaller $D_{outer} / t_s$ ratio can confine the concrete on the compression side better, similar to the situation of a CFT section under concentric axial compression. In particular, for a section with a relatively thick steel tube, the occurrence of local buckling in the steel tube may not necessarily signify the strength degradation of confined concrete inside and hence the section flexural resistance (Ichinohe et al. 1991). In Ichinohe's (1991) tests, the $D_{outer} / t_s$ ratios studied were all below 53. As a result, a CFT section with a smaller $D_{outer} / t_s$ ratio has a greater section ductility (Sugano and Nagashima 1992; Toshiyuki et al. 1996; Elchalakani et al. 2001).

The axial load ratio not only has an effect on section behaviour but also influences the member behaviour. The influence on section behaviour can be illustrated clearly by a CFT interaction diagram which has been well established (Tsuda et al. 1996; Hajjar 2000; Fam et al. 2004; Han and Yang 2005). A balanced point exists on this curve. When the axial load level is below that of the balanced point, the flexural strength is enhanced when a higher axial load level exists. On the contrary, the flexural strength degrades rapidly with an increase of the axial load level if the axial load level is higher than that of the balanced point. The axial load ratio influences member behaviour because the axial load level determines the importance of the second order effect, especially in relatively long beam-columns. When the axial load level increases, the second-order effect also increases, and the lateral resistance and ductility of the beam-column degrades rapidly (Sugano and Nagashima 1992; Boyd et al. 1995; Toshiyuki et al. 1996; Han and Yang 2005)

The $L_0 / D_{outer}$ ratio has an effect on CFT member behaviour in two ways: (1) for a given cross-section, if the column is sufficiently long, it fails because of instability and the maximum section flexural strength cannot be achieved (Tsuda et al. 1996; Hajjar 2000). Tsuda et al. (1996) conducted a series of tests on circular CFT columns with two pinned ends under eccentric axial loads and another series of tests on CFT cantilevers. Based on the test observations and results, they found that the strength of the column with a $L_0 / D_{outer}$ =4 could exceed the corresponding full plastic strength due to the confining effect from the steel tube to the concrete core inside. On the contrary, the strength of a column with a $L_0 / D_{outer}$ >12 could not reach the corresponding full plastic strength because of instability. Hajjar (2000) produced an interaction diagram of a circular column with a $L_0 / D_{outer}$ of 30 according to different standards (EC 4 2004; BS 5400 2005; ACI 318 2008) and showed the loss of strength due to flexural buckling of such a long CFT column.; (2) even if the maximum section flexural strength can be achieved, a larger-second order effect exists in a longer beam-column, leading to more rapid lateral strength degradations (Wu et al. 2006b).

## 2.4 EXISTING SEISMIC RETROFIT METHODS FOR COLUMNS

A number of methods have been proposed for the seismic retrofit of hollow steel tubes as bridge piers where enhancement of ductility without a significant strength increase is preferred. These techniques include: (1) filling of the steel tube with concrete in the critical region (Kitada et al. 2002) and ; (2) addition of stiffeners of various forms generally inside the tube for practical and aesthetical reasons (Hsu and Chang 2001; Kitada et al. 2002; Yamao et al. 2002); (3) the creation of an energy absorption segment in the column by leaving a small vertical gap in the filling of the steel tube with concrete (Kitada et al. 2002); and (4) the use of an outer circular tube segment with a clearance between the existing column and the retrofitting segment to provide confinement to the existing steel tube after the development of deformations in the elephant's foot buckling mode (Nishikawa et al. 1998). Method (1) can lead to a significantly higher ultimate load that may endanger the foundation which is costly and often extremely difficult to strengthen, while Method (2) is costly and inconvenient and may also lead to undesirable strength enhancements. In Method (3), the hollow part needs to be very short to avoid early local buckling there, although local buckling can still occur with outward deformations elsewhere. This method involves the welding of diaphragms inside the tube to create the short hollow tube segment and can lead to a larger seismic force for the column due to the additional weight of the concrete. Method (4) is expected to be able to successfully enhance ductility without a significant enhancement in strength, but the tests by Nishikawa et al. (1998) did not reveal the full potential of the method as the clearance was arbitrarily set.

Several methods have also been developed for the seismic retrofit of existing reinforced concrete columns. The column may be retrofitted by : (1) steel jacketing (Priestley et al. 1992; Chai et al. 1994; Mao and Xiao 2006); (2) reinforced concrete jacketing (Chapman and Park 1991); (3) the addition of a reinforced concrete infill wall between two adjacent columns (Haroun et al. 2002); and FRP jacketing (Saadatmanesh et al. 1994; Saadatmanesh et al. 1997; Seible et al. 1997; Teng et al. 2002). The enhancement of column strength and ductility by techniques (2) and (3) is always accompanied by an increase of stiffness of the column which may attract much greater seismic forces to the column during an earthquake attack (Elsanadedy 2002). As a result, these two techniques are not ideal for seismic retrofit applications. FRP jackets however offer many advantages over steel jackets, including excellent corrosion resistance, a very high strength-to-weight ratio and flexibility in shape. The latter two characteristics lead to greatly reduced labour cost and construction time and hence reduced disturbance to services supported by the structure. An additional advantage of an FRP jacket over a steel jacket is that while steel is an isotropic material with the same strength and stiffness in all directions so that a steel jacket may buckle under axial compression, an FRP jacket can be formed with fibres mainly or only in the hoop direction to offer confinement without attracting significant axial stresses. FRP jacketing has thus become a popular method for the seismic retrofit of concrete structures (fib 2001; ACI 440 2002; Concrete Society 2004). Furthermore, following Xiao’s (2004) pioneering work, many researchers have recently studied the behaviour of FRP-jacketed circular CFTs (Gu et al. 2004; Xiao et al. 2005; Shan et al. 2007; Tao et al. 2007; Wang et al. 2008; Liu and Lu 2010) and square/rectangular CFTs (Mao and Xiao 2006; Tao et al. 2007; Wang et al. 2008; Park et al. 2010). Further details of these tests are discussed in Chapter 5.

## 2.5 SEISMIC DAMAGE INDICES

In the case of concrete structures, damage indices have been developed to provide a way to quantify numerically the seismic damage sustained by an individual member, a part of a structure and a complete structure (Williams and Sexsmith 1995). In the present study, only damage indices for individual structural elements are of interest. Researchers have tried to use these indices for assessing and evaluating the structural behaviour of a member through defining a certain loading history and a failure criterion. These seismic damage indices in the existing literature can be divided into four different categories according to the different parameters used in the definition, namely, deformation-based indices (Park and Paulay 1975; Priestley and Park 1987; Park 1989; Usami and Ge 1994; Toshiyuki et al. 1996; Mirmiran et al. 1999; Wu et al. 2006b; Shim et al. 2008), energy-based indices (Banon et al. 1981; Darwin and Nmai 1986; Usami and Ge 1994; Mirmiran et al. 1999; Iacobucci et al. 2003; Julio and Branco 2008; Shim et al. 2008), stiffness-based indices (Banon et al. 1981; Roufaiel and Meyer 1987; Zhang et al. 2007) as well as combined indices (Park and Ang 1985).

### 2.5.1 Deformation-Based Indices

Deformation-based indices are widely used as one of the most important criteria in structural evaluation not only for structural design but also for structural assessment purposes. Such an index can be given in terms of displacements, rotations as well as curvatures. The non-cumulative indices (Eq. 2.1) which ignore the accumulated effect of cyclic loading and are commonly used by most researchers to quantify ductility include displacement ductility, rotation ductility and curvature ductility and are given by

$$\mu_\delta = \frac{\delta_u}{\delta_y}; \quad \mu_\alpha = \frac{\alpha_u}{\alpha_y}; \quad \mu_\phi = \frac{\phi_u}{\phi_y} \tag{2.1}$$

where $\mu_\delta$ , $\mu_\alpha$ and $\mu_\phi$ are the deformation indices in terms of displacements, rotations and curvatures respectively; $\delta_y , \alpha_y$ and $\phi_y$ are the yield displacement, yield rotation and yield curvature of the structural member respectively; and $\delta_u$ , $\alpha_u$ and $\phi_u$ are the ultimate displacement, ultimate rotation and ultimate curvature of the structural member respectively.

Some researchers (Banon et al. 1981; Wang and Shah 1987; Iacobucci et al. 2003) have proposed cumulative indices based on deformations within the prior cycles to evaluate the damage of the structures.

The yield deformation is often not obvious and may be difficult to define or detect, if various parts of a system commence their yielding at different load levels or if the materials do not have a sharp yielding point. Various alternative definitions which have been used by previous researchers (Mahin and Bertero 1976; Park 1989; Boyd et al. 1995; Mirmiran et al. 1999; Elremaily and Azizinamini 2002; Wu et al. 2006b) include the following: (1) the yield deformation is defined as the deformation where yielding first occurs in the system (Figure 2.1a); (2) the yield deformation is defined as the elastic limit of an equivalent elastic-perfectly plastic curve with the same elastic stiffness and peak strength as those of the test curve [(Figure 2.1b); (Mirmiran et al. 1999)]; (3) the yield deformation is defined as the elastic limit of an equivalent elastic-perfectly plastic curve which provides an equal area to that of the test envelope curve before the peak strength, with the real test strength being taken as the equivalent strength [(Figure 2.1c) (Mahin and Bertero 1976; Wu et al. 2006b)]; and (4) the yield deformation is defined as the elastic limit of an equivalent elastic-perfectly plastic curve with a reduced stiffness being equal to the secant stiffness at either first yield or at a certain value (e.g. 75%) of the peak strength, whichever is less [(Figure 2.1d) (Park 1989; Rodriguez and Park 1994; Boyd et al. 1995; Elremaily and Azizinamini 2002)].

Definition (1) is inappropriate as the occurrence of first yielding in a system may not necessarily coincide with the start of an obvious stiffness degradation in a test curve. The other three definitions are all widely used. Among them, the yield deformation according to definition (3) is more difficult to determine. Definition (4) provides the most appropriate and general way and has been claimed to be suitable for various structures such as concrete, masonry, steel as well as timber structures (Park 1989).

The definition of the ultimate state of a member is also subjective to a certain extent. Some possible definitions for the ultimate deformation are as follows: (1) the ultimate deformation is defined as that corresponding to a particular limiting value for the material ultimate strain (e.g. the attainment of a specified concrete ultimate compressive strain in the case of reinforced concrete structures; see Figure 2.2a); (2) the ultimate deformation is defined as that corresponding to the ultimate load of a test curve (Figure 2.2b); (3) the ultimate deformation is defined as the value where the load resistance of a test curve has undergone a small reduction, for example, a 10% to 30% reduction [(Priestley and Park 1987; Iacobucci et al. 2003; Wu et al. 2006a) see Figure 2.2c] ; (4) the ultimate deformation is defined as the value when the material fractures or elements buckle [for example, the fracture of the transverse reinforcing steel or the buckling of the longitudinal reinforcing steel in the case of reinforced concrete (Park 1989); see Figure 2.2d].

Definition (1) is inappropriate as it is evident that the maximum available deformation does not necessarily correspond to a specified extreme fibre concrete compressive strain (Park and Paulay 1975). It should be recognized that most structures have some deformation capacity after achieving their ultimate load without a significant reduction in load resistance [e.g. CFT columns with a relatively thick steel tube; (Schneider 1998)]. It is reasonable to include this extra deformation capacity beyond the ultimate load in defining the ultimate deformation. Hence, definition (2) is conservative. Park (1989) recommended defining the ultimate deformation using criteria (3) and (4) together, whichever occurs first.

### 2.5.2 Energy-Based Indices

The energy absorption capacity of a structure is also a common criterion in structural evaluation. The following non-cumulative index was first proposed by Naaman and Jeong (1995) for concrete beams pre-stressed with FRP tendons:
:

$$\mu_{e,nonc} = \frac{1}{2}\left(\frac{E_{total}}{E_{el}} + 1\right) \tag{2.2}$$

where $\mu_{e,nonc}$ is the non-cumulative index based on energy; $E_{total}$ is the total absorbed energy at failure and is calculated through integrating the area under the load-deflection curve; $E_{el}$ is the elastic energy absorbed.

It can be noted that this index is equivalent to the non-cumulative displacement-based index (Eq. 2.1) for a structure with an elastic-perfectly plastic load-deflection curve. This index was then used by Mirmiran et al. (1999) for evaluating the structural behaviour of concrete-filled FRP tube beam-columns . .

In fact, cumulative energy-based damage indices have been much more widely used. The first and basic index of this type was proposed by Gosain et al. (1977) through their cyclic flexural tests on RC members and is given as follows. The objective of their study was to devise a means of comparing tests reported in the literature and to suggest design requirements for shear in members under cyclic loading.

$$\mu_{e,cumu} = \sum_j \frac{H_j \delta_j}{H_y \delta_y} \tag{2.3}$$

where $\mu_{e,cumu}$ is the cumulative index based on energy; $H_j$ and $\delta_j$ are the transverse load and displacement at *j*th cycle; and $H_y$ and $\delta_i$ are the yield transverse load and displacement respectively; In order to achieve a reasonable correlation with the observed damage in the test, Gosain et al. (1977) also introduced the effect of shear span ratio and axial load level. This index or other similar indices with some modifications have been used by other researchers, mainly for members under flexural loading (Banon et al. 1981; Darwin and Nmai 1986; Nmai and Darwin 1986; Usami and Ge 1994; Iacobucci et al. 2003; Julio and Branco 2008; Shim et al. 2008).

### 2.5.3 Stiffness-Based Indices

A number of indices related to stiffness degradations have been proposed. Banon (1981) defined the flexural damage ratio as

$$\mu_K = \frac{K_0}{K_u} \tag{2.4}$$

where $\mu_K$ is the flexural damage ratio based on stiffness; $K_0$ is the initial flexural stiffness; $K_u$ is the ultimate flexural stiffness. Though this is a non-cumulative index, it takes some account of the stiffness and strength degradations under cyclic loading. This index was later modified by Roufaiel and Mayer (1987) to

$$\mu_{K,\text{mod}} = \frac{K_u}{K_{\text{int}e}} \cdot \frac{\left(K_{\text{int}e} - K_0\right)}{\left(K_u - K_0\right)} \tag{2.5}$$

where $\mu_{K,\text{mod}}$ is the modified flexural damage ratio based on stiffness; and $K_{\text{int}e}$ is the flexural stiffness at an internal point; This index showed a good correlation with the residual strength and stiffness of test specimens tested mainly in flexure, while some of the tests also included significant shear and axial load (Williams and Sexsmith 1995) Some other stiffness-based indices have also proposed and used (Zhang et al. 2007).

### 2.5.4 Combined Indices

The best-known and most widely used of all the cumulative damage indices is that of Park and Ang (1985) for reinforced concrete under flexural loading. This index consists of a simple linear combination of normalized deformation and energy absorption. It is defined as follows:

$$\mu_{comb} = \frac{\delta_{\text{int}e}}{\delta_u} + \beta_e \frac{\int dE_{\text{int}e}}{P_y \delta_u} \tag{2.6}$$

where $\mu_{comb}$ is the index in terms of both displacement and energy; $\delta_{\text{int}e}$ and $E_{\text{int}e}$ are the displacement and the absorbed energy at the examined point; and $\beta_e$ is the constant for taking account of strength deterioration. The first term in Eq. 2.6 is a non-cumulative displacement measure while the second energy term includes the cyclic effect. Park et al. (1987) suggested a value of 0.4 as a threshold value between repairable and irreparable damage. The advantages of this model are its simplicity and its validity as achieved through calibration with a significant amount of observed seismic damage (Williams and Sexsmith 1995).

## 2.6 STRESS-STRAIN MODELS FOR CONFINED CONCRETE

It has been well established that both the strength and ductility of concrete can be enhanced significantly if external confinement is provided. This external confinement can be from steel stirrups (Richart et al. 1929; Ahmad and Shah 1982; Mander et al. 1988), steel jacket (Priestley et al. 1992; Chai et al. 1994; Rodriguez and Park 1994), and FRP jackets (Xiao and Wu 2000; Teng et al. 2002; Jiang and Teng 2007). Among other researchers, Mander et al. (1988) proposed a well-known stress-strain model applicable to steel-confined and actively confined concrete. The model is based on a single equation that describes the axial stress-strain response of both confined and unconfined concrete and accounts for increases in both strength and ductility due to confinement. This well-established model has served as a basis for modelling the stress-strain behaviour of concrete in most subsequent research, where the concrete was confined by steel tubes (Elremaily and Azizinamini 2002) or FRP jackets [e.g. (Mirmiran and Shahawy 1996; Fam and Rizkalla 2001; Binici 2005; Teng et al. 2007; Xiao et al. 2010)]

There is some existing research on the modelling of the stress-strain behaviour of concrete confined by circular steel tubes (Tang et al. 1996; Susantha et al. 2001; Elremaily and Azizinamini 2002; Johansson 2002; Sakino et al. 2004; Hatzigeorgiou 2008; Choi and Xiao 2010b). Choi and Xiao (2010b) employed the model developed by Xiao (1989). The model is based on the octahedral stress-strain relationship and laboratory tests. By contrast, all the other researchers considered the biaxial stress state of the steel tube in their model and related the confined concrete strength to the lateral confining pressure from the steel tube through an empirical equation. However, among these researchers, only Johansson (2002) revealed the passive characteristic of the steel tube confinement. In his model, the hoop stress of the steel tube depends on the lateral expansion of the concrete core. Oliveira et al. (2010) reviewed the models of Susantha et al. (2001), Johansson (2002) and Hatzigeorgiou (2008). They concluded that these three models can generally predict the strength of 95 CFT columns in their database well.

The concept of establishing a passive-confinement stress-strain model from an active-confinement base model through an incremental approach has previously been employed for concrete confined with steel ties by Ahmad and Shah (1982). Mirmiran and Shahawy (1996) was the first to extend this approach to the modelling of FRP-confined concrete. To date, there has been extensive research on stress-strain models for FRP-confined concrete (Jiang 2008). Regardless of the confining material, it has been concluded that the accuracy of a stress-strain model for FRP-confined concrete depends strongly on (1) the lateral-to-axial strain relationship for confined concrete (concrete dilation properties); (2) the axial stress-axial strain relationship; and (3) the peak axial stress point of the active-confinement base model (Jiang and Teng 2007; Jiang 2008).

The monotonic-loading stress-strain curve has commonly assumed to form an envelope to the cyclic-loading stress-strain response. This assumption has been found to valid through experimental studies for plain concrete (Sinha et al. 1964; Karsan and Jirsa 1969), reinforced concrete (Shah et al. 1983; Mander et al. 1984; Castellani et al. 1993), steel tube confined concrete (Wei et al. 1995; Zhang and Liu 2007) and FRP-confined concrete (Ilki and Kumbasar 2002; Lam et al. 2006). As a result, this assumption has used in all existing theoretical stress-strain models for confined-concrete subjected to cyclic compression (Mander et al. 1988; Martinez-Rueda and Elnashai 1997; Bahn and Hsu 1998; Sakai and Kawashima 2006; Lam and Teng 2009). Once the envelope curve is determined, the definition of the unloading and reloading paths becomes the key to the modelling of stress-strain behaviour for cyclic compression.

## 2.7 THEORETICAL ANALYSIS OF COLUMNS

The most commonly used numerical or analytical methods for simulating the behaviour of CFT columns/beam-columns are: (1) three-dimensional finite element models (Schneider 1998; Shams and Saadeghvaziri 1999; Johansson and Gylltoft 2002; Hu et al. 2003; Hu et al. 2005; Varma et al. 2005; Han et al. 2008);

and (2) one-dimensional column analysis models for member behaviour (Newmark 1943; Neogi et al. 1969; Cranston 1972; Shen and Lu 1983; Shakir-Khalil and Zeghiche 1989; Han et al. 2004; Choo et al. 2006; Jiang 2008) in conjunction with fibre models for section analysis (Neogi et al. 1969; Tomii and Sakino 1979; Shakir-Khalil and Zeghiche 1989; Hajjar and Gourley 1996; Uy 2000; Fam et al. 2004; Han et al. 2004). Method (1) is more accurate but is more complicated and computationally less efficient. By contrast, method (2) is simpler because it is uni-dimensional in nature. The fundamental process and assumptions of fibre models for section analysis are presented below. In addition, two well-established analytical methods for column analysis are also briefly reviewed.

There are several basic assumptions in a fibre model: (1) plane sections remain plane after bending; this assumption is widely accepted and is generally valid; (2) shear deformation is neglected; for this reason, the fibre method is generally only suitable for the analysis of flexure-dominated members; (3) the uniaxial constitutive relationship includes the effect of a multi-axial stress state (i.e. concrete under confinement); and (4) tensile stresses in the concrete are ignored. In a typical fibre model, the section is divided into a number of areas referred to as “fibres”. Each fibre can be assigned appropriate concrete or steel properties. According to the constitutive models, the fibre stresses are calculated from the fibre strains. The calculated stresses are then integrated over the cross-sectional area to obtain the resultant force and the resultant moment. In this way, the moment-curvature-thrust (i.e. section properties) curve can be obtained.

Various analytical methods have been proposed for the analysis of columns, as can be found in many textbooks (Chen and Atsuta 1976). Two well-established analytical methods are briefly reviewed here.

In the first method, the deflected shape of a pin-ended column is assumed to be a half-sine wave and equilibrium is only checked at the critical section (the section at the mid-height of the column) where the maximum lateral deflection of the column takes place. This method has been widely adopted in the analysis of RC columns (Bazant et al. 1991) and of CFT columns (Shakir-Khalil and Zeghiche 1989; Han et al. 2004).

The second method is more sophisticated and more versatile than the first one. This method is generally known as the numerical integration method, in which a column is divided into a reasonable number of segments and the lateral displacement at each grid point is found from numerical integration by making use of moment-curvature-thrust curves derived from fibre models. This method allows the end eccentricities to be unequal and allows the presence of end restraints. This method was originally proposed by Newmark (1943) and has been widely adopted in the analysis of RC columns (Cranston 1972; Choo et al. 2006), steel columns (Shen and Lu 1983) and composite columns including CFT columns (Neogi et al. 1969) and FRP-confined RC columns (Jiang 2008).

## 2.8 CONCLUDING REMARKS

This chapter has presented a wide-ranging review of the existing literature that is relevant to the present study. The local buckling phenomenon of hollow steel tubes and concrete-filled steel tubes was addressed first, followed by an introduction of traditional retrofit techniques for columns. The advantages of FRP jacketing over existing column retrofit methods was examined. The review indicated that FRP jacketing of hollow steel tubes and CFT columns is a very promising technique for improving the performance of such columns by delaying or suppressing local buckling but has so far received very limited attention in the past. Against the above background, this thesis presents a series of experimental and theoretical studies on the behaviour of FRP-confined hollow steel tubes and CFT members.

This chapter has also examined the existing literature on the modelling of various behavioural aspects of hollow steel tubes and CFT columns with or without FRP confinement, including the stress-strain behaviour of confined concrete, section analysis, column analysis and damage indices. These elements will all be considered in the theoretical modelling work of the present PhD study.

Table 2. 1 $D_{outer} / t_s$ limitations in different design codes

| *Code* | *Axial compression* | *Bending* | |
|---|---|---|---|
| | | *Plastic limit* | *Yield limit* |
| ACI 318 | $\sqrt{\frac{8E_s}{f_y}}$ | N/A | N/A |
| EC 4 | $90\frac{235}{f_y}$ | N/A | N/A |
| BS 5950 | $80\frac{275}{f_y}$ | $40\frac{275}{f_y}$ | $140\frac{275}{f_y}$ |
| AISC 360 | $0.11\frac{E_s}{f_y}$ | $0.07\frac{E_s}{f_y}$ | $0.31\frac{E_s}{f_y}$ |
| AS 4100 | $82\frac{250}{f_y}$ | $50\frac{250}{f_y}$ | $120\frac{250}{f_y}$ |

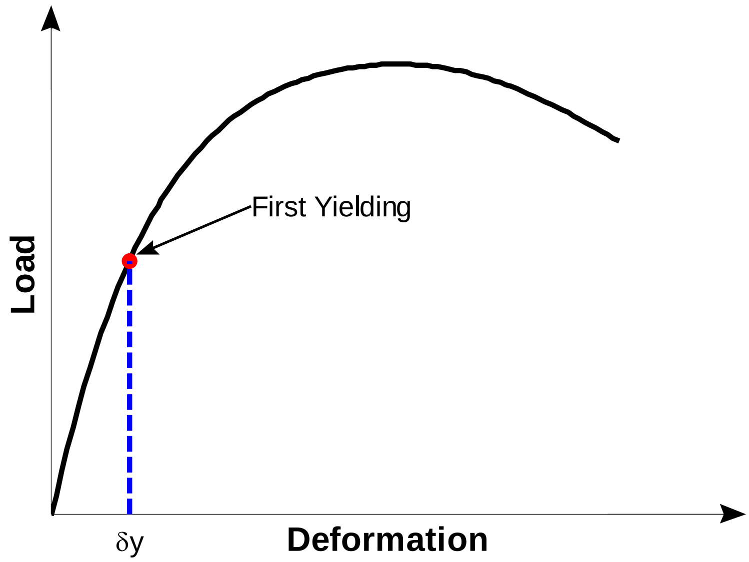


(a) Definition (1) of yield deformation

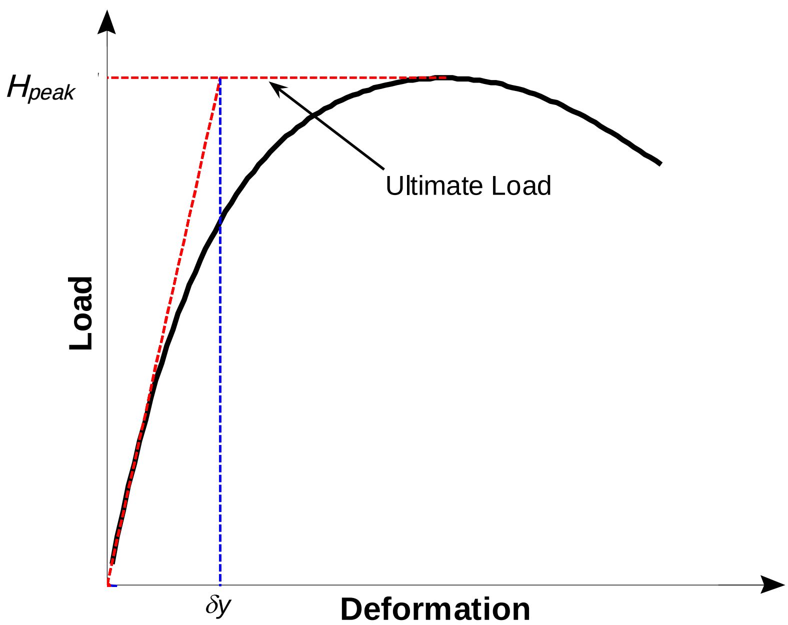


(b) Definition (2) of yield deformation

Figure 2.1 Different definitions of yield deformation

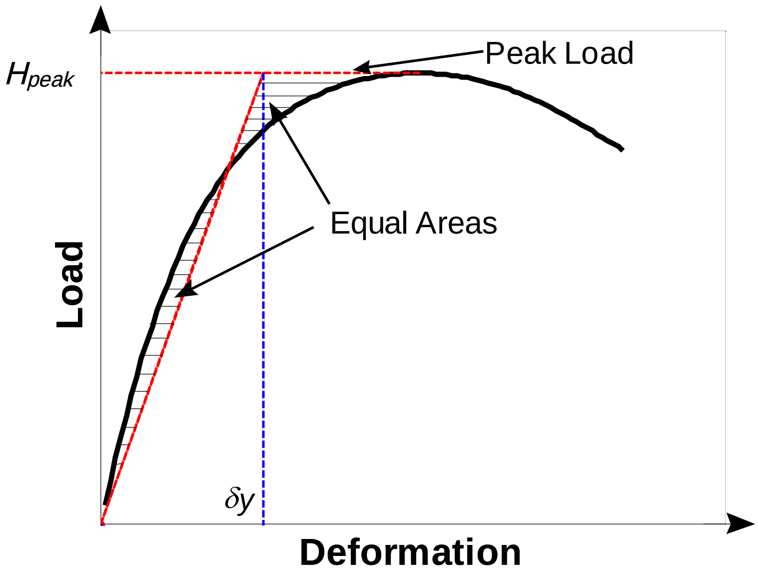


(c) Definition (3) of yield deformation

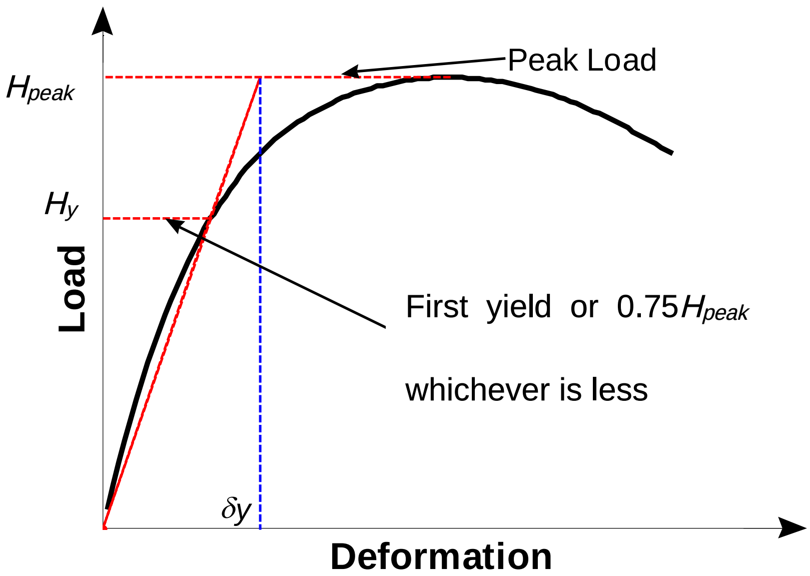


(d) Definition (4) of yield deformation

Figure 2.1 Different definitions of yield deformation (continued)

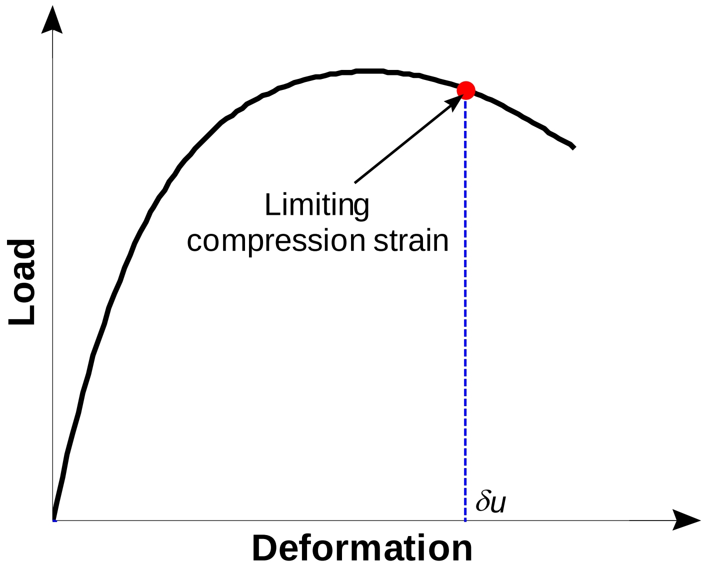


(a) Definition (1) of ultimate deformation

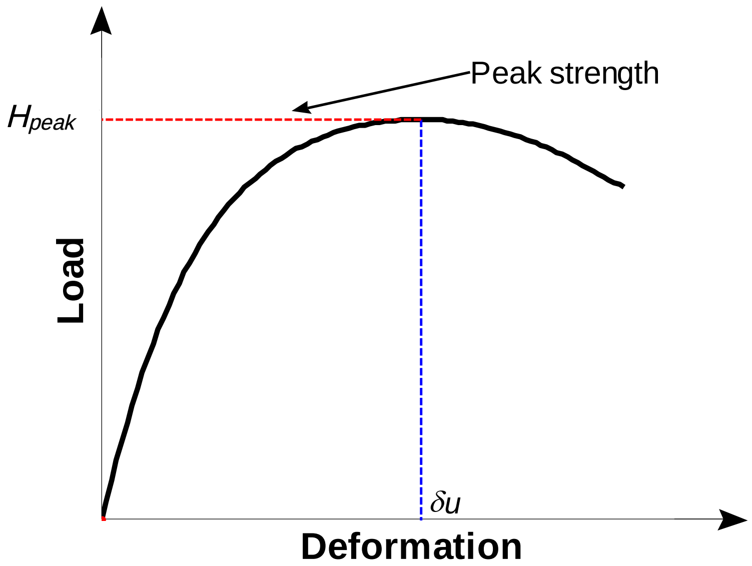


(b) Definition (2) of ultimate deformation

Figure 2.2 Different definitions of ultimate deformation

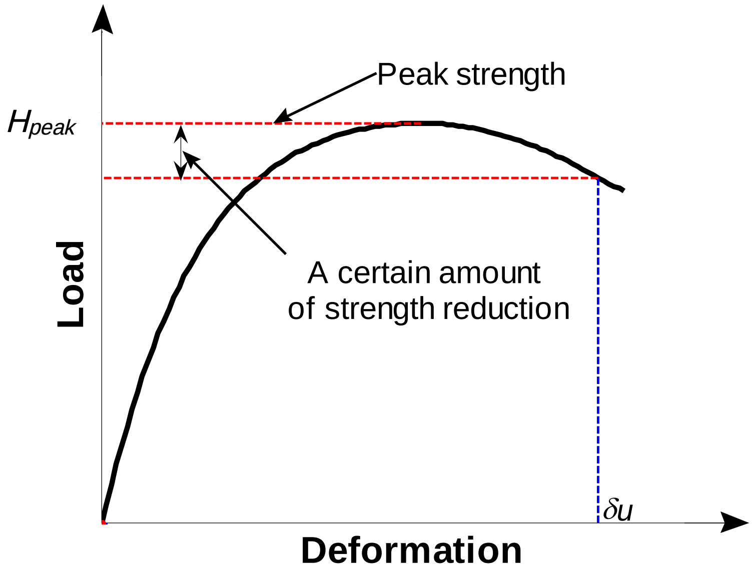


(c) Definition (3) of ultimate deformation

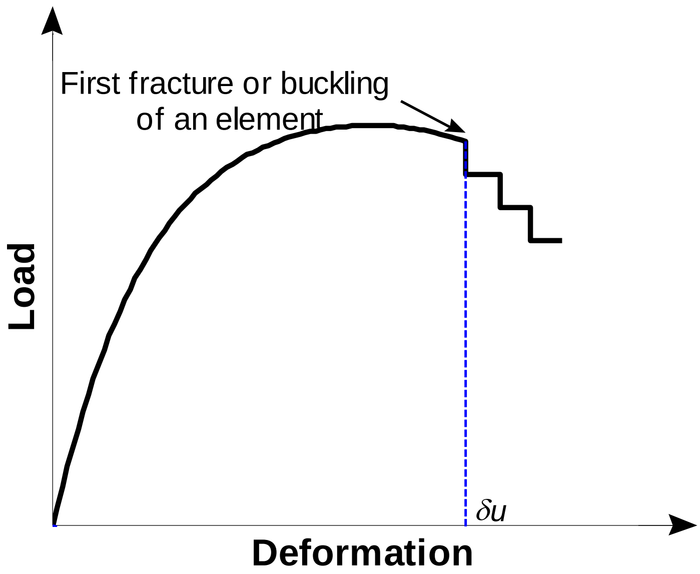


(d) Definition (4) of ultimate deformation

Figure 2.2 Different definitions of ultimate deformation (continued)

# CHAPTER 3

# BEHAVIOUR OF FRP-CONFINED CIRCULAR STEEL TUBES AND CYLINDRICAL SHELLS UNDER AXIAL COMPRESSION

## 3.1 INTRODUCTION

As reviewed in Chapter 2, circular hollow steel tubes are widely used as columns in many structural systems and a common failure mode of such tubes when subjected to axial compression and bending is local buckling near a column end. In typical circular tubular members, elephant's foot buckling appears after yielding and the appearance of this inelastic local buckling mode normally signifies the exhaustion of the load carrying capacity and/or the end of ductile response. The latter is of particular importance in seismic design, as the ductility and energy absorption capacity of the column dictates its seismic resistance. A number of methods have been proposed for the seismic retrofit of hollow steel tubes as bridge piers where enhancement of ductility without a significant strength increase is preferred, but each method suffers from some limitations.

Over the past decade, fibre-reinforced polymer (FRP) composites have been widely used in the strengthening of concrete structures (Teng et al. 2002; Teng et al. 2003). More recently, the use of FRP to strengthen metallic structures has also attracted a significant amount of attention (Hollaway and Cadei 2002; Zhao and Zhang 2007; Teng et al. 2009b). Xiao (2004) and Xiao et al. (2005) explored the use of FRP jackets for the confinement of the critical regions of concrete-filled steel tubes. Teng and Hu (2004) extended Xiao's concept to circular hollow steel tubes and showed that even in hollow tubes where inward local buckling is not prevented, FRP jacketing provides a simple and effective method for the ductility enhancement and hence seismic retrofit of such columns. Nishino and Furukawa (2004) explored the same technique for hollow steel tubes independently.

The idea of FRP jacketing of circular steel tubes can be further extended to circular cylindrical shells (or even general shells of revolution) if the elephant's foot buckling mode is the critical failure mode. Many such failures have been observed during earthquakes. In addition to the base of a shell, the elephant's foot failure mode can also occur at a discontinuity that leads to local bending, such as at a lap joint (Teng 1994). For such steel cylindrical shells, FRP confinement appears to be an effective method of retrofit and may also be considered in new tank/silo designs.

This chapter presents the results of a study in which the benefit of FRP confinement of hollow steel tubes under axial compression was examined. Axial compression tests on FRP-confined steel tubes are described first. Finite element modelling of these tests is next discussed. Both the test and the numerical results show that FRP jacketing is a very promising technique for the retrofit and strengthening of circular hollow steel tubes. In addition, finite element results for FRP-jacketed thin cylindrical shells under combined axial compression and internal pressure are presented to show that FRP jacketing is also an effective strengthening method for such shells failing by elephant's foot collapse near the base.

## 3.2 EXPERIMENTS

### 3.2.1 Specimens

In order to demonstrate the effect of FRP confinement on steel tubes, four steel tubes with or without a GFRP jacket were tested at The Hong Kong Polytechnic University. The four tubes were cut from a single long tube and their details are shown in Table 3.1. GFRP was used instead of carbon FRP (CFRP) in these tests as GFRP does not suffer from galvanic corrosion problems which may be a concern for CFRP directly bonded to steel and possesses a larger ultimate tensile strain which is a favorable property for ductility enhancement applications. The four tubes are named respectively, HST-0-40-A, HST-1G-40-A, HST-2G-40-A, and HST-3G-40-A. The four parts indicate steel tube, number of FRP plies, $D_{outer}/t_s$ ratio and loading type (i.e. monotonic axial compression) respectively (Table 3.1). The GFRP jacket was formed in a wet lay-up process, and each ply consisted of a single lap of a glass fibre sheet impregnated with epoxy resin. A continuous glass fibre sheet was wrapped around the steel tube to form a jacket with the required number of plies, with the finishing end of the fibre sheet overlapping its starting end by 150 mm to ensure circumferential continuity. Before the wrapping of GFRP, the surface of the steel tube was cleaned using alcohol.

Three steel coupon tests were conducted according to BS 18 (1987) to determine the tensile properties of the steel. The tensile test specimens were cut from a single steel tube which in turn was cut from the same long tube as the tube specimens for compression tests. The average values of the elastic modulus, yield stress, ultimate strength, and elongation after fracture from these tensile tests were 201.0GPa, 333.6 MPa, 370.0 MPa and 0.347 respectively.

Five tensile tests according to ASTM 3039 (2000) were also conducted for the GFRP material which had a nominal thickness of 0.17mm per ply. The average values of the elastic modulus and tensile strength from these tests, calculated on the basis of the nominal ply thickness of 0.17 mm, were 80.1 GPa and 1,825.5 MPa respectively, leading to an ultimate tensile strain of 0.0228.

### 3.2.2 Instrumentation and Loading

For the bare steel tube, four unidirectional strain gauges with a gauge length of 8 mm were installed at the mid-height to measure axial strains. For each

FRP-confined steel tube, four bidirectional strain gauges with a gauge length of 20mm were installed at the mid-height of the FRP jacket. The layout of strain gauges is shown in Figure 3.1 for each FRP-confined specimen. The compression tests were all conducted using an MTS machine with displacement control (Figure 3.2). The loading rate was 0.5mm/min. The total shortening of the steel tube was taken to be the same as the relative movement between the two loading platens recorded by the MTS machine. Some steel block spacers existed between the steel tube and the loading platens (Figure 3.2), but their deformation was small and was ignored.

### 3.2.3 Test Observations and Results

The failure mode of the bare steel tube was outward buckling around the circumference. This local buckling mode near the tube end, widely known as the elephant's foot buckling mode (Figure 3.3), is normally found in steel tubes whose diameter-to-thickness ratio is relatively small. Two load-axial strain curves of the steel tube are shown in Figure 3.4. One of the curves is for the average strain from the four strain gauges at the mid-height of the steel tube, while the other curve is for the nominal axial strain, which is equal to the average total axial shortening divided by the height of the steel tube. The four strain gauges recorded axial strains very close to each other until unloading took place. During the post-buckling regime, the axial strain at the mid-height reduces as the load reduces, but the nominal axial strain steadily increases. This means that load-strain curves in the post-buckling regime from strain gauge readings depend strongly on strain gauge locations and do not reflect the global behaviour of the tube (e.g. the energy absorption capacity of the tube). Therefore, from here onwards, only load-axial shortening curves are shown.

The three FRP-confined steel tubes after failure are shown in Figure 3.5. Readings from strain gauges at the mid-height indicated that the axial load was well centred in all three tests. The load-axial shortening curves of these three specimens together with that of the bare steel tube are shown in Figure 3.6. While the load-axial shortening curve of the bare steel tube features a descending branch immediately after the linearly ascending branch, those of the three FRP-confined tubes all feature a long and slowly ascending branch before reaching the peak load, showing great ductility. Figure 3.6 shows that the tube confined with a single-ply FRP jacket is almost as ductile as those with a two-ply or a three-ply jacket. For practical applications, methods need to be developed to achieve optimum designs of FRP jackets.

In the steel tube with a single-ply FRP jacket, failure involved outward local buckling deformations near the ends, causing the FRP jacket to eventually rupture due to hoop tension. It should be noted that in these steel tubes, local rupture of the FRP jacket at one or more locations did not affect the load-axial shortening behaviour significantly, so it is not possible to identify from a load-axial shortening curve when local rupture of FRP was first reached. Some inward buckling deformations also developed in this specimen, but the outward deformations dominated the behaviour. In the tube with a two-ply FRP jacket, the FRP jacket also ruptured near one of the ends due to the expanding local buckling deformations but inward buckling deformations became more important in this tube. When a three-ply FRP jacket was used, local rupture of the FRP jacket did not occur and failure was dominated by inward buckling deformations away from the two ends. It is obvious that in such steel tubes, as the thickness of the FRP jacket increases, the outward buckling deformations near the ends are increasingly restrained, making inward buckling deformations away from the ends increasingly more important. Since the FRP jacket offers little resistance to inward buckling deformations, once the behaviour is dominated by inward bucking, the use of a thicker jacket leads to little additional benefit (Figure 3.6).

Key test results are summarized in Table 3.2, where $N_y$ is the yield load defined as the yield stress of the steel from tensile coupon tests times the cross-sectional area of the steel tube (taking the diameters of all specimens to be 160.8 mm) and $N_{peak}$ is the peak load obtained from the compression tests. $\Delta_{peak,bhst}$ is the axial shortening of the bare steel tube at peak load from the bare steel tube compression test, while $\Delta_{peak,chst}$ is the axial shortening of an FRP-confined steel tube at peak load. It can be found that both $N_{peak}$ and $\Delta_{peak,chst}$ increase with the thickness of the FRP jacket within the thickness range examined in the present study.

The confinement effectiveness of the FRP jacket can be gauged by examining the degrees of enhancement in the ultimate load and the axial shortening at peak load. As seen in Table 3.2, the ultimate load of the steel tube was enhanced by 5% to 10% by FRP jackets of different thicknesses. The ultimate load increases with the thickness of the FRP jacket, although this increase is generally very limited. Table 3.2 and Figure 3.6 both show that the ductility of the steel tube was greatly enhanced by FRP confinement. The axial shortening at peak load is enhanced by around 10 times through FRP confinement. It is worth noting that FRP confinement of circular hollow steel tubes leads to great increase in ductility with very limited increases in strength, a feature that is highly desirable in the seismic retrofit of structures. Therefore, FRP jacketing appears to be a very promising technique for the seismic retrofit of circular steel tubular columns.

## 3.3 FINITE ELEMENT MODELLING OF THE BARE STEEL TUBE

### 3.3.1 General

The general-purpose finite element software package ABAQUS (2003) was employed to simulate the test tubes in this study. To model these tests, both geometric and material nonlinearities were considered and the nonlinear load-deformation path was followed by the arc-length method. Symmetry conditions were not exploited so that the deformation pattern was not restricted by imposing such conditions. The modelling of the bare steel tube is first examined in this section. As for the test results, the finite element results are also reported in terms of the load-axial shortening curves.

The steel tube was modelled using element S4R. Element S4R is a 4-node doubly curved general-purpose shell element with the effect of transverse shear deformation included. Each node has six degrees of freedom (three translations and three rotations). Nine integration points were adopted for integration across the thickness. A mesh convergence study was conducted, leading to a uniform mesh of 5mm x 10mm elements for the steel tube, which was found to provide accurate predictions. The longer side of the element lies in the circumferential direction, as the number of waves of the deformations of the tube in the circumferential direction is generally small. The stress-strain curve for the steel adopted in the finite element model is shown in Figure 3.7. This curve is based on the average values of the yield stress and the elastic modulus, and the shape of its strain-hardening part is based on test curve 1 shown in Figure 3.17.

Based on numerical results obtained with the finite element model, the final finite element model arrived at include the following two features, the need of which is not apparent in a straightforward finite element modelling exercise: (a) the two ends are fully fixed except that the axial displacement of the top end is left unrestrained to allow the application of axial loading; (b) a small geometric imperfection is included to guide the finite element model into a deformation pattern similar to that found in the test. The rationale for these choices is explained below, where the finite element results are from a finite element model with the above features included unless otherwise specified.

### 3.3.2 Boundary Conditions

In the experiment, the steel tube was in contact with stiff loading plates at the two ends (Figure 3.2). While this support condition may appear to be close to a simply-supported condition, the numerical comparison shown in Figure 3.8 indicates that a clamped support condition for the two ends leads to much closer predictions of the test results. Furthermore, the deformed shape of the tube from the finite element model with clamped ends is also in much close agreement with that from the test (Figure 3.9). Therefore, the clamped end condition is more appropriate for this tube. This means that the tube wall was sufficiently thick that the loading plates in contact provided significant restraints at the ends against meridional rotations.

### 3.3.3 Geometric Imperfection

For a perfect steel tube under axial compression, the two ends are each expected to develop a local elephant's foot buckle. In an experiment, this generally does not occur due to small geometric and material imperfections (Figure 3.3). Therefore, for the finite element analysis to capture the experimental behaviour realistically, a geometric imperfection was included in the finite element model. In the finite element model with two clamped ends, an axisymmetric outward imperfection in the form of a half-wave sine curve along the meridian (i.e. a local outward bulge) was added near one end of the tube and centred at the position of maximum radial displacement from a linear elastic analysis. In the finite element model with pinned ends, the same half-wave imperfection was made to start at the support. The half-wave length of the sine curve was $1.728\sqrt{R_s t_s}$ (31.75mm), where $R_s$ is the radius of the tube middle surface and $t_s$ is the tube thickness. This value is equal to the critical half-wave length for the classical axisymmetric elastic buckling mode of axially-compressed cylinders (Rotter 2004). The imperfection amplitude adopted was 0.02mm. Such a small local axisymmetric imperfection has little effect on the load-axial shortening behaviour, except that it provided the necessary disturbance to guide the steel tube into the development of only a single local buckle at one of the two ends. Values smaller than 0.02 mm were also tried and were not found to be successful in guiding the tube into the desired pattern of deformation.

## 3.4 FINITE ELEMENT MODELLING OF FRP-CONFINED STEEL TUBES

The FRP jacket was modelled using beam elements oriented in the hoop direction, which means that the small stiffness of the FRP jacket in the meridional direction was ignored in the finite element model. Each beam element was assigned a narrow rectangular section, with its section width being equal to the thickness of the FRP jacket and its section height being the distance from the mid-height of the shell element above to that of the shell element below the beam element. Element B33 in ABAQUS (2003) was used, which is a two-node cubic beam element with six degrees of freedom (three translations and three rotations) per node. FRP was treated as a linear elastic material. The nodes of the beam elements (FRP) formed a node-based surface, which was regarded as the slave surface, and were tied to the shell surface (the steel tube) which was regarded as the master surface. The tensile rupture behaviour of the FRP was not included in the model, but strains developed in the FRP jacket can be compared with the ultimate tensile strain of the FRP from tensile tests to see whether local rupture is predicted.

Similar to the bare steel tube, a geometric imperfection was included in the finite element model for FRP-confined steel tubes to match experimental observations. Ideally, the geometric imperfections should be precisely surveyed and modelled, as has been done in research on much thinner shells (Zhao and Teng 2001; Teng and Lin 2005), but even when such an approach is followed for geometric imperfections, the effects of material imperfections such as residual stresses from cold bending (Quach et al. 2004) are still not included. In the present study, a much simpler approach was adopted. The failure modes of FRP-confined steel tubes (Figure 3.5) are no longer axisymmetric and inward buckling deformations away from the two ends are important. To guide the tube into such deformations, a non-axisymmetric geometric imperfection was included in the finite element model for FRP-confined steel tubes. The shape of the imperfection was assumed to be of the following form (Figure 3.10):

$$w = w_0 \sin\left(\frac{\pi y}{l_w}\right)\cos n_\theta \theta \tag{3.1}$$

where $y$ is the axial coordinate from one end of the tube, $\theta$ is the circumferential angle (radian), $w_0$ is the maximum amplitude of the imperfection, $l_w$ is the half-wave length of the imperfection in the meridional direction, and $n_\theta$ is the number of circumferential waves of the imperfection.

Figures 3.11-3.13 show the results of a series of finite element simulations where the effects of varying three parameters are illustrated. It is found that, the finite element predictions are sensitive to the chosen imperfection parameters only in the final stage of deformation (the descending part of the load-axial shortening curve); within the ranges examined, the finite element results match the experimental results closely for all three specimens when the three parameters are: $w_0$ = 0.01 mm, n = 2, and $l_w$ = $1.728\sqrt{R_s t_s}$ (31.75mm). The final imperfection is a very small imperfection describing sectional ovalization, with a meridional half-wave length being that of the classical axisymmetric buckling mode. This imperfection, although derived from numerical corroboration, can be realistically expected to exist in such steel tubes. The choice of a geometric imperfection for the finite element model of an FRP-confined steel tube with a more rational basis is an issue that requires further investigation.

Each FRP jacket included an overlapping zone and within this overlapping zone, the FRP jacket was thicker. Two alternative treatments of this overlapping zone were explored: (a) the additional thickness of the overlapping zone of 150 mm was directly included in the finite element mode; b) the additional thickness of the overlapping zone was smeared around tube. In both options, the additional ply is taken to be completely effective, which is an optimistic treatment as part of this ply is unlikely to be effective due to the need for stress transfer between plies. Option (a) was used in all simulations presented in Figures 3.11-3.13. For option (b), the smeared equivalent thicknesses of the single-, two- and three-ply FRP jackets are respectively 0.22 mm, 0.37 mm and 0.53mm. Figure 3.14 shows the test results in comparison with the finite element predictions for the two different modelling options for the overlap. It is seen that the finite element results from the two options are very close to each other except for the one-ply jacket where a significant difference is seen following the attainment of the peak load.

The finite element failure modes of the FRP-confined steel tubes from option (a) are shown in Figure 3.15. These deformed shapes are for an advanced state of deformation corresponding closely to the end of the test (Figure 3.15). They match those from the tests reasonably well, given the well-known fact that the buckling mode of a real imperfect axially compressed cylindrical shell is notoriously difficult to predict precisely even when the geometric imperfection is accurately surveyed and included into the finite element model. For the steel tube confined with a single-ply FRP jacket, the experimental failure mode was primarily outward buckling around the circumference near one of the ends. The finite element model showed that at the ultimate load, the hoop strains in the jacket at the crest of the elephant’s foot buckle are higher than those elsewhere and reach mean values of around 0.028 and 0.025 for options (a) and (b). These values are higher than the ultimate strain obtained from tensile tests (0.0228), indicating that in the experiment, local rupture may have been reached before the attainment of the peak load. However, in the experiment, the maximum value of the hoop strain of the jacket detected was only around 0.012 and this is because FRP rupture did not occur at the mid-height of the tube where the strain gauges were located. It should be noted that based on existing research on FRP jackets confining concrete cylinders (Lam and Teng 2004; Teng and Lam 2004), the ultimate hoop rupture strain achievable in a circular jacket may be significantly lower than the coupon test result (0.0228) due to the detrimental effect of curvature, although the present tests did not provide enough information to either confirm or refute this observation.

For the steel tubes confined with two-ply and three-ply FRP jackets respectively, the finite element results showed the hoop strains in the FRP jacket at the ultimate load are not uniformly distributed and high values of hoop strains exceeding 0.0228 in the jacket are highly localised. Hoop strains both near the ends and at the mid-height of the tube are generally below 0.017 at the attainment of the ultimate load, which is closer to the values recorded by strain gauges at the mid-height for both tubes (both around 0.013). These results confirm that in these two specimens, inward buckling deformations were much more important.

Since the tie constraint was adopted to model the interaction between the FRP jacket and the steel tube in the present finite element model, the possibility of debonding between the FRP jacket and the steel tube when the steel tube buckles inward was not considered. Since debonding did occur in the test of the steel tube confined with a three-ply FRP jacket, the use of tie constraint is believed to be the main cause for the significant difference between the finite element and the test load-shortening curves in the descending branch for the two-ply and three-ply jackets (Figures 3.15b & c).

It should be noted that when the overlap is directly modelled, the thicker overlapping zone represents a disturbance to the axisymmetry of the tube geometry. In such a case, the use of a non-axisymmetric imperfection is unnecessary to guide the tube into non-axisymmetric buckling deformations. This option was not adopted in the present study as the same non-axisymmetric imperfection given by Eq. 2. was used in all finite element models for FRP-confined steel tubes to facilitate easy comparison.

## 3.5 STRENGTHENING OF THIN CYLINDRICAL SHELLS AGAINST LOCAL COLLAPSE

It is well known that large thin steel cylindrical shells such as liquid storage tanks and steel silos for storage of bulk solids may fail in the elephant's foot buckling mode when subjected to the combined action of axial compression and internal pressure (Rotter 1990; Rotter 2004). Many such failures have been observed during earthquakes. The idea of FRP jacketing is extended to the strengthening of thin circular cylindrical shells in this section.

In order to demonstrate the strengthening effect of FRP, a bare thin cylindrical shell and three FRP-confined thin cylindrical shells under the combined action of axial compression and internal pressure were analysed using finite element models similar to those developed for steel tubes presented above. The main difference is that the radius is now much larger and an internal pressure exists in addition to axial compression. The radius and thickness of this cylindrical shell are 10,000 mm and 10 mm respectively. The height of this cylindrical shell is 1543mm which is twice the linear elastic meridional bending half-wave length ($2\times2.44\times\sqrt{R_s t_s}$), where $R_s$ and $t_s$ are the radius and thickness of the middle surface of the cylindrical shell (Rotter 2004). The axial compression and the internal pressure have a fixed ratio ($\sigma_{x,s} / p_r = R_s / t_s$).The steel is assumed to be elastic-perfectly plastic with an elastic modulus of 200,000 MPa and a yield stress of 250 MPa.

Only axisymmetric collapse was considered, so a one-degree axisymmetric model was adopted in the analysis to save computational time. The bottom end of the shell is simply-supported (i.e. only meridional rotations are allowed). The top end is allowed to move radially and axially but is restrained against meridional rotations. These boundary conditions mean that local buckling can only occur at the base, so the inclusion of an imperfection to guide the shell into a single buckle at the base is not needed.

Three commercially available FRP systems were examined, including the GFRP system (System I) used in the axial compression tests on steel tubes presented earlier in the paper. The other two systems are CFRP systems and the properties given by the supplier were used in the finite element analyses. System II is a normal modulus CFRP system with an elastic modulus of 230 GPa, a tensile strength of 3450 MPa and a nominal thickness of 0.17 mm. The corresponding values for system III, which is a high modulus CFRP system, are 640 GPa, 2560 MPa and 0.19 mm. In each case, the shell is wrapped with a ten-ply jacket. The four load-axial shortening curves from finite element analyses are shown in Figure 3.16. It can be seen that the ultimate load increases with increases in the elastic modulus of the FRP as can be expected. The failure mode (Figure 3.17) remains similar in shape but the length of the buckle reduces with increases in the elastic modulus of the FRP. It can be concluded that FRP confinement provides an effective method for the strengthening of steel cylindrical shells against local collapse failure.

## 3.6 CONCLUSIONS

In this Chapter, the use of FRP confinement to enhance the ductility and hence the seismic resistance of circular steel tubes has been explored. A series of axial compression tests has been presented to demonstrate the effectiveness of FRP confinement of steel tubes whose ductility is otherwise limited by the development of the elephant's foot buckling mode. A finite element model for predicting the behaviour of these FRP-confined tubes has also been presented. Both the load-axial shortening curves and the failure modes from the finite element model are in close agreement with those from the tests, although the degree of accuracy depends significantly on the geometric imperfection included in the finite element model. The choice of geometric imperfections in the finite element model for FRP-confined steel tubes is an issue that requires further investigation in the future. Based on both test and numerical results, the following conclusions can be drawn:

1. With the provision of a thin FRP jacket, the ductility of the steel tube can be greatly enhanced. However, when the jacket thickness reaches a threshold value for which inward buckling deformations dominate the behaviour; further increases in the jacket thickness do not lead to significant additional benefits as the jacket provides little resistance to inward buckling deformations.

2. It is significant to note that FRP confinement of steel tubes leads to large increases in ductility but limited increases in the ultimate load, which is desirable in seismic retrofit so that the retrofitted tube will not attract forces which are so high that adjacent members may be put in danger.

3. The use of FRP jackets to strengthen thin steel cylindrical shells against local elephant's foot buckling failure at the base has also been explored through finite element analyses. The limited numerical results for a thin cylindrical shell with a radius-to-thickness ratio of 1000 and subjected to axial compression in combination with internal pressure indicate that the method leads to significant increases of the ultimate load. The FRP jacketing of steel cylindrical shells can also be used in the construction of new tanks and silos to enhance their performance.

Table 3.1 Specimen details

| ***Specimen*** | $D_{outer}$ ***(mm)*** | $t_s$ ***(mm)*** | $D_{outer} / t_s$ | $l_{col}$ ***(mm)*** | $t_{frp}$ ***(mm)*** |
|---|---|---|---|---|---|
| **HST-0-40-A** | 165 | 4.2 | 39.5 | 450 | N/A |
| **HST-1G-40-A** | 166 | 4.2 | 39.5 | 450 | 0.17 |
| **HST-2G-40-A** | 165 | 4.2 | 39.5 | 450 | 0.34 |
| **HST-3G-40-A** | 165 | 4.2 | 39.5 | 450 | 0.51 |

Table 3.2 Summary of test results

| ***Specimen*** | $N_y$ ***(kN)*** | $N_{peak}$ ***(kN)*** | $N_{peak} / N_y$ | $\Delta_{peak,bhst}$ ***(mm)*** | $\Delta_{peak,chst}$ ***(mm)*** | $\Delta_{peak,chst} / \Delta_{peak,bhst}$ |
|---|---|---|---|---|---|---|
| **ST-0-40-A** | | 717.5 | 1.01 | | 0.9 | 1.2 |
| **ST-1G-40-A** | 707.4 | 740.4 | 1.05 | 0.747 | 8.7 | 11.6 |
| **ST-2G-40-A** | | 771.0 | 1.09 | | 9.7 | 13.0 |
| **ST-3G-40-A** | | 782.2 | 1.10 | | 10.1 | 13.5 |

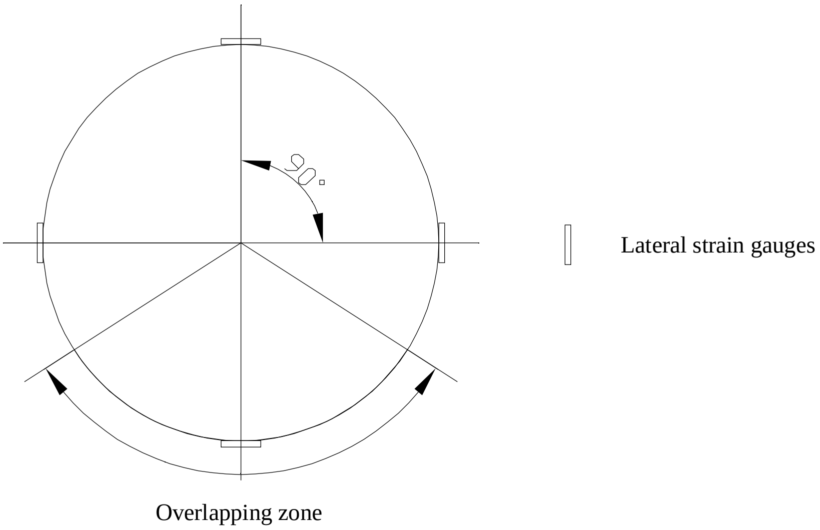


Figure 3.1 Layout of strain gauges for FRP-confined steel tube specimens


Figure 3.2 Test set-up

Figure 3.3 Bare steel tube after compression test

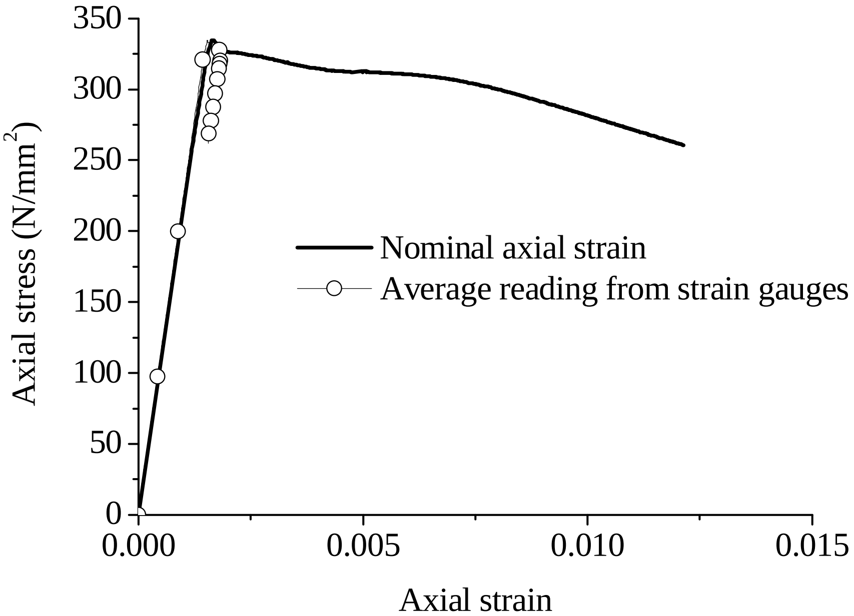


Figure 3.4 Experimental axial stress-axial strain curves of the bare steel tube


Figure 3.5 FRP-confined steel tubes after compression test

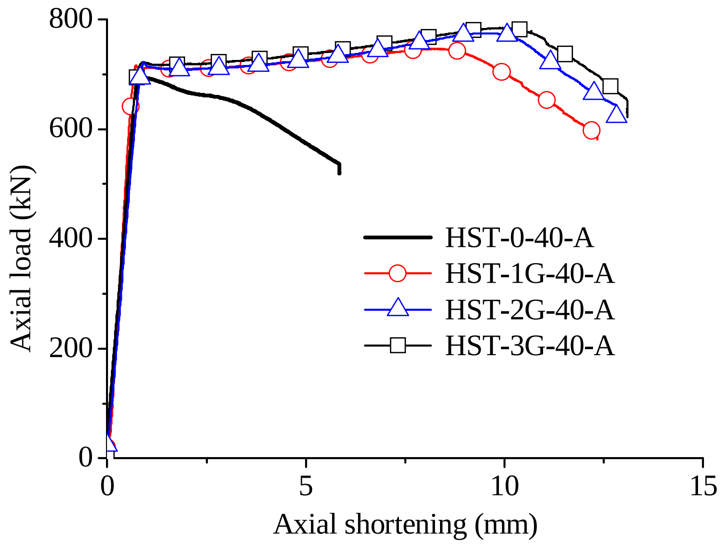


Figure 3.6 Experimental load-axial shortening curves of all four steel tubes

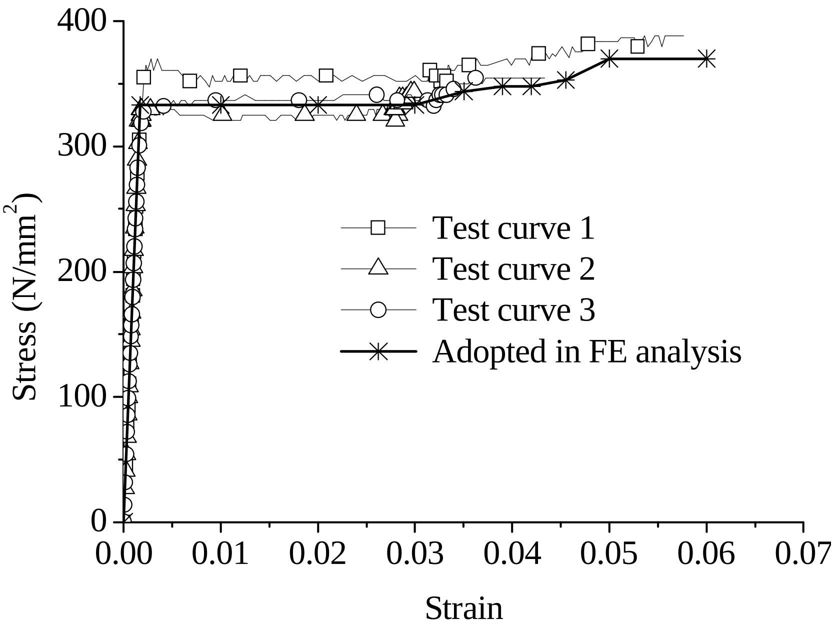


Figure 3.7 Tensile stress-strain curves of steel

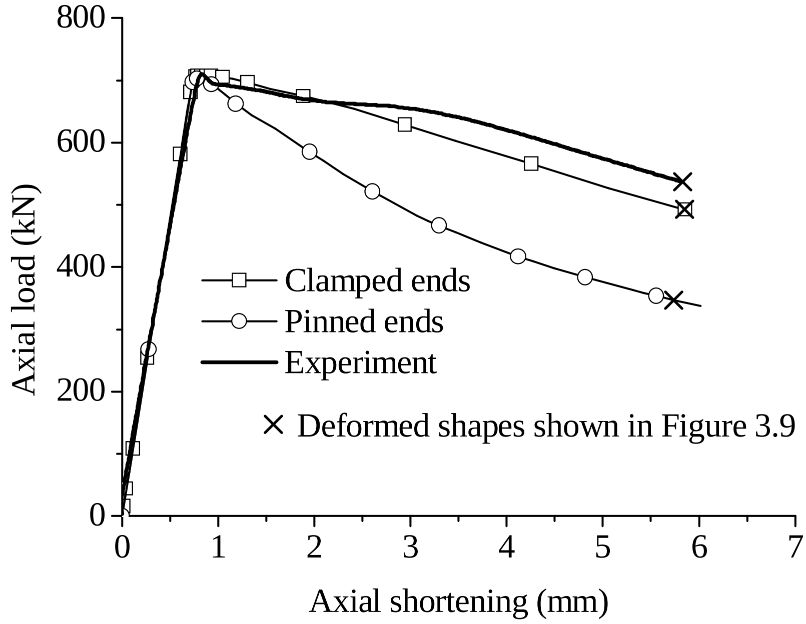


Figure 3.8 Load-axial shortening curves of the bare steel tube with different boundary conditions

(a) FE analysis, pinned ends

(b) FE analysis, clamped ends

(b) Experiment

Figure 3.9 Failure modes of the bare steel tube with different boundary conditions

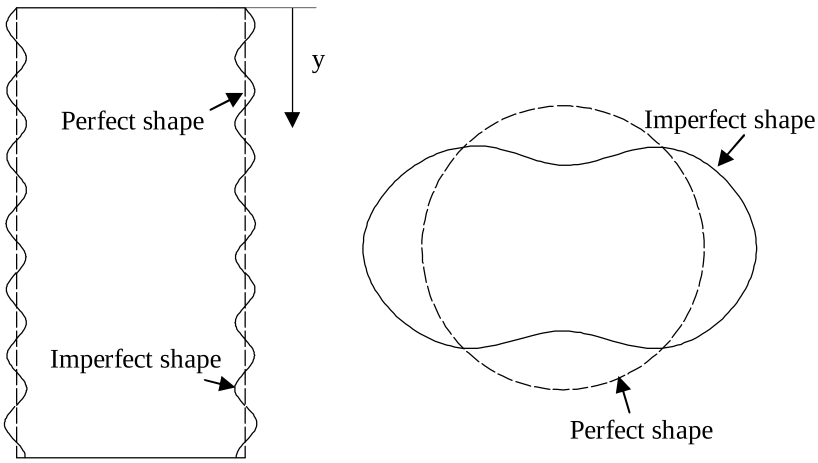


Figure 3.10 Imperfection assumed for the FRP-confined steel tubes

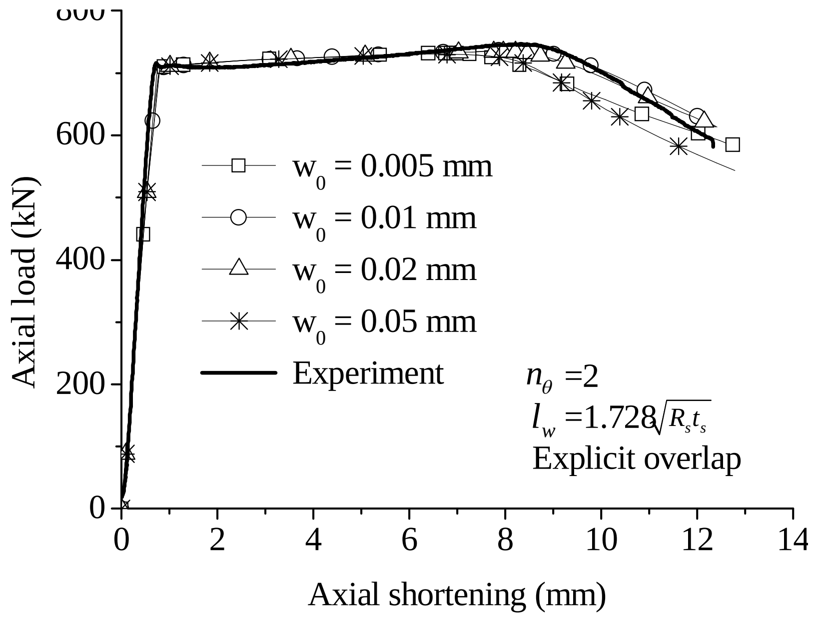


(a) HST-1G-40-A

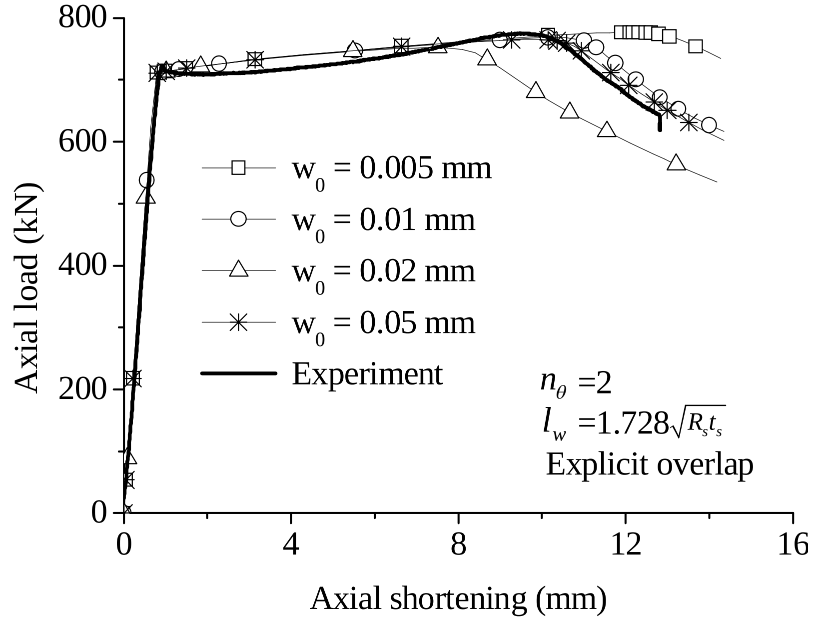


(b) HST-2G-40-A

Figure 3.11 Effect of imperfection amplitude on load-axial shortening curves

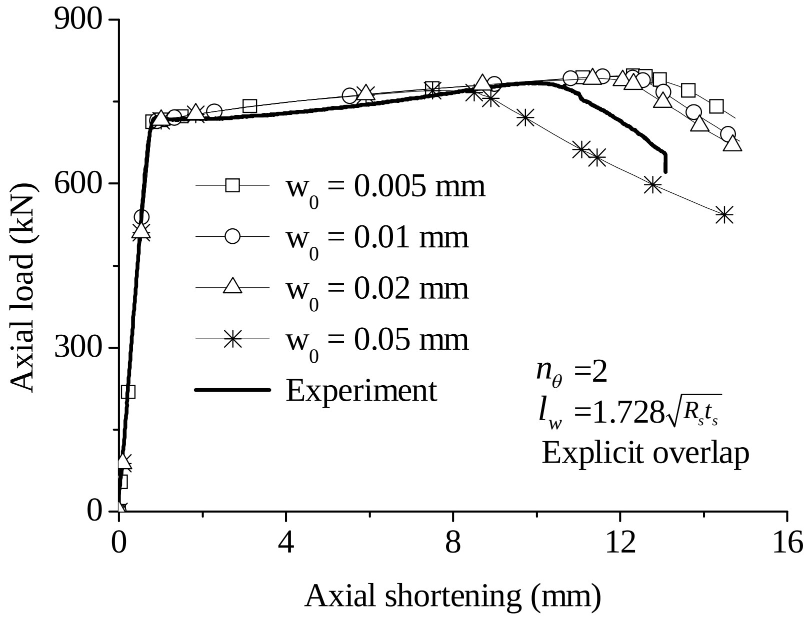


(c) HST-3G-40-A

Figure 3.11 Effect of imperfection amplitude on load-axial shortening curves (continued)

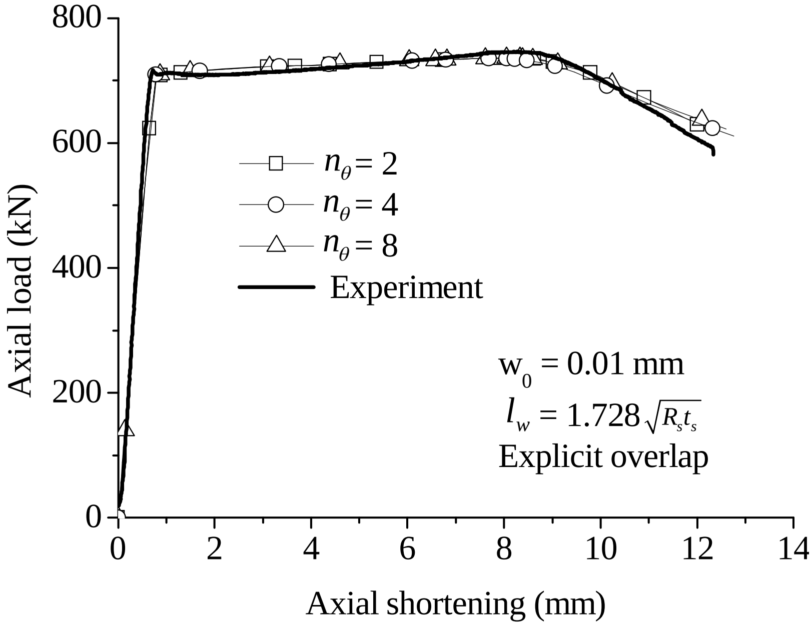


(a) HST-1G-40-A

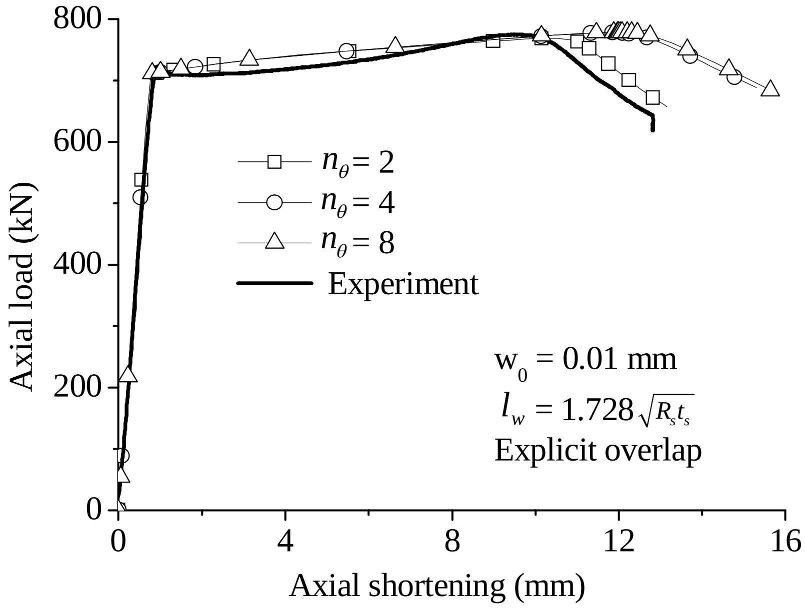


(b) HST-2G-40-A

Figure 3.12 Effect of circumferential wave number on imperfection on load-axial shortening curves

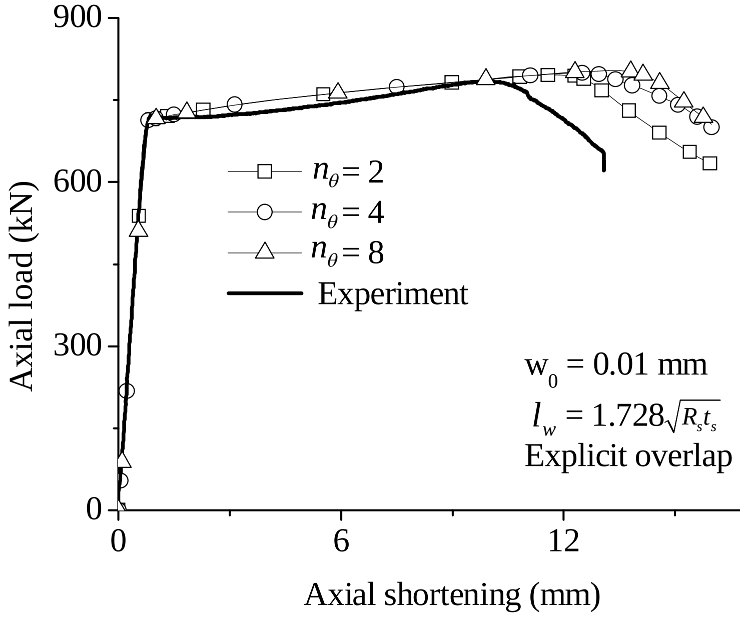


(c) HST-3G-40-A

Figure 3.12 Effect of circumferential wave number on imperfection on load-axial shortening curves (continued)

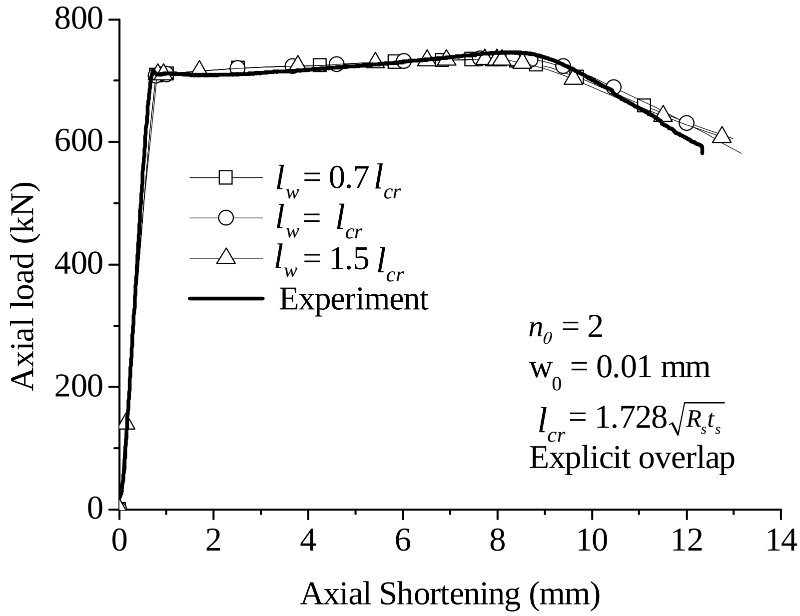


(a) HST-1G-40-A

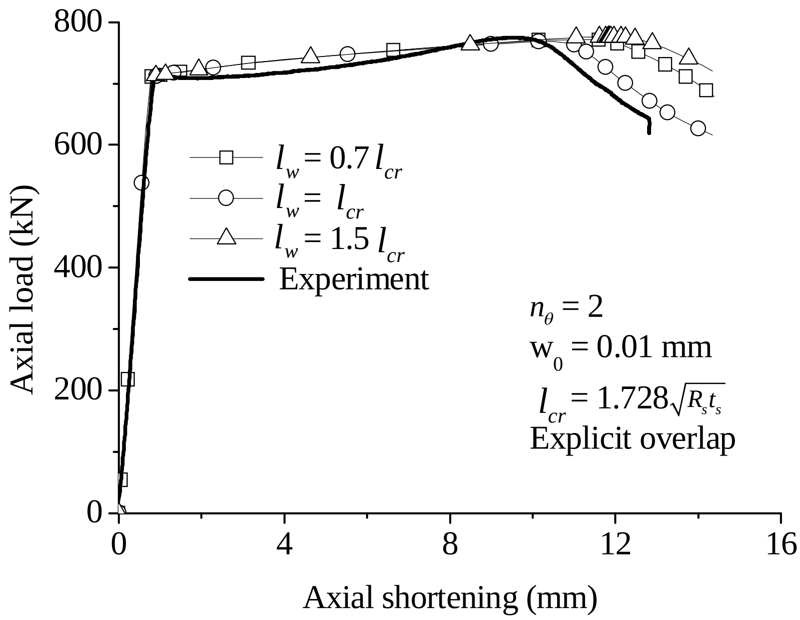


(b) HST-2G-40-A

Figure 3.13 Effect of meridional half wavelength of imperfection on load-axial shortening curves

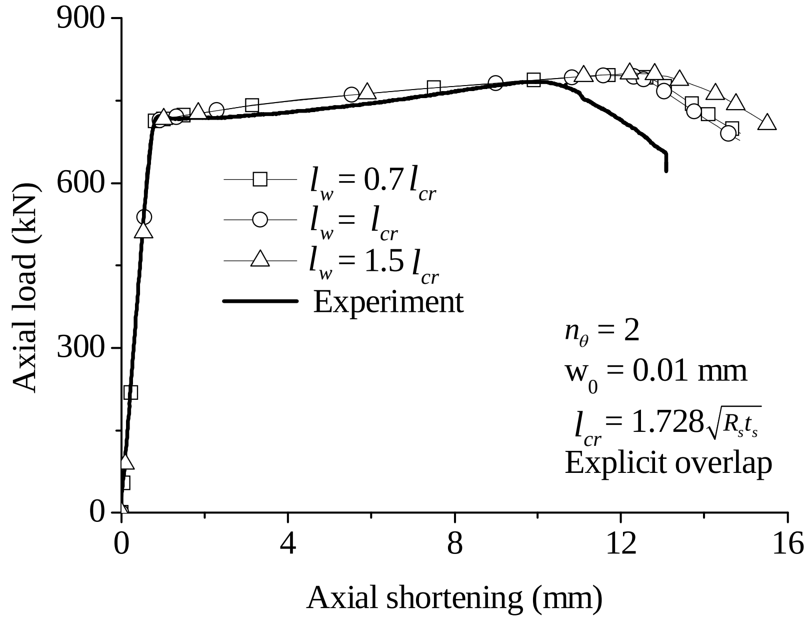


(c) HST-3G-40-A

Figure 3.13 Effect of meridional half wavelength of imperfection on load-axial shortening curves (continued)

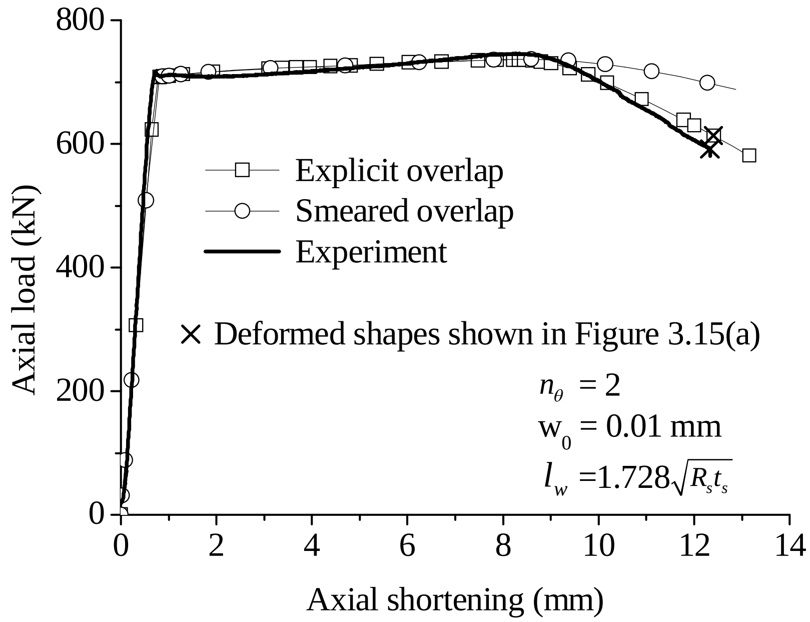


(a) HST-1G-40-A

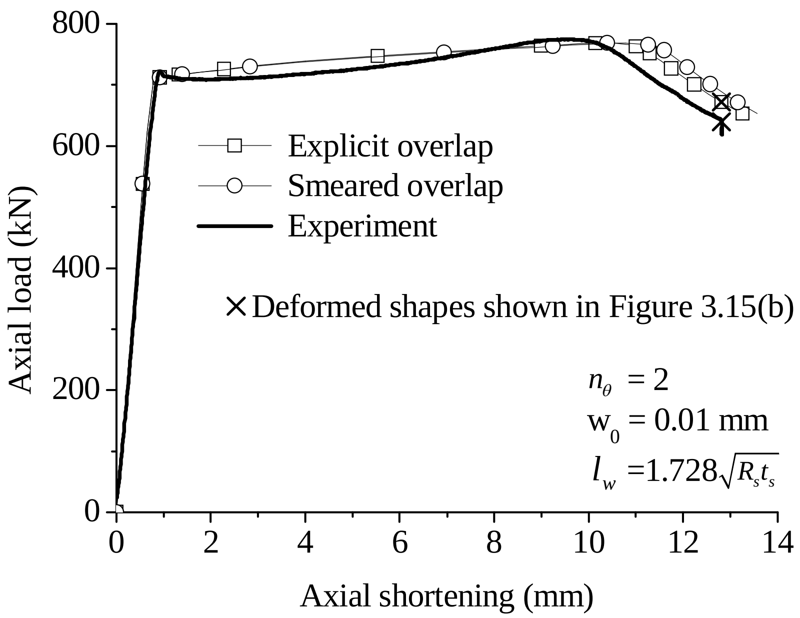


(b) HST-2G-40-A

Figure 3.14 Load-axial shortening curves of FRP-confined steel tubes: explicit overlap versus smeared overlap

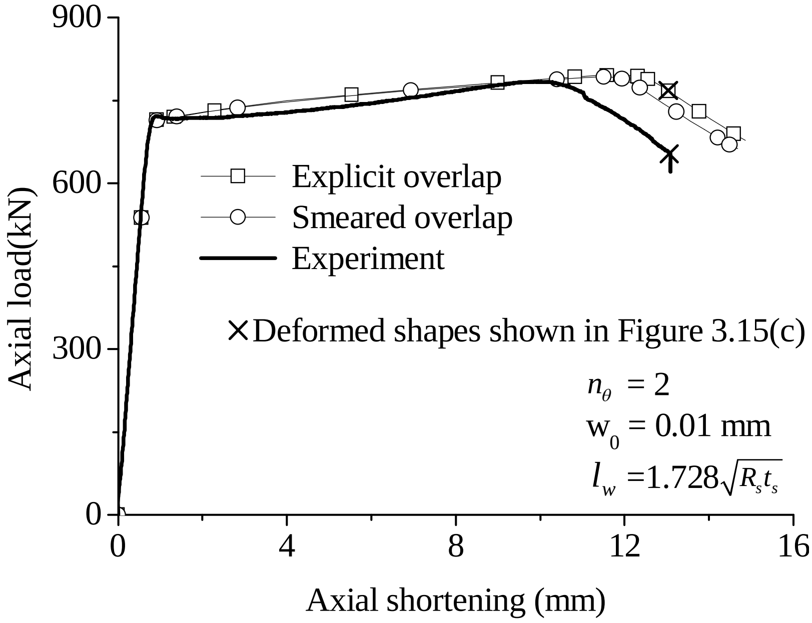


(c) HST-3G-40-A

Figure 3.14 Load-axial shortening curves of FRP-confined steel tubes: explicit overlap versus smeared overlap

(a) HST-1G-40-A

(b) HST-1G-40-A

Figure 3.15 Failure modes of FRP-confined steel tubes: finite element analysis versus experiment

(c) HST-1G-40-A

Figure 3.15 Failure modes of FRP-confined steel tubes: finite element analysis versus experiment (continued)

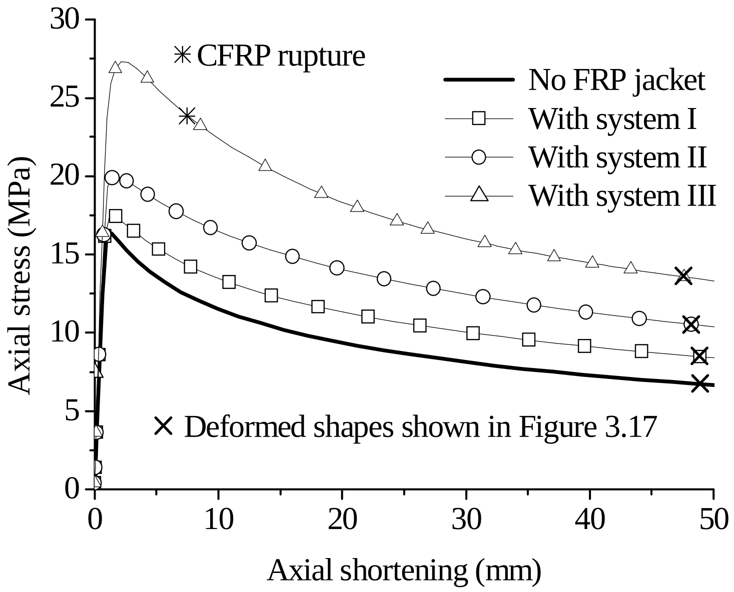


Figure 3.16 Load-axial shortening curves of pressurized thin cylindrical shells under axial compression

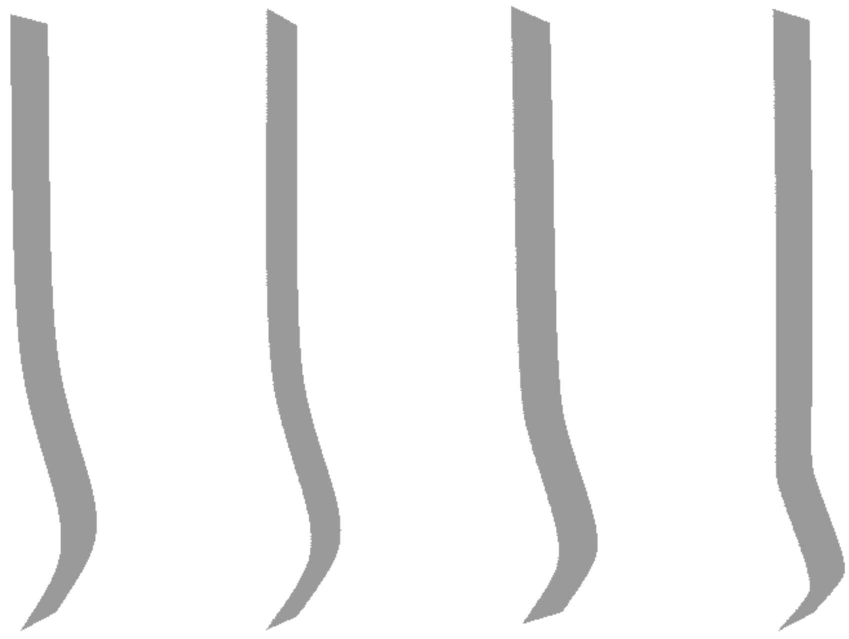

(a) No FRP jacket (b) With system I (c) With system II (d) With system III

Figure 3.17 Failure modes of pressurized thin cylindrical shells under axial compression

# CHAPTER 4

# BEHAVIOUR OF FRP-CONFINED CIRCULAR CONCRETE-FILLED THIN STEEL TUBES UNDER AXIAL COMPRESSION

## 4.1 INTRODUCTION

In Chapter 3, the use of FRP jackets has recently been extended for the suppression of outward buckling (i.e. elephant's foot buckling) in hollow circular steel tubes and shells. Results presented in Chapter 3 confirmed that FRP confinement of hollow circular tubes can be very effective in enhancing ductility without a significant strength increase. Recently, Xiao (2004) proposed a novel form of concrete-filled tubular (CFT) columns, named by him as confined CFT (or CCFT) columns in which the end portions are confined with steel tube segments or FRP jackets. Here, by providing an FRP or steel jacket, the through-tube is prevented from deforming inwards by the concrete core and outwards by the jacket, so both the ductility and strength of the steel through-tube can be substantially enhanced in the end regions. In addition, the concrete is better confined with the additional confinement from the FRP or steel jacket. It is obvious that such FRP confinement of concrete-filled steel tubes can be exploited in both structural strengthening and new construction.

Following Xiao's (2004) initial work, a number of other studies have been conducted by Xiao's group (Xiao et al. 2005; Mao and Xiao 2006; Shan et al. 2007), Tao's group (Tao et al. 2007; Wang et al. 2008) and other researchers (Gu et al. 2004; Teng and Hu 2006; Liu and Lu 2010; Park et al. 2010) on the effectiveness of FRP jacketing in improving the structural behaviour of both circular (Gu et al. 2004; Xiao et al. 2005; Teng and Hu 2006; Shan et al. 2007; Tao et al. 2007; Wang et al. 2008; Liu and Lu 2010) and square/rectangular CFTs (Mao and Xiao 2006; Tao et al. 2007; Wang et al. 2008; Park et al. 2010). While these studies have clearly demonstrated the benefits of FRP jacketing of CFT columns, much more research is still needed to develop a good understanding of the structural behaviour of and appropriate design methods for FRP-confined CFTs. In particular, the above studies have been concerned only with relatively thick steel tubes and the circular steel tubes examined had a diameter-to-thickness ratio below 84.7. Teng and Hu (2006) conducted tests on three CCFT columns for which the outer diameter-to-thickness ($D_{outer}/t_s$) ratio of the steel tube was 60. These tests showed that for CFT columns with such steel tubes for which the effect of local buckling is limited, FRP jacketing can effectively enhance the strength of the column but not the ultimate axial strain.

This chapter presents and interprets the results of three series of axial compression tests on CCFT columns where thinner steel tubes were used. In CFTs with thinner steel tubes, the confinement from the steel tube is smaller and the local buckling problem is more pronounced, so the benefit of FRP jacketing is expected to be more obvious. Thin steel tubes are also deemed to be particularly appropriate for CCFTs where the additional confinement available in the critical regions allows the thickness of the steel through-tube to be reduced. All steel tubes used in the tests presented in this chapter had a $D_{outer}/t_s$ ratio exceeding 100.

## 4.2 EXPERIMENTAL PROGRAMME

### 4.2.1 Test Specimens

In total, twelve specimens were prepared and tested in three series (Table 4.1). Each series included one concrete-filled steel tube (i.e. CFT) specimen and three FRP-confined CFT (i.e. CCFT) specimens with three different FRP jacket thicknesses respectively. The steel tubes used in the same series had the same $D_{outer}/t_s$ ratio, but the $D_{outer}/t_s$ ratios were different for the different series. The concrete was cast in three batches for the three series respectively but had the same mix ratio. All the specimens had an outer diameter of around 200 mm and a height of 400 mm. Other details of the specimens are summarized in Table 4.1. Each specimen is given a name, which starts with "CFT" (concrete-filled steel tube) followed by a number and a letter representing the number of plies in and the type of FRP jacket. The subsequent number (e.g. 102) is used to indicate the $D_{outer}/t_s$ ratio of the steel tubes. Finally, the letter "A" indicates the monotonic axial loading manner. For example, specimen CFT-1G-102-A is a concrete-filled steel tube specimen that has a steel tube with a $D_{outer}/t_s$ ratio of 102 and a one-ply GFRP jacket.

### 4.2.2 Preparation of Specimens

All steel tubes used in this experimental programme were rolled from steel plates in a commercial workshop and welded in the laboratory. A stiff steel mould was used inside and several steel belts were used outside during welding (Figure 4.1) to achieve a nearly perfect shape and an accurate diameter for the tube. Before the casting of concrete, a 25 mm thick bottom steel plate was welded to each steel tube. This was followed by the casting of concrete into the steel tube with the top surface of concrete left rough. After several days of curing, a thin layer of gypsum was applied on the rough concrete surface and then another 25 mm thick steel plate was welded the other end of to close the steel tube. This procedure was adopted to minimize the effect of concrete shrinkage to ensure direct contact between the steel plates and the concrete infill so that the steel tube and the concrete can be loaded simultaneously during testing.

The GFRP jackets were formed using the wet lay-up method: the steel tube surface was first cleaned using alcohol and then a continuous glass fibre sheet was wrapped around the steel tube to form a jacket with the required number of plies, with the finishing end of the fibre sheet overlapping its starting end by 200 mm (i.e. approximately the same as the diameter of the specimen). The longitudinal welding seam of the steel tube was placed at the middle of the overlapping zone (Figure 4.2).

### 4.2.3 Material Properties

Three plain concrete cylinders (152.5mm x 305mm) were tested for each series to determine the concrete properties. The average concrete elastic modulus ($E_c$), compressive strength ($f'_{co}$) and the corresponding strain ($\varepsilon_{co}$) obtained from these tests are given in Table 4.2.

Three types of steel plates, with thicknesses of 1 mm, 1.5 mm, 2 mm respectively, were used to fabricate the steel tubes to achieve three different $D_{outer}/t_s$ ratios. Tensile tests of three steel coupons were conducted for each steel plate type following BS 18 (1987). The average values of the elastic modulus $E_s$, yield stress $f_y$, and tensile strength $f_u$ for each type of steel plates are given in Table 4.1.

The material properties of GFRP have been presented in Chapter 3 (see Section 3.2.1). In summary, the GFRP jacket had an elastic modulus of 80.1 GPa, a tensile strength of 1,825.5 MPa and an ultimate tensile strain of 0.0228, which were calculated on the basis of the nominal ply thickness of 0.17 mm. It should be noted here that the FRP jacket thickness $t_{frp}$ given in Table 4.1 is also the nominal thickness and is equal to 0.17 mm times the number of plies of the jacket.

The adhesive used had an elastic modulus of 4.5 GPa and a ultimate tensile stress of 30 MPa according to the manufacturer.

### 4.2.4 Instrumentation and Loading

For each FRP-confined CFT specimen, six strain gauges in the hoop direction and two strain gauges in the axial direction were installed at the mid-height of the FRP jacket (Figure 4.2). The two axial strain gauges were at $180^{o}$ apart from each other, both being located outside the overlapping zone. Of the six hoop strain gauges, one of them was inside the overlapping zone while the other five were evenly distributed within the half circumference opposite the overlapping zone. Besides the mid-height strain gauges, five strain gauges in the hoop direction were installed near (20 mm from) each end of the specimen to measure any buckling deformation that would occur in those regions. The circumferential locations of these strain gauges were the same as the five mid-height hoop strain gauges outside the overlapping zone. The layout of the strain gauges on each bare CFT specimens was exactly the same as that for FRP-confined specimens. All strain gauges on FRP-confined CFT specimens had a gauge length of 20 mm while those on CFT specimens had a gauge length of 5 mm.

All the axial compression tests were conducted using an MTS machine (Figure 4.3) with a displacement control rate of 0.5mm/min until failure. The total axial shortening of the specimen was measured using three linear variable displacement transducers (LVDTs) placed at $120^{0}$ apart from each other. All the test data, including the strains, loads, and displacements, were recorded simultaneously by a data logger.

## 4.3 EXPERIMENTAL RESULTS AND OBSERVATIONS

### 4.3.1 General Observations

All bare CFT specimens experienced continuous dilation in the mid-height region and localized outward buckling of the steel tube near both ends of the tube at large axial shortenings (Figure 4.4). The load decreased rapidly after the peak load had been reached (Figure 4.5).

All FRP-confined CFT specimens failed by explosive rupture of the FRP jacket in the mid-height region due to the lateral expansion of the concrete, leading to a sudden and rapid load drop. Before this final failure, localized FRP rupture occurred near one end in some of the specimens (i.e. specimens CFT-2G-102-A, CFT-3G-102-A and CFT-2G-135-A) due to the localized outward buckling deformation of the steel tube, but this local FRP rupture only had a small effect on the load-carrying capacity of the specimen (see Figures 4.5a & b).

### 4.3.2 Axial Load-Axial Shortening Behaviour

The axial load-axial shortening curves of all specimens are shown in Figure 4.5, where the axial shortening is the average value of the three LVDTs. The curves of all CFT specimens feature a smooth but relatively steep descending branch after the peak load, while those of the FRP-confined specimens either have an approximately elastic-perfectly plastic curve or an approximately bilinear curve before final failure which is associated with a sudden load drop.

The key test results for all specimens are summarized in Table 4.3. Here, $N_u$ and $\Delta_u$ are the load and the axial shortening of a specimen at the ultimate state respectively, $N_{peak}$ is the peak load, and $\varepsilon_{rupt,frp}$ is the hoop strain of the FRP jacket at the ultimate state; $N_{peak,cft}$ and $\Delta_{u,cft}$ are respectively the peak load and the axial shortening at the ultimate state of the corresponding bare CFT specimen. For the FRP-confined CFT specimens, the ultimate state is defined as the state when explosive rupture of the FRP jacket occurs at the mid-height region. Based on this definition, the axial strain at the ultimate state of an FRP-confined specimen is also the corresponding ultimate axial strain. The load at the ultimate state of FRP-confined CFT specimens is either the same as or slightly lower than their peak load. The latter is due to either the end rupture of the FRP jacket (for specimens CFT-2G-102-A, CFT-3G-102-A and CFT-2G-135-A, see Figures 4.5a & b) or a slightly descending second portion of the load-shortening curve (for specimen CFT-1G-102-A, see Figure 4.5a). For the bare CFT specimens, the ultimate state is defined as the state when the load is reduced to 80% of the peak load.

The effect of FRP confinement is evident in Figure 4.5 and Table 4.3. With this additional confinement, the load-carrying capacity can be increased by 60% while the axial shortening capacity can be increased by up to 150%; the energy dissipation capacity is also much enhanced. As expected, a thicker FRP jacket led to a greater enhancement in performance. For the same FRP jacket thickness, the degree of enhancement in the load-carrying capacity is seen to be greater for CFTs with a thinner steel tube where the contribution of the steel tube to the load-carrying capacity is smaller.

### 4.3.3 Nominal Axial Strains versus Axial Strain Gauge Readings

There are two ways to obtain the axial strain of a specimen. One is to take the axial strain as the average reading from the two mid-height axial strain gauges, while the other is to take it as the average strain over the whole height of the specimen based on the average overall axial shortening of the three LVDTs. The strain value obtained from the latter approach is referred to as the nominal axial strain in this chapter.

Figure 4.6 shows a comparison between the nominal axial strain and the axial strain gauge reading for all specimens except specimen CFT-1G-102-A where the two axial strain gauges were damaged during the test. The axial strain gauge readings shown in Figure 4.6 were averaged from those of the two axial strain gauges except for specimen CFT-2G-135-A. In specimen CFT-2G-135-A, one of the axial strain gauges was damaged, so the readings from the only surviving axial strain gauge are shown. For the specimens of Series 102-A (except specimen CFT-1G-102-A), Figure 4.6a shows that the axial strains found using both approaches are in close agreement until a threshold strain value (around 0.008), beyond which the nominal axial strain becomes significantly larger than the axial strain gauge reading, indicating that significant localized deformation occurred outside the mid-height region of the steel tube. This is consistent with the experimental observation that significant localized buckling deformation occurred near both ends in specimen CFT-0-102-A and near one of the ends in specimens CFT-2G-102-A and CFT-3G-102-A. The outward buckling deformation caused localized FRP rupture near one of the ends of specimens CFT-2G-102-A and CFT-3G-102-A. The same trend can also be seen for specimen CFT-2G-135-A and the two bare CFT specimens of Series 135-A and 202-A (Figures 4.6b & c), where localized buckling deformation also appeared in the later stage of loading. On the contrary, for all the other FRP-confined specimens (see Figures 4.6b & c), the axial strains obtained from both approaches are similar throughout the entire loading process, indicating that localized buckling deformation was not significant in these specimens.

As the axial stiffness of the FRP jacket is very small and the local buckling deformation of the steel tube is outward, it is reasonable to expect the slip between the FRP jacket and the steel tube, if any, is very limited. Therefore, readings from the axial strain gauges, which were attached to the FRP jacket, can be taken to closely reflect the strain state of the steel tube at the mid-height. These axial strain gauge readings were thus employed in the analysis of the stress state of the steel tube in the present study. By contrast, significant slips may have existed between the steel tube and the concrete, especially after the development of localized buckling deformation of the steel tube, which means that the axial strain gauge readings cannot be assumed to closely reflect the strain state of the confined concrete. In the subsequent sections, the nominal axial strain is used to represent the axial strain of the confined concrete. It should be noted that the nominal axial strain represents the average deformation of the concrete over the column height, where the deformation near the ends may be different from that near the mid-height because of the lateral constraints from the two ends. Nevertheless, the nominal axial strain still reflects better the behaviour of the confined concrete as it does not suffer from the effect of the buckling of the steel tube.

## 4.4 BEHAVIOUR OF THE STEEL TUBE

Assuming that the steel tube of a bare or FRP-confined CFT specimen is in a state of plane stresses, the stress state of the mid-height section of the tube during the loading process can be determined from the two strains (i.e. the axial strain and the hoop strain) through an incremental analysis based on the $J_2$ flow theory of plasticity (Calladine 1985). In the present study, the steel is simply assumed to be an elastic-perfectly plastic material. The analysis basically involves the calculation of stress increments from strain increments using the following two equations (Eq. 4.1 for the elastic range and Eq. 4.2 for the elastic-plastic range):

$$\begin{Bmatrix} d\sigma_{x,s}^{i} \\ d\sigma_{\theta,s}^{i} \end{Bmatrix} = \frac{E_s}{1-\nu^2}\begin{bmatrix} 1 & \nu \\ \nu & 1 \end{bmatrix}\begin{Bmatrix} d\varepsilon_{x,s}^{i} \\ d\varepsilon_{\theta,s}^{i} \end{Bmatrix} \tag{4.1}$$

$$\begin{Bmatrix} d\sigma_{x,s}^{i} \\ d\sigma_{\theta,s}^{i} \end{Bmatrix} = \frac{E_s}{1-\nu^2}\begin{bmatrix} 1-\dfrac{S_a^{\ 2}}{S_c} & \nu-\dfrac{S_aS_b}{S_c} \\ \nu-\dfrac{S_aS_b}{S_c} & 1-\dfrac{S_b^{\ 2}}{S_c} \end{bmatrix}\begin{Bmatrix} d\varepsilon_{x,s}^{i} \\ d\varepsilon_{\theta,s}^{i} \end{Bmatrix} \tag{4.2}$$

where

$$S_a = s_x + \nu s_\theta \tag{4.3}$$

$$S_b = s_\theta + \nu s_x \tag{4.4}$$

$$S_c = s_x^{\ 2} + s_\theta^{\ 2} + 2\nu s_x s_\theta \tag{4.5}$$

$$s_x = \frac{1}{3}(2\sigma_{x,s}^{i-1} - \sigma_{\theta,s}^{i-1}) \tag{4.6}$$

$$s_\theta = \frac{1}{3}(2\sigma_{\theta,s}^{i-1} - \sigma_{x,s}^{i-1}) \tag{4.7}$$

where $\sigma_{x,s}$ and $\sigma_{\theta,s}$ are the axial and the lateral stresses respectively; $\varepsilon_{x,s}$ and $\varepsilon_{\theta,s}$ are the axial and the lateral strains respectively; $E_s$ and $\nu$ are the elastic modulus and Poisson's ratio of the steel respectively; and $i$ is the present strain increment number. The von Mises yield criterion is employed to identify whether the steel tube has yielded or not and is given by:

$$(\sigma_{x,s}^{i-1})^2 + (\sigma_{\theta,s}^{i-1})^2 + \sigma_{x,s}^{i-1}\sigma_{\theta,s}^{i-1} - f_y^{\ 2} = 0 \tag{4.8}$$

where $f_y$ is the yield stress. In addition, Eq. 4.9 is used to identify the loading or unloading stress state of steel tube with the present axial and lateral strain increments.

$$dg = \frac{\partial g}{\partial \sigma} d\sigma \tag{4.9}$$

if $dg < 0$, then steel is unloaded. The stresses increments in both directions can then be obtained through Eq. 4.1. Otherwise, the stresses are determined according to Eq. 4.2.

Noted that there exists a situation that is required to address (i.e. the stress state of steel tube is elastic in the previous strain level or iteration but is plastic under the current strain level or iteration). Therefore, only a portion of the current strain increment should be treated as elastic. A positive number $\zeta$ between zero and unity can then be found so that the yield surface is satisfied by part of the strain increments in both directions.

$$\sigma_{x,s,y} = \sigma_{x,s}^{i-1} + \zeta d\sigma_{x,s}^{i} \tag{4.10a}$$

$$\sigma_{\theta,s,y} = \sigma_{\theta,s}^{i-1} + \zeta d\sigma_{\theta,s}^{i} \tag{4.10b}$$

in which $\sigma_{x,s,y}$ and $\sigma_{\theta,s,y}$ define as the axial and circumferential steel stress, which is on the yield surface (Eqs. 4.8 & 4.11), or

$$\Pi(\sigma_{x,s,y},\sigma_{\theta,s,y,}) - f_y^{\ 2} = 0 \tag{4.11}$$

and $d\sigma_{x,s}^{i}$, $d\sigma_{\theta,s}^{i}$ are the stress increments calculated by assuming that the whole strain increments produce an elastic response. Substituting Eqs. 4.10a & b into Eq. 4.11 and rearranging leads to the quadratic

$$A\zeta^2 + B\zeta + C = 0 \tag{4.12}$$

in which

$$A = (d\sigma_{x,s}^{i})^2 + (d\sigma_{x,s}^{i})^2 - d\sigma_{x,s}^{i} d\sigma_{\theta,s}^{i} \tag{4.13a}$$

$$B = d\sigma_{x,s}^{i}(2\sigma_{x,s}^{i-1} - \sigma_{\theta,s}^{i-1}) + d\sigma_{\theta,s}^{i}(2\sigma_{\theta,s}^{i-1} - \sigma_{x,s}^{i-1}) \tag{4.13b}$$

$$C = (\sigma_{x,s}^{i-1})^2 + (\sigma_{x,s}^{i-1})^2 - \sigma_{x,s}^{i-1}\sigma_{\theta,s}^{i-1} - f_y^2 \tag{4.13c}$$

The value of $\zeta$ is obtained by ignoring the negative root. Thus, for an increment of strain, only $\zeta d\varepsilon_{x,s}^{i}$ and $\zeta d\varepsilon_{\theta,s}^{i}$ is taken as elastic (Eq. 4.1), while the remaining is an elastic-plastic strain increment and is dealt with using the nonlinear elastic plastic constitutive relations (Eq. 4.2).

In the process of evaluating the stress state of a steel tube using Eqs. 4.1-4.13, tensile stresses and strains are defined to be negative while compressive stresses and strains are defined to be positive. This sign convention for stresses and strains are used throughout this chapter unless otherwise specified.

Due to measurement noises, the difference between two consecutive strain gauge readings, being a very small quantity, may be in significant error. Therefore, for some of the specimens (i.e. all bare CFT specimens, CFT-2G-102-A and CFT-3G-102-A), the experimental axial strain-hoop strain curves were smoothened before being employed to calculate the stress state of the steel tube. As an illustration of this process, Figure 4.7 shows a comparison of the experimental and smoothened axial strain-hoop strain curves for specimen CFT-3G-102-A and the corresponding axial stress-strain curves; the comparison of experimental and smoothened curves for other specimens are similar. The stress states obtained from the smoothened axial strain-hoop strain curves are used in the discussion below unless otherwise specified.

The axial stress-strain curves of the steel tubes obtained from the incremental approach presented above are shown in Figure 4.8 for all specimens. All curves are terminated at the ultimate state except those of specimens CFT-2G-102-A, CFT-3G-102-A and CFT-4G-135-A which are terminated at the failure of one of the axial strain gauges. Figure 4.8 shows that all steel tubes behaved linear-elastically in the initial stage until a stress level approximately equal to or slightly higher than the yield stress of the steel tube. The slight difference between the peak stress and the steel yield stress of the steel tube, mainly for FRP-confined CFT specimens, is attributed to the positive effect of FRP confinement. After the peak load point, the axial stress begins to decrease with the axial strain because of the increasing hoop tensile stresses induced by the lateral expansion of the concrete. The axial stress keeps decreasing until the attainment of the ultimate state for all bare CFT specimens and some of the FRP-confined specimens (i.e. specimens CFT-2G-102-A, CFT-3G-102-A, CFT-2G-135-A, referred to as type I specimens hereafter) but remains approximately constant or increases slowly in the final stage of deformation for the other FRP-confined specimens (e.g. specimens CFT-3G-135-A, CFT-4G-135-A and all specimens of Series 202-A, referred to as type II specimens hereafter). For type I specimens, it may be noted that localized buckling deformation occurred near both ends in bare CFT specimens and near one of the ends in the FRP-confined specimens , which resulted in a very slow increase in the axial strain at the mid-height (see Figures 4.6a & b) in the final stage of deformation. This slow increase in the axial strain together with the much more rapid increase in the hoop expansion led to a continuously decreasing axial stress. The instants of initiation of localized buckling deformation, as determined from Figure 4.6, are shown in Figure 4.8, to show how local buckling deformation affects the development of axial stress in the steel tube. Similar observations have been made by O'Shea and Bridge (1999) about concrete-filled steel tubes; they concluded that the end buckling of a steel tube prevents the axial load transfer. On the contrary, for type II specimens where local buckling deformation was not detected, the axial strain of the mid-height steel section kept increasing during the loading process and the lateral expansion of the concrete was eventually counter-balanced by the confinement of the FRP jacket, leading to an almost constant axial stress in the final stage of deformation.

The mid-height hoop stress in the steel tube obtained using the incremental approach is shown against the nominal axial strain in Figure 4.9 for all specimens. In all cases, the hoop stress is seen to be positive (i.e. compressive) in the initial stage until an axial strain of around 0.002. This can be explained by noting that the initial Poisson’s ratio of steel is larger than that of concrete and that of the FRP jacket, so the steel tube tended to expand more than the other two components and interfacial radial stresses were thus development between them. That is, in the initial stage of loading, the steel tube was subjected to radial tensile stresses from the concrete as long as the bond between the steel tube and concrete did not break (Johansson and Gylltoft 2002) and radial compressive stresses from the FRP jacket (for FRP-confined CFT specimens), leading to compressive hoop stresses in the steel tube.

Beyond a certain axial strain level, the concrete began to expand more quickly than the steel tube, leading to tensile hoop stresses in the steel tube. The mid-height hoop stress is seen to increase rapidly until an axial strain of around 0.006, after which the hoop stress either remains almost constant (for type II specimens) or keeps increasing at a smaller rate (for type I specimens) (Figure 4.9). The same explanation as presented above for the axial stress response also applies here to the hoop stress response, as after the yielding of steel, these two stresses are related by Eq. 4.8.

## 4.5 BEHAVIOUR OF THE CONFINED CONCRETE

### 4.5.1 Axial Stress-Strain Behaviour

Once the axial stress-strain curve of the steel tube is known, the axial load carried by the confined concrete can be found by deducting the axial load carried by the steel tube from the total load acting on the specimen, assuming that the small axial stiffness of the FRP jacket is negligible. The axial stress of the confined concrete, assumed to be uniform within its cross-section, can then be obtained by dividing the deduced load by its cross-sectional area. The nominal axial strain is used for interpreting the behaviour of the confined concrete as mentioned earlier. The key values of the stress and the strain of the confined concrete deduced from this process are summarized in Table 4.4, in which $f'_{cc}$ is the peak concrete stress, $f'_{cc,cft}$ is the peak concrete stress of the corresponding bare CFT specimen, $f'_{cu}$ and $\varepsilon_u$ are respectively the concrete stress and the axial strain at the ultimate state as defined earlier, and $\varepsilon_{u,cft}$ is the axial strain at the ultimate state of a corresponding bare CFT specimen. It is evident from Table 4.4 that both the stress and the axial strain at the ultimate state can be significantly enhanced as a result of FRP confinement.

The axial stress-strain curves of the confined concrete are shown in Figure 4.10 for all specimens. For all bare CFT specimens, the curve features a descending branch following the attainment of the peak stress at a relatively small axial strain. By contrast, all curves for the FRP-confined CFT specimens have a continuously ascending shape which consists of two approximately linear portions (i.e. the first and third portions) connected by a smooth curved portion (i.e. the second portion). As expected, the slope of the third portion is higher for specimens with a thicker FRP jacket which provides a larger amount of confinement.

To clarify the effect of the steel tube thickness on the confinement effectiveness, the normalized stress-strain curves are plotted in four groups (Figure 4.11), where the specimens in each group have the same FRP jacket thickness but different steel tubes. In Figure 4.11, the stresses are normalized with respect to the unconfined concrete strength while the strains are normalized with respect to the strain at the peak stress of unconfined concrete to facilitate comparisons. Figure 4.11 reveals that the curves of the specimens in each group all have a similar first portion, indicating that the steel tube confinement does not affect the first portion significantly; and that those of specimens with a thicker steel tube generally have a higher second portion and third portion, reflecting the greater confinement provided by the steel tube. Despite this difference, it is interesting to note that the third portion of the three curves all have a similar slope. This is believed to be due to the fact that beyond a certain axial strain level, the confining pressure from the steel tube became nearly constant or only slightly increased (see Figure 4.9) and the increase in axial stress of the confined concrete basically came from the increasing confining pressure provided by the FRP jacket which determines the slope of the final linear portion.

### 4.5.2 Confining Mechanism

The confining pressure provided by the FRP jacket and the steel tube can be calculated using the following two equations respectively:

$$\sigma_{r,frp} = \frac{E_{frp} t_{frp} \varepsilon_{frp}}{R_s - t_s / 2} \tag{4.14}$$

$$\sigma_{r,s} = \frac{\sigma_{\theta,s} t_s}{R_s - t_s / 2} \tag{4.15}$$

where $\sigma_{r.frp}$ is the confining pressure provided by the FRP jacket; $E_{frp}$ and $t_{frp}$ are the elastic modulus in the hoop direction and the thickness of the FRP jacket respectively; $\varepsilon_{frp}$ is the hoop strain of the FRP jacket and is taken here as the averaged of the readings from the five hoop strain gauges outside the overlapping zone; $R_s$ radius of the tube middle surface; $\sigma_{r.s}$ is the confining pressure provided by the steel tube; and $\sigma_{\theta,s}$ and $t_s$ is the hoop stress and thickness of the steel tube respectively, where the former can be obtained from Eqs. 4.1 & 4.2.

The total confining pressure received by the concrete, being the sum of the confining pressures from the FRP jacket and the steel tube as found using Eqs 4.14 & 4.15, are shown against the nominal axial strain in Figure 4.12 to examine the confining mechanism for the concrete in an FRP-confined CFT. In particular, the contribution of the steel tube and that of the FRP jacket are compared in Figure 4.13 for specimen CFT-3G-135-A for further clarification. Figures 4.12 & 4.13 reveal that the development of confining pressures can be generally divided into three stages. In the first stage (with the axial strain being smaller than around 0.002), the confining pressure from the steel tube is negative or nearly zero while that from the FRP jacket develops slowly; the total confining pressure is therefore very small or even negative (i.e. radial tensile stresses exist at the steel-to-concrete interface). In the second stage (from the end of the first stage to an axial strain of around 0.006), both the confining pressures from the steel tube and the FRP jacket increase, but at different rates which depend primarily on their hoop stiffnesses; the total confining pressure increases rapidly in this stage. In the third stage, the confining pressure from the steel tube is almost constant (for specimens without local buckling) or increases slowly (for specimens with local buckling), while that from the FRP jacket keeps increasing at a similar rate to that of the second stage, leading to a lower rate of overall confining pressure increase than that of the second stage.

With reference to Figure 4.10, it is not difficult to notice that the three stages of confining pressure development correspond to the three portions of the axial stress-strain curves. The confining mechanism of the concrete in an FRP-confined CFT can now be explained as follows. In an FRP-confined CFT column where the steel tube and the concrete are loaded simultaneously, the confinement received by the concrete is a result of the interaction between the three components of concrete, steel tube and FRP jacket and this interaction depends strongly on their different lateral expansion characteristics (e.g. different Poisson's ratios in the initial stage). In the initial stage of loading, the steel tube expands faster than the concrete because of its larger initial Poisson's ratio (i.e. around 0.3 compared to around 0.18), but its expansion is constrained by the FRP jacket whose Poisson's ratio is nearly zero as it only has fibres in the hoop direction. As a result, the concrete is subjected to small tensile radial stresses from the steel tube unless the bond between the steel tube and the concrete breaks down; these radial stresses are so small that they have little effect on the behaviour of the concrete. Beyond a certain axial strain level (i.e. approximately 0.002), the concrete starts to dilate significantly and faster than the steel tube, and it pushes the steel tube outward, which in turn pushes the FRP jacket outward, resulting in a confining pressure at the interfaces and hoop tensile stresses in both the steel tube and the FRP jacket. In other words, the FRP jacket constrains the lateral expansion of the steel tube which in turn constrains the lateral expansion of the concrete. If local buckling of the steel tube does not occur, the hoop tensile stresses in and the confining pressure provided by the steel tube which has now yielded remain constant once the dilation rate of the concrete is reduced to be the same as that of the steel tube subjected to axial compression, but the FRP jacket continues to provide an increasing confining pressure to the concrete through the steel tube, due to its linear elastic behaviour. If local buckling of the steel tube occurs near one of the ends, the mid-height axial strain of the steel tube becomes nearly constant, while the tensile stresses in and the confining pressure provided by the steel tube keeps increasing as the dilation of the concrete increases. In this sense, the end local buckling of the steel tube has a positive effect on the behaviour of the concrete, as it allows a larger confining pressure from the steel tube to be developed. A similar observation was made by O'Shea and Bridge (1999) about bare concrete-filled steel tubes.

### 4.5.3 Lateral Expansion Behaviour

The hoop-to-axial strain curves are shown in Figure 4.14 for all the specimens, where the nominal axial strain is once again used while the lateral strain is the average of readings of the five hoop strain gauges outside the overlapping zone. Figure 4.14 shows that the curves are generally higher for specimens with a thicker FRP jacket, indicating that at the same axial strain, the lateral expansion of the concrete is smaller when a thicker FRP jacket is used as is expected. It is also interesting to note that the difference in the curves appears more pronounced in Series 202-A where the thinnest steel tube was used, suggesting that the effectiveness of the FRP confinement is more significant for CFT with a thinner steel tube.

## 4.6 EFFICIENCY OF THE FRP JACKET

Figure 4.15 shows the distributions of the mid-height hoop strain around the circumference at the ultimate state for all the specimens. These strains were recorded by the six hoop strain gauges at the mid-height of the FRP jacket (Figure 4.2). It is obvious that the distribution is non-uniform around the circumference. For those specimens with a relatively thin FRP jacket (e.g. CFT-1G-102-A), the strain in the overlapping zone is seen to be smaller than those outside the overlapping zone, but such differences cannot be seen for the other specimens. These observations are different from the findings for FRP-confined concrete columns (Lam and Teng 2004) where the strain within the overlapping zone is always smaller. This might be attributed to two reasons: (a) due to the existence of the steel tube, the action of the steel tube on the FRP jacket is closer to that of uniform radial expansion than a uniform radial pressure which is closer to the situation of FRP-confined concrete columns; and (b) the weld seam of the steel tube located within the overlapping zone may have complicated the local stress/strain state in that region for the present specimens.

The efficiency of the FRP jacket is often evaluated by the so-called FRP efficiency factor $k_{\varepsilon}$ which is defined to be the ratio of the average FRP hoop rupture strain in a confined column to the ultimate tensile strain obtained from flat coupon tests (Pessiki et al. 2001; Lam and Teng 2003; Lam and Teng 2004). The FRP efficiency factor $k_{\varepsilon}$ can be interpreted as the product of two components (Pessiki et al. 2001) as given blow:

$$k_{\varepsilon} = k_{\varepsilon 1} k_{\varepsilon 2} \tag{4.16}$$

where $k_{\varepsilon 1}$ is the ratio of the average hoop strain to the maximum hoop strain at the ultimate state to account for the effect of non-uniform strain distribution in the FRP jacket and $k_{\varepsilon 2}$ is the ratio of the maximum hoop strain in an FRP jacket at the ultimate state to the ultimate tensile strain from flat coupon tests.

The values of $k_{\varepsilon 1}$ and $k_{\varepsilon 2}$ obtained from the present tests are shown in Figures 4.16 & 4.17 respectively. In calculating $k_{\varepsilon 1}$, only the readings from the strain gauges outside the overlapping zone were used. The value of $k_{\varepsilon 1}$ is seen to vary from 0.693 to 0.961, with a mean value of 0.865. The value of $k_{\varepsilon 2}$ is seen to vary from 0.824 to 1.133, with a mean value of 0.948. The average $k_{\varepsilon 1}$ value is similar to the average value of 0.908 for GFRP-confined concrete found by Lam and Teng (2004) from their tests, while the average $k_{\varepsilon 2}$ value is higher than the average value of 0.820 for GFRP-confined concrete found by Lam and Teng (2004) from their tests. The larger $k_{\varepsilon 2}$ values may be due to the larger diameter of the specimens presented in this paper [i.e. around 200 mm compared to around 150 mm of the specimens examined in Lam and Teng (2004)] which means that the detrimental effect of curvature is less significant, or due to the less significant stress concentration because of the presence of a steel tube, which means that the maximum strain recorded by the discrete strain gauges is closer to the real maximum strain within the continuous FRP jacket.

## 4.7 CONCLUSIONS

This chapter has presented an experimental study aimed at gaining a better understanding of the behaviour of FRP-confined concrete-filled thin steel tubes under axial compression. The experimental programme included three series of tests where the main parameters examined were the thickness (or the diameter-to-thickness ratio) of the steel tube and the stiffness of the FRP jacket. Based on the detailed instrumentation employed in the tests and in-depth examination on test results, the following conclusions can be drawn.

1. The FRP jacket is very effective in improving the axial compressive behaviour of concrete-filled thin steel tubes, in terms of both the load-carrying capacity and the ductility. The local buckling of the steel tube in a CFT specimen can be either substantially delayed or completely suppressed by the FRP jacket. As expected, the benefit of the FRP jacket increases as the jacket thickness increases or the steel tube thickness reduces.

2. The axial stress-strain behaviour of the concrete has been shown to possess three distinctive stages: an initial stage where the behaviour of the concrete is similar to that of unconfined concrete, a second stage where the confining pressure increases rapidly as a result of the combined contribution from the FRP jacket and the steel tube, and a third stage where increases in the confining pressure come predominantly from the FRP jacket.

Table 4.1 Details of specimens

| ***Series*** | ***Specimen*** | ***Steel tube*** | | | | | | ***Concrete*** | ***FRP*** |
|---|---|---|---|---|---|---|---|---|---|
| | | $D_{outer}$ *(mm)* | $t_s$ *(mm)* | $D_{outer}/t_s$ | $E_s$ *(mm)* | $f_y$ *(MPa)* | $f_u$ *(MPa)* | $f'_{co}$ *(MPa)* | $t_{frp}$ *(mm)* |
| **102-A** | **CFT-0-102-A** | 204 | 2 | 102 | 203 | 226 | 331 | 42.2 | N/A |
| | **CFT-1G-102-A** | | | | | | | | 0.17 |
| | **CFT-2G-102-A** | | | | | | | | 0.34 |
| | **CFT-3G-102-A** | | | | | | | | 0.51 |
| **135-A** | **CFT-0-135-A** | 203 | 1.5 | 135 | 204 | 242 | 349 | 42.1 | N/A |
| | **CFT-2G-135-A** | | | | | | | | 0.34 |
| | **CFT-3G-135-A** | | | | | | | | 0.51 |
| | **CFT-4G-135-A** | | | | | | | | 0.68 |
| **202-A** | **CFT-0-202-A** | 202 | 1 | 202 | 203 | 231 | 334 | 35.9 | N/A |
| | **CFT-2G-202-A** | | | | | | | | 0.34 |
| | **CFT-3G-202-A** | | | | | | | | 0.51 |
| | **CFT-4G-202-A** | | | | | | | | 0.68 |

Table 4.2 Properties of concrete

| ***Series*** | $E_c$ ***(GPa)*** | $f'_{co}$ ***(MPa)*** | $\varepsilon_{co}$ |
|---|---|---|---|
| **Series 102-A** | 27.9 | 42.2 | 0.00258 |
| **Series 135-A** | 28.8 | 42.1 | 0.00259 |
| **Series 202-A** | 26.7 | 35.9 | 0.00250 |

Table 4.3 Summary of test results

| ***Series*** | ***Specimen*** | $N_{peak}$ ***(kN)*** | $N_u$ ***(kN)*** | $N_u / N_{peak,cft}$ | $\Delta_u$ ***(mm)*** | $\Delta_u / \Delta_{u,cft}$ | $\varepsilon_{rupt}$ |
|---|---|---|---|---|---|---|---|
| **102-A** | **CFT-0-102-A** | 1864 | 1491 | 0.8 | 3.72 | 1 | N/A |
| | **CFT-1G-102-A** | 1993 | 1878 | 1.01 | 5.28 | 1.42 | -0.0179 |
| | **CFT-2G-102-A** | 2172 | 2127 | 1.14 | 8.45 | 2.27 | -0.0199 |
| | **CFT-3G-102-A** | 2427 | 2231 | 1.20 | 9.43 | 2.53 | -0.019 |
| **135-A** | **CFT-0-135-A** | 1699 | 1359 | 0.8 | 3.60 | 1 | N/A |
| | **CFT-2G-135-A** | 2014 | 1950 | 1.15 | 6.20 | 1.72 | -0.0161 |
| | **CFT-3G-135-A** | 2244 | 2244 | 1.32 | 6.85 | 1.90 | -0.0167 |
| | **CFT-4G-135-A** | 2561 | 2561 | 1.51 | 7.52 | 2.09 | -0.0179 |
| **202-A** | **CFT-0-202-A** | 1380 | 1104 | 0.8 | 4.09 | 1 | N/A |
| | **CFT-2G-202-A** | 1749 | 1710 | 1.24 | 6.73 | 1.65 | -0.0212 |
| | **CFT-3G-202-A** | 1961 | 1961 | 1.42 | 7.76 | 1.90 | -0.0191 |
| | **CFT-4G-202-A** | 2265 | 2265 | 1.64 | 8.68 | 2.12 | -0.0192 |

Table 4.4 Summary of key test results for confined concrete

| ***Series*** | ***Specimen*** | $f'_{cc}$ ***(MPa)*** | $f'_{cu}$ ***(MPa)*** | $f'_{cu}$ / $f'_{cc,cft}$ | $\varepsilon_u$ | $\varepsilon_u$ / $\varepsilon_{u,cft}$ |
|---|---|---|---|---|---|---|
| **102-A** | **CFT-0-102-A** | 51.6 | 45.1 | 0.87 | 0.0093 | 1 |
| | **CFT-1G-102-A** | N/A | | | | |
| | **CFT-2G-102-A** | 68.3 | 68.3 | 1.32* | 0.021 | 2.27 |
| | **CFT-3G-102-A** | 77.0 | 73.5 | 1.42* | 0.0236 | 2.53 |
| **135-A** | **CFT-0-135-A** | 50.5 | 43.4 | 0.86 | 0.009 | 1 |
| | **CFT-2G-135-A** | 64.1 | 62.1 | 1.23 | 0.0155 | 1.72 |
| | **CFT-3G-135-A** | 67.1 | 67.1 | 1.33 | 0.0171 | 1.90 |
| | **CFT-4G-135-A** | 77.2 | 77.2 | 1.53* | 0.0188 | 2.09 |
| **202-A** | **CFT-0-202-A** | 41.9 | 35.1 | 0.84 | 0.0102 | 1 |
| | **CFT-2G-202-A** | 52.9 | 52.2 | 1.25 | 0.0168 | 1.65 |
| | **CFT-3G-202-A** | 61.0 | 61.0 | 1.46 | 0.0194 | 1.90 |
| | **CFT-4G-202-A** | 68.5 | 68.5 | 1.63 | 0.0217 | 2.12 |

*****value at the failure of an axial strain gauge; the real value is expected to be slightly higher than the value shown here.

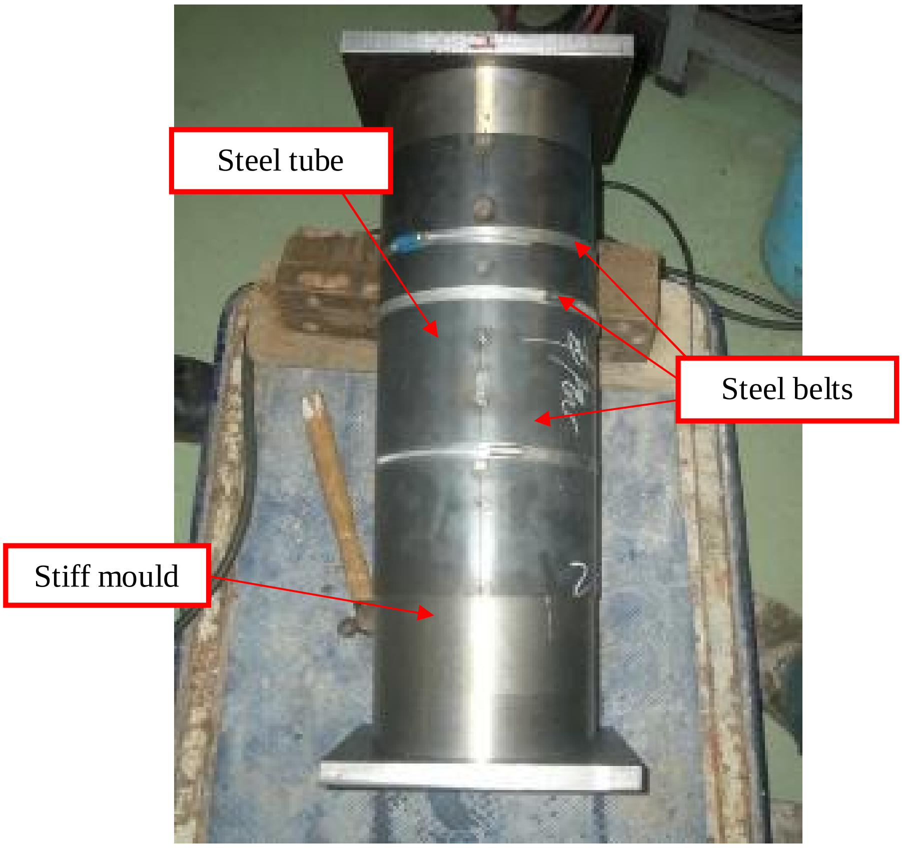


Figure 4.1 Mould for welding steel tubes

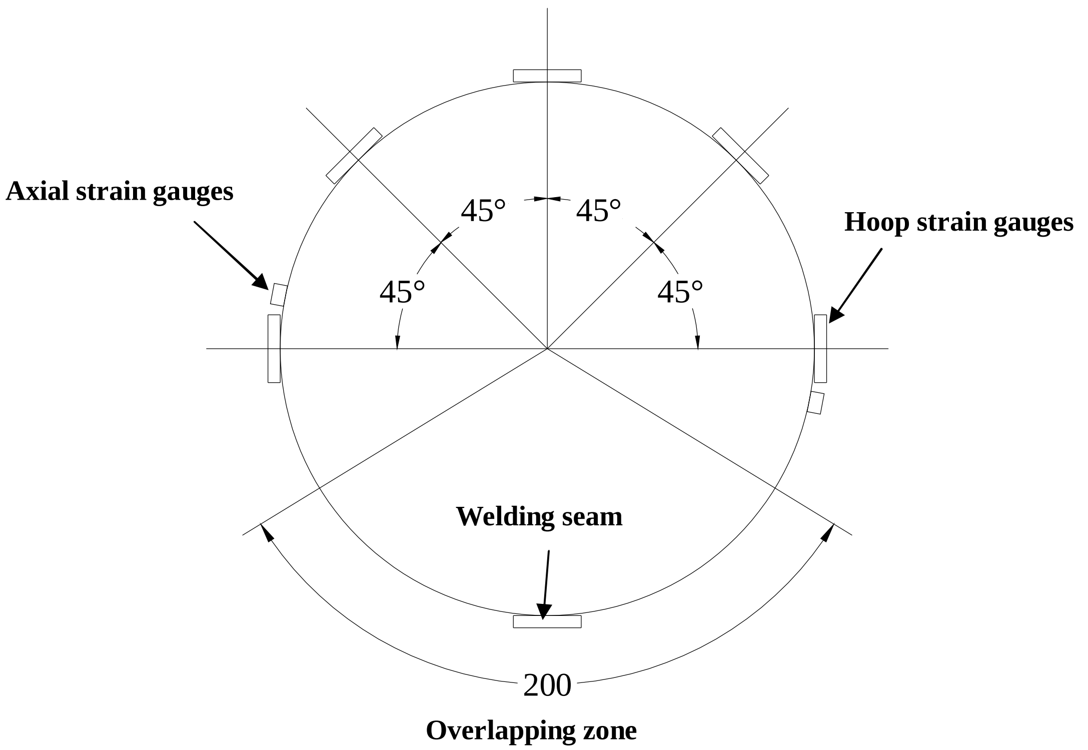


Figure 4.2 Layout of strain gauges at mid-height

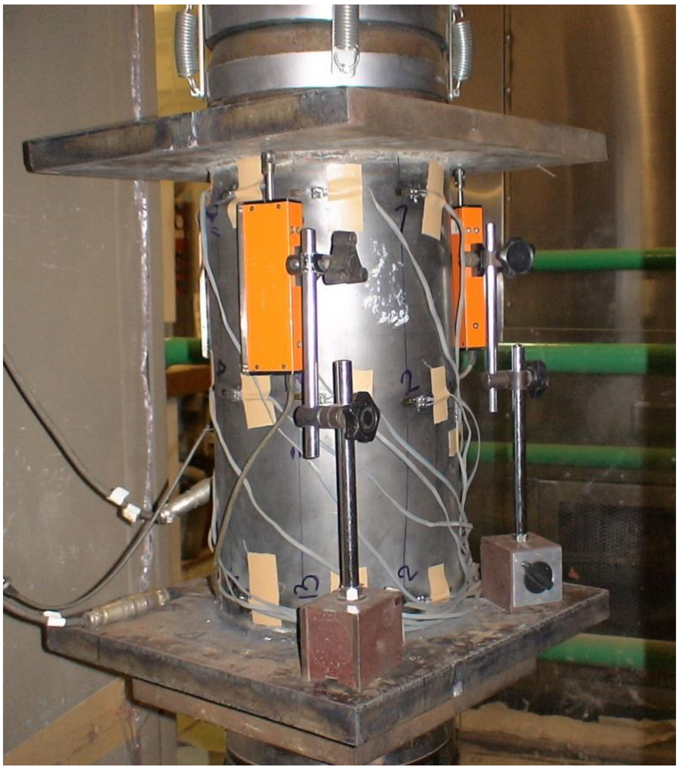

Figure 4.3 Test setup


(a) Series102-A


(b) Series 135-A

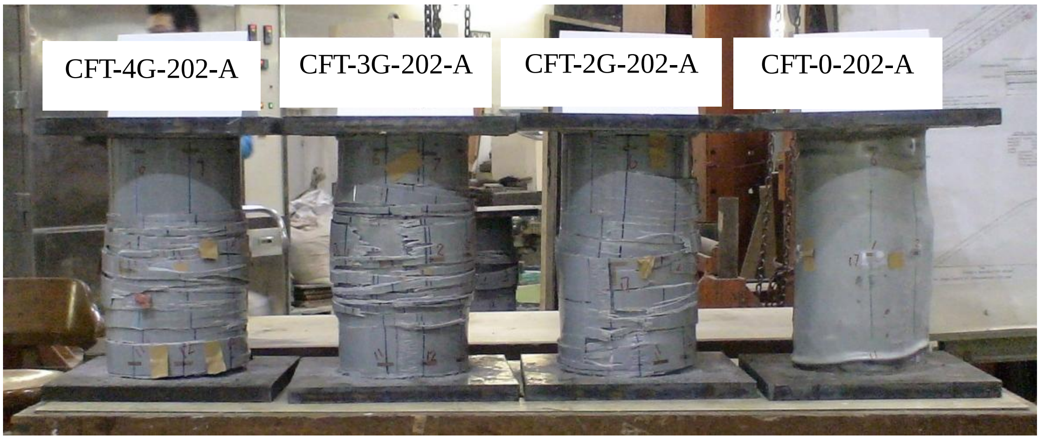


(c) Series 202-A

Figure 4.4 Failure modes of test specimens

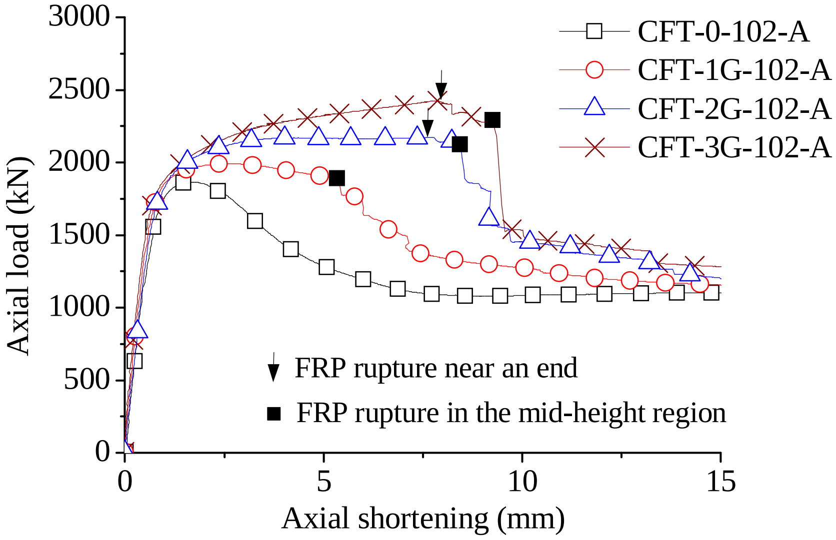


(a) Series 102-A

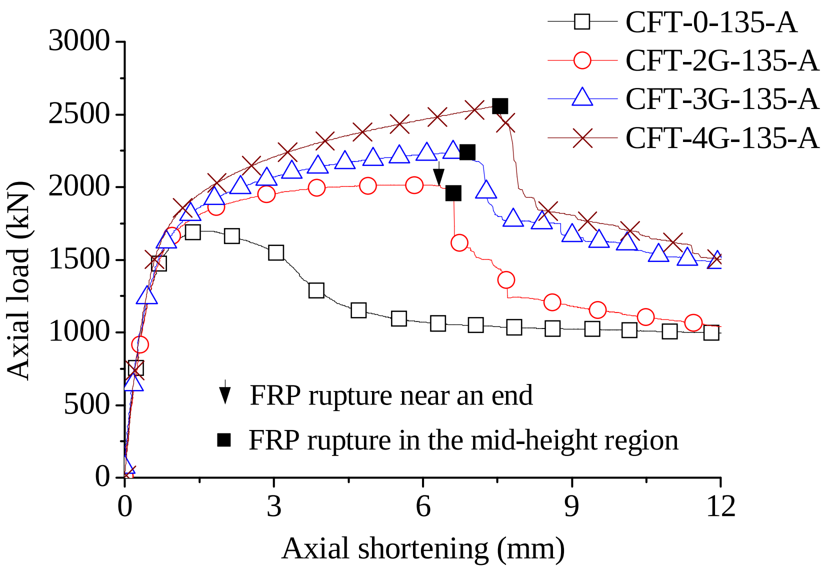


(b) Series 135-A

Figure 4.5 Axial load-axial shortening curves

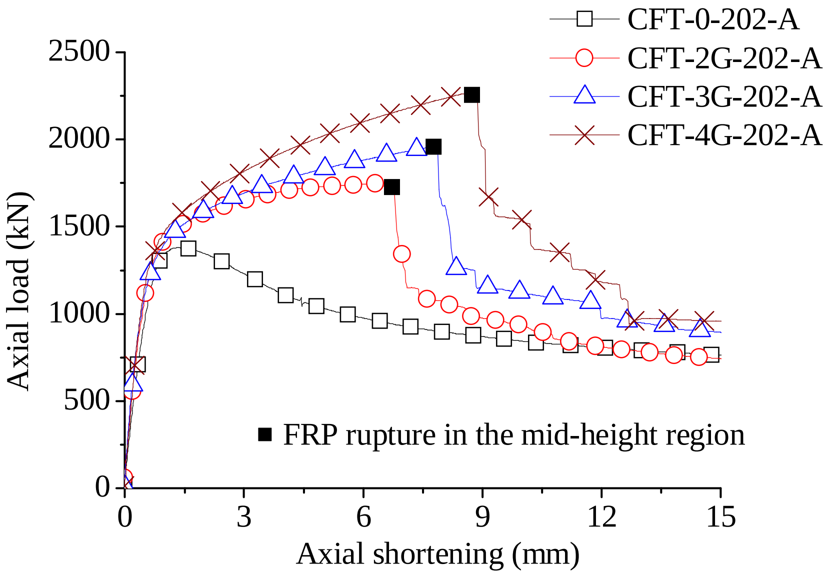


(c) Series 202-A

Figure 4.5 Axial load-axial shortening curves (continued)

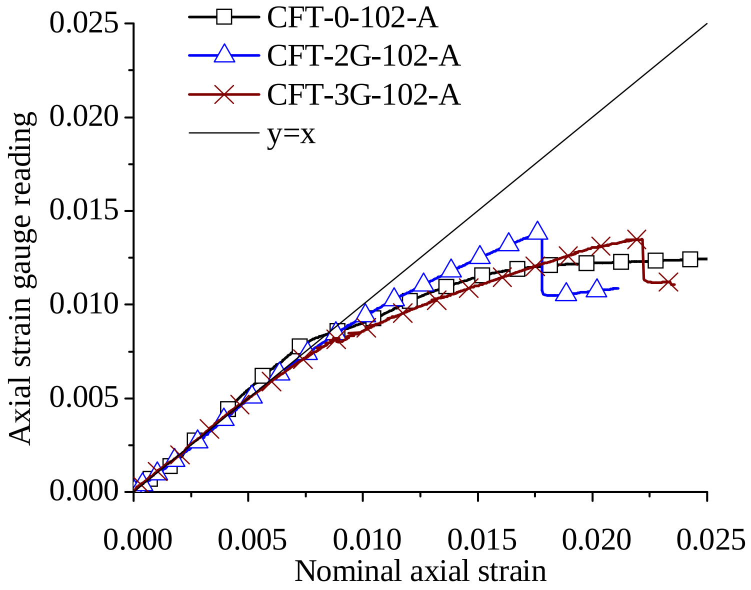


(a) Series 102-A

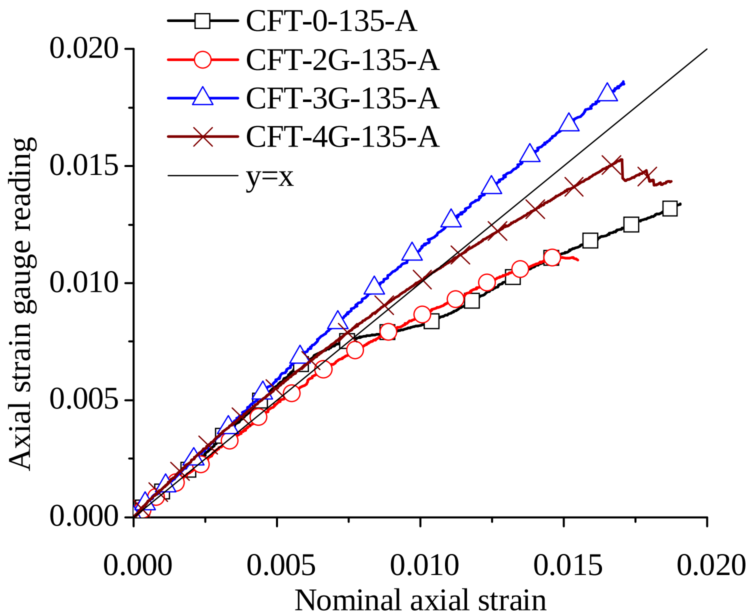


(b) Series 135-A

Figure 4.6Nominal axial strain versus axial strain gauge reading

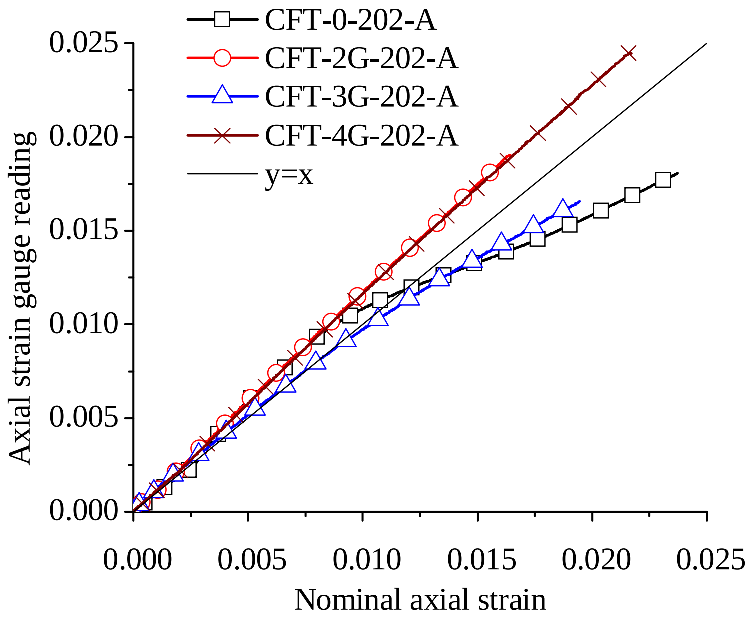


(c) Series 202-A

Figure 4.6 Nominal axial strain versus axial strain gauge reading (continued)

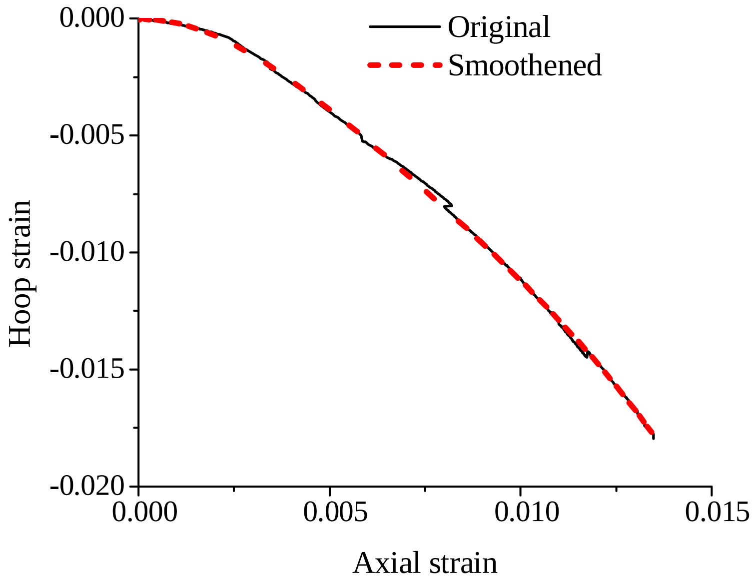


(a) Axial strain hoop strain curve

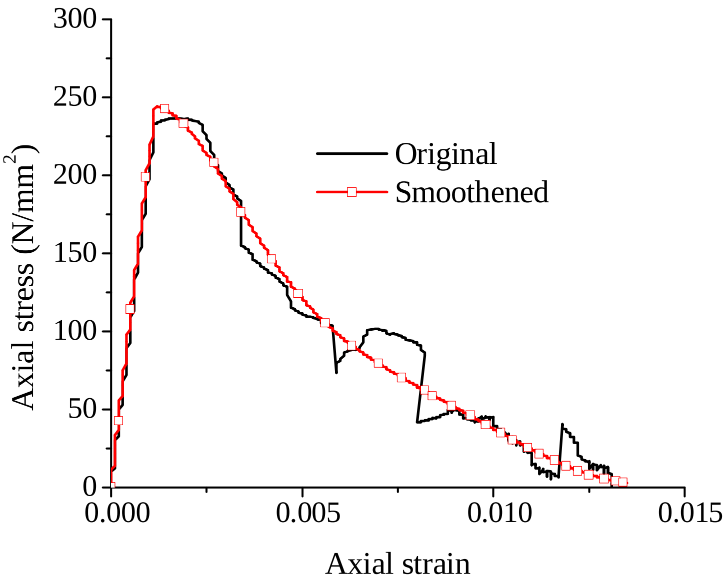


(b) Axial stress strain curve

Figure 4.7 Axial stress strain curve for specimen CFT-3G-102-A based on the smoothened axial strain hoop strain curve

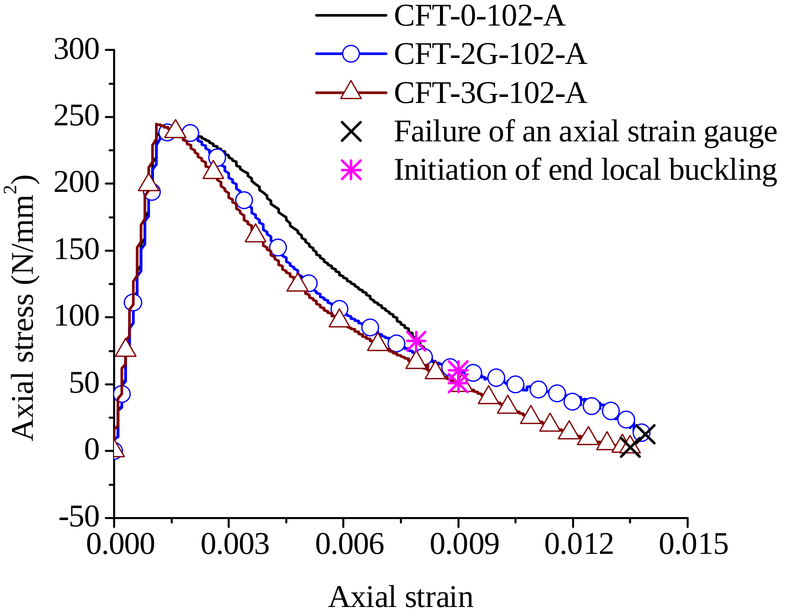


(a) Series 102-A

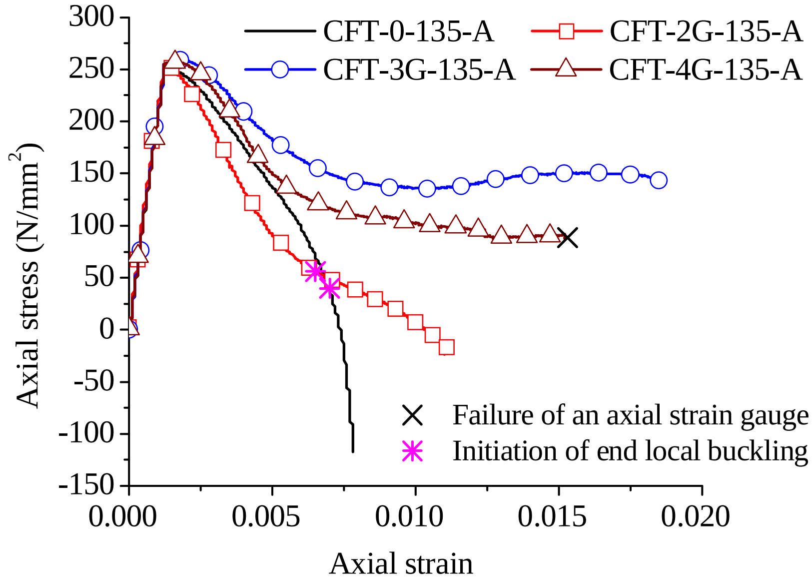


(b) Series 135-A

Figure 4.8 Axial stress-strain curves for steel tubes

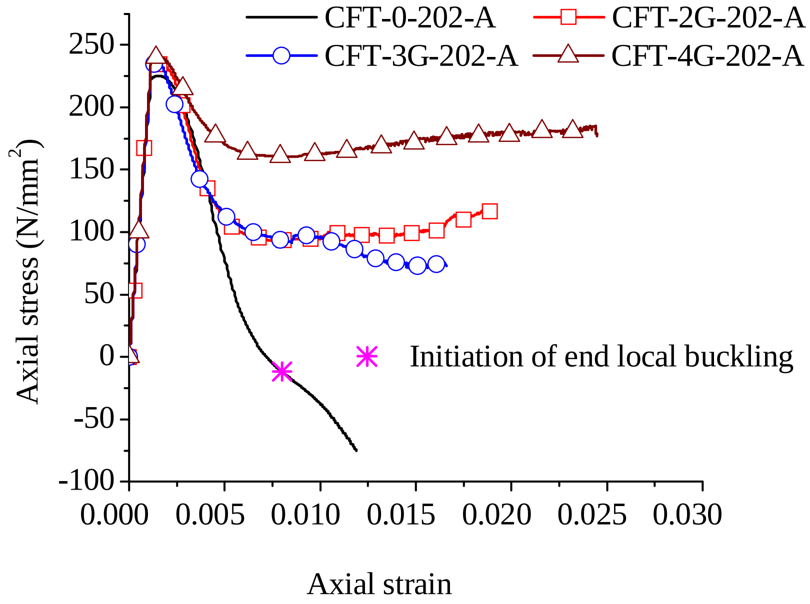


(c) Series 202-A

Figure 4.8 Axial stress-strain curves for steel tubes (continued)

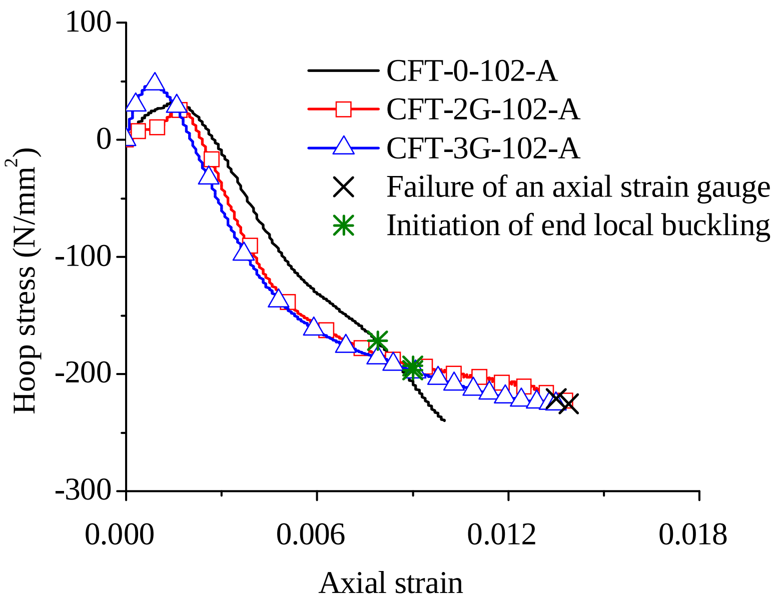


(a) Series 102-A

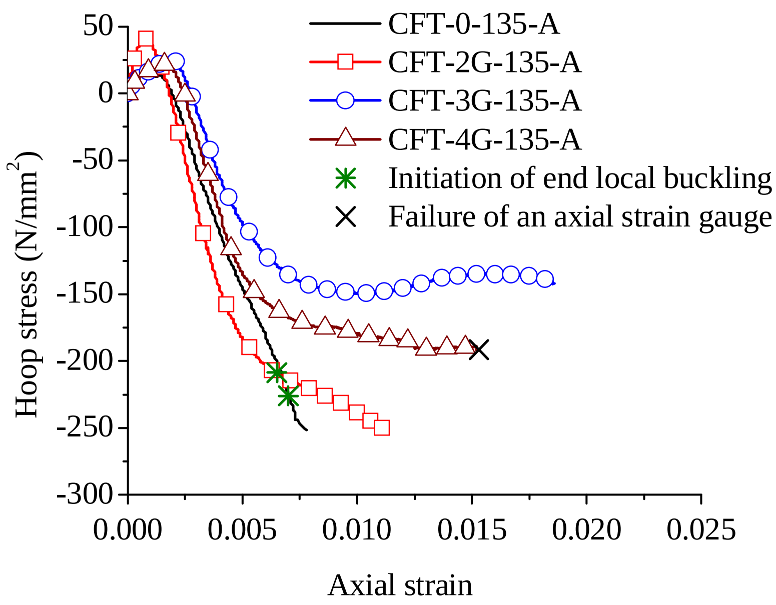


(b) Series 135-A

Figure 4.9Hoop stress-axial strain curves for steel tubes

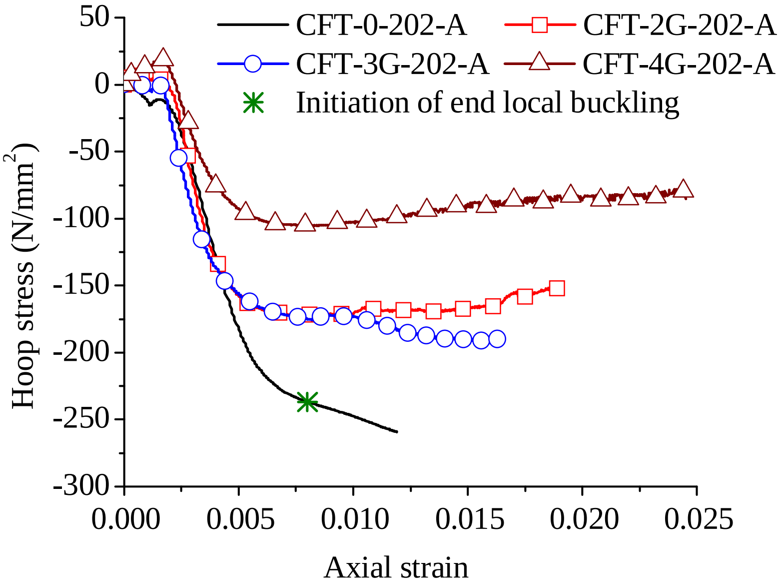


(c) Series 202-A

Figure 4.9 Hoop stress-axial strain curves for steel tubes (continued)

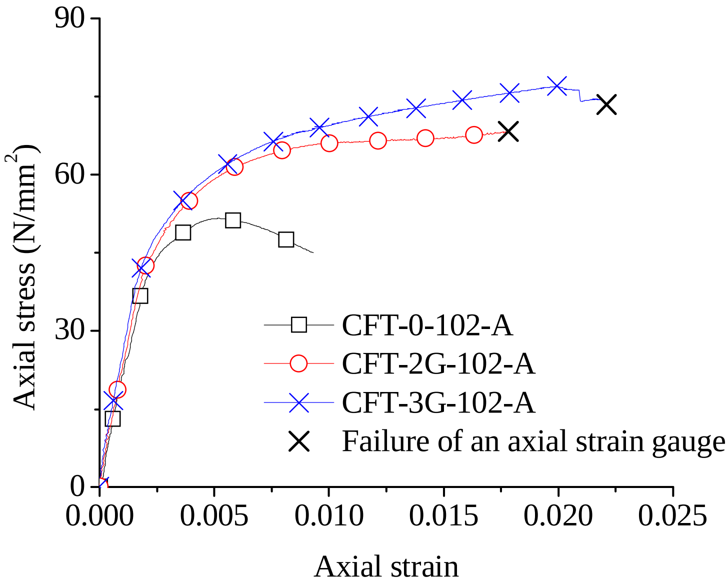


(a) Series 102-A

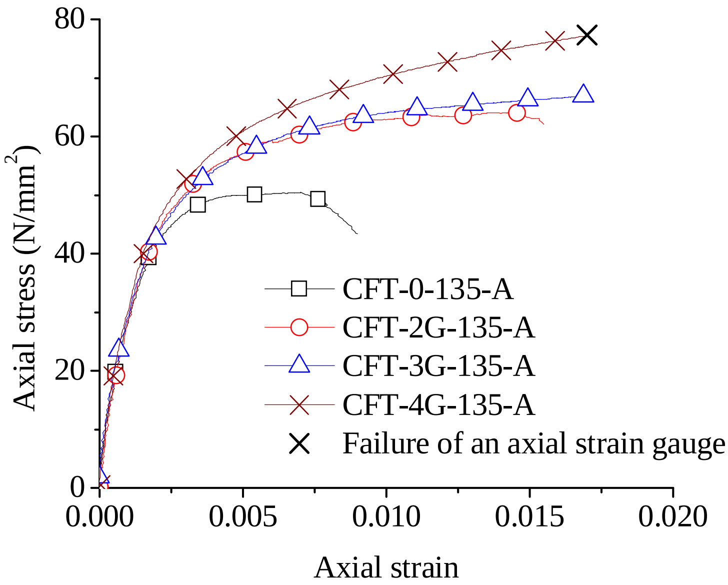


(b) Series 135-A

Figure 4.10Axial stress-strain curves of concrete

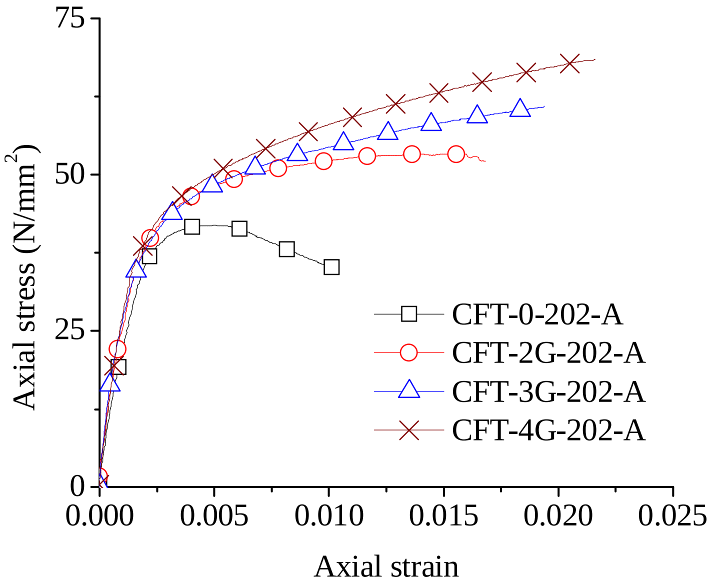


(c) Series 202-A

Figure 4.10 Axial stress-strain curves of concrete (continued)

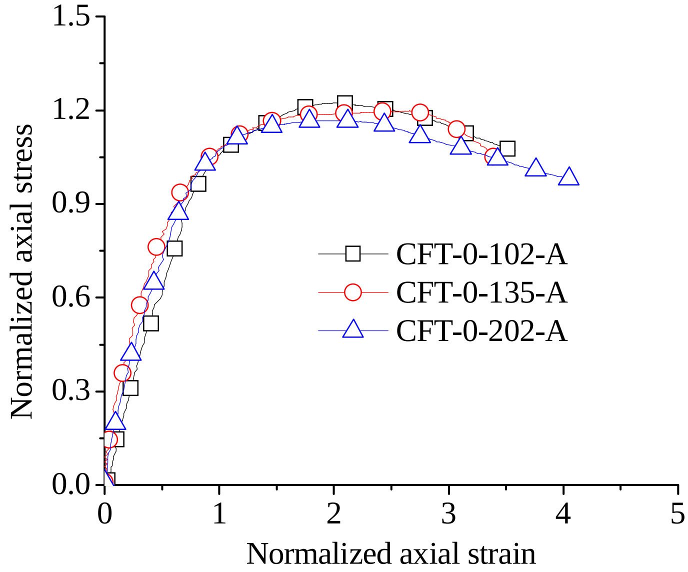


(a) Bare specimens

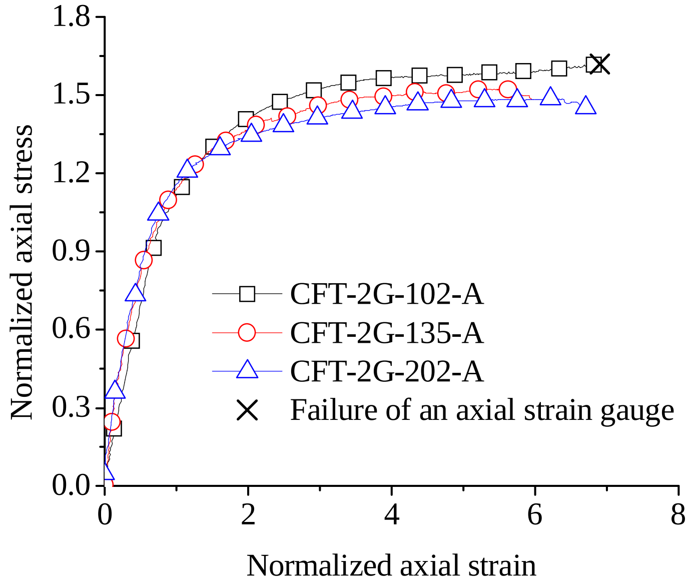


(b) 2-ply confined specimens

Figure 4.11 Effect of steel tube thickness on axial stress-strain behaviour of concrete

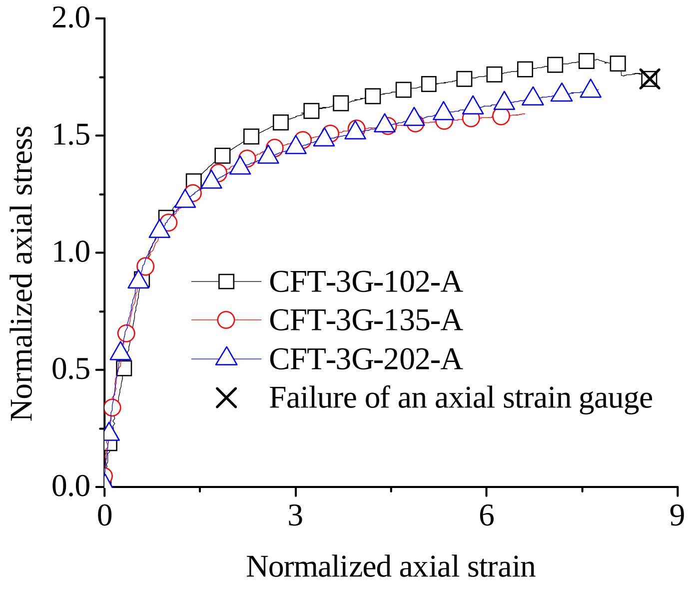


(c) 3-ply confined specimens

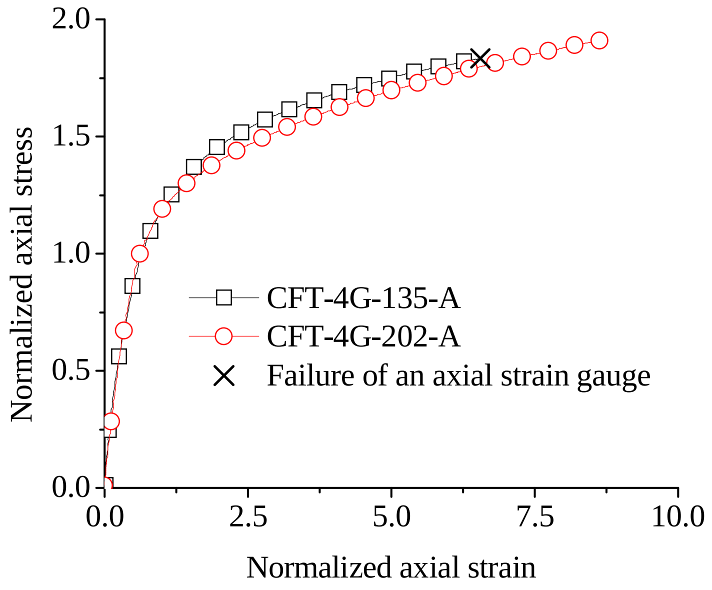


(d) 4-ply confined specimens

Figure 4.11 Effect of steel tube thickness on axial stress-strain behaviour of concrete (continued)

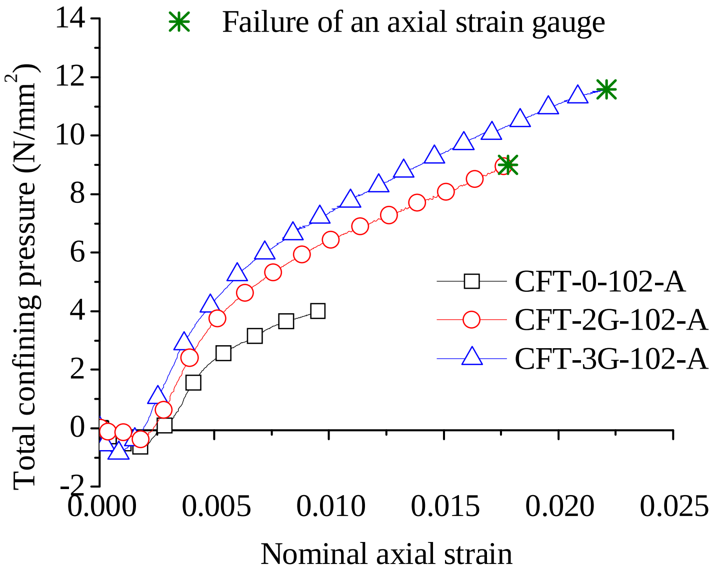


(a) Series 102-A

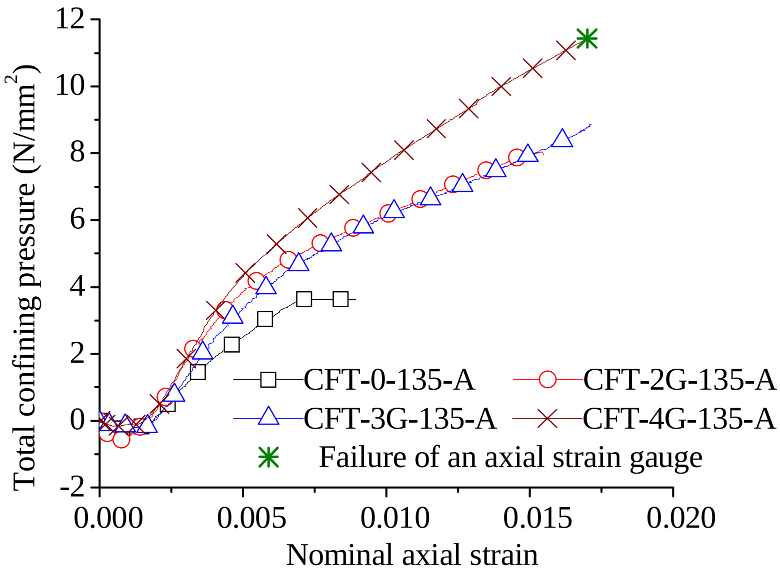


(b) Series 135-A

Figure 4.12 Total confining pressure to concrete core

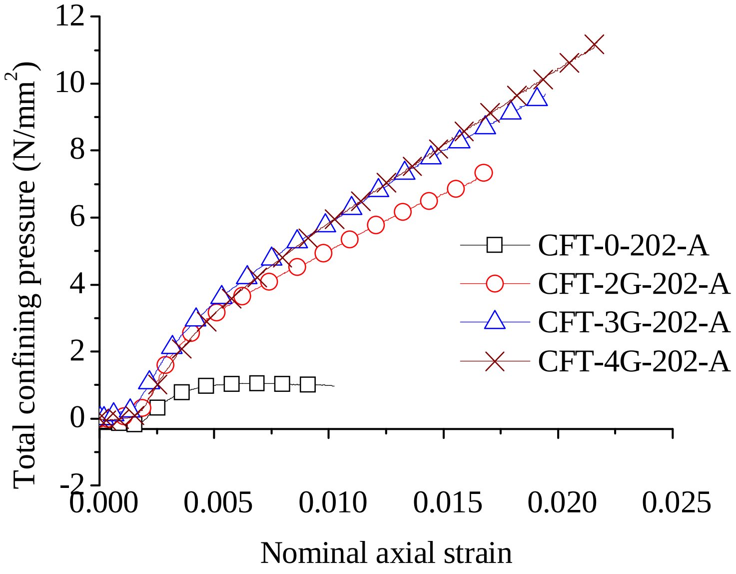


(c) Series 202

Figure 4.12 Total confining pressure to concrete core (continued)

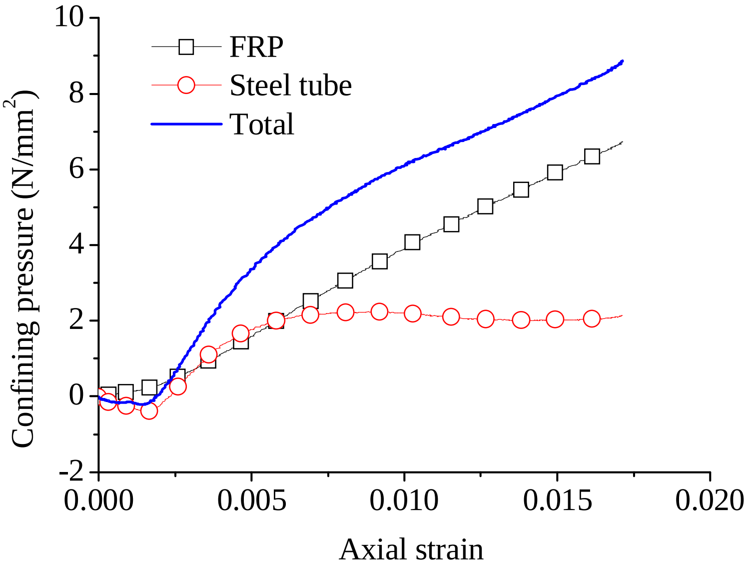


Figure 4.13Confining pressure from FRP jacket and steel tube for specimen CFT-3G-135-A

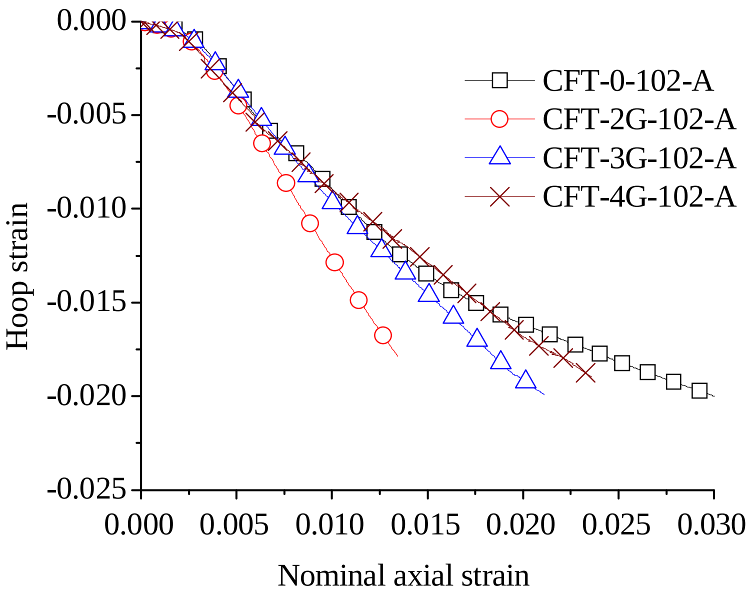


(a) Series 102-A

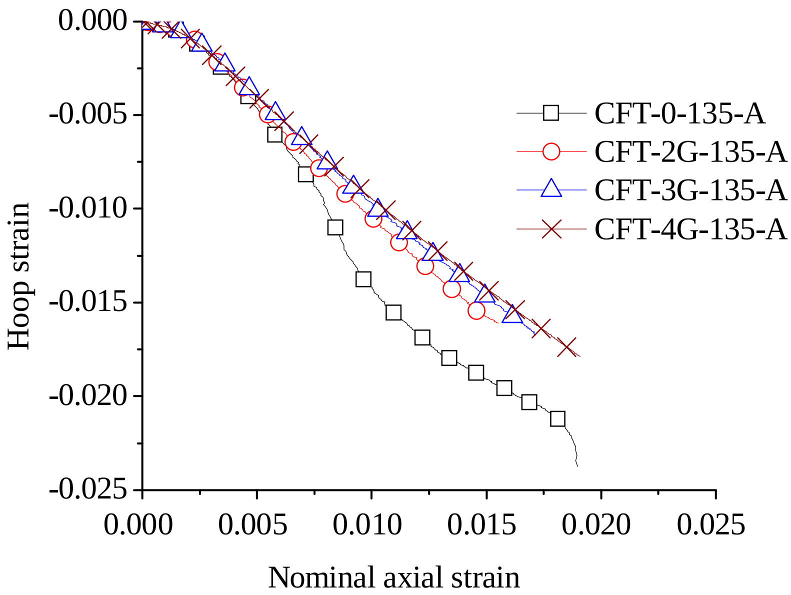


(b) Series 135-A

Figure 4.14 Nominal axial strain versus hoop strain

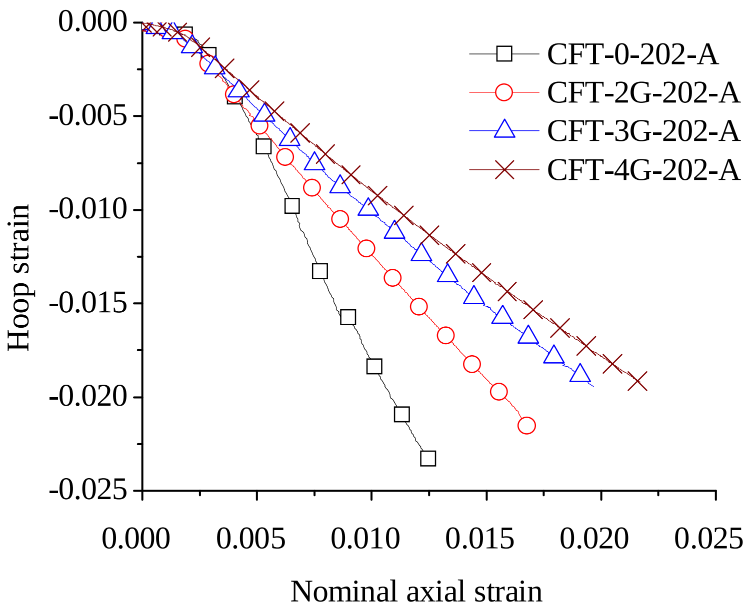


(c) Series 202-A

Figure 4.14 Nominal axial strain versus hoop strain (continued)

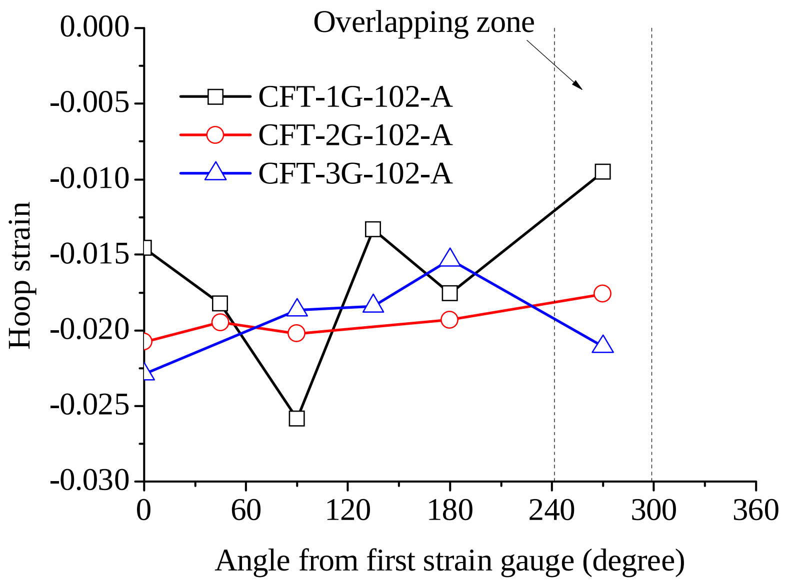


(a) Series 102-A

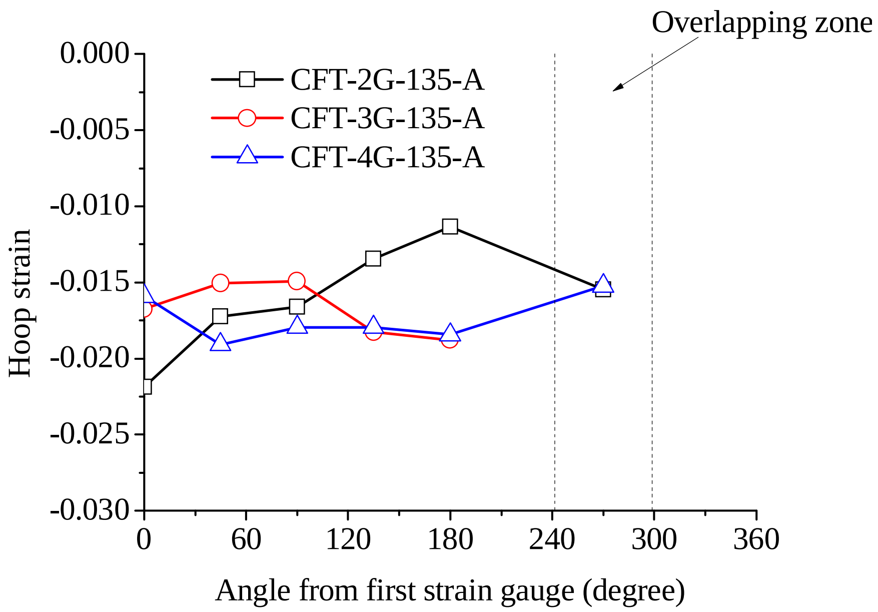


(b) Series 135-A

Figure 4.15 Distributions of hoop strain at ultimate state

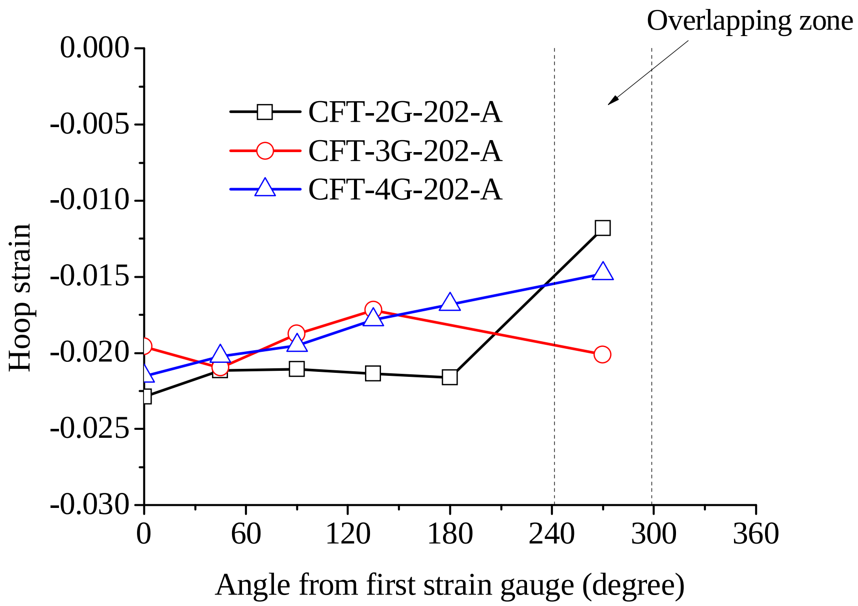


(c) Series 202-A

Figure 4.15 Distributions of hoop strain at ultimate state (continued)

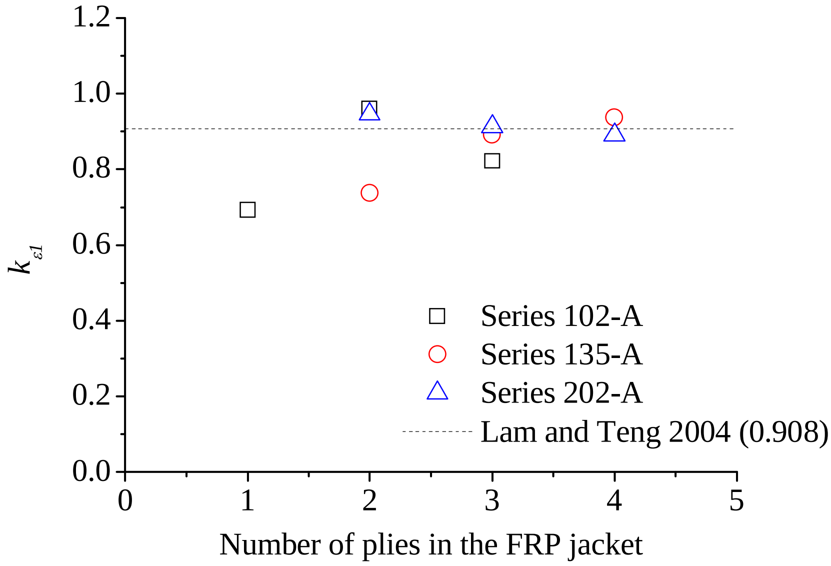


Figure 4.16 Strain non-uniformity factor

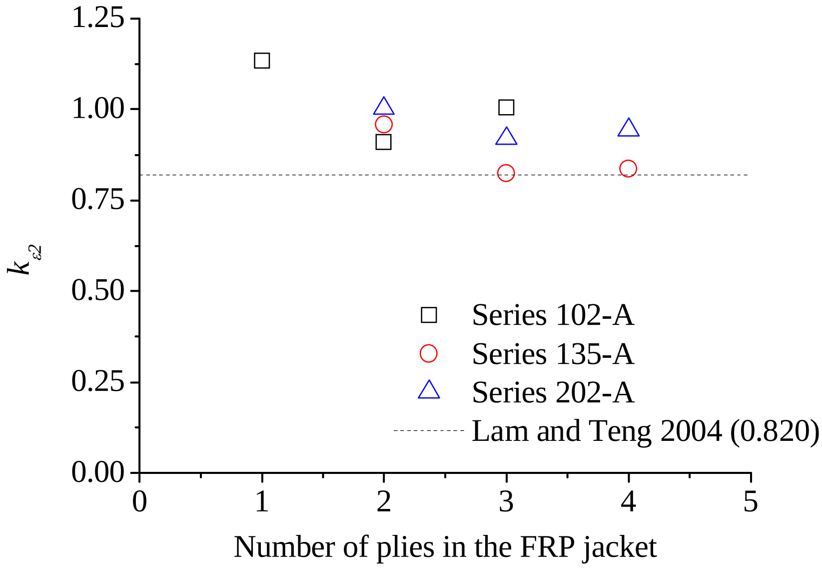


Figure 4.17 Ratio between in-situ and material strain capacities

# CHAPTER 5

# MODELLING OF FRP-CONFINED CIRCULAR CONCRETE-FILLED STEEL TUBULAR COLUMNS UNDER AXIAL COMPRESSION

## 5.1 INTRODUCTION

While some researchers have investigated experimentally the behaviour of FRP-confined concrete-filled steel tubes (CCFTs) under axial compression (Gu et al. 2004; Xiao et al. 2005; Tao et al. 2007), no theoretical model has been developed for predicting this behaviour except for the model published by Choi and Xiao (2010a) during the finalization process of this thesis. Choi and Xiao's (2010a) model is briefly discussed in the next section. This chapter is aimed at the development of a theoretical model, in a different approach, which can closely predict the axial compressive behaviour of CCFTs, with the focus being on the modelling of the stress-strain behaviour of the confined concrete. The model proposed in this chapter adopts an approach different from and conceptually simpler than that used in Choi and Xiao's (2010a) model.

This chapter starts with a review of existing theoretical models for the confined concrete in similar columns (i.e. FRP-confined concrete columns and concrete-filled steel tubes), based on which the rationale of the proposed models for CCFTs is explained. The proposed models are then presented in detail, and verified with test results from both the present study and the existing studies.

## 5.2 STRESS-STRAIN MODELS FOR CONFINED CONCRETE

Extensive research has been conducted on the modelling of the stress-strain behaviour of FRP-confined concrete. Existing stress-strain models include design-oriented models in closed-form expressions (Lam and Teng 2003; Teng et al. 2009a) and analysis-oriented models (Jiang and Teng 2007; Teng et al. 2007) which predict stress-strain curves via an incremental procedure. Design-oriented models are based on the direct interpretation and regression analysis of experimental results, so the accuracy of these models depends on whether the test database is reliable and sufficiently large, and whether the variables selected for inclusion in the closed-form equations are reasonable and sufficient to reflect the mechanical behaviour of FRP-confined concrete. Apparently, existing design-oriented stress-strain models for FRP-confined concrete (Lam and Teng 2003; Teng et al. 2009a) are unsuitable and very difficult to be extended for direct extension for the predict on of the stress-strain behaviour of concrete in CCFTs, given the unique behaviour of such concrete as discussed in Chapter 4. Analysis-oriented models consider the responses of the concrete and the FRP jacket as well as their interaction in an explicit manner. Most of the existing analysis-oriented models for FRP-confined concrete take the path-independence assumption, which means that the axial stress and axial strain of concrete confined with FRP at a given lateral strain are assumed to be the same as those of the same concrete actively confined with a constant confining pressure (referred to as actively-confined concrete hereafter) equal to that supplied by the FRP jacket. These models are thus based on a model for actively-confined concrete (referred to as active-confinement model hereafter), force equilibrium and displacement compatibility in the radial direction between the concrete core and the FRP jacket. The accuracy of this category of models consequently relies on the accurate evaluation of the lateral expansion behaviour of the confined concrete (often represented by a relationship between the axial strain and the lateral strain of concrete), and the use of an accurate active-confinement model. Analysis-oriented models explicitly consider the interaction between the concrete and the confining material, so they are easily extendable to concrete confined by other materials, such as concrete in CCFTs. Among the existing analysis-oriented models for FRP-confined concrete, Jiang and Teng’s (2007) model, which is a refined version of the model proposed by Teng et al. (2007), appears to be the most accurate. The empirical equation used in Jiang and Teng’s (2007) model for the axial strain-lateral strain relationship was shown to provide accurate predictions of unconfined and various confined concretes (i.e. actively-confined concrete and FRP-confined concrete).

A number of stress-strain models have also been developed for concrete confined by a circular steel tube (Tang et al. 1996; Susantha et al. 2001; Johansson 2002; Sakino et al. 2004; Hatzigeorgiou 2008). Most of these models (Susantha et al. 2001; Sakino et al. 2004; Hatzigeorgiou 2008) are based on the assumption that the confining pressure provided by the steel tube is constant during the loading process. With the use of this assumption, the behaviour of the concrete is taken to be the same as actively-confined concrete. Though this assumption may lead to reasonable predictions for concrete confined by a steel tube, it is obviously not suitable for concrete in CCFTs, as Chapter 4 has clearly revealed that the confinement to the concrete in CCFTs continuously increases during the loading process (Figure 4.12). For concrete confined by a circular tube, Johansson (2002) proposed a model which accounts for the varying confining pressure provided by the steel tube. Johansson’s (2002) model is based on the same approach as the analysis-oriented models for FRP-confined concrete (Teng et al. 2007) by proposing equations to predict the lateral dilation behaviour of concrete and by making use of an active-confinement model. As discussed above, this approach applies to concrete confined by various confining materials.

Choi and Xiao (2010a) proposed an analytical model for CCFTs. Choi and Xiao’s (2010a) model also explicitly considered the interaction between the three components (i.e. concrete, steel tube and FRP jacket) of a CCFT through force equilibrium and deformation compatibility, but they adopted a constitutive model involving concrete plasticity for the concrete core. Their model therefore involves the calculation of both elastic strains and plastic strains in the concrete for each incremental step after the yielding of concrete, and is relatively complex in terms of the analysis process.

Based on the existing studies reviewed above, an analysis-oriented model is proposed in the present study for concrete in CCFTs, using the same approach as Teng et al. (2007). Similar to Teng et al.'s (2007) model, the proposed analysis-oriented model adopts the path-independence assumption and is composed of the following three elements: (1) an active-confinement base model, (2) the lateral strain equation depicting the relationship between the axial strain and the lateral/hoop strain of the concrete, and (3) a relationship between the lateral strain and the confining pressure. The first element is for predicting the stress-strain curve of actively-confined concrete, so the active-confinement model adopted in Teng et al. (2007) can be directly employed here. Teng et al. (2007) also proved that their lateral strain equation provides accurate predictions for unconfined concrete, actively-confined concrete and FRP-confined concrete, so it can be expected that this equation may also work for concrete in CCFTs. For FRP-confined concrete, the relationship between the lateral strain and the confining pressure (i.e. the third element) can be easily defined because of the linear elastic nature of the FRP jacket, but this relationship is much more complicated for concrete in CCFTs as the confining pressure comes from both the steel tube and the FRP jacket and the steel tube possesses an elastic-plastic behaviour. The three elements adopted in the present study are described in detail in the following section.

## 5.3 PROPOSED MODEL I

### 5.3.1 Perfect Bond Assumption

In this proposed model, it is assumed that the three components of a CCFT column (i.e. the concrete, the steel tube and the FRP jacket) are perfectly bonded at the two interfaces (i.e. the concrete/steel interface and the steel/FRP interface).

As a result, strain compatibility in both the axial and the hoop directions needs to be satisfied, as depicted by the following equations:

$$\varepsilon_{x,c} = \varepsilon_{x,s} = \varepsilon_x \tag{5.1}$$

$$\varepsilon_{\theta,c} = \varepsilon_{\theta,s} = \varepsilon_{\theta,frp} = \varepsilon_\theta \tag{5.2}$$

where $\varepsilon_{x,c}$ and $\varepsilon_{\theta,c}$ are the axial strain and the hoop strain of the concrete; $\varepsilon_{x,s}$ and $\varepsilon_{\theta,s}$ are the axial strain and the hoop strain of the steel tube; $\varepsilon_{\theta,frp}$ is the hoop strain of the FRP jacket. Because of strain compatibility, only $\varepsilon_x$ and $\varepsilon_\theta$ are used in the following sections to represent strains in the axial direction and the hoop direction respectively. In this chapter, compressive stresses and strains are defined to be positive unless otherwise specified.

### 5.3.2 Active-Confinement Model

#### *5.3.2.1 Axial stress-strain equation*

The following axial stress-axial strain equation, which was originally proposed by Popovics (1973) and has been widely used in the existing literature including Jiang and Teng (2007), is adopted as part of the present model:

$$\frac{\sigma_c}{f'^{*}_{cc}} = \frac{\left(\varepsilon_x / \varepsilon^{*}_{cc}\right) r}{r - 1 + \left(\varepsilon_x / \varepsilon^{*}_{cc}\right)^r} \tag{5.3}$$

where $\sigma_c$ is the axial stress of concrete, $f'^{*}_{cc}$ and $\varepsilon^{*}_{cc}$ are respectively the peak axial stress and the corresponding axial strain of concrete under a specific constant confining pressure. The constant $r$ in Eq. 5.3, approximately accounting for the brittleness of concrete, is defined in Carreira and Chu (1985) as

$$r = \frac{E_c}{E_c - f_{cc}'^{*} / \varepsilon_{cc}^{*}} \tag{5.4}$$

where $E_c$ is the elastic modulus of concrete.

*5.3.2.2 <u>Peak axial stress</u>*

Jiang and Teng (2007) adopted the following equation for the peak axial stress $f_{cc}'^{*}$:

$$\frac{f_{cc}'^{*}}{f_{co}'} = 1 + 3.5 \frac{\sigma_r}{f_{co}'} \tag{5.5}$$

where $\sigma_r$ is the total confining pressure, $f_{co}'$ is the cylinder compressive strength of unconfined concrete. They also suggested that, in their model, the elastic modulus of unconfined concrete ($E_c$) should be taken as $4730\sqrt{f_{co}'}$ if it is not available from tests.

*5.3.2.3 <u>Axial strain at peak axial stress</u>*

Jiang and Teng (2007) adopted the following equation for the axial strain at peak axial stress $\varepsilon_{cc}^{*}$:

$$\frac{\varepsilon_{cc}^{*}}{\varepsilon_{co}} = 1 + 17.5 \left( \frac{\sigma_r}{f_{co}'} \right)^{1.2} \tag{5.6}$$

where $\varepsilon_{co}$ is the axial strain at the peak compressive strength of unconfined concrete. They also suggested that the axial strain at the peak stress of unconfined concrete should be taken to 0.0022 if it is not available from tests.

The active-confinement model presented above has been calibrated with the test data of FRP-confined concrete by Jiang and Teng (2007).

### 5.3.3 Lateral Strain Equation

Jiang and Teng (2007) adopted the following equation for the axial strain-lateral strain relationship which was originally proposed by Teng et al. (2007):

$$\frac{\varepsilon_x}{\varepsilon_{co}}+0.85\left(1+8\frac{\sigma_r}{f_{co}^{'}}\right)\left\{\left[1+0.75\left(\frac{\varepsilon_\theta}{\varepsilon_{co}}\right)\right]^{0.7}-\exp\left[-7\left(\frac{\varepsilon_\theta}{\varepsilon_{co}}\right)\right]\right\}=0 \tag{5.7}$$

where $\varepsilon_x$ and $\varepsilon_\theta$ are the axial strain and the lateral strain, respectively. As discussed earlier, Eq. 5.7 was verified with test results of unconfined concrete, actively-confined concrete and FRP-confined concrete, so it is expected to be applicable to the confined concrete in CCFTs and is thus directly adopted in the present model. In a circular column where the concrete is subjected to uniform confinement, the lateral strain is equal to the hoop strain. Hereafter in this thesis, the lateral strain-axial strain relationship is also referred to as the hoop strain-axial strain relationship.

### 5.3.4 Confining Pressure

In a CCFT column, the concrete core is confined by both the steel tube and the FRP jacket. The total confining pressure supplied to the concrete core ($\sigma_r$) is equal to the sum of that from the steel tube ($\sigma_{r,s}$) and that from the FRP jacket ($\sigma_{r,frp}$). That is,

$$\sigma_r=\sigma_{r,frp}+\sigma_{r,s} \tag{5.8}$$

The confining pressure from the steel tube and the FRP jacket can be found from the hoop stresses in these two components, based on the force equilibrium condition illustrated in Figure 5.1. Because of the linear elastic nature of the FRP jacket, $\sigma_{r,frp}$ can be simply related to its elastic modulus and hoop strain. Eq. 5.8 can then be rewritten as:

$$\sigma_r = \frac{2\sigma_{\theta,s}t_s + 2E_{frp}t_{frp}\varepsilon_\theta}{D_c} \tag{5.9}$$

in which, $\sigma_{\theta,s}$ is the hoop stress in the steel tube; $E_{frp}$ is the elastic modulus of the FRP jacket; $t_{frp}$ and $t_s$ are the thickness of the FRP jacket and that of the steel tube respectively; and $D_c$ is the diameter of concrete core.

The determination of the hoop stress in the steel tube is more involved after the yielding of steel. In the present study, two assumptions are made: (1) the steel tube does not experience any bending or buckling deformations; this assumption basically reflects the experimental observations presented in Chapter 4 especially for the mid-height region of CCFTs before the rupture of FRP; (2) the steel is an elastic-perfectly plastic material; this assumption is reasonable as strain hardening of steel normally occurs at strains which are very unlikely to be reached in CCFT columns (e.g. for the tests presented in Chapter 4, this assumption reflects the experimental observation well). Based on these two assumptions, the stress state (i.e. the axial stress and the hoop stress) of the steel tube during the loading history can be found from the history of the two strains (i.e. axial strain and hoop strain) through an incremental approach employing the $J_2$ flow theory (i.e. using Eqs. 4.1-4.13 provided in Chapter 4) (Calladine 1985). It may be noted that the axial stress-strain history of the steel tube can also be found through this process (i.e. using Eqs. 4.1-4.13).

### 5.3.5 Generation of Axial Stress-Axial Strain Curve

The generation of the axial stress-axial strain curve of the confined concrete involves an incremental process. In each increment, a constant small increment of hoop strain $d\varepsilon_\theta$ is specified first (e.g. 0.01%), with which the total hoop strain in the current increment (i.e. $i^{th}$ increment) $\varepsilon_\theta^i$ can be obtained based on the hoop strain of the last increment $\varepsilon_\theta^{i-1}$. An increment in the axial strain is then assumed, with which a total axial strain $\varepsilon_{x1}^i$ is obtained based on $\varepsilon_x^{i-1}$, and the corresponding total confining pressure can be calculated following the way explained in Section 5.3.4. With the total confining pressure, another total axial strain $\varepsilon_{x2}^i$ can be calculated using Eq. 5.7. If $\varepsilon_{x1}^i$ and $\varepsilon_{x2}^i$ are sufficiently close (i.e. the difference between them being within a certain tolerance), the values of the lateral strain increment, the axial strain increment and the confining pressure are regarded as the converged solution for the present increment. A point on the stress-strain curve can then be obtained using Eqs. 5.3, 5.5 & 5.6. If $\varepsilon_{x1}^i$ and $\varepsilon_{x2}^i$ are not sufficiently close, an iterative process is needed using the bisection method to find the solution. A tolerance of 0.1% of the axial strain was used in obtaining the results presented later in this chapter. In the analysis, the above process needs to be repeated for each increment to obtain the whole stress-strain curve of the confined concrete, which is terminated at the rupture of the FRP jacket. Figure 5.2 shows the flow chat of this incremental process.

In the initial loading stage, the lateral expansion of the steel tube tends to be larger than that of the concrete because of the larger Poisson's ratio of the former, which results in positive (i.e. compressive) hoop stresses in the steel tube in the analysis because of the perfect bond assumption. As a result, the corresponding confining pressure is negative in the initial stage. In the proposed model, this small negative confining pressure is assumed to be zero. This assumption leads to slight discontinuity of the slope in the initial portion of the predicted stress-strain curve (see Figure 5.3a), but has little effect on the overall accuracy of the predicted curve.

### 5.3.6 Generation of the Axial Load-Axial Shortening Curve

With the axial stress-strain curve of the concrete and that of the steel tube [which can also be obtained through the above analysis (see Section 5.3.4)] defined, the axial load-axial shortening curve of a CCFT column can be easily obtained by using:

$$N_{app} = \sigma_c A_c + \sigma_{x,s} A_s \tag{5.10}$$

$$\Delta = \varepsilon_x l_{col} \tag{5.11}$$

where $N_{app}$ is the axial load resisted by the CCFT column; $\sigma_{x,s}$ is the axial stress of the steel tube; $A_c$ and $A_s$ are the cross-sectional areas of the concrete core and the steel tube respectively; $\Delta$ is the axial shortening; and $l_{col}$ is the length of the column.

## 5.4 VERIFICATION AND REFINEMENT OF MODEL I

### 5.4.1 Comparison with Test Results Presented in Chapter 4

The details of the test specimens can be found in Section 4.2. In Figure 5.3, the experimental stress-strain curves of the confined concrete are compared with the predictions from the analysis-oriented model presented above (i.e. Eqs. 5.3-5.9 and referred to as Model I). The comparisons shown in Figure 5.3 are for all the CCFT specimens presented in Chapter 4 except specimen CFT-1G-102-A for which the concrete stress-strain curve is not available because of the premature damage of the two axial strain gauges (see Section 4.3.3). In obtaining the predictions, the curve was terminated at a hoop strain equal to the average value of the five hoop strain gauge readings outside the overlapping zone (see Figure 4.2) at FRP rupture. Figure 5.3 shows that the proposed model generally underestimates the experimental curves after the initial linear portion.

To examine the reason behind this underestimation, the experimental hoop strain-axial strain curves are compared with the predictions of the proposed model in Figure 5.4. It is seen from Figure 5.4 that the proposed model also underestimates the hoop strain at a given axial strain. The underestimation of hoop strains can lead to underestimation of the confining pressure and in turn underestimation of the axial stress of the confined concrete. For further clarification, another set of predicted axial stress-strain curves were produced, employing the experimental hoop strain-axial strain curves instead of Eq. 5.7 in the analysis-oriented model. By doing so, Figure 5.3 shows that the predictions now agree very well with the test results except for specimens CFT-2G-102-A, CFT-3G-102-A and CFT-2G-135-A (Figures 5.3a-c). The predictions for these three specimens are still lower than the experimental curves. It may be noted that these three specimens are all classified as type I specimens (see Chapter 4), where significant local buckling occurred near one or both ends of the steel tube. Because of this local buckling, the axial deformation of the concrete in the mid-height region is likely to be smaller than that near the ends, and the nominal axial strain which is obtained from the total axial shortening of the column is likely to be higher than the axial strain of the concrete in the mid-height region. Therefore, the experimental hoop strain-nominal axial strain curves of these three specimens may still underestimate the hoop strain at a given axial strain of the concrete in the mid-height region. Considering also the fact that the predictions for all the other specimens are very accurate, end local buckling deformation is believed to be the main reason causing the discrepancies seen in Figures 5.3a-c.

The above discussions suggest that Eq. 5.7 is not accurate for concrete in CCFTs, even when the steel tube does not experience any buckling. Eq. 5.7, however, was established by Teng et al. (2007) based on a large test database of actively-confined concrete and FRP-confined concrete. One major difference between the concrete in CCFTs and other confined concretes is that in the initial stage, the concrete in CCFTs is subjected to a zero or even negative confining pressure because of the larger Poisson's ratio of the steel tube. As a result, the growth of micro-cracks in the early stage of loading is expected to be more severe in the concrete of CCFTs. These more severe micro-cracks may lead to a larger lateral expansion of concrete in the subsequent loading process, and is deemed to be at least one of the main reasons for the inaccuracy of Eq. 5.7 for concrete in CCFTs.

### 5.4.2 Refinement of Lateral Strain Equation

Due to the limited test data as presented in Chapter 4 (i.e. only five CCFTs without significant local buckling of the steel tube), only a simple modification to Eq. 5.7 is possible. As Eq. 5.7 provides lower predictions for the hoop strain (see Figure 5.4), the easiest way for refinement is to replace the constant of 0.85 in Eq. 5.7 with a smaller value. To do this, Eq. 5.7 is divided into two parts as follows:

$$\Phi_1 = \frac{\varepsilon_x}{\varepsilon_{co}} \qquad \text{(Eq. 5.12a)}$$

$$\Phi_2 = \left(1 + 8\frac{\sigma_r}{f_{co}^{'}}\right)\left\{\left[1 + 0.75\left(\frac{\varepsilon_\theta}{\varepsilon_{co}}\right)\right]^{0.7} - \exp\left[-7\left(\frac{\varepsilon_\theta}{\varepsilon_{co}}\right)\right]\right\} \qquad \text{(Eq. 5.12b)}$$

The task now becomes to find a best-fit $c_\Phi$ value to satisfy the following equation:

$$\Phi_1 + c_\Phi \Phi_2 = 0 \qquad \text{(Eq. 5.13)}$$

Figure 5.5 shows that the $c_\Phi$ value for each specimen is basically a constant except for the initial stage of loading. The $c_\Phi$ values for different specimens are also shown to be almost the same. A summary of the $c_\Phi$ values for all the five specimens is given in Table 5.2 and the mean value of the five (i.e. 0.66) instead of 0.85 is adopted in the refined lateral strain equation. Eq. 5.7 can then be rewritten as:

$$\frac{\varepsilon_x}{\varepsilon_{co}}+0.66\left(1+8\frac{\sigma_r}{f_{co}^{'}}\right)\left\{\left[1+0.75\left(\frac{\varepsilon_\theta}{\varepsilon_{co}}\right)\right]^{0.7}-\exp\left[-7\left(\frac{\varepsilon_\theta}{\varepsilon_{co}}\right)\right]\right\}=0 \qquad (5.14)$$

The predictions generated by the refined model (referred to as Model II hereafter), with all the components being the same as Model I presented in Section 5.3 except that Eq. 5.7 is replaced by Eq. 5.14, are compared with the test results of Chapter 4 in Figure 5.6 & 5.7 for the axial stress-strain curves and the lateral strain-axial strain curves respectively. The predictions are shown to agree closely with the test results of specimens without significant local buckling of the steel tube. For the specimens with local buckling near the column ends, the predictions are also reasonably accurate except that they overestimate the lateral strain at a given axial strain. This overestimation is explained in Section 5.4.1.

It should however be noted that the refinement of the lateral strain equation (i.e. Eq. 5.14) is based on only limited test results. Apparently, this equation needs to be further verified and/or refined when more reliable test results become available.

## 5.5 COMPARISON WITH OTHER TEST RESULTS

### 5.5.1 General

In this section, predictions from both Model I and Model II (i.e. Eqs. 5.3-5.7, 5.9 & 5.14) are compared with test results from other researchers (Gu et al. 2004; Xiao et al. 2005; Teng and Hu 2006; Tao et al. 2007). The existing test results cover a wide range of $D_{outer}/t_s$ ratios (from 29.6 to 86) and yield strengths (from 230 MPa to 385.9MPa) of the steel tube, and two types of FRP jackets (i.e. CFRP and GFRP).

### 5.5.2 Teng and Hu's (2006) Results

Teng and Hu (2006) tested three CCFTs under axial compression. The steel tubes all had an outer diameter of 165 mm, a thickness of 2.75 mm (i.e. a $D_{outer} / t_s$ ratio of 60), a length of 450 mm and were filled with concrete with a cube compressive strength of 56 MPa determined from three cube tests. In the present study, it is assumed that the concrete cylinder strength is 80% of the reported cube strength (i.e. cylinder strength = 44.8 MPa). The elastic modulus of unconfined concrete and the axial strain at the peak stress of unconfined concrete are assumed to be $4730\sqrt{f_{co}^{'}}$ and 0.0022 respectively. The average values of the elastic modulus, yield stress and tensile strength of the steel obtained from tensile tests of three coupons taken from the same long steel tube which provided the four steel tubes in the test specimens were 201.3 GPa, 385.9 MPa, and 486.8 MPa respectively. GFRP was used in their experimental investigation. The average values of the elastic modulus and tensile strength of the GFRP obtained from five coupon tests were 80.1 GPa and 1825.5 MPa respectively based on a nominal thickness of 0.17 mm per ply, leading to an ultimate tensile strain of 0.0228. The details of the specimens are summarized in Table 5.1. In Teng and Hu (2006), only the axial load-axial shortening curves are reported, without any information for the lateral strain-axial strain history of the column.

The experimental and predicted axial load-axial shortening curves for the three CCFTs are compared in Figure 5.8. As no information for the experimental FRP rupture strain in CCFTs is available, all predicted curves are terminated at a hoop strain of 0.228 which is the ultimate value obtained from the tensile coupon tests. Figure 5.8 shows that the predictions from Model I are closer to the test curves, which is contrary to what was expected, and the predictions from Model II slightly over-estimate the test results. These discrepancies may be due to the use of imprecise material properties of the concrete in making the predictions (e.g. the cylinder strength is estimated from the cube strength and the elastic modulus and the strain at peak stress are also estimated). The predicted curves are also seen to be longer than the experimental curves (i.e. larger ultimate axial strains), due to the use of the rupture strain from flat coupon tests which is normally larger than that reached in column tests.

### 5.5.3 Xiao et al.'s (2005) Results

Xiao et al. (2005) conducted a series of axial compression tests on eight CCFTs, among which four CCFTs had a gap between the steel tube and the CFRP jacket and cannot be predicted by the model presented above. The other four CCFTs without a gap included two pairs of identical specimens with the only difference between the two pairs being the CFRP jacket thickness (i.e. two-ply and four-ply CFRP jackets). The two identical specimens of each pair had approximately the same axial load-strain curves, so they were treated as one specimen in the present study. The steel tube used in all specimens had a yield stress of 356 MPa, an outer diameter of 152 mm and a thickness of 2.95 mm, leading to a $D_{outer}/t_s$ ratio of 52. The concrete cylinder strength was 46.6 MPa. The elastic modulus of steel, the elastic modulus of unconfined concrete and the axial strain at the peak stress of unconfined concrete were not provided by Xiao et al. (2005) and are assumed to be 205 GPa, $4730\sqrt{f_{co}^{'}}$ and 0.0022 respectively. The CFRP jacket they used had an elastic modulus of 64.9 GPa and a tensile rupture strength of 897 MPa based on a nominal thickness of 1.4mm per ply. The test results, including the axial load-axial strain curves, the axial strain-hoop strain curves and the hoop rupture strains are reported in either Xiao et al. (2005) and a later paper by the same group [i.e. Choi and Xiao (2010a)]. The details of their specimens are summarized in Table 5.1.

The experimental and predicted axial load-axial strain curves and axial load-hoop strain curves for the two CCFTs are compared in Figure 5.9. It is evident that both models provide very accurate predictions for the axial load-hoop strain curves and the ultimate axial load for both specimens, but the predictions from Model II are closer to the test results. However, the axial load-axial strain curves are generally not accurately predicted by either model, although the predictions from Model I for the later stage of specimen CCFT-4L are close to the test results. The predicted axial strain is always lower than the experimental value, even in the initial elastic stage. A careful examination of the initial stiffness of the column reveals that the elastic stiffness indicated by the experimental stress-strain curves is significantly lower than that calculated from the elastic constants of the steel tube and the concrete. Therefore, it is believed that the axial stains reported by Xiao et al. (2005), which were obtained from axial shortening readings, are larger than the actual axial strains of the column, probably because the axial shortening readings include also deformation of the testing system. According to the foregoing discussion, the close predictions from Model I for the later stage of deformation of specimen CCFT-4L may not necessarily indicate that Model I is more accurate than Model II because 1) it still cannot predict the initial stage well and 2) the predicted curve would be lower if the test axial strains are adjusted in order to exclude the shortening within the testing frame. Considering also the very good predictions for the axial load-hoop strain curves and the ultimate axial load, it may be concluded that Model II performs also very well for Xiao et al.'s (2005) results.

### 5.5.4 Tao et al.'s (2007) Results

Tao et al. (2007) conducted axial compression tests on four circular CCFTs. The steel tube they used had an outer diameter of 156 mm or 250 mm, and a thickness of 3 mm, leading to two $D_{outer}/t_s$ ratios (i.e. 52 and 83). The specimen lengths were either 470 mm (for the 156 mm tube) or 750 mm (for the 250 mm tube) so that the length-to-diameter ratio is three. The elastic modulus, yield stress and yield strain of both steel tubes were 206 GPa, 230 MPa and 0.0030 respectively. CFRP jackets with two different nominal thicknesses (i.e. 0.17 mm and 0.34 mm) were used in their study. The elastic modulus, tensile strength and ultimate strain of the CFRP jackets were 255 GPa, 4212 MPa and 0.0167 respectively. The hoop rupture strains of the CFRP jackets in the column tests can also be found from the paper and are summarized in Table 5.1. These FRP rupture strains were employed in the present analysis to determine the ultimate state of CCFTs. The concrete they used had an elastic modulus of 35.8 GPa and a cylinder strength of 46 MPa at the time of testing as reported in the paper. The axial strain at the peak stress of unconfined concrete is assumed to be 0.0022. Details of the test specimens are summarized in Table 5.1.

The experimental and predicted axial load-axial strain curves and axial load-hoop strain curves for the two CCFTs are compared in Figure 5.10. Figure 5.10 shows that Model II provides better and reasonably accurate predictions for the test results, but underestimates some curves. The reason for this underestimation could be the scatter of test results and/or the imprecise information used in the model.

### 5.5.5 Gu et al.'s (2004) Results

Gu et al. (2004) tested eight CCFTs under axial compression. Similar to the specimens presented in Chapter 4, all the steel tubes were fabricated from steel plates. The thicknesses used were 1.5 mm, 2.5 mm, 3.5 mm and 4.5 mm respectively. The yield stress of the plates with thicknesses of 1.5 mm and 2.5 mm was 350 MPa. For the plates with the other two thicknesses (i.e. 3.5 mm and 4.5 mm), the yield stress was 310 MPa. The elastic moduli for both types of steel plates were not reported and are therefore assigned a value of 205 GPa in the present study. The outer diameters of the specimens varied from 127 mm to 133 mm, leading to $D_{outer}/t_s$ ratios from 30 to 86). All these columns had a constant height of 400 mm. CFRP jackets were used with two different nominal thicknesses (i.e. 0.17 mm and 0.34 mm). Only the ultimate tensile stress (1260 MPa) of the jacket obtained from coupon tests was reported. The elastic modulus of 230 GPa was assumed in the present study, which is a common value for such CFRP formed from dry carbon fibre sheets via a wet layup process, leading to an ultimate strain of 0.0055. Only concrete cube strength (obtained from tests of 150 mm concrete cubes) was reported. Again, the concrete cylinder strength is assumed to be 80% of the reported cube strength of 40.15MPa (i.e. 32 MPa). The elastic modulus and the axial strain at the peak stress of unconfined concrete are assumed to be $4730\sqrt{f_{co}^{'}}$ and 0.0022 respectively. Details of the test specimens are also summarized in Table 5.1. Only the axial load-nominal axial strain curves were provided, without any information for the lateral strain-axial strain history.

The experimental and predicted axial load-axial strain curves are compared in Figure 5.11. The initial stiffness is seen to be overestimated for all the specimens, which is similar to the observation from Figure 5.9 for Xiao et al.'s (2005) tests. A careful examination of the initial stiffness with reference to the elastic constants of the concrete and the steel tube revealed that this lower experimental stiffness seen in Figure 5.11 is also very likely to be due to the inclusion of deformation of the testing system in the axial shorting readings, which were used to calculate the nominal axial strains. Model II is thus more accurate based on the above comparison, even if the test axial strains are adjusted in order to exclude the shortening of the testing system. The predicted ultimate loads and the ultimate axial strains also appear to be different from the test results, which could be due to: (1) the experimental nominal axial strains include machine deformations, as discussed above; and (2) the hoop rupture strain and the elastic modulus of the CFRP jacket were not provided in Gu et al. (2004) and estimated values were used which could be inaccurate.

## 5.6 CONCLUSIONS

This chapter has been concerned with the modelling of the behaviour of circular CCFTs under monotonic axial compression, with the focus being on the stress-strain behaviour of the confined concrete. The development of analysis-oriented stress-strain models for concrete in CCFTs has been presented, following the approach adopted by Jiang and Teng (2007) for FRP-confined concrete. With this approach, an analysis-oriented model generally includes three main components: an active-confinement model, a lateral strain equation, and equations for calculating the confining pressure from the strains. Two models (Model I and Model II) were developed in the present study. Model I is the same as Jiang and Teng's (2007) model except that a more complicated process is used for calculating the confining pressure from both the steel tube and the FRP jacket;

Model II was refined from Model I by replacing the lateral strain equation used in Jiang and Teng (2007) with a new one, to account for the test observation that the lateral expansion of concrete in CCFTs is larger than that of FRP-confined concrete, for a given axial strain. This difference in lateral expansion is believed to be due to the more severe micro-cracks experienced by the concrete in CCFTs as it is subjected to a zero or even negative confining pressure in the initial stage of loading. The predictions using Model II have been shown to be closer to the test results presented in Chapter 4 and other test results than those using Model I.

It should be noted that while Model II has been shown to provide close predictions of test results, the lateral strain equation used in Model II was based only on limited test results. Further research is needed to verify/refine this equation when a larger test database is available.

Table 5.1 Details of CCFT specimens reported in existing studies

| ***Specimen*** | $D_{outer}$ ***(mm)*** | $t_s$ ***(mm)*** | $D_{outer}/t_s$ | $\sigma_y$ ***(MPa)*** | $f_{cu}$ ^1)^***or*** $f'_{co}$ ^2)^ ***(MPa)*** | $t_{frp}$ ***(mm)*** | $\varepsilon_{rupt}$ | $E_{frp}$ ***(GPa)*** |
|---|---|---|---|---|---|---|---|---|
| | | | | | ***Teng and Hu (2006)*** | | | |
| **F0-60** | 165 | 2.75 | 60 | 385.9 | $56^{1)}$ | N/A | 0.0228 | 80.1 |
| **F1-60** | 165 | 2.75 | 60 | 385.9 | $56^{1)}$ | 0.17 | 0.0228 | 80.1 |
| **F2-60** | 165 | 2.75 | 60 | 385.9 | $56^{1)}$ | 0.34 | 0.0228 | 80.1 |
| **F3-60** | 165 | 2.75 | 60 | 385.9 | $56^{1)}$ | 0.51 | 0.0228 | 80.1 |
| | | | | | ***Xiao et al. (2005)*** | | | |
| **CCFT-2L** | 152 | 2.95 | 52 | 356 | $47^{2)}$ | 2.8 | 0.0060 | 64.9 |
| **CCFT-4L** | 152 | 2.95 | 52 | 356 | $47^{2)}$ | 5.6 | 0.0060 | 64.9 |
| | | | | | ***Tao et al. (2007)*** | | | |
| **C1-1** | 156 | 3.0 | 52 | 230 | $46^{2)}$ | 0.17 | 0.0105 | 255 |
| **C1-2** | 156 | 3.0 | 52 | 230 | $46^{2)}$ | 0.34 | 0.0086 | 255 |
| **C2-1** | 250 | 3.0 | 52 | 230 | $46^{2)}$ | 0.17 | 0.0097 | 255 |
| **C2-2** | 250 | 3.0 | 52 | 230 | $46^{2)}$ | 0.34 | 0.0078 | 255 |
| | | | | | ***Gu et al. (2004)*** | | | |
| **1-1.5** | 127 | 1.5 | 84.7 | 350 | $55^{1)}$ | 0.17 | <u>0.0055</u> | <u>230</u> |
| **1-2.5** | 129 | 2.5 | 51.6 | 350 | $55^{1)}$ | 0.17 | <u>0.0055</u> | <u>230</u> |
| **1-3.5** | 131 | 3.5 | 37.4 | 310 | $55^{1)}$ | 0.17 | <u>0.0055</u> | <u>230</u> |
| **1-4.5** | 133 | 4.5 | 29.6 | 310 | $55^{1)}$ | 0.17 | <u>0.0055</u> | <u>230</u> |
| **2-1.5** | 127 | 1.5 | 84.7 | 350 | $55^{1)}$ | 0.34 | <u>0.0055</u> | <u>230</u> |
| **2-2.5** | 129 | 2.5 | 51.6 | 350 | $55^{1)}$ | 0.34 | <u>0.0055</u> | <u>230</u> |
| **2-3.5** | 131 | 3.5 | 37.4 | 310 | $55^{1)}$ | 0.34 | <u>0.0055</u> | <u>230</u> |
| **2-4.5** | 133 | 4.5 | 29.6 | 310 | $55^{1)}$ | 0.34 | <u>0.0055</u> | <u>230</u> |

[#] underlined values are assumed values

Table 5.2 Values $c_{\Phi}$ deduced from tests presented in Chapter 4

| ***Specimens*** | $c_{\Phi}$ |
|---|---|
| **CFT-3G-135-A** | 0.70 |
| **CFT-2G-135-A** | 0.65 |
| **CFT-2G-202-A** | 0.63 |
| **CFT-3G-202-A** | 0.62 |
| **CFT-4G-202-A** | 0.71 |
| **Mean** | 0.66 |

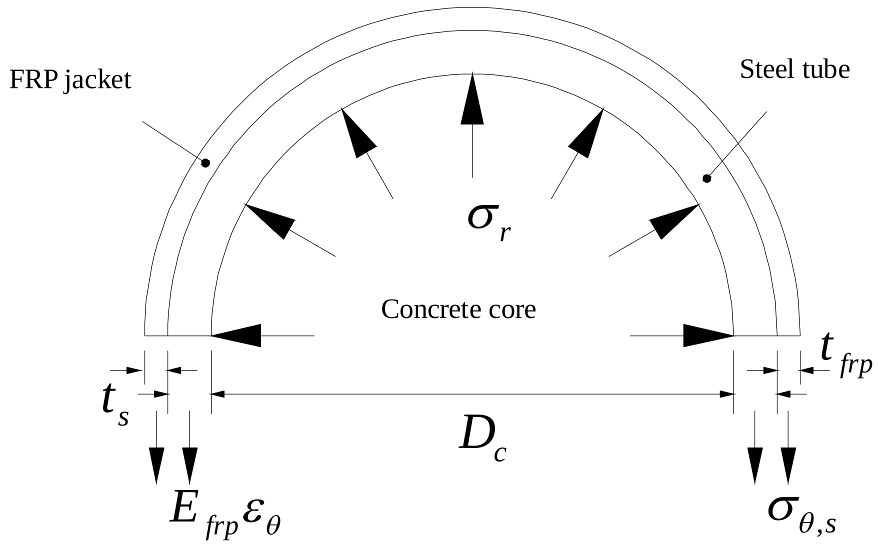


Figure 5.1 Confining mechanism for concrete in CCFTs

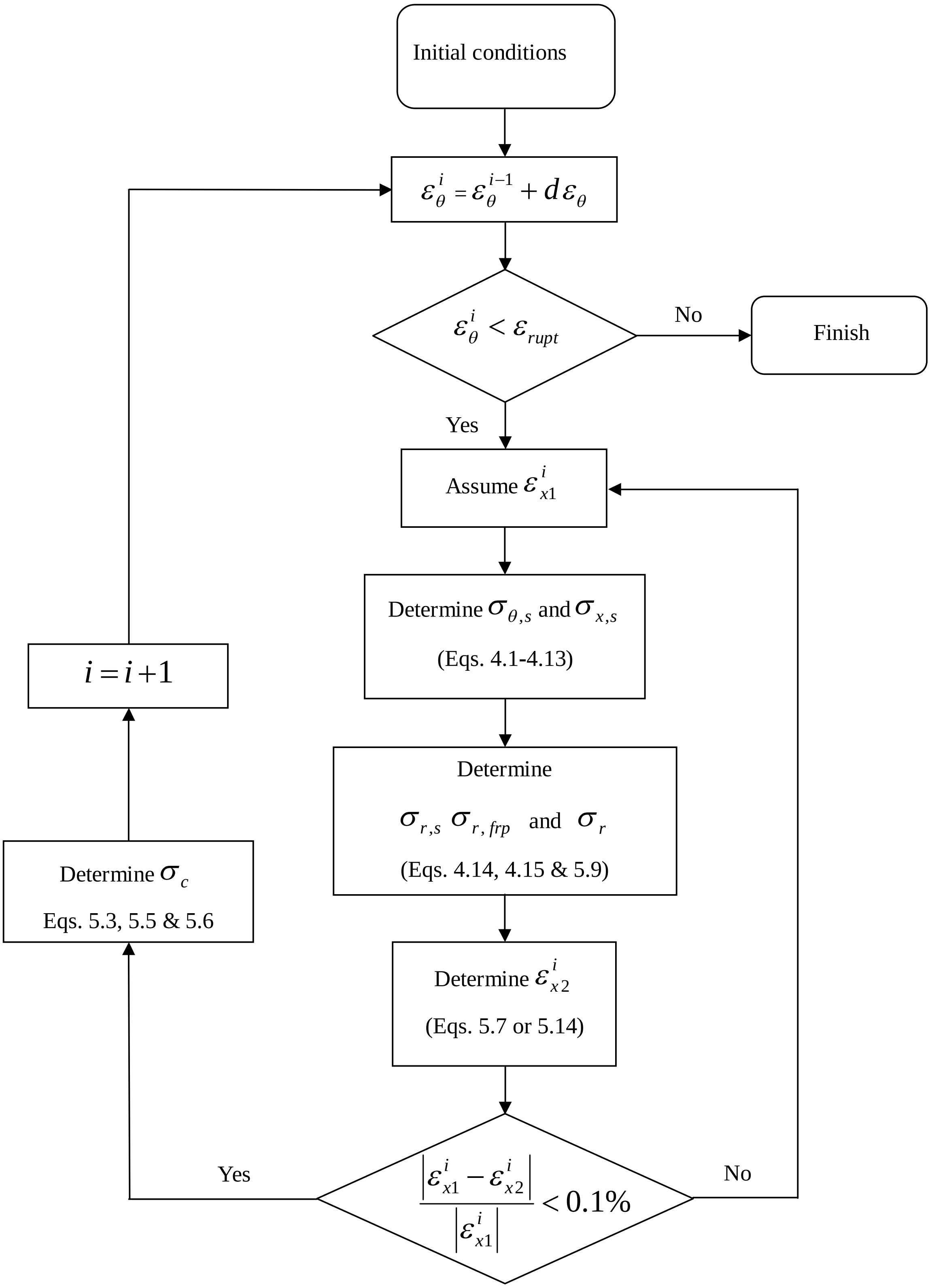


Figure 5.2 Generation of axial stress-axial strain curve

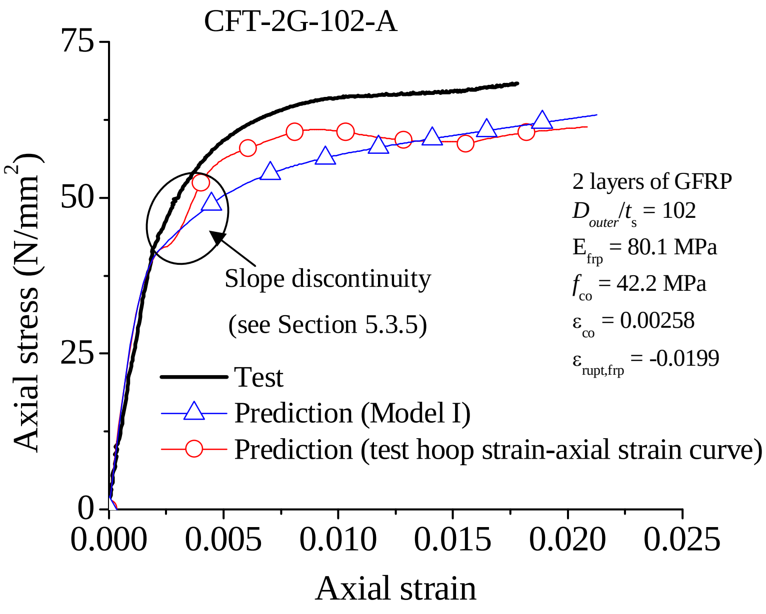


(a) Specimen CFT-2G-102-A

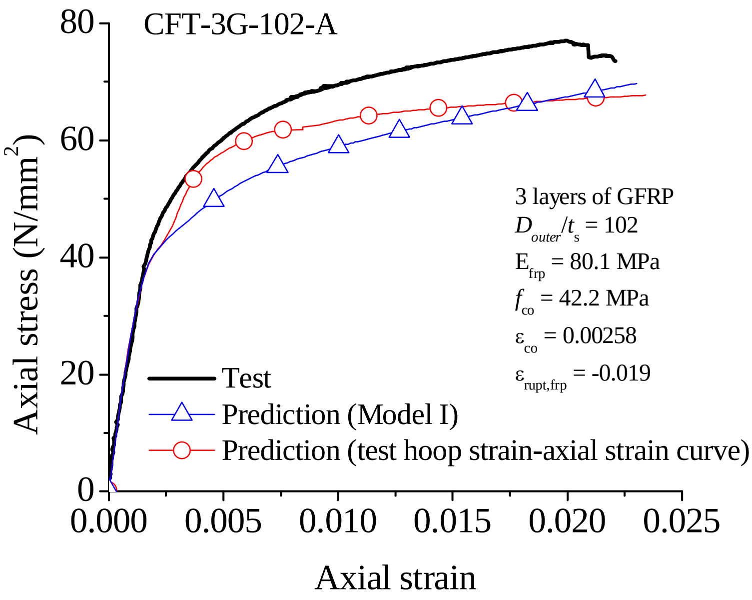


(b) Specimen CFT-3G-102-A

Figure 5.3 Stress-strain curves of concrete in CCFT tests of Chapter 4

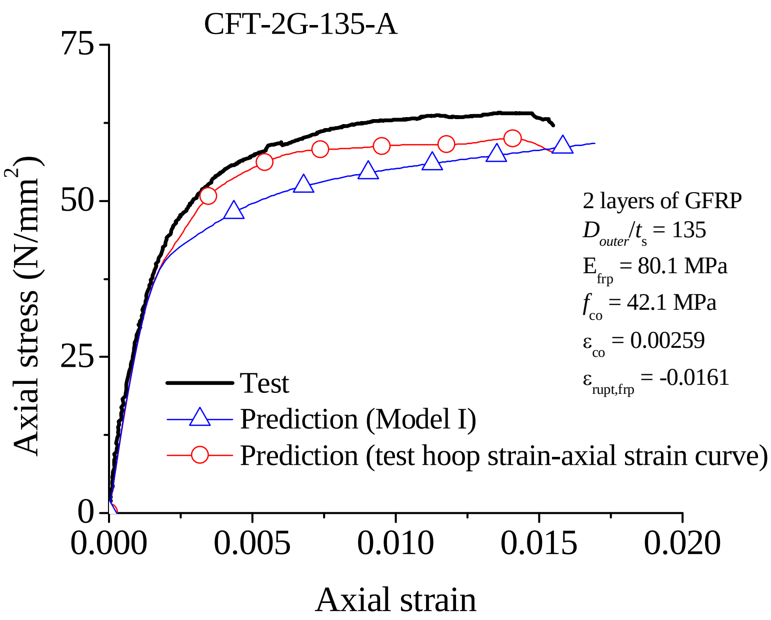


(c) Specimen CFT-2G-135-A

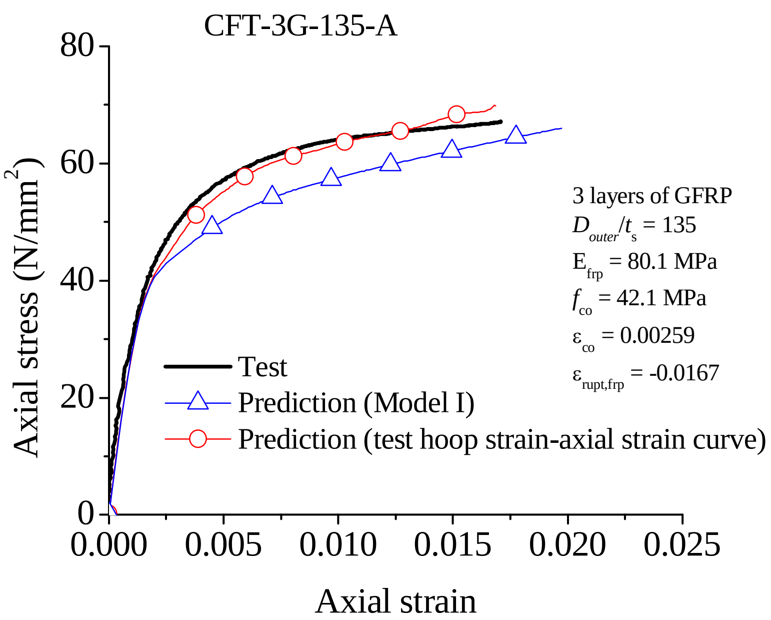


(d) Specimen CFT-3G-135-A

Figure 5.3 Stress-strain curves of concrete in CCFT tests of Chapter 4 (continued)

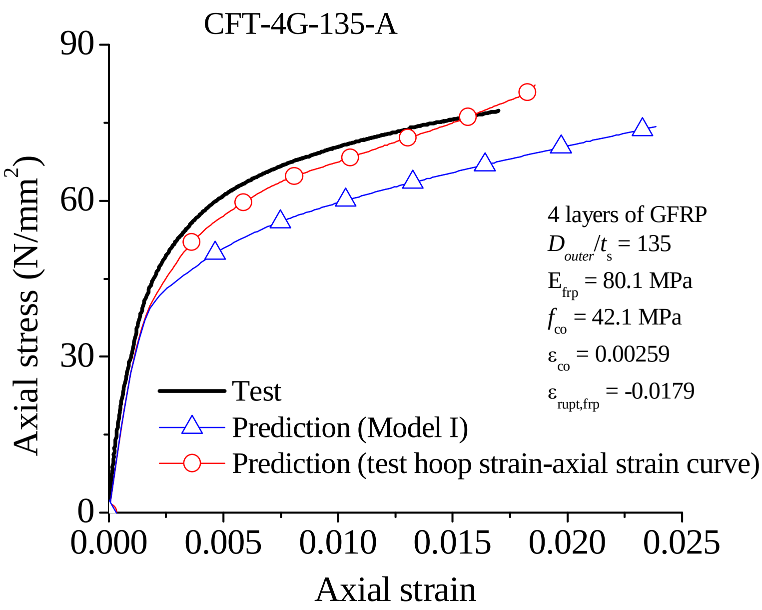


(e) Specimen CFT-4G-135-A

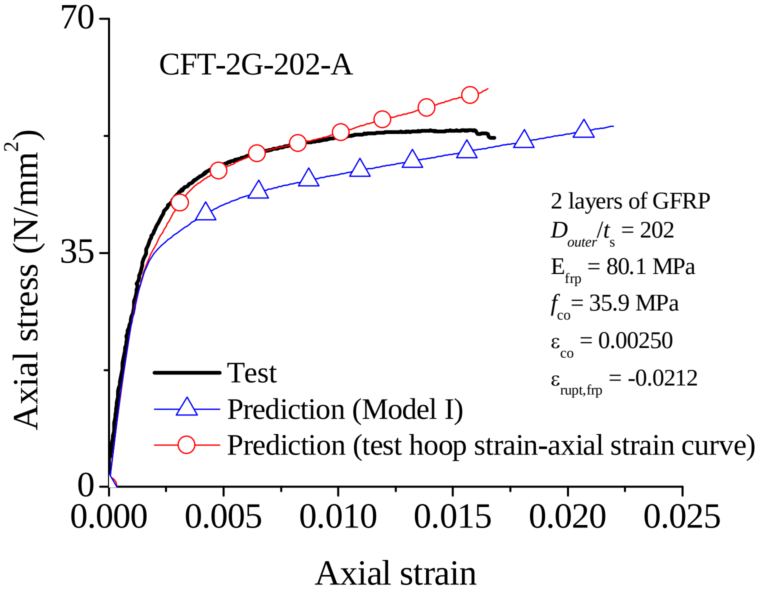


(f) Specimen CFT-2G-202-A

Figure 5.3 Stress-strain curves of concrete in CCFT tests of Chapter 4 (continued)

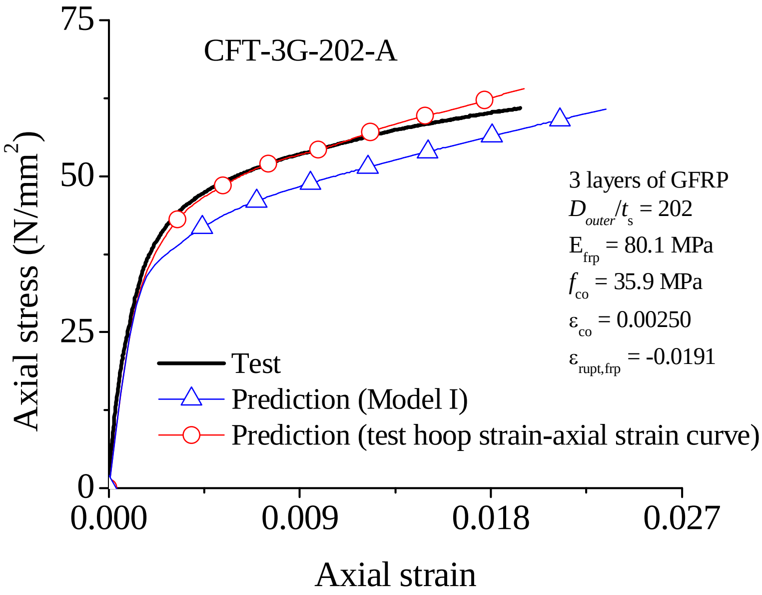


(g) Specimen CFT-3G-202-A

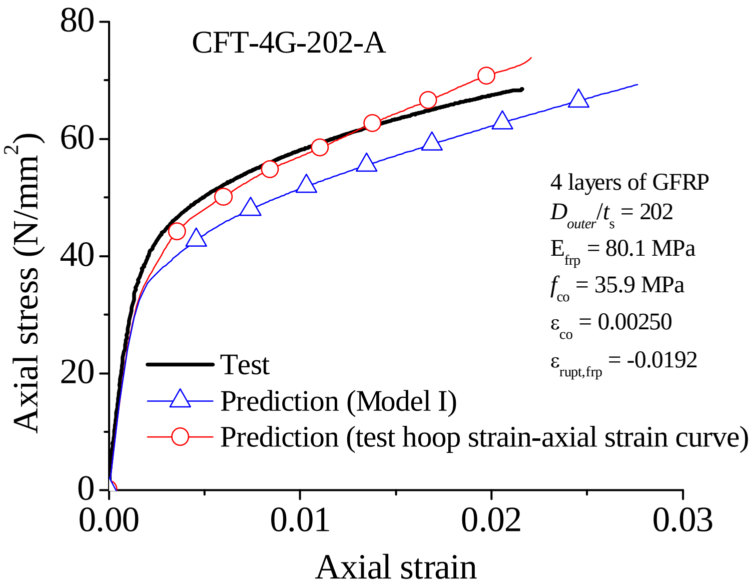


(h) Specimen CFT-4G-202-A

Figure 5.3 Stress-strain curves of concrete in CCFT tests of Chapter 4 (continued)

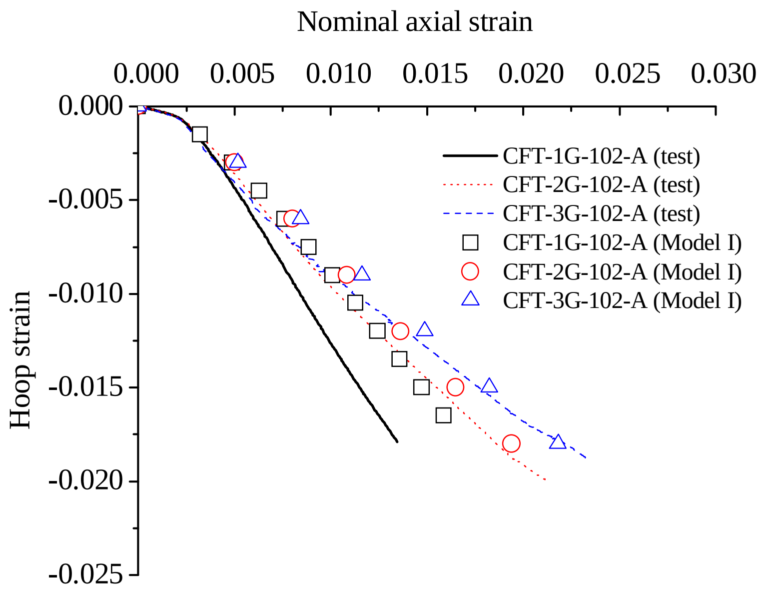


(a) Series 102-A

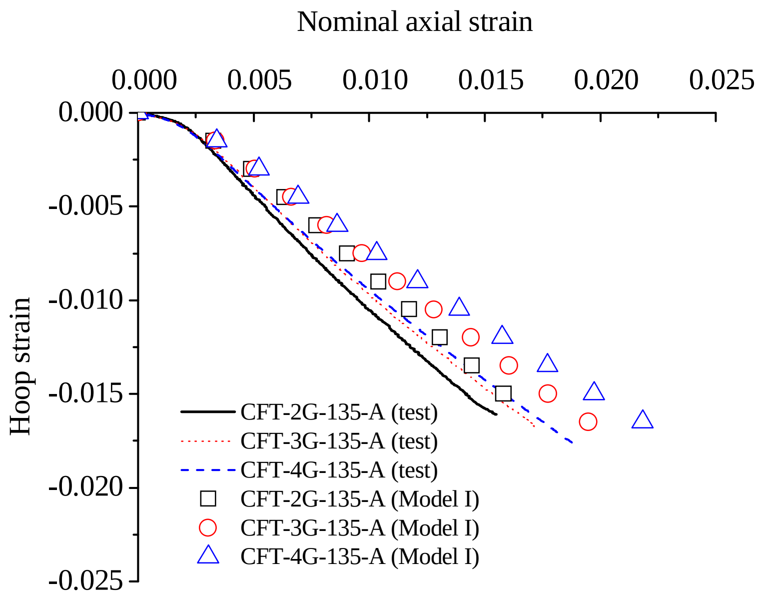


(b) Series 135-A

Figure 5.4 Hoop strain-axial strain curves for CCFT tests of Chapter 4

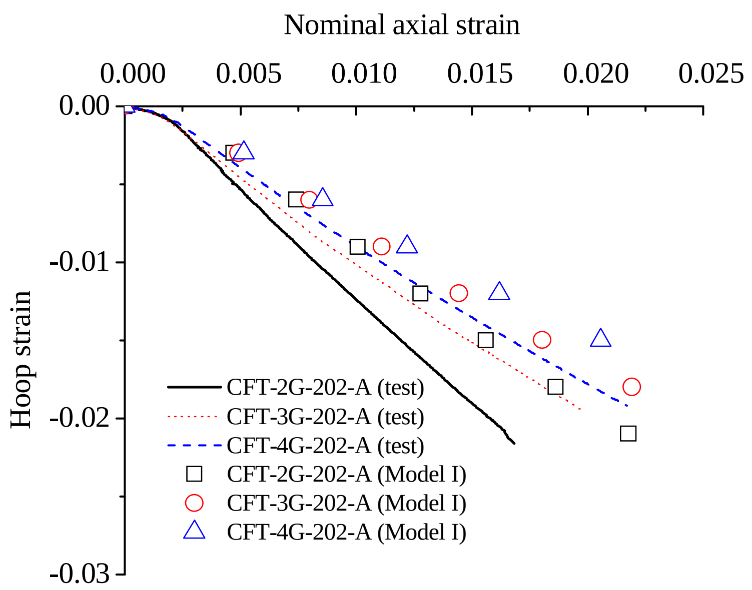


(c) Series 202-A

Figure 5.4 Hoop strain-axial strain curves for CCFT tests of Chapter 4 (continued)

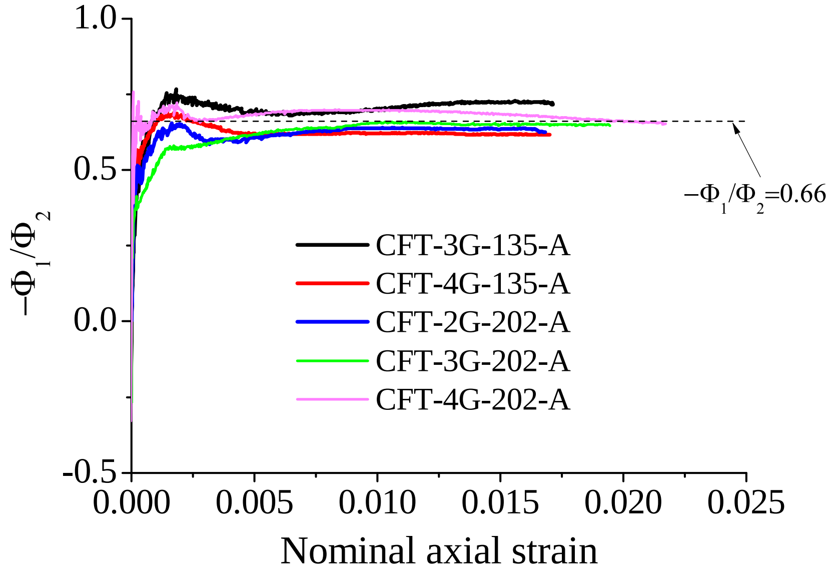


Figure 5.5 Deduced $c_\Phi$ value for Eq. 5.12c

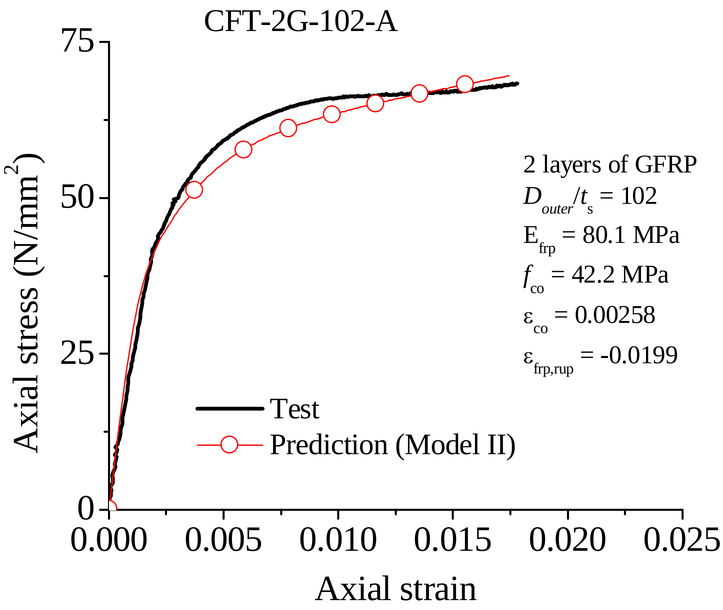


(a) Specimen CFT-2G-102-A

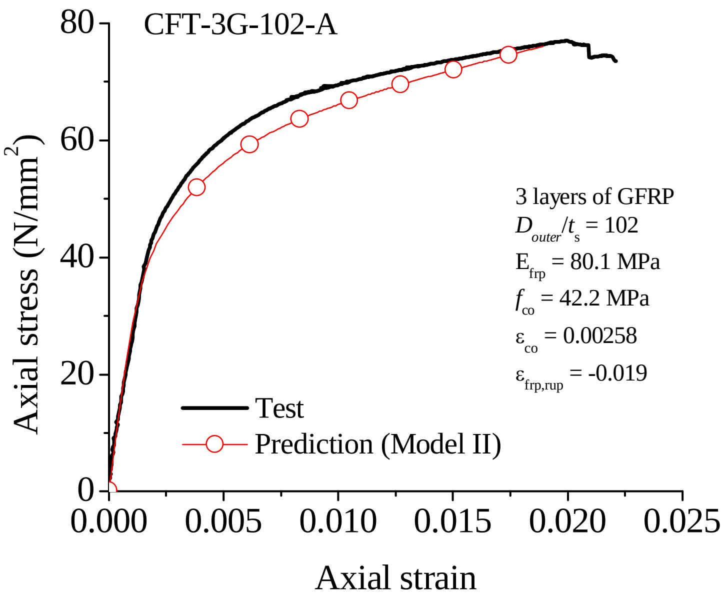


(b) Specimen CFT-3G-102-A

Figure 5.6 Performance of Model II: stress-strain curves of concrete

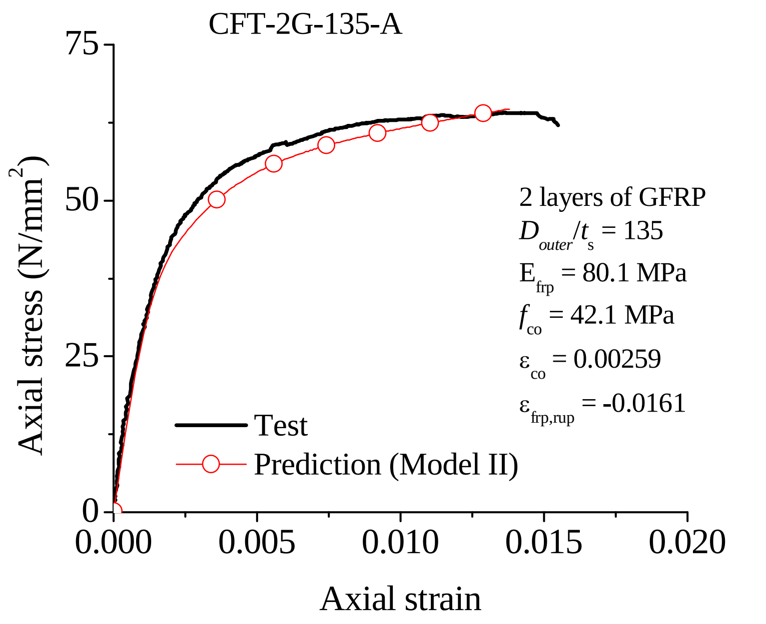


(c) Specimen CFT-2G-135-A

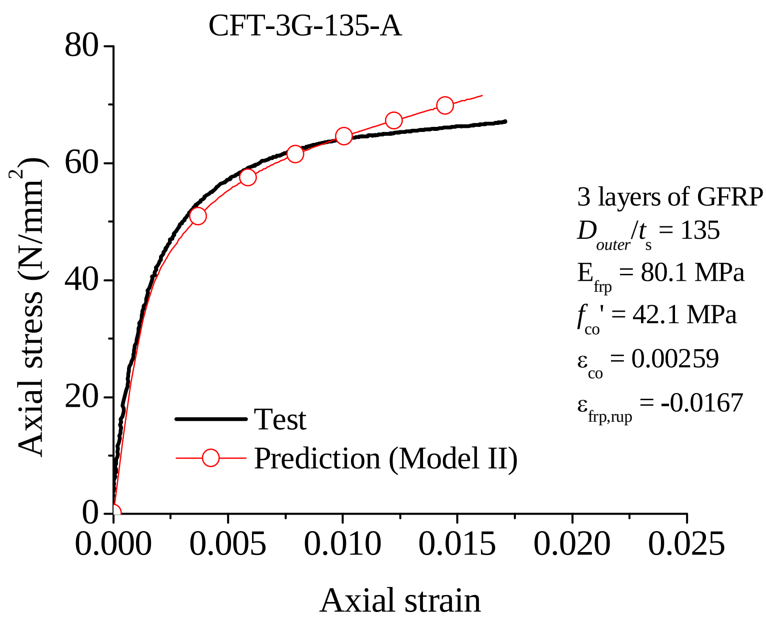


(d) Specimen CFT-3G-135-A

Figure 5.6 Performance of Model II: stress-strain curves of concrete (continued)

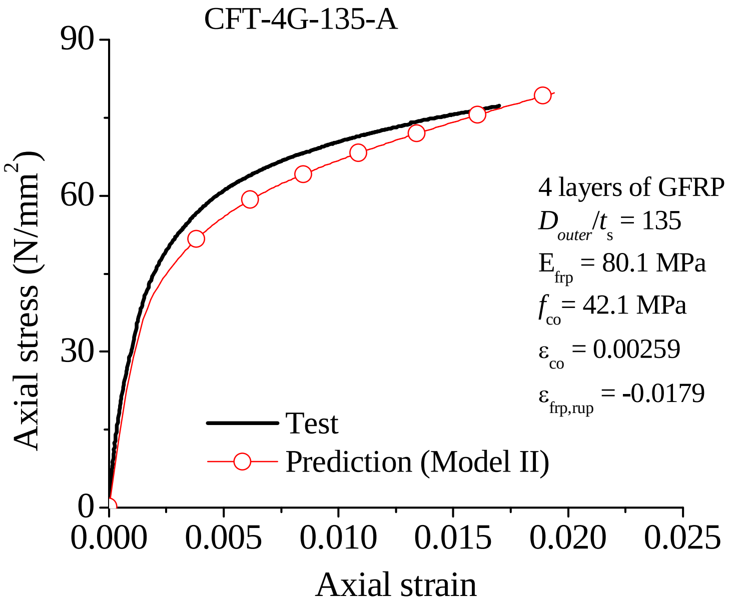


(e) Specimen CFT-4G-135-A

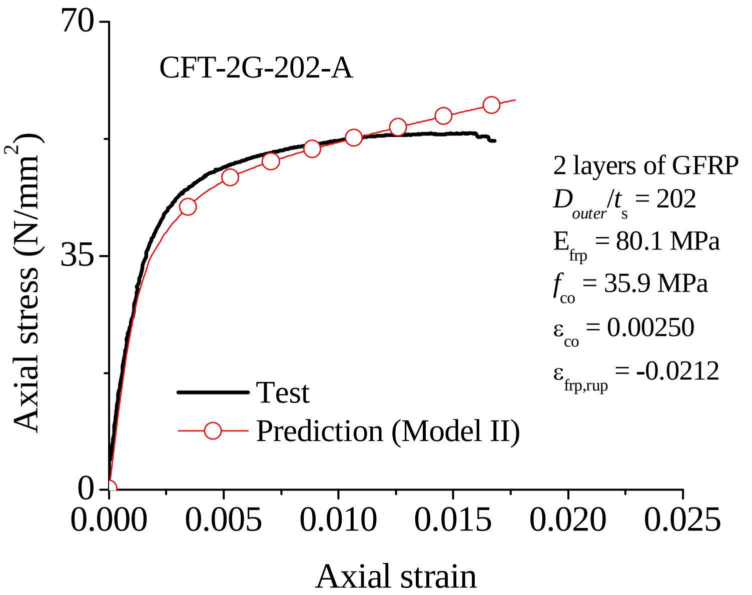


(f) Specimen CFT-2G-202-A

Figure 5.6 Performance of Model II: stress-strain curves of concrete (continued)

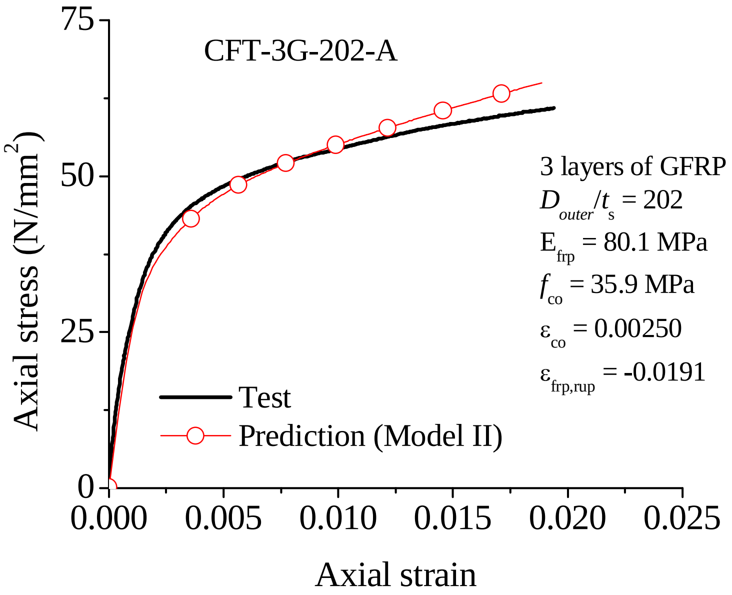


(g) Specimen CFT-3G-202-A

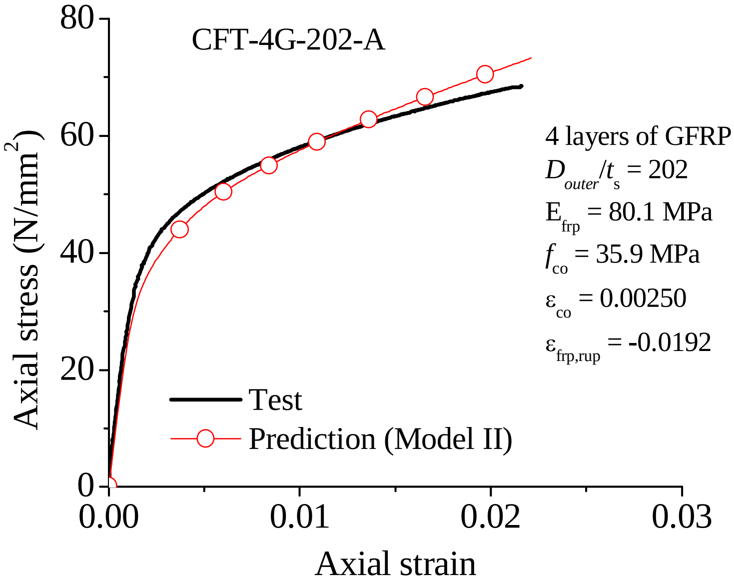


(h) Specimen CFT-4G-202-A

Figure 5.6 Performance of Model II: stress-strain curves of concrete (continued)

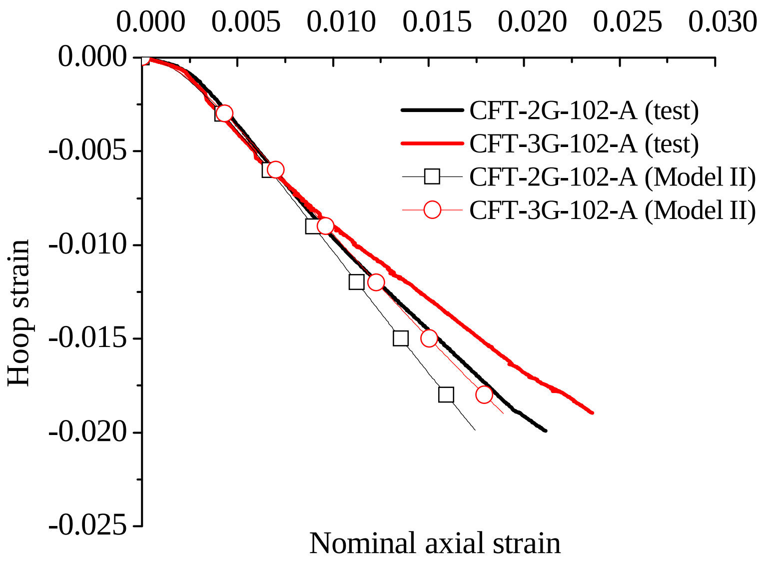


(a) Series 102-A

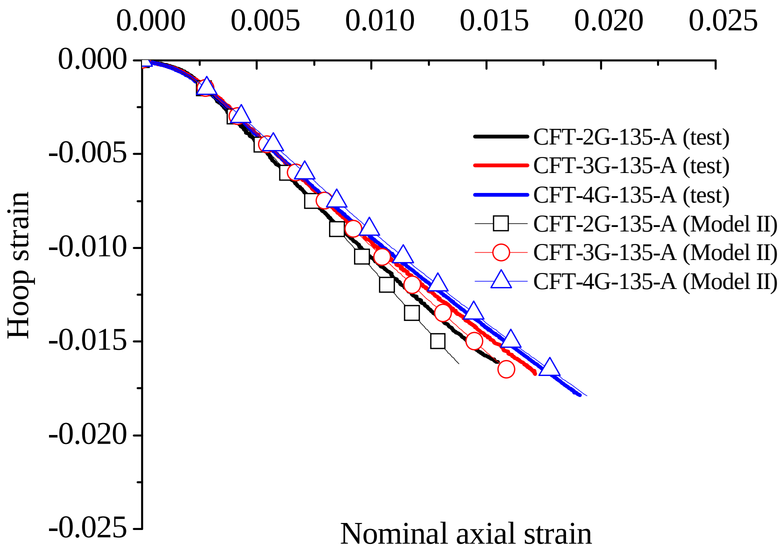


(b) Series 135-A

Figure 5.7 Performance of model II: hoop strain-axial strain curves of concrete

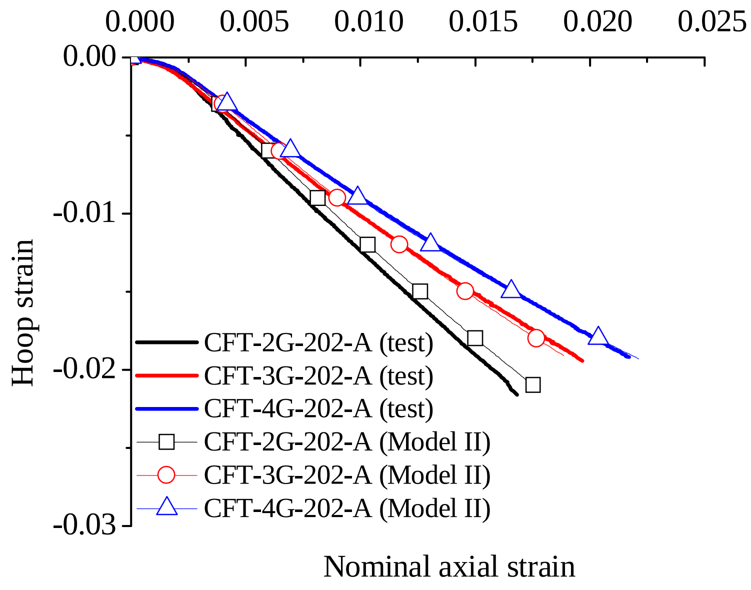


(c) Series 202-A

Figure 5.7 Performance of Model II: hoop strain-axial strain curves of concrete (continued)

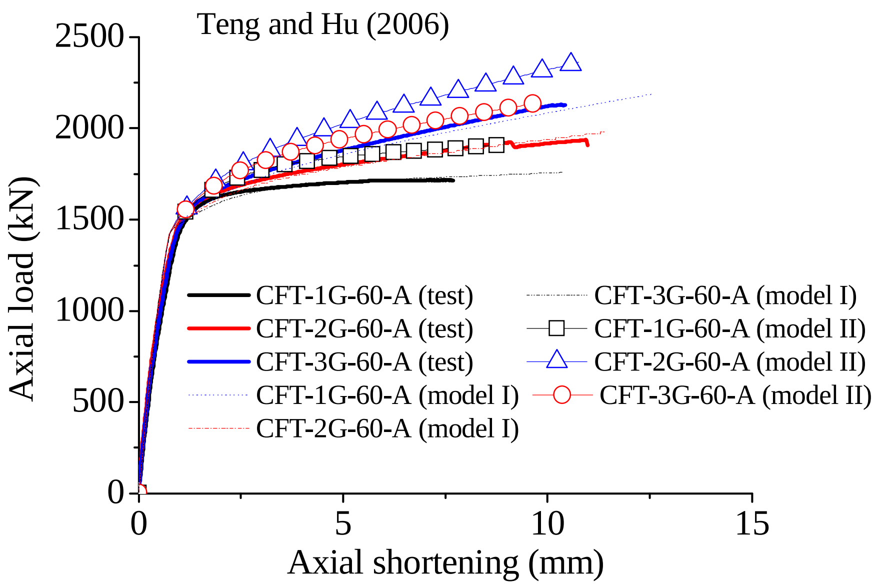


Figure 5.8 Axial load-axial shortening curves for CCFTs tested by Teng and Hu (2006)

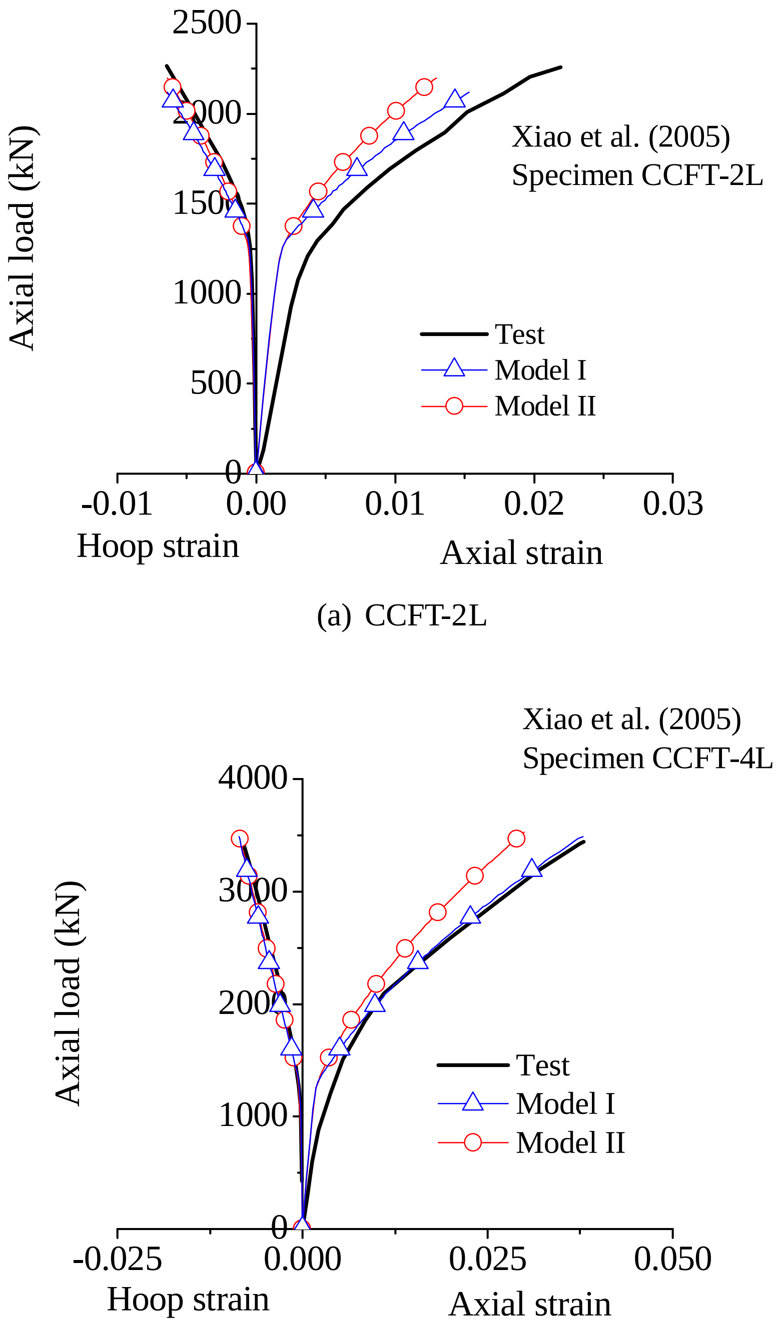


(a) CCFT-2L



(b) CCFT-4L

Figure 5.9 Axial load-axial (hoop) strain curves for CCFTs tested by Xiao et al. (2005)

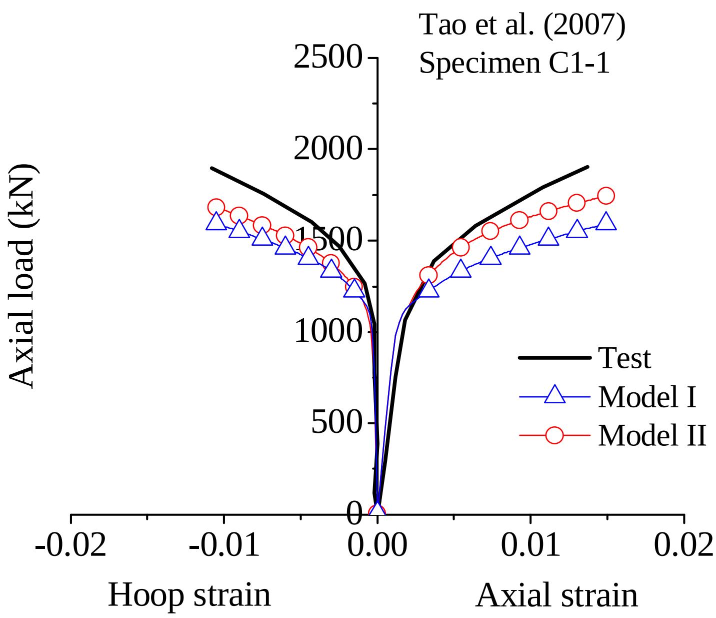


(a) Specimen C1-1

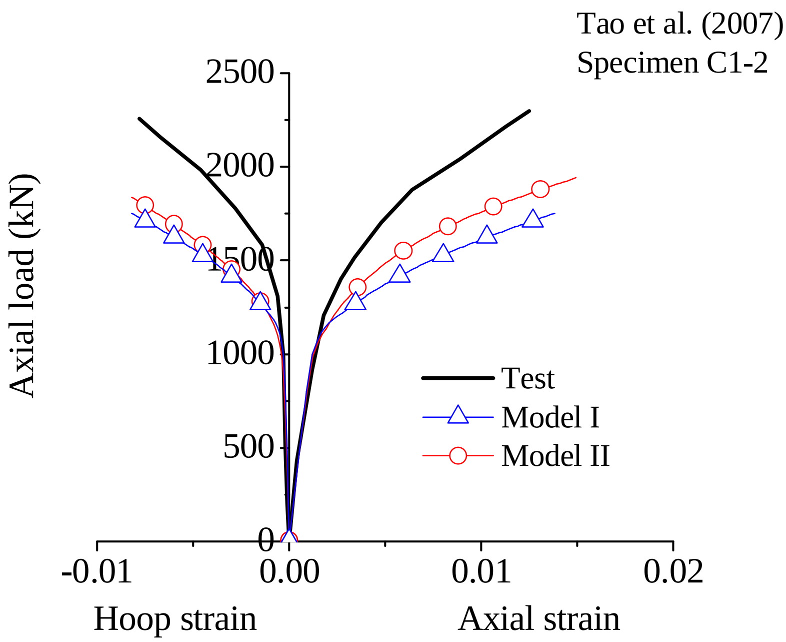


(b) Specimen C1-2

Figure 5.10 Axial load-axial (hoop) strain curves for CCFTs tested by Tao et al. (2007)

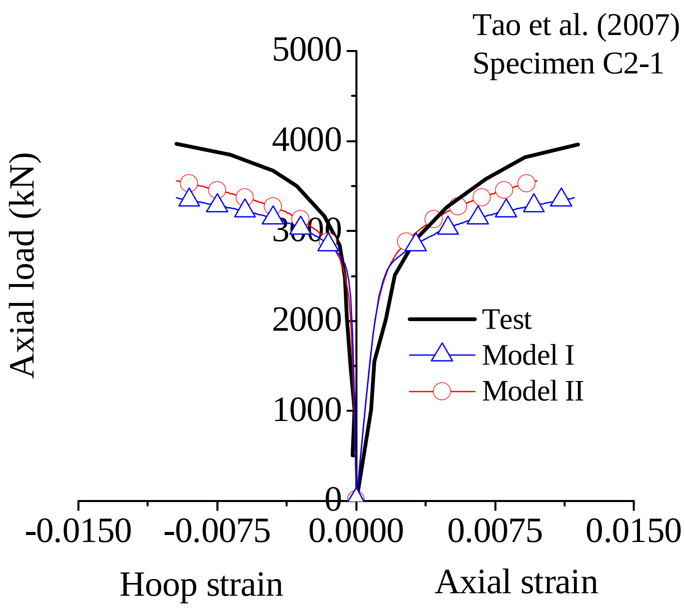


(c) Specimen C2-1

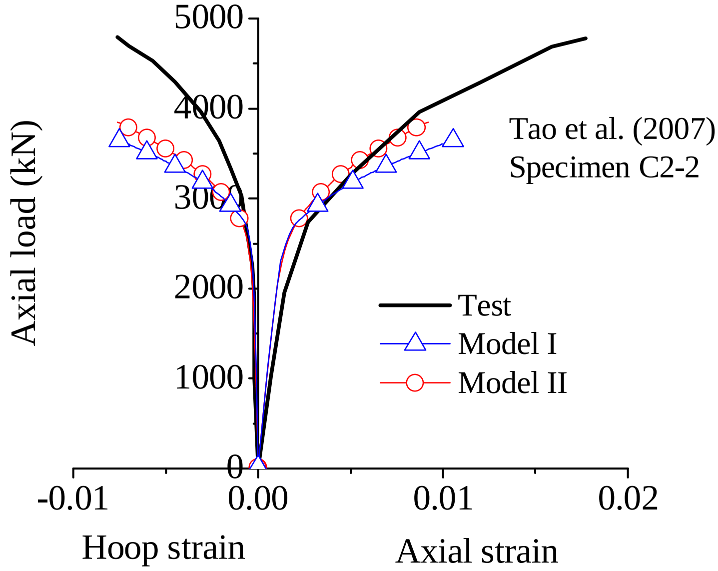


(d) Specimen C2-2

Figure 5.10 Axial load-axial (hoop) strain curves for CCFTs tested by Tao et al. (2007) (continued)

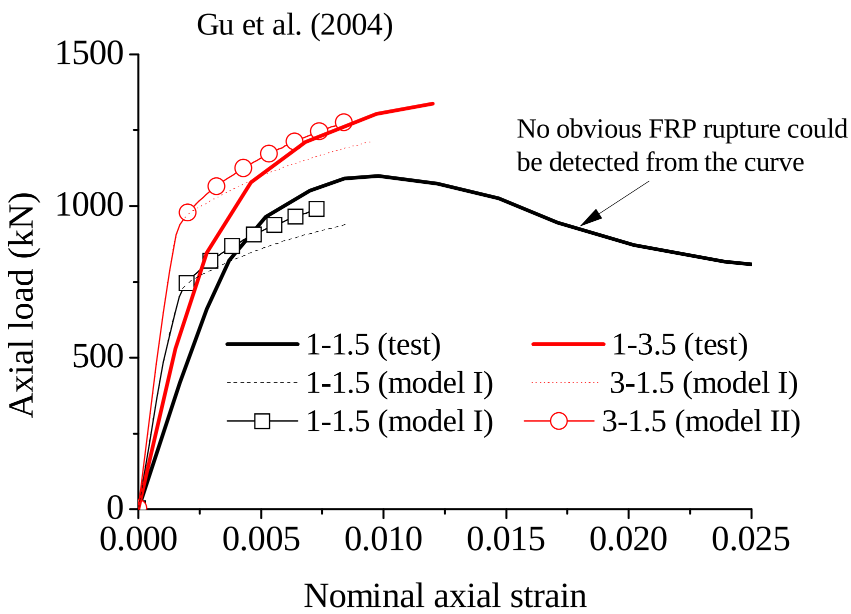


(a) Series 1.5 and 3.5 with 1-ply CFRP jacket

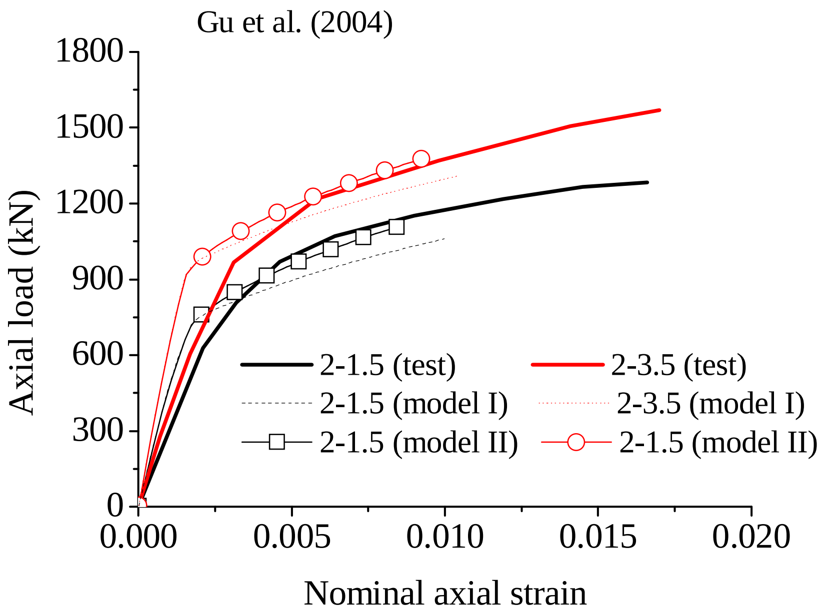


(b) Series 1.5 and 3.5 with 2-ply CFRP jacket

Figure 5.11 Axial load-axial strain curves for CCFTs tested by Gu et al. (2004)

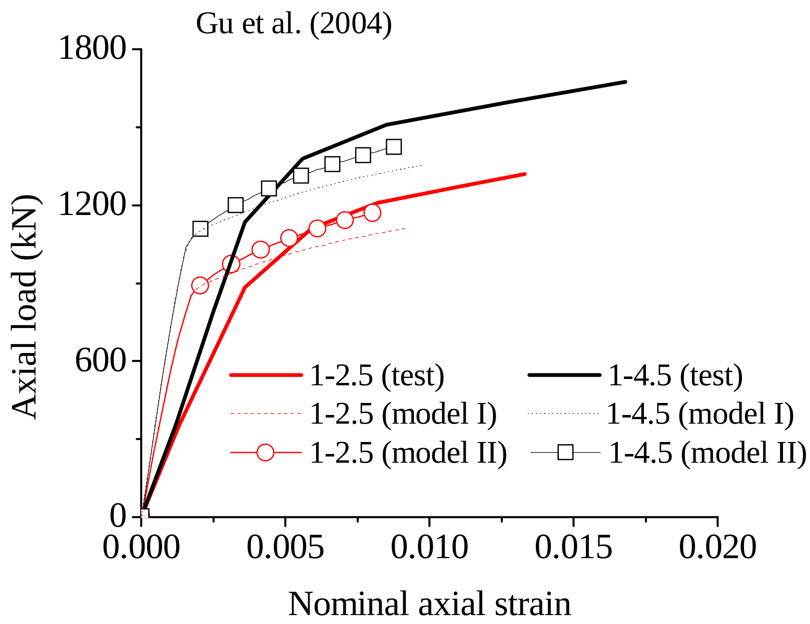


(c) Series 2.5 and 4.5 with 1-ply CFRP jacket

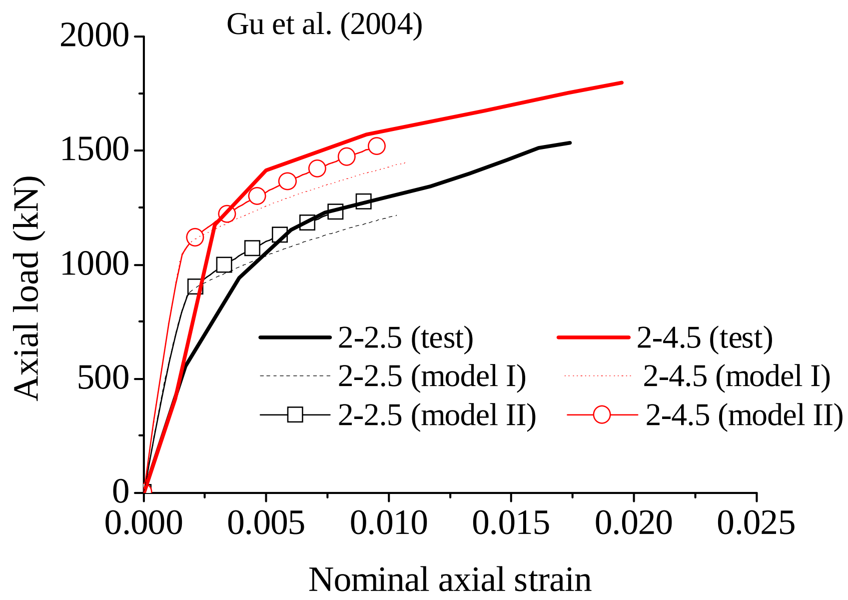


(d) Series 2.5 and 4.5 with 2-ply CFRP jacket

Figure 5.11 Axial load-axial strain curves for CCFTs tested by Gu et al. (2004) (continued)

# CHAPTER 6

# BEHAVIOUR AND MODELLING OF FRP-CONFINED CIRCULAR CONCRETE-FILLED STEEL TUBULAR COLUMNS UNDER AXIAL CYCLIC COMPRESSION

## 6.1 INTRODUCTION

The behaviour of FRP-confined concrete-filled steel tubes (CCFTs) under axial monotonic compression has been studied experimentally and theoretically in Chapters 4 and 5 respectively. This chapter presents a combined experimental and theoretical study on the behaviour of CCFTs under axial cyclic compression. Results from a series of axial cyclic compression tests of CCFTs are first presented and discussed, followed by the development of a cyclic stress-strain model for the confined concrete in such columns. The stress-strain model is important for future modelling of CCFTs under seismic loadings.

## 6.2 EXPERIMENTS

### 6.2.1 Test Specimens

Two series of specimens (i.e. Series 3G-102 and 4G-202) were prepared and tested. Series 3G-102 included three identical specimens tested under two different loading schemes. All the specimens in Series 3G-102 had a steel tube with a $D_{outer}/t_s$ ratio of 102 and were confined with a three-ply GFRP jacket. Series 4G-102 included four identical specimens tested under three different loading schemes. All the specimens in Series 4G-202 had a steel tube with a $D_{outer}/t_s$ ratio of 202 and were confined with a four-ply GFRP jacket. Other details of the specimens are summarized in Table 6.1. The preparation process of the specimens and the material properties of the steel plates are the same as those presented in Chapter 4 (see Section 4.2.3), while the material properties of the GFRP jackets and the adhesive are the same as those presented in Chapter 3 (see Section 3.2.1). In summary, the GFRP jackets used had an elastic modulus of 80.1 GPa and an ultimate strain of 2.28%, based on a nominal thickness of 0.17 mm per ply while the adhesive had an elastic modulus of 4.5 Gpa and an ultimate tensile stress of 30 MPa according to the manufacturer. The naming system is also very similar to that in Chapter 4 (see Section 4.2.1), except the last letter which indicates the type of loading (i.e. types B, C and D loading in this chapter rather than type A loading in Chapter 4). Details of these three types of loading schemes (i.e. types B, C and D loading schemes) are discussed in Section 6.2.2. The material properties found from standard cylinder (152.5 mm x 305 mm) tests are summarized in Table 6.2.

### 6.2.2 Instrumentation and Loading

A number of strain gauges were attached at different heights (i.e. vertical locations) of the specimens. The layout of the strain gauges is the same as that in the axial monotonic compression tests presented in Chapter 4 (Figure 4.2), except that a smaller number of hoop strain gauges were used at the two circumferences adjacent to the ends of each specimen. For the specimens in Series 3G-102, five instead of six hoop strain gauges were used around each near-end circumference, by excluding the one in the overlapping zone; for the specimens in Series 4G-202, only three hoop strain gauges were attached at each near-end circumference and distributed evenly within the half side opposite to the overlapping zone, as end buckling in these specimens was expected to be well controlled according to results from the monotonic axial compression tests. The gauge length was 20 mm for all the strain gauges.

Besides the strain gauges, three LVDTs placed $120^0$ apart from each other were installed to measure the total axial shortening of the specimen. The axial cyclic compression tests were all conducted using an MTS machine under displacement control (stroke control) at a constant rate of 0.5 mm/min. It should be noted that this displacement included not only the shortening of the specimens but also the deformation of the whole loading system itself. All test data, including the strains, loads, and displacements, were recorded simultaneously by a data logger.

Axial cyclic compression involving unloading/reloading cycles was applied at several prescribed unloading displacement values before failure. The prescribed unloading displacement values were selected based on results from the axial monotonic compression tests (see Chapter 4) so that one unloading strain was within 0.001 and 0.0035, and the other four unloading strains were larger than 0.0035 and were evenly distributed on the axial load-strain curve. The two distinctive ranges of unloading strain were determined according to Lam and Teng (2009) for investigating the unloading/reloading behaviour of the confined concrete at different levels of plastic deformation. For some specimens (e.g. CFT-3G-102-B1), an unloading/reloading cycle was also applied at an unloading strain smaller than 0.001; such a small unloading strain was found to lead to an approximately linear elastic unloading/reloading path (i.e. no residual strain) and is not further discussed in the following sections.

In each series, two specimens were subjected to type B loading while one specimen was subjected to type C loading. One additional specimen in Series 4G-202 was subjected to type D loading. Both type B and type C loadings were designed for full unloading/reloading cycles where the unloading of each cycle is terminated at zero load (in the present study a small load of 20 kN was used instead of zero load for a more stable control of the MTS machine) and the reloading of each cycle is terminated at the unloading displacement of the same cycle (i.e. where the unloading starts) or after reaching the envelope curve. The only difference between the two loading schemes was that at each prescribed displacement level, one single unloading/reloading cycle was applied for type B loading, but three repeated cycles were applied for type C loading. The type D loading was designed to be a mixed loading scheme which involved: (1) a single full unloading/reloading cycle at the first prescribed displacement value; (2) three repeated full unloading/reloading cycles at the second prescribed displacement value; (3) six repeated partial unloading (and reloading to the reference strain) cycles at the third prescribed displacement value; (4) four repeated partial reloading (and unloading to zero stress) cycles at the fourth prescribed displacement value; (5) twelve repeated full unloading/reloading cycles at the fifth prescribed displacement value. Partial unloading means the unloading of each cycle is terminated at a load level significantly larger than zero, while partial reloading means the reloading of each cycle is terminated well before reaching the unloading displacement of the same cycle. During the testing of specimen CFT-4G-202-D (i.e. the specimen under type D loading), a problem occurred in the MTS machine when the specimen was unloaded for the first time at the fifth prescribed displacement value, so the last designed step (i.e. twelve repeated full unloading/reloading cycles) was not completed.

### 6.2.3 Results and Discussions

#### *6.2.3.1 Failure modes*

The specimens all failed by explosive rupture of the FRP jacket in the mid-height region, in a manner similar to that of their counterparts under axial monotonic compression (see Chapter 4). For the specimens in Series 3G-102, before this final failure, localized FRP rupture occurred near one end due to the localized outward buckling deformation of the steel tube, but this local FRP rupture only had minor effects on the load-carrying capacity of the specimen as discussed in Chapter 4. The tests were all terminated immediately after the explosive FRP rupture in the mid-height region, except for specimen CFT-4G-202-B1. After the completion of each test, the FRP jacket was removed for further examination of the steel tube, and no local buckling was found in the mid-height region, confirming that it was the dilation of concrete which caused the FRP rupture in this region. All the specimens after test are shown in Figure 6.1.

*6.2.3.2 <u>Axial load-shortening curves</u>*

The normalized axial load-axial shortening curves for all the specimens are shown in Figures 6.2 & 6.3, where the axial shortening was averaged from readings of the three LVDTs, and the axial load obtained from the test is normalized with respect to the corresponding squash load ( $N_{sq}$ ) defined by the following equation:

$$N_{sq,cft} = f_y A_s + f'_{co} A_c \tag{6.1}$$

where $f_y$ and $A_s$ are the yield stress and cross-sectional area of the steel tube respectively; and $f'_{co}$ and $A_c$ are the cylinder compressive strength and cross-sectional area of the concrete respectively.

Figures 6.2 & 6.3 show that similar to CCFTs under axial monotonic compression, the specimens under cyclic compression also had a very ductile behaviour with a large ultimate axial shortening (i.e. over 8 mm); the ultimate loads of the specimens are also seen to be considerably higher than their squash loads calculated using 6.1, suggesting that the confining effect of the FRP and the steel tube is substantial.

For comparison, the curves of the two corresponding specimens tested under axial monotonic compression (i.e. specimens CFT-3G-102-A and CFT-4G-202-A, see Chapter 4) are also shown in Figures 6.2 & 6.3. These two monotonic compression specimens had the same steel tube but a concrete with a slightly different unconfined strength when compared with their cyclic compression counterparts. The effect of this slight difference in the concrete strength is believed to be effectively eliminated by normalizing the axial load with the squash load, so that the comparisons shown in Figures 6.2 & 6.3 reflect mostly the effect of different loading scenarios.

It is evident from Figures 6.2 & 6.3 that the envelope curves of the specimens subjected to cyclic compression, which provide an upper boundary of their responses under different cyclic loading schemes, are almost the same as the curves of the corresponding specimens under monotonic compression, suggesting that the unloading/reloading cycles have little effect on the envelope response of the CCFTs. Figures 6.2 & 6.3 also clearly illustrate the cumulative effect of loading history on plastic deformation (i.e. the deformation at zero load increases with repeated loading cycles).

#### *6.2.3.3 Plastic strain*

As described earlier, in all the specimens, the steel tube was welded to two steel plates (i.e. a bottom plate and a top plate) which were in intimate contact with the concrete inside. This ensures that the axial strain of the concrete and that of the steel tube were always the same during the unloading/reloading cycles. However, this does not necessarily mean that the two components (i.e. concrete and steel tube) could be unloaded to zero stress simultaneously, as the axial plastic strains of the two materials can be quite different. Figure 6.4 shows that the nominal plastic strain-nominal unloading strain for CCFTs cannot be closely predicted using Lam and Teng's (2009) model. In this chapter, similar to the approach adopted in Chapter 4, the concrete and the steel tube are also separated in order to investigate the interaction between these two components.

The plastic strain of a material is defined as its residual axial strain when it is unloaded to zero stress. Readings from the strain gauges attached at the mid-height of the steel tube were used to examine the stress state of the steel tube during unloading/reloading cycles (through Eqs. 5.8-5.12 & 5.14-5.17), and to evaluate the plastic strain of the steel tube. The so-obtained axial stress-strain curves for the steel tubes are shown in Figure 6.5 & 6.6.

It is clear from Figure 6.5 & 6.6 that in the unloading process of a CCFT, the steel tube reached zero compressive stress first, after which tensile stresses were developed until the specimen was unloaded to the target load level. As the CCFT was always subjected to a compressive load during the test, this observation means that the plastic strain of the steel tube was larger than the overall nominal strain of the CCFT at zero load which was in turn larger than the plastic stain of the concrete.

*6.2.3.4 Axial stress-strain curves of concrete*

The axial stress of the concrete in CCFTs is defined as the load carried by the concrete core divided by its cross-sectional area. The load carried by the concrete core is assumed to be equal to the difference between the load carried by the CCFT and that carried by the steel tube; the latter was found based on readings from the axial and lateral strain gauges, as introduced earlier.

The normalized axial stress-strain curves for the two series of specimens are shown in Figure 6.7 & 6.8 respectively, where the axial stress and the axial strain are normalized by the cylinder compressive strength of the unconfined concrete and the corresponding strain, respectively. For comparison, the curves of the corresponding specimens tested under axial monotonic compression are also shown in Figure 6.7 & 6.8.

Similar to the finding for FRP-confined concrete in a solid cylinder (Lam et al. 2006), Figure 6.7 & 6.8 show that the envelope curves for the specimens tested under cyclic compression are almost the same as the axial stress-strain curves of the corresponding specimens under monotonic compression. It is also interesting to note that while the specimens were subjected to full unloading/reloading cycles (i.e. unloading was terminated at a very small load), the axial stresses at the termination points of unloading are significantly larger than zero. This phenomenon is due to the development of tensile stresses in the steel tube, as discussed earlier.

The plastic strain of the confined concrete can be estimated from Figure 6.7 & 6.8 by extending the unloading curve to intersect with the horizontal axis. In the present study, the unloading curves were extended according to their slopes at the termination point of unloading (Figure 6.9), and the so-obtained plastic strains of concrete are summarized in Table 6.4 & 6.5 for all the unloading paths except those of partial unloading or partial reloading cycles (i.e. the unloading paths starting from the third and fourth unloading points in specimen CFT-4G-202-D). As can be observed from Figures 6.7 & 6.8, the slope of the unloading path generally decreases with the reduction of stress. Therefore, the plastic strain obtained by extending an incomplete unloading path (see Figure 6.9) can be expected to be larger than the real value, and the difference becomes larger when the termination stress of unloading is larger. In this sense, it can also be expected that the so-obtained plastic strains are more accurate for specimens in Series 4G-202, where the reloading stress (i.e. stress at the termination of unloading) of concrete was smaller because of the use of a thinner steel tube. Nevertheless, it is believed that the plastic strains obtained in this way still represent a close approximation of the real values as the reloading stresses were relatively small. Table 6.4 & 6.5 also demonstrate again that the strain at zero load of a CCFT is significantly larger than the plastic stain of the concrete.

Figure 6.7 & 6.8 show that the unloading/reloading cycles at the same unloading strain generally do not coincide with each other, indicating that the effect of loading history on the cyclic response of confined concrete is not negligible. Instead, the loading history has a cumulative effect on both the plastic strain and the stress deterioration of the confined concrete. Figure 6.7 & 6.8 also show that the difference between two subsequent loading cycles becomes increasingly small with the number of repeated cycles. These observations agree well with the findings of existing studies on unconfined concrete, steel-confined concrete and FRP-confined concrete (Karsan and Jirsa 1969; Bahn and Hsu 1998; Lam et al. 2006; Sakai and Kawashima 2006), and further confirm that the uniqueness concept proposed by Sinha et al. (1964) cannot apply here. The uniqueness concept means that the locus of common points, where the reloading path of an unloading/reloading cycle crosses the unloading path, can be considered as a stability limit.

### *6.2.3.5 Lateral strain-axial strain curves*

The normalized lateral strain-axial strain curves of all the cyclically loaded specimens are shown in Figure 6.10, where the strains are obtained from the strain gauge readings and normalized by their respective axial strains at the peak stress of unconfined concrete. Again, the curves of the corresponding monotonically loaded specimens are also shown for comparison. Figure 6.10 reveals that the envelope curves of the specimens under cyclic compression basically agree well with the curve of the corresponding specimen under monotonic compression, indicating that the static lateral expansion behaviour of concrete was not much affected by the unloading/reloading cycles. By contrast, it is clear from these figures that the unloading/reloading paths do not coincide with the envelope curve; the lateral strains on unloading/reloading paths are generally higher than the corresponding lateral strain at the same axial strain on the envelope curve.

### *6.2.3.6 Ultimate condition of FRP jacket*

Figure 6.11 shows the distribution of hoop strains over the circumference of the mid-height section at the ultimate state, while the maximum hoop strain readings at the ultimate state $\varepsilon_{rupt,\max}$ are summarized in Table 6.3. The average ultimate hoop strains $\varepsilon_{rupt}$ are also summarized in Table 6.3, where the strain values are averaged from the five hoop strain gauges outside the overlapping zone for all the specimens, except for specimens CFT-3G-102-A and CFT-3G-102-B2 where readings from only four strain gauges were used as the other one was damaged during the test. It is noted that the average ultimate hoop strains of the cyclically loaded specimens are considerably smaller than the value obtained from flat coupon tests (i.e. 0.0228), and are similar to those of the corresponding monotonically loaded specimens (Table 4.3). The ultimate hoop strain distributions of the two types of specimens are also similar. It should be noted that Lam and Teng (2006) and Rousakis (2001) reported that for FRP-confined concrete cylinders, a higher hoop rupture strain could be reached when the cylinder is subjected to cyclic compression instead of monotonic compression. The same observation cannot be made from the limited results of the present study on CCFTs.

## 6.3 STRESS-STRAIN MODEL FOR CONFINED CONCRETE IN CCFTS SUBJECTED TO CYCLIC AXIAL COMPRESSION

### 6.3.1 General

Many studies have examined the stress-strain behaviour of unconfined, steel-confined and FRP-confined concrete under axial cyclic compression (Karsan and Jirsa 1969; Bahn and Hsu 1998; Lam et al. 2006; Sakai and Kawashima 2006). Lam and Teng (2009) proposed a cyclic stress-strain model for FRP-confined concrete based on a comprehensive review of the existing studies and their own experimental observations. Lam and Teng (2009) showed that their model could provide accurate predictions of test results.

As has been discussed earlier, the cyclic response of the confined concrete in CCFTs is similar to that of FRP-confined concrete. Based on this observation, a cyclic stress-strain model can be developed for the former by basing it on Lam and Teng's (2009) model but taking due account of the differences between the confined concrete in CCFTs and FRP-confined concrete. This section first compares the cyclic behaviour of the two types of confined concrete with reference to Lam and Teng's (2009) model, then presents the proposed cyclic stress-strain model for the concrete in CCFTs, which is verified against the test results of the present study.

### 6.3.2 Key Characteristics

*6.3.2.1 FRP-confined concrete*

As discussed in Lam and Teng (2009), the key characteristics of the cyclic stress-strain behaviour of FRP-confined concrete include: (1) the envelope curve is basically the same as the stress-strain curve of the corresponding specimen under monotonic compression; (2) the loading history has a cumulative effect on both the plastic strain and the stress deterioration; (3) the unloading paths are generally nonlinear with a continuously decreasing slope while the reloading paths are approximately linear; (4) the plastic strain and the stress deterioration are both independent of the confinement level. The success of Lam and Teng's (2009) model lies in its ability to capture all these key characteristics and accurately predict the plastic strain, the stress deterioration and the shape of unloading/reloading curves.

*6.3.2.2 Unloading path*

It is clear from the discussions in Section 6.2.3 that the cyclic stress-strain behaviour of confined concrete in CCFTs also possesses the first three characteristics summarized above (see Figure 6.7 & 6.8). Figure 6.7 & 6.8 show that the unloading path of concrete in CCFTs is generally nonlinear. Lam and Teng (2009) proposed a successful polynomial equation for the unloading path (i.e. Eqs. 6.15-6.20 presented later in this chapter) of FRP-confined concrete which has a similar shape as that shown in Figures 6.7 & 6.8, with the key parameters in the equation being the unloading strain, the unloading stress and the plastic strain. To further compare the unloading paths of these two types of confined concrete, the predictions of Lam and Teng's (2009) equations are compared with the experimental curves in Figure 6.9 for one specimen subjected to type B loading in each series, while the comparisons for other specimens are similar. In making the predictions, the experimental unloading strain and unloading stress, and the plastic strain obtained by extending the experimental stress-strain curve of concrete (see Section 6.2.3.4 for details) were used. Figure 6.9 shows that the predictions agree reasonably closely with the test results, especially for the specimen in Series 4G-202. The differences between the predictions and the test results are believed to be mainly due to the use of imprecise plastic strains. As discussed in Section 6.2.3.4, the method adopted in the present study to obtain the experimental plastic strains tends to overestimate the real values and such overestimation is more pronounced when a thicker steel tube is used; this also explains why the predictions are closer to the test results for the specimen in Series 4G-202.

*6.3.2.3* *Plastic strain*

For the fourth characteristic summarized above for FRP-confined concrete, Lam and Teng (2009) indicated that it also applies to unconfined concrete and steel-confined concrete. As the plastic strain and the stress deterioration are both independent of the confinement level, it can be expected that the equations proposed by Lam and Teng (2009) for these two parameters are also applicable to the confined concrete in CCFTs. To further clarify this point, the predictions of Lam and Teng's (2009) equations are also listed in Table 6.4 & 6.5 and compared with the experimental stress deterioration values ($\sigma_{new,\exp}$) and the plastic strains ($\varepsilon_{pl,\exp}$) obtained by extending the experimental stress-strain curve of concrete in Figure 6.12. The equations (i.e. Eqs. 6.2-6.11) proposed by Lam and Teng (2009) for these two parameters (i.e. $\sigma_{new,pre}$ and $\varepsilon_{pl,pre}$) are presented later in this chapter. In the calculations, the corresponding experimental unloading strain and stress were used. Table 6.4 & 6.5 as well as Figure 6.12 show that the predictions agree very closely with the test results for the stress deterioration values. For the plastic strain, the predictions are reasonably close to but generally larger than the plastic strains obtained from tests; the difference is seen to be larger for specimens in Series 3G-102. Again, this difference is believed to be due to the imprecise estimation of the plastic strain from the incomplete experimental unloading path, as explained earlier. It can therefore be expected that the equations proposed by Lam and Teng (2009) (Eqs. 6.2-6.11) should perform even better than is indicated by Table 6.4 & 6.5 and Figure 6.12.

By making use of this predicted plastic strain and the experimental unloading stress and strain, another set of unloading paths was produced using Lam and Teng's (2009) equations (Eqs. 6.13-6.18) for specimen CFT-3G-102-B1 and is also shown in Figure 6.9a. The predictions are very close to the experimental results, further confirming the very similar behaviour of the concrete in CCFTs and FRP-confined concrete, in terms of both the unloading path and the plastic strain.

#### *6.3.2.4 Effective unloading/reloading cycles*

It has been shown that similar to FRP-confined concrete, the prior unloading/reloading history has a cumulative effect on the plastic strain and stress deterioration of the concrete in CCFTs. It is, however, generally believed that an unloading/reloading cycle will not affect the subsequent cyclic stress–strain behaviour if the amplitude of the cycle is not large enough (Sakai and Kawashima 2006; Lam and Teng 2009). Based on this assumption, Lam and Teng (2009) also proposed an equation (i.e. Eq. 6.12 presented later in this chapter) for the so-called effective unloading/reloading cycles. With their equation (Eq. 6.12), the unloading/reloading cycle is effective only when the stress/strain at the termination of unloading is sufficiently low and the strain at the termination of reloading is sufficiently large. The stress-strain curve of the concrete in specimen CFT-4G-202-D is used to examine this assumption (Figure 6.13). Figure 6.13 shows that at the third envelope unloading point, stress deterioration always occurs no matter how close the reloading strain (i.e. the strain at the starting point of reloading) and the unloading strain (the strain at the starting point of unloading) are; at the fourth envelope unloading point, no increase in the plastic strain is seen until the last two cycles for which the unloading strains are close to the envelope unloading strain. These observations suggest that for the concrete in CCFTs, the equation proposed by Lam and Teng (2009) is at least inadequate in terms of the requirement of a sufficiently low unloading strain for an effective unloading/reloading cycle. It should however be noted that the equation was proposed by Lam and Teng (2009) based on their assumption instead of test observations, so the above discussions do not necessarily mean that the behaviour of the concrete in CCFTs and that of FRP-confined concrete are different in terms of the effective unloading/reloading cycles. Instead, this may suggest that Lam and Teng's (2009) model needs to be improved in this aspect, even for FRP-confined concrete. Further research is needed to clarify this issue.

### 6.3.3 Stress-Strain Model

#### *6.3.3.1 General*

The above discussions suggest that the cyclic responses of FRP-confined concrete and the confined concrete in CCFTs, including the unloading/reloading path, the plastic strain, the stress deterioration and the cumulative effect of loading history, are all very similar. The only difference between the two types of confined concrete lies in their different envelope curves, which are approximately the same as their respective stress-strain curves when they are subjected to monotonic compression.

Given the above observation, a stress-strain model for concrete in CCFTs is proposed in the present study, which consists of the monotonic stress-strain model presented in Chapter 5 for predicting the envelope curve, and Lam and Teng's (2009) predictive equations for determining the plastic strain, stress deterioration and unloading/reloading path. The equation proposed by Lam and Teng (2009) for counting effective unloading/reloading cycles has been shown to be inappropriate for concrete in CCFTs. However, given the limited test results from the present study (only at one specified unloading strain in one single specimen can this issue be examined), this equation is simply adopted as a preliminary measure. The error introduced by the use of this equation is expected to only affect the predictions for a single specimen (i.e. specimen CFT-4G-202-D). Apparently, further refinement to this equation is necessary when more test data become available.

The cyclic stress-strain model for concrete in CCFTs is summarized below.

*6.3.3.2 Terminology*

The cyclic stress-strain history consists of unloading curves and reloading curves. The unloading curves are defined as the paths that concrete experiences when its strain reduces. The unloading paths can be further divided into envelope unloading paths (i.e. unloading paths starting from the envelope curve) and internal unloading paths (i.e. the previous reloading path does not reach the envelope curve). They should be both independent of the subsequent terminating point. However, internal unloading paths are dependent on the prior loading history. The stress and strain where an unloading curve starts are named the unloading stress $\sigma_{un}$ and the unloading strain $\varepsilon_{un}$ respectively. For envelope unloading, the two terms are denoted by $\sigma_{un,env}$ and $\varepsilon_{un,env}$ respectively. The strain value at the intersection of an unloading path and the strain axis is defined as the plastic strain $\varepsilon_{pl}$ .The reloading curves are defined as the paths that concrete experiences when its strain increases. Similar to unloading paths, reloading paths are also independent on the subsequent terminating point where the concrete once again starts to unload or the concrete reaches the envelope curve. The stress and strain where a reloading curve starts are named the reloading stress $\sigma_{re}$ and the reloading strain $\varepsilon_{re}$ respectively. The stress and strain where a reloading curve meets with the corresponding envelope curve are referred as envelope returning stress $\sigma_{ret,env}$ and strain $\varepsilon_{ret,env}$ respectively.

The internal cycles which are defined as those repeated within the envelope curve need to be numbered so that the effects resulting from previous internal cycles on subsequent cycles can be considered. Envelope unloading is always regarded as the first cycle (i.e. $n = 1$). When the subsequent unloading stress is not greater than the present envelope unloading stress $\sigma_{un,env}$, the cycle number needs to be updated (i.e. $n = n + 1$). The number will be reset to zero when a subsequent unloading stress is greater than this envelope unloading stress $\sigma_{un,env}$. It is possible to encounter an unloading stress which is larger than the corresponding envelope unloading stress $\sigma_{un,env}$ but is smaller than the envelope returning stress $\sigma_{ret,env}$. Unloading from such an unloading stress is treated as an envelope unloading cycle in the present model following Lam and Teng (2009).

The definitions of $\sigma_{un}$, $\varepsilon_{un}$, $\sigma_{un,env}$, $\varepsilon_{un,env}$, $\varepsilon_{pl}$, $\sigma_{re}$, $\varepsilon_{re}$, $\sigma_{ret,env}$ and $\varepsilon_{ret,env}$ in both envelope and internal cycles are illustrated in Figure 6.14.

*6.3.3.3* *Envelope curve*

The analysis-oriented stress-strain model presented in Chapter 5 with the revised lateral strain equation (Eq. 5.17) (i.e. Model II) is adopted to predict the envelope curve. The predictions are compared with the experimental curves in Figure 6.7 & 6.8. In making the predictions shown in Figures 6.7 & 6.8, the ultimate axial strain was determined using the average ultimate hoop rupture strain for specimens CFT-3G-102-B1 and CFT-4G-202-B1 for series 3G-102 and series 4G-202 respectively. The comparison of the test ultimate axial strains and the predicted ultimate axial strains for all the specimens using their respective average ultimate hoop rupture strains are shown in Figure 6.15. It can be concluded that the proposed model can predict both the envelope stress-strain curve and the ultimate state reasonably closely.

It should be noted that different from the monotonic stress-strain model used in Lam and Teng (2009) which is a design-oriented model and adopts closed-form equations to express the stress-strain curve, the monotonic model used in the present study is an analysis-oriented model and requires an incremental procedure to produce the stress-strain curve. This leads to some differences in the generation of cyclic stress-strain curves (particularly the reloading path) which are elaborated later in this section.

*6.3.3.4* *Plastic strain*

Lam and Teng (2009) proposed the following equations for predicting the plastic strain:

$$\varepsilon_{pl,1} = \begin{cases} 0, & 0 < \varepsilon_{un,env} \le 0.001 \\ [1.4(0.87 - 0.004 f_{co}^{'}) - 0.64](\varepsilon_{un,env} - 0.001), & 0.001 < \varepsilon_{un,env} \le 0.0035 \\ (0.87 - 0.004 f_{co}^{'})\varepsilon_{un,env} - 0.0016 & 0.0035 < \varepsilon_{un,env} \le \varepsilon_{cu} \end{cases} \tag{6.2}$$

$$\varepsilon_{pl,n} = (1 - \omega_n)\varepsilon_{un,n} + \omega_n \varepsilon_{pl,n-1} \qquad n \ge 2 \tag{6.3}$$

$$\omega_n = \min \begin{cases} 1 \\ \omega_{n,ful} - 0.25(\gamma_{re,n-1} - 1) \end{cases} \tag{6.4}$$

$$\omega_{n,ful} = \begin{cases} 1 & 0 < \varepsilon_{un,env} \le 0.001 \\ 1 + 400(0.0212 n_e - 0.12)(\varepsilon_{un,env} - 0.001) & 0.001 < \varepsilon_{un,env} \le 0.0035 \\ 0.0212 n_e + 0.88 & 0.0035 < \varepsilon_{un,env} \le \varepsilon_{cu} \end{cases} \tag{6.5}$$

$$\gamma_{re,n} = \frac{\varepsilon_{un,n+1} - \varepsilon_{pl,n}}{\varepsilon_{ref,n} - \varepsilon_{pl,n}} \tag{6.6}$$

in which $\varepsilon_{pl,1}$ and $\varepsilon_{pl,n}$ are the plastic strain in the first unloading cycle and the subsequent unloading cycles from an envelope unloading strain $\varepsilon_{un,env}$; $f_{co}^{'}$ is the unconfined concrete cylinder strength; $\varepsilon_{cu}$ is the ultimate axial strain; $\omega_n$ is defined as the strain recovery ratio; $\omega_{n,ful}$ is the strain recovery ratio for the case of $\gamma_{re,n-1}=1$ in which $\gamma_{re,n}$ is defined as the partial reloading factor; $\varepsilon_{ref,n}$ is the reference strain and is discussed in detail in Section 6.3.3.6; and $n_e$ is defined as the number of effective cycles.

*6.3.3.5 New stress*

The new stress on a reloading path at the reference strain can be found from (Lam and Teng 2009):

$$\sigma_{new,n}=\varphi_n\sigma_{ref,n} \tag{6.7}$$

$$\varphi_1=\begin{cases} 1 & 0<\varepsilon_{un,env}\leq 0.001 \\ 1-80(\varepsilon_{un,env}-0.001) & 0.001<\varepsilon_{un,env}\leq 0.002 \\ 0.92 & 0.002<\varepsilon_{un,env}\leq \varepsilon_{cu} \end{cases} \tag{6.8}$$

$$\beta_{un,n}=\begin{cases} \dfrac{\sigma_{un,env}-\sigma_{re,n}}{\sigma_{un,env}} & n=1 \\ \dfrac{\sigma_{un,n}-\sigma_{re,n}}{\sigma_{new,n-1}} & n\geq 2 \end{cases} \tag{6.9}$$

$$\varphi_n=\min\begin{cases} 1 \\ \varphi_{n,ful}-0.2(\beta_{un,n}-1) \end{cases} \qquad n\geq 2 \tag{6.10}$$

$$\varphi_{n,ful}=\begin{cases} 1 \\ 1+1000(0.013n_e-0.075)(\varepsilon_{un,env}-0.001) \\ 0.013n_e+0.925 \end{cases} \tag{6.11}$$

$$\begin{matrix} 0<\varepsilon_{un,env}\leq 0.001 \\ 0.001<\varepsilon_{un,env}\leq 0.002 \quad n\geq 2 \\ 0.002<\varepsilon_{un,env}\leq\varepsilon_{cu} \end{matrix}$$

in which, $\sigma_{new,n}$ is the new stress at the reference strain $\varepsilon_{ref,n}$; $\sigma_{ref,n}$ is the reference stress; $\varphi_1$ is the stress deterioration ratio for the cycle which is unloaded from the envelope curve. $\sigma_{un,env}$ is the envelope unloading stress; $\sigma_{un,n}$ and $\sigma_{re,n}$ are stresses at the starting point and the terminating point of the unloading curve respectively; $\varphi_n$ and $\varphi_{n,ful}$ are the stress deterioration ratio and its value for the case of $\beta_{un}=1$, where $\beta_{un}$ is defined as the partial unloading factor. The definition of the new stress $\sigma_{new,n}$ is clearly shown in Figure 6.14, while the reference stress $\sigma_{ref,n}$ is discussed in detail in Section 6.3.3.6.

*6.3.3.6 Reference strain point*

The reference strain point is defined by the following equations:

$$\begin{aligned} \varepsilon_{ref,1} &= \varepsilon_{un,env} \\ \sigma_{ref,1} &= \sigma_{un,env} \end{aligned} \tag{6.12}$$

$$\begin{aligned} &\varepsilon_{ref,n} = \max(\varepsilon_{ref,n-1}, \varepsilon_{un,n}) \\ &\sigma_{ref,n} = \begin{cases} \sigma_{new,n-1} & \varepsilon_{un,n} \le \varepsilon_{ref,n-1} \\ \sigma_{un,n} & \varepsilon_{un,n} > \varepsilon_{ref,n-1} \end{cases} \end{aligned} \qquad n > 2 \tag{6.13}$$

*6.3.3.7 Criterion for effective cycles*

Lam and Teng (2009) specified that an effective unloading/reloading cycle should satisfy the following conditions:

$$\beta_{un} \ge 0.7 \quad \text{and} \quad \gamma_{re} \ge 0.7 \tag{6.14}$$

*6.3.3.8 Unloading path*

The unloading curves are defined as the paths that the concrete experiences when its strain reduces. The following equations (Eqs. 6.15-6.20) proposed by Lam and Teng (2009) for both internal and envelope unloading are adopted in the present model:

$$\sigma_c = a\varepsilon_{x,c}^{\eta} + b\varepsilon_{x,c} + c \tag{6.15}$$

$$a = \frac{\sigma_{un} - E_{un,0}(\varepsilon_{un} - \varepsilon_{pl})}{\varepsilon_{un}^{\eta} - \varepsilon_{pl}^{\eta} - \eta\varepsilon_{pl}^{\eta-1}(\varepsilon_{un} - \varepsilon_{pl})} \tag{6.16}$$

$$b = E_{un,0} - \eta\varepsilon_{pl}^{\eta-1}a \tag{6.17}$$

$$c = -a\varepsilon_{pl}^{\eta} - b\varepsilon_{pl} \tag{6.18}$$

$$\eta = 350\varepsilon_{un} + 3 \tag{6.19}$$

$$E_{un,0} = \min\begin{cases} \dfrac{0.5 f_{co}^{'}}{\varepsilon_{un}} \\ \dfrac{\sigma_{un}}{\varepsilon_{un} - \varepsilon_{pl}} \end{cases} \tag{6.20}$$

in which, $\sigma_c$ and $\varepsilon_{x,c}$ are the axial stress and strain of concrete; and $E_{un,0}$ is the slope of the unloading path at zero stress (Figure 6.14).

*6.3.3.9* <u>*Reloading path*</u>

The expressions for the linear reloading portion are as follows:

$$\sigma_c = \sigma_{re} + E_{re}(\varepsilon_{x,c} - \varepsilon_{re}) \quad (\varepsilon_{re} \le \varepsilon_{x,c} \le \varepsilon_{ref}) \tag{6.21}$$

where the slope of the linear portion $E_{re}$ is found from:

$$E_{re} = (\sigma_{new} - \sigma_{re}) / (\varepsilon_{ref} - \varepsilon_{re}) \;\; (\varepsilon_{re} \le \varepsilon_{x,c} \le \varepsilon_{ref}) \tag{6.22}$$

In most cases, this linear portion is followed by a parabola portion from the reference strain point to the envelope returning point. The determination of the parabola portion is described in the next paragraph. In some cases, however, the reloading path consists of only a straight line that returns to the envelope curve directly at the envelope unloading point, i.e. $\varepsilon_{ret,env} = \varepsilon_{un,env}$. These cases are (1) $\varepsilon_{un,env} < 0.001$ ; (2) $n = 1$; $\varepsilon_{un,env} > 0.001$; $\sigma_{re,1} > 0.85\sigma_{un,env}$ ; and (3) $n > 1$; $\varepsilon_{un,env} > 0.001$; $\sigma_{re,n} > 0.85\sigma_{un,env}$.

As the concrete envelope curve cannot be explicitly expressed in the present study, a trial and error process is involved in order to evaluate the parabolic portion in the reloading path. An initial return envelope strain is determined by assuming a straight line for the whole reloading path (i.e. this initial envelope return strain is the intersection point of the extended line of the first linear portion and the envelop curve). As long as this initial value is found, the slope of the envelope curve at that envelope return strain can be determined by the central difference method. A small value of strain difference $\Delta\varepsilon_x$ is assumed first. A good value could be $10^{-3}$ of the return envelope strain. The envelope stresses corresponding to the strains $\left[\varepsilon_{ret,env} - (1/2)\Delta\varepsilon_x\right]$ and $\left[\varepsilon_{ret,env} + (1/2)\Delta\varepsilon_x\right]$ can then be found. The slope $E_{ret,env}$ at the envelope return strain is then simply calculated to be the ratio of the stress difference over the strain difference. The constants $A_2$, $B_2$ and $C_2$ can then be determined by:

$$A_2 = \frac{(E_{re} - E_{ret,env})^2}{4\left[\sigma_{new} - (\sigma_{ret,env} - E_{ret,env}\varepsilon_{ret,env}) - E_{ret,env}\varepsilon_{ref}\right]} \tag{6.23}$$

$$B_2 = E_{re} - 2A_2\varepsilon_{ref} \tag{6.24}$$

$$C_2 = \sigma_{new} - A_2\varepsilon_{ref}{}^2 - B_2\varepsilon_{ref} \tag{6.25}$$

Once these constants are determined, the new envelope return strain can be determined using:

$$\varepsilon_{ret,env} = \frac{E_{ret,env} - B_2}{2A_2} \tag{6.26}$$

If the difference of the new calculated envelope strain and the assumed one are not sufficiently close (i.e. the difference being greater than $10^{-3}$ of the assumed return envelope strain), the iteration process is continued by using the new calculated envelope strain as the assumed strain; otherwise the trial and error process is terminated. The stress-strain relationship for the parabolic reloading path can then be determined using:

$$\sigma_c = A_2\varepsilon_{x,c}{}^2 + B_2\varepsilon_{x,c} + C_2 \quad (\varepsilon_{ref} \le \varepsilon_{x,c} \le \varepsilon_{ret,env}) \tag{6.27}$$

### 6.3.4 Generation of Cyclic Stress-Strain Curves

The step-by-step process of generating stress–strain curves for confined concrete in CCFTs under cyclic compression using the model presented above is summarized in Figure 6.16.

### 6.3.5 Comparison with Test Results

The predicted cyclic stress-strain curves of concrete using the model presented above are compared with the present test results in Figures 6.17 & 6.18. The unloading and reloading strains in the experimental curves were adopted as the input data for the corresponding predictions. The predicted curves terminate when the hoop strain reaches the rupture value in the test.

It is evident from Figures 6.17 & 6.18 that the proposed cyclic stress-strain model can provide reasonably accurate predictions of the test results. It is also noted that there are some small discrepancies between the predicted and the experimental curves: in some unloading paths, the predicted curve is slightly lower than the experimental curve. As explained earlier, the determination of experimental stress-strain curves of concrete involved the deduction of the load taken by the steel tube from the total load taken by the specimen; the load taken by the steel tube was obtained using Eqs. 5.8-5.12 & 5.14-5.17 which assume a bilinear hysteretic stress-strain curve for steel (Figure 6.19). This process ignores the well-known Bauschinger effect [Figure 6.20; (Monti and Nuti 1992; Gomes and Appleton 1997)] in the cyclic behaviour of steel, and thus leads to an overestimation of the steel tensile stress when the steel is approaching tensile yielding (Figure 6.20) and in turn an overestimation of the compressive stress in the concrete. Therefore, the “actual” experimental stress-strain curves of concrete should be somewhat lower than the curves shown in Figures 6.17 & 6.18, and should be in closer agreement with the predictions.

## 6.4 CONCLUSIONS

This chapter has been concerned with the behaviour and modelling of FRP-confined concrete-filled steel tubular columns subjected to axial cyclic compression. Results from two series of axial cyclic compression tests on CCFTs have been presented and discussed. A cyclic stress-strain model for the confined concrete in CCFTs has also been proposed and has been shown to compare well with the present test results. The following conclusions can be drawn from the study presented in this chapter:

1. The test specimens subjected to axial cyclic compression all failed by explosive rupture of the FRP jacket in the mid-height region, in a manner similar to that of their counterparts tested under axial monotonic compression.

2. The stress-strain curve of the confined concrete in CCFTs under axial monotonic compression can be taken as the envelope curve for the stress-strain history of the confined concrete in an identical specimen subjected to cyclic axial compression.

3. For a CCFT column subjected to cyclic compression, when the load carried by the CCFT column is reduced to zero, the axial strain of the column is normally larger than the plastic strain of the concrete and smaller than the plastic strain of the steel tube.

4. Repeated unloading/reloading cycles have a cumulative effect on the plastic strain and stress deterioration of concrete, so the uniqueness concept of cyclic stress-strain responses is invalid.

5. The envelope curve, unloading/reloading responses and plastic strain of the concrete in CCFTs can be closely predicted by the proposed cyclic stress-strain model.

6. Further research is needed to refine the proposed cyclic stress-strain model, in particular, in the definition of effective unloading/reloading cycles.

Table 6.1 Specimen details

| ***Specimen*** | $D_{outer}$ ***(mm)*** | $t_s$ ***(mm)*** | $l_{col}$ ***(mm)*** | $D_{outer}/t_s$ | $f_y$ ***(MPa)*** | $f'_{co}$ ***(MPa)*** | $t_{frp}$ ***(mm)*** |
|---|---|---|---|---|---|---|---|
| **CFT-3G-102-B1**<br>**CFT-3G-102-B2**<br>**CFT-3G-102-C** | 204 | 2 | 400 | 102 | 226 | 45.6 | 0.54 |
| **CFT-4G-202-B1**<br>**CFT-4G-202-B2**<br>**CFT-4G-202-C**<br>**CFT-4G-202-D** | 202 | 1 | 400 | 202 | 231 | 37.1 | 0.68 |

Table 6.2 Properties of concrete

| ***Series*** | $E_c$ ***(GPa)*** | $f'_{co}$ ***(MPa)*** | $\varepsilon_{co}$ |
|---|---|---|---|
| **CFT-3G-102** | 28.2 | 45.6 | 0.002344 |
| **CFT-4G-202** | 27.1 | 36.1 | 0.002338 |

Table 6.3 Summary of key test and predicted results

| ***Specimen*** | $N_u$ ***(kN)*** | $\Delta_u$ ***(mm)*** | $\Delta_{u,pre}$ ***(mm)*** | $\varepsilon_{rupt}$ | $\varepsilon_{rupt,\max}$ |
|---|---|---|---|---|---|
| **CFT-3G-102-A** | 1593 | 9.43 | 9.21 | 0.0188 | 0.0228 |
| **CFT-3G-102-B1** | 1719 | 8.37 | 7.92 | 0.0181 | 0.0197 |
| **CFT-3G-102-B2** | | 7.53 | 8.57 | 0.0191 | 0.0205 |
| **CFT-3G-102-C** | | 8.16 | 7.21 | 0.0162 | 0.0201 |
| **CFT-4G-202-A** | 1283 | 8.68 | 10.98 | 0.0191 | 0.0215 |
| **CFT-4G-202-B1** | 1311 | 9.45 | 11.36 | 0.0206 | 0.0237 |
| **CFT-4G-202-B2** | | 10.15 | 11.73 | 0.0213 | 0.0227 |
| **CFT-4G-202-C** | | 9.47 | 10.22 | 0.0189 | 0.0202 |

Table 6.4 Summary of test and predicted plastic strains and new stresses for series CFT-3G-102

| *Specimen* | *Unloading point* | *Cycle No.* | $\varepsilon_{pl,\exp}$ | $\varepsilon_{pl,pre}$ | $\varepsilon_{pl,pre} / \varepsilon_{pl,\exp}$ | $\sigma_{new,\exp}$ | $\sigma_{new,pre}$ | $\sigma_{new,pre} / \sigma_{new,\exp}$ |
|---|---|---|---|---|---|---|---|---|
| **CFT-3G-102-B1** | 1 | 1 | 0.00014 | 0.00009 | 0.62 | 31.9 | 32.6 | 1.02 |
| | 2 | 2 | 0.00035 | 0.00070 | 1.98 | 51.9 | 52.0 | 1.00 |
| | 3 | 3 | 0.00285 | 0.00256 | 0.90 | 57.4 | 62.0 | 1.08 |
| | 4 | 4 | 0.00517 | 0.00444 | 0.86 | 63.3 | 65.4 | 1.03 |
| | 5 | 5 | 0.00723 | 0.00660 | 0.91 | 64.7 | 67.1 | 1.03 |
| | 6 | 6 | 0.01040 | 0.00875 | 0.84 | 65.2 | 67.1 | 1.02 |
| **CFT-3G-102-B2** | 1 | 1 | 0.00044 | 0.00068 | 1.54 | 52.8 | 52.3 | 0.99 |
| | 2 | 2 | 0.00222 | 0.00254 | 1.14 | 60.7 | 62.0 | 1.02 |
| | 3 | 3 | 0.00537 | 0.00462 | 0.86 | 63.1 | 65.5 | 1.04 |
| | 4 | 4 | 0.00778 | 0.00667 | 0.86 | 63.5 | 62.5 | 0.99 |
| | 5 | 5 | 0.01082 | 0.00888 | 0.82 | 65.7 | 68.3 | 1.04 |
| **CFT-3G-102-C** | 1 | 1 | 0.00043 | 0.00068 | 1.59 | 53.6 | 51.1 | 0.95 |
| | | 2 | 0.00057 | 0.00084 | 1.48 | 49.5 | 49.2 | 0.99 |
| | | 3 | 0.00058 | 0.00095 | 1.63 | 50.0 | 47.7 | 0.95 |
| | 2 | 1 | 0.00247 | 0.00257 | 1.04 | 60.1 | 59.4 | 0.99 |
| | | 2 | 0.00292 | 0.00284 | 0.97 | 58.4 | 57.3 | 0.98 |
| | | 3 | 0.00314 | 0.00302 | 0.96 | 55.4 | 55.6 | 1.01 |
| | 3 | 1 | 0.00506 | 0.00463 | 0.91 | 62.8 | 64.5 | 1.03 |
| | | 2 | 0.00556 | 0.00497 | 0.89 | 60.9 | 62.0 | 1.02 |
| | | 3 | 0.00568 | 0.00520 | 0.92 | 58.6 | 59.9 | 1.02 |
| | 4 | 1 | 0.00763 | 0.00677 | 0.89 | 66.2 | 66.9 | 1.01 |
| | | 2 | 0.00822 | 0.00719 | 0.87 | 63.1 | 64.2 | 1.02 |
| | | 3 | 0.00829 | 0.00747 | 0.90 | 60.2 | 61.8 | 1.03 |
| | 5 | 1 | 0.01062 | 0.00891 | 0.84 | 66.6 | 67.5 | 1.01 |
| | | 2 | 0.01098 | 0.00941 | 0.86 | 63.5 | 64.7 | 1.02 |
| | | 3 | 0.01142 | 0.00974 | 0.85 | 61.1 | 62.3 | 1.02 |

Table 6.5 Summary of test and predicted plastic strains and new stresses for series CFT-4G-202

| ***Specimen*** | ***Unloading point*** | ***Cycle No.*** | $\varepsilon_{pl,\exp}$ | $\varepsilon_{pl,pre}$ | $\varepsilon_{pl,pre} / \varepsilon_{pl,\exp}$ | $\sigma_{new,\exp}$ | $\sigma_{new,pre}$ | $\sigma_{new,pre} / \sigma_{new,\exp}$ |
|---|---|---|---|---|---|---|---|---|
| CFT-4G-202-B1 | 1 | 1 | 0.00019 | 0.00022 | 1.14 | 29.5c | 29.7 | 1.01 |
| | 2 | 2 | 0.00148 | 0.00177 | 1.19 | 45.1 | 46.2 | 1.02 |
| | 3 | 3 | 0.00320 | 0.00419 | 1.31 | 51.5 | 52.0 | 1.01 |
| | 4 | 4 | 0.00651 | 0.00663 | 1.02 | 53.4 | 54.6 | 1.02 |
| | 5 | 5 | 0.00958 | 0.00923 | 0.96 | 59.0 | 60.1 | 1.02 |
| | 6 | 6 | 0.01184 | 0.01174 | 0.99 | 62.5 | 61.5 | 0.99 |
| CFT-4G-202-B2 | 1 | 1 | 0.00024 | 0.00019 | 0.79 | 29.7 | 30.1 | 1.01 |
| | 2 | 2 | 0.00161 | 0.00168 | 1.04 | 46.0 | 45.8 | 1.00 |
| | 3 | 3 | 0.00381 | 0.00407 | 1.07 | 52.6 | 52.6 | 1.00 |
| | 4 | 4 | 0.00657 | 0.00650 | 0.99 | 57.0 | 56.9 | 1.00 |
| | 5 | 5 | 0.00922 | 0.00895 | 0.97 | 60.4 | 63.1 | 1.04 |
| | 6 | 6 | 0.01192 | 0.01150 | 0.96 | 63.5 | 64.2 | 1.01 |

Table 6.5 Summary of test and predicted plastic strains and new stress for series CFT-4G-202 (Continued)

| ***Specimen*** | ***Unloading point*** | ***Cycle No.*** | $\varepsilon_{pl,\exp}$ | $\varepsilon_{pl,pre}$ | $\varepsilon_{pl,pre} / \varepsilon_{pl,\exp}$ | $\sigma_{new,\exp}$ | $\sigma_{new,pre}$ | $\sigma_{new,pre} / \sigma_{new,\exp}$ |
|---|---|---|---|---|---|---|---|---|
| CFT-4G-202-C | 1 | 1 | 0.00116 | 0.00137 | 1.18 | 46.0 | 46.1 | 1.00 |
| | | 2 | 0.00126 | 0.00158 | 1.25 | 41.7 | 44.1 | 1.06 |
| | | 3 | 0.00132 | 0.00172 | 1.30 | 41.8 | 42.4 | 1.01 |
| | 2 | 1 | 0.00347 | 0.00369 | 1.07 | 52.7 | 47.4 | 0.90 |
| | | 2 | 0.00387 | 0.00397 | 1.03 | 50.3 | 45.2 | 0.90 |
| | | 3 | 0.00405 | 0.00416 | 1.03 | 48.8 | 43.3 | 0.89 |
| | 3 | 1 | 0.00645 | 0.00654 | 1.01 | 57.6 | 58.2 | 1.01 |
| | | 2 | 0.00703 | 0.00691 | 0.98 | 54.7 | 55.3 | 1.01 |
| | | 3 | 0.00709 | 0.00715 | 1.01 | 53.2 | 52.6 | 0.99 |
| | 4 | 1 | 0.00942 | 0.00900 | 0.96 | 60.1 | 60.0 | 1.00 |
| | | 2 | 0.00985 | 0.00944 | 0.96 | 57.9 | 57.0 | 0.98 |
| | | 3 | 0.01006 | 0.00973 | 0.97 | 55.7 | 54.1 | 0.97 |
| | 5 | 1 | 0.01329 | 0.01218 | 0.92 | 63.8 | 64.5 | 1.01 |
| | | 2 | 0.01372 | 0.01270 | 0.93 | 61.4 | 61.1 | 0.99 |
| | | 3 | 0.01395 | 0.01306 | 0.94 | 59.6 | 58.0 | 0.97 |
| CFT-4G-202-D | 1 | 1 | 0.00147 | 0.00157 | 1.07 | 47.2 | 47.0 | 1.00 |
| | 2 | 1 | 0.00379 | 0.00393 | 1.03 | 53.8 | 54.3 | 1.01 |
| | | 2 | 0.00398 | 0.00421 | 1.06 | 51.2 | 51.6 | 1.01 |
| | | 3 | 0.00428 | 0.00441 | 1.03 | 49.7 | 49.3 | 0.99 |

Table 6.6 Summary of partial reloading/unloading factors

| ***Specimens*** | ***Unloading point*** | ***Cycle No.*** | $\gamma_{re}$ | $\beta_{un}$ | ***Cumulative effect*** |
|---|---|---|---|---|---|
| CFT-4G-202-D | 3 | 1 | 1 | 0.13 | Yes |
| | | 2 | 1 | 0.18 | Yes |
| | | 3 | 1 | 0.35 | Yes |
| | | 4 | 1 | 0.61 | Yes |
| | | 5 | 1 | 0.81 | Yes |
| | | 6 | 1 | 0.894 | Yes |
| | 4 | 1 | 0.26 | 0.90 | N/A |
| | | 2 | 0.32 | 0.24 | No |
| | | 3 | 0.61 | 0.50 | No |
| | | 4 | 0.80 | 0.70 | Yes |
| | | 5 | 0.91 | 0.78 | Yes |


(a) Series CFT-3G-102


(b) Series CFT-4G-202

Figure 6.1 Specimens after tests

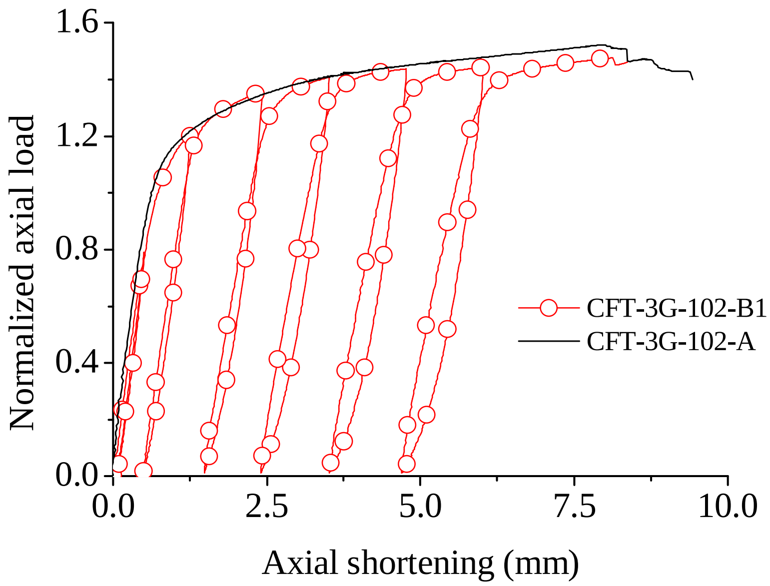


(a) CFT-3G-102-B1

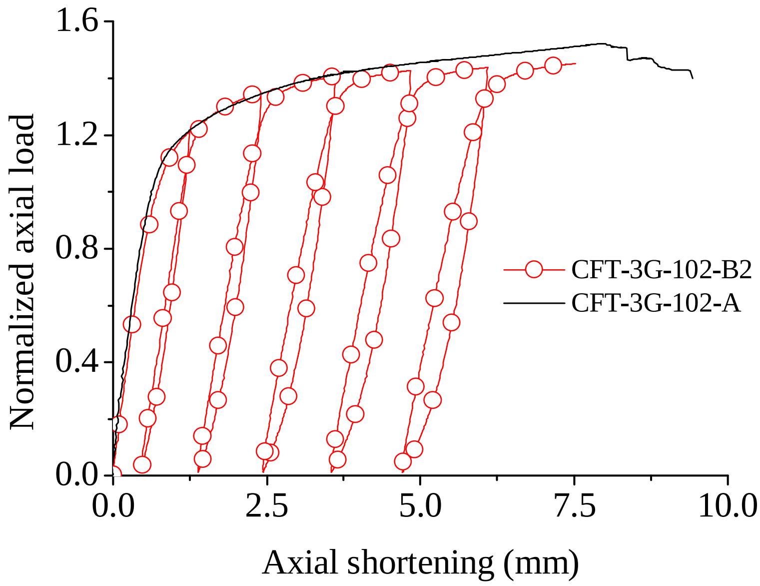


(b) CFT-3G-102-B2

Figure 6.2 Normalized axial load-shortening curves of specimens in series CFT-3G-102

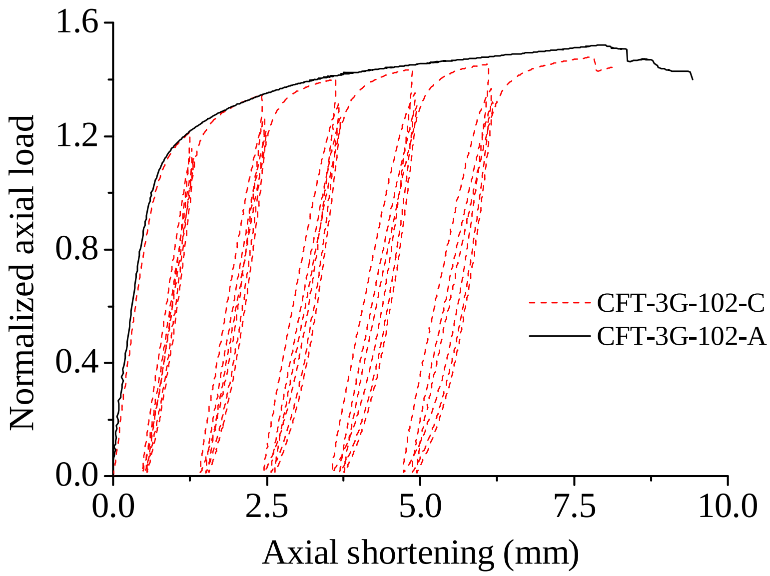


(c) CFT-3G-102-C

Figure 6.2 Normalized axial load-shortening curves of specimens in series CFT-3G-102 (continued)

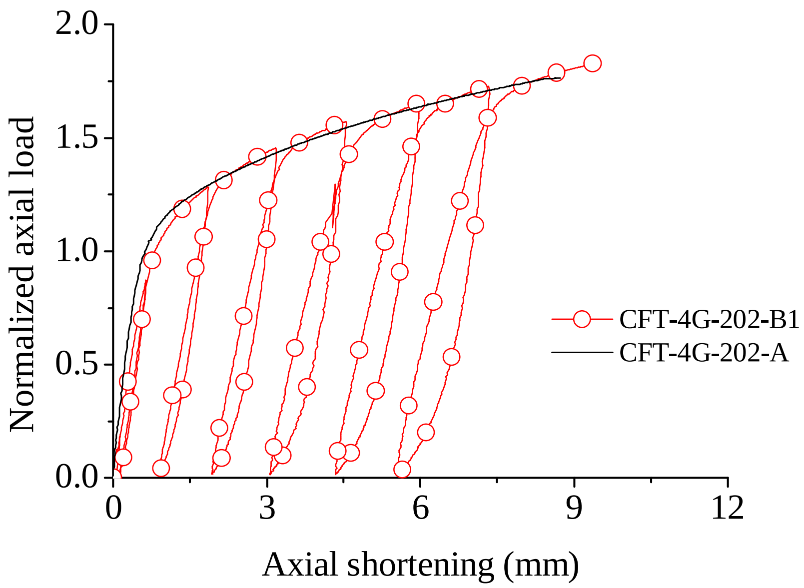


(a) CFT-4G-202-B1

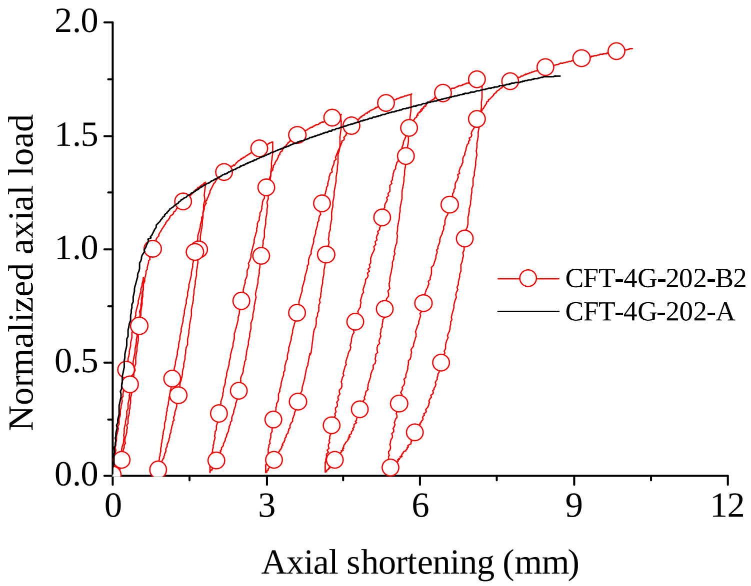


(b) CFT-4G-202-B2

Figure 6.3 Normalized axial load-shortening curves of specimens in series CFT-4G-202

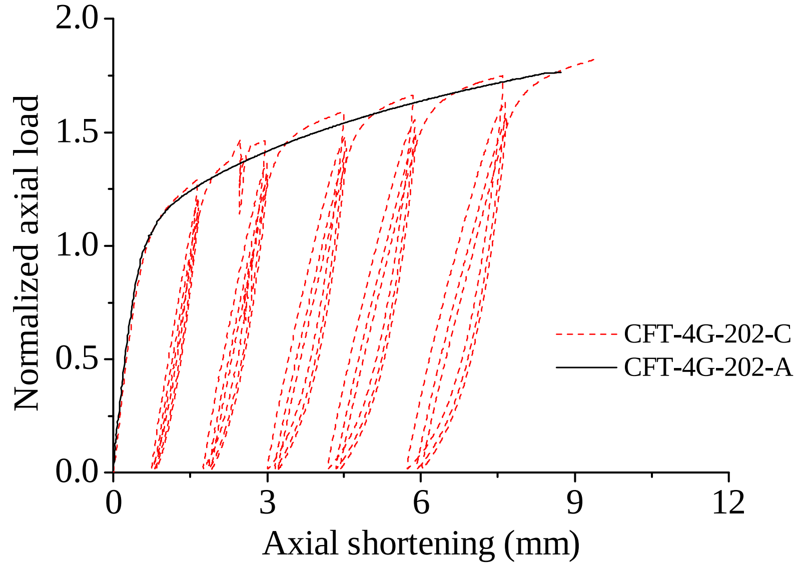


(c) CFT-4G-202-C

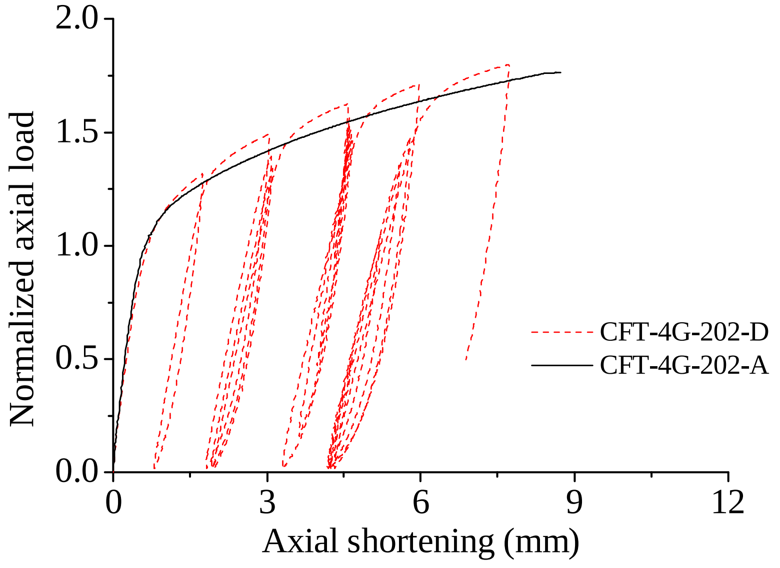


(d) CFT-4G-202-D

Figure 6.3 Normalized axial load-shortening curves of specimens in series CFT-4G-202 (continued)

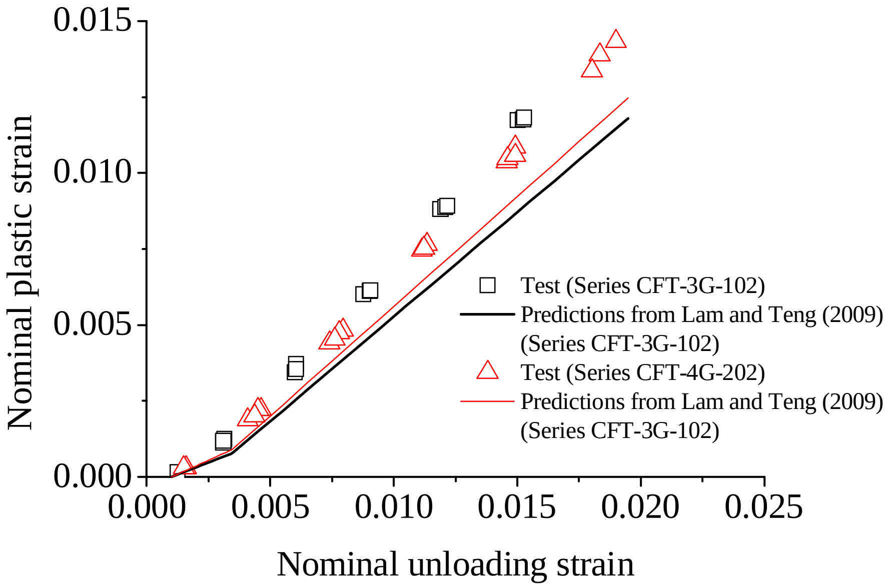


Figure 6.4 Nominal plastic strain versus envelope unloading strains for CCFT columns

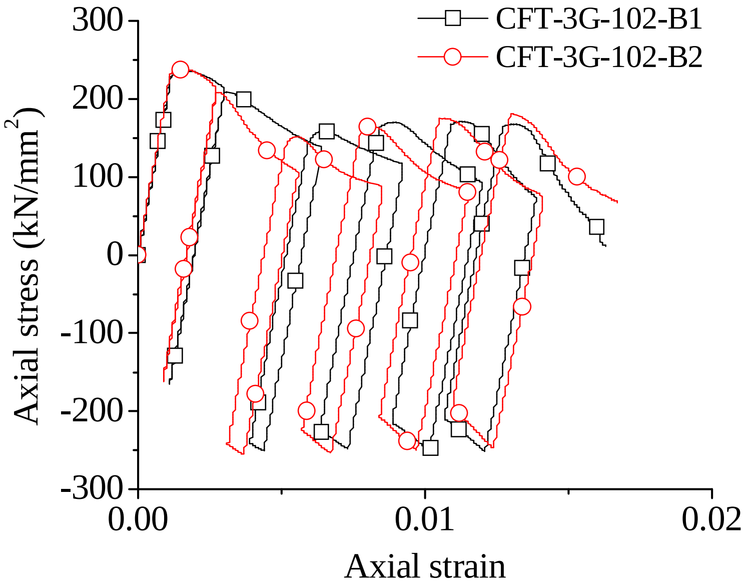


(a) Type B loading

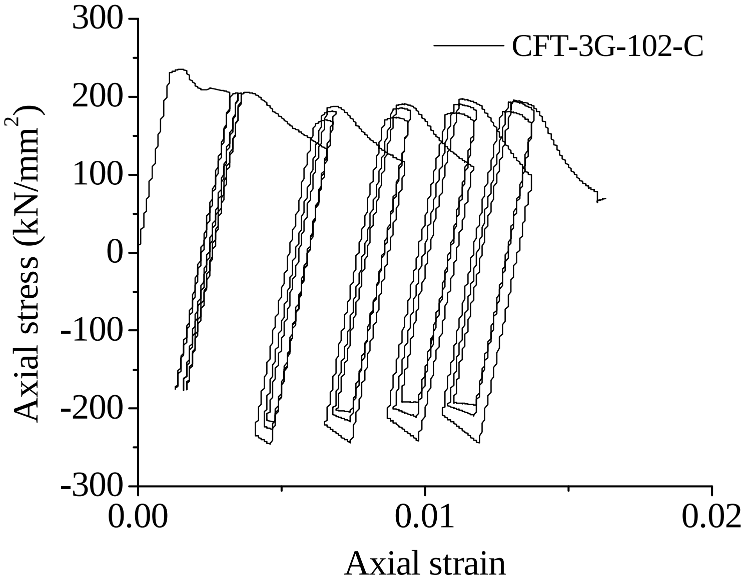


(b) Type C loading

Figure 6.5 Axial stress-strain curves of steel in series CFT-3G-102

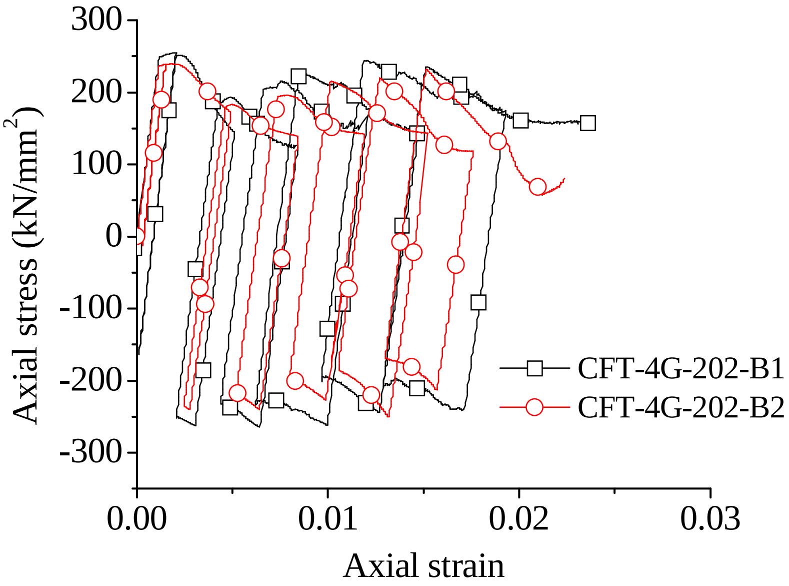


(a) Type B loading

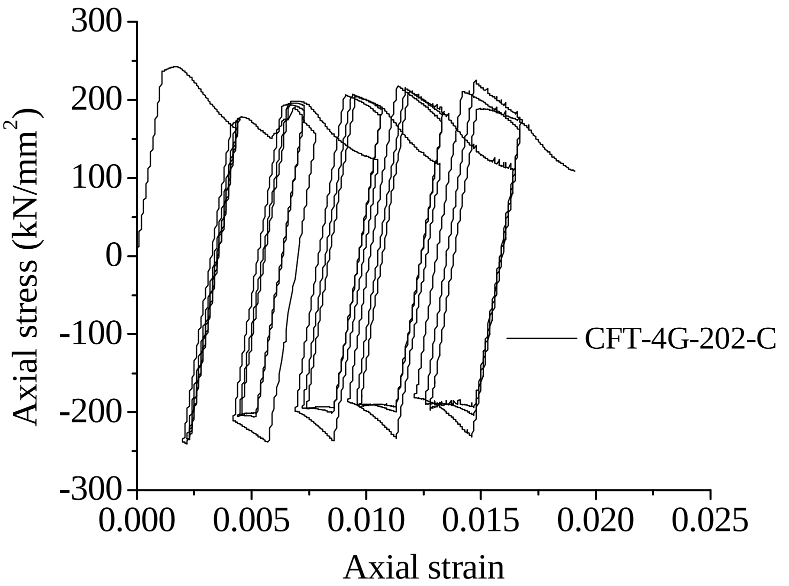


(b) Type C loading

Figure 6.6 Axial stress-strain curves of steel in series CFT-4G-202

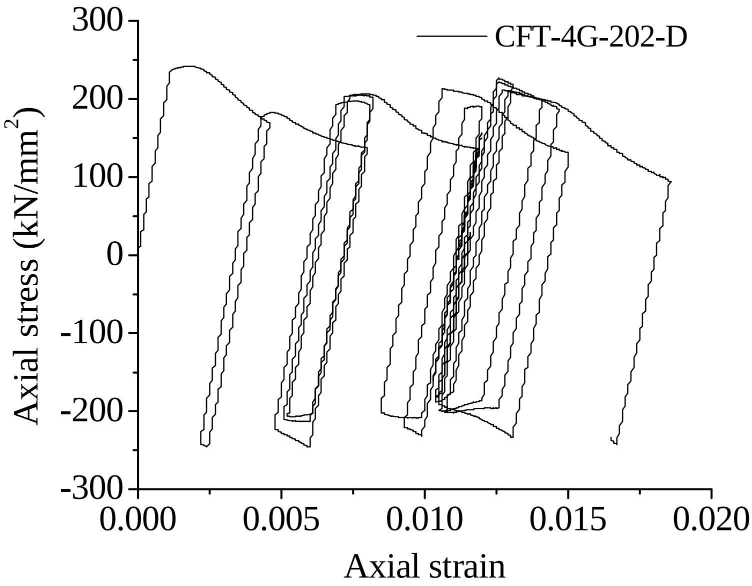


(c) Type D loading

Figure 6.6 Axial stress-strain curves of steel in series CFT-4G-202 (continued)

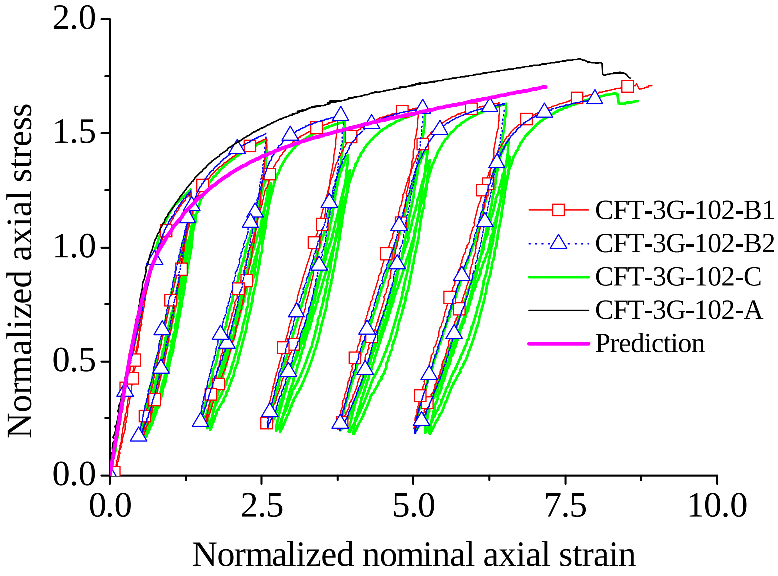


Figure 6.7 Normalize axial stress-strain curves of concrete in series CFT-3G-102

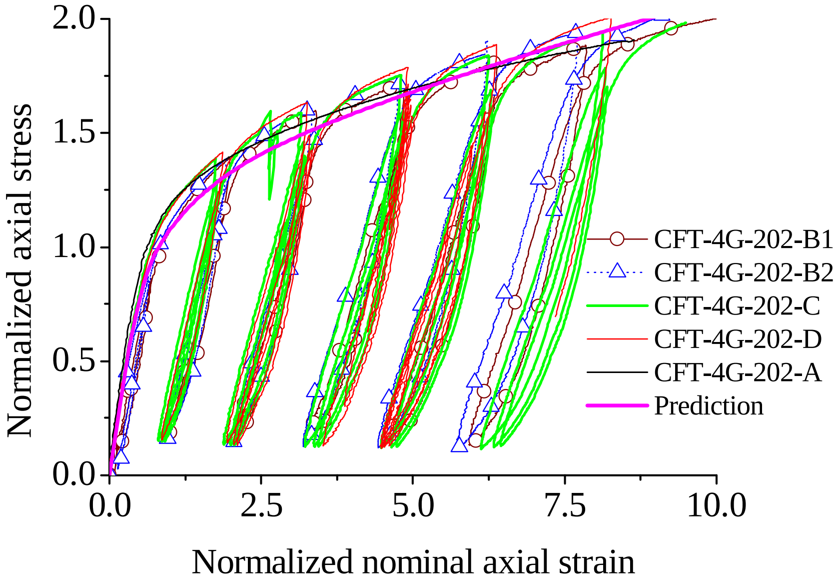


Figure 6.8 Normalized axial stress-strain curves of concrete in series CFT-4G-202

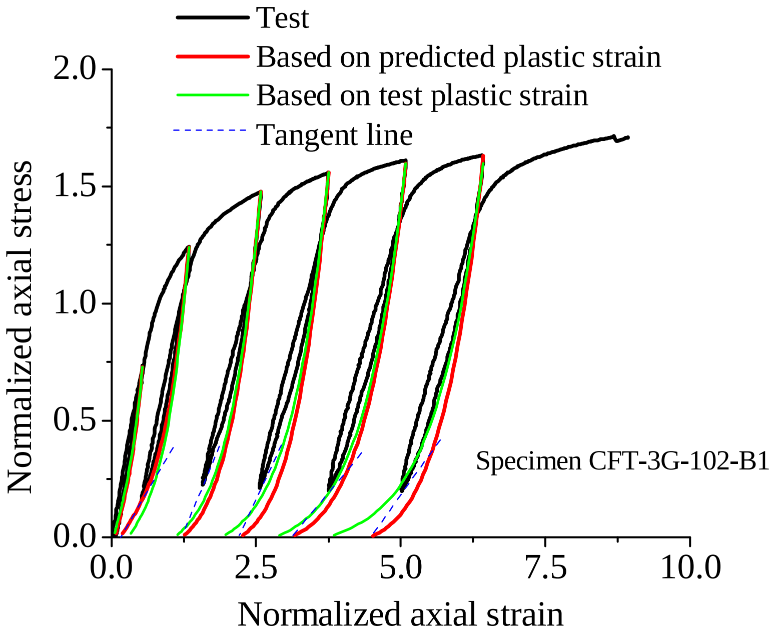


(a) CFT-3G-102-B1

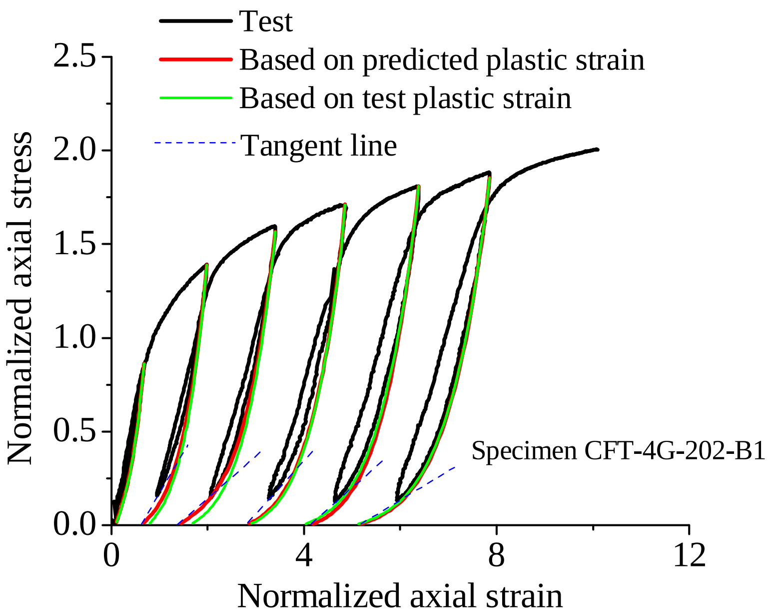


(b) CFT-4G-202-B1

Figure 6.9 Unloading paths of two specimens

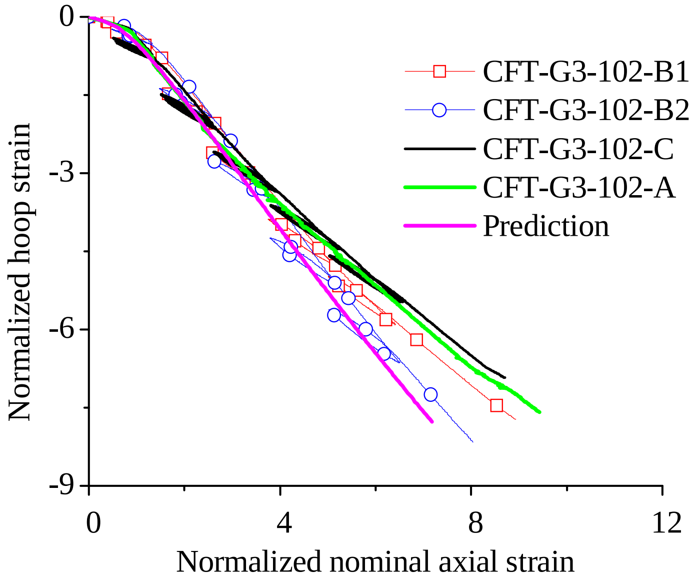


(a) Series CFT-3G-102

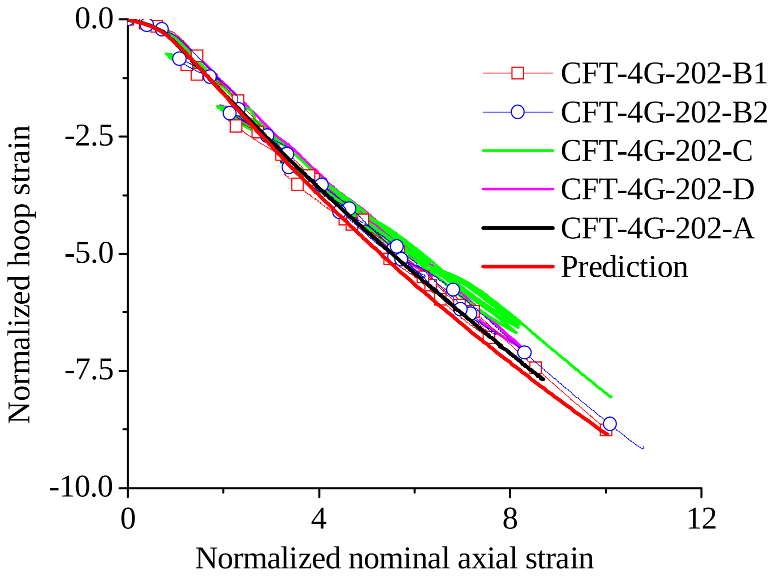


(b) Series CFT-4G-202

Figure 6.10 Normalized hoop strain-axial strain curves of concrete

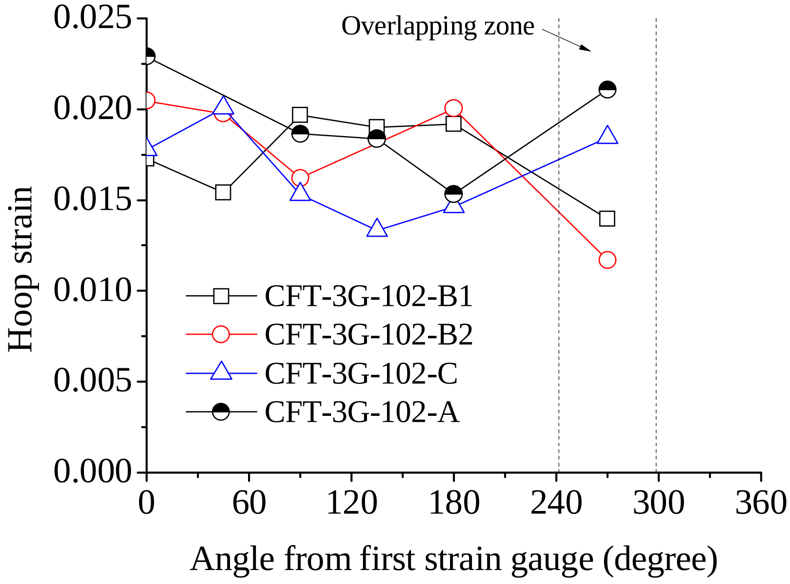


(a) Series CFT-3G-102

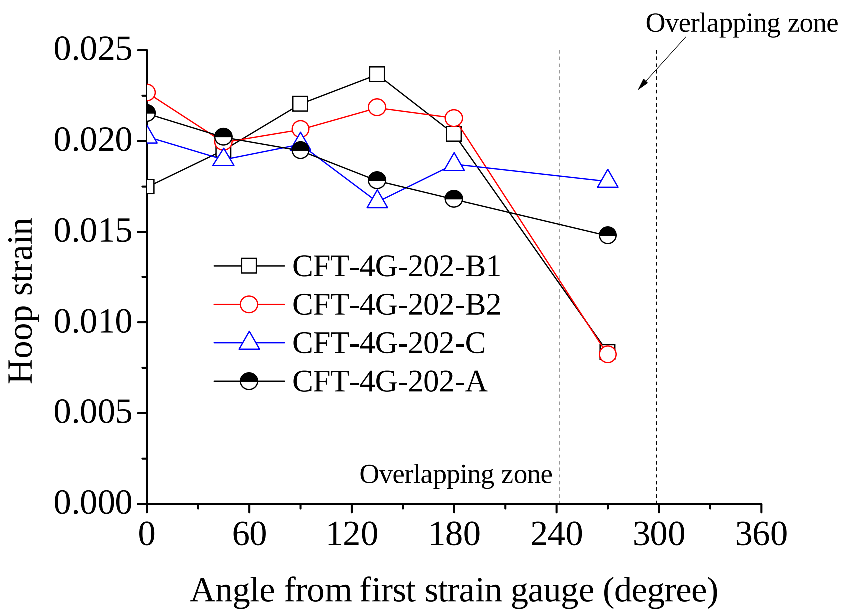


(b) Series CFT-4G-202

Figure 6.11 Ultimate hoop strain distribution at mid-height

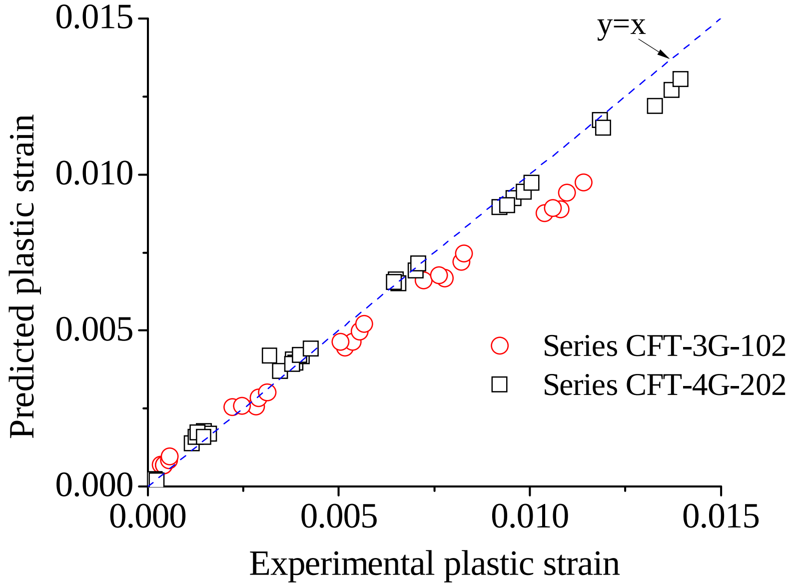


(a) Plastic strains

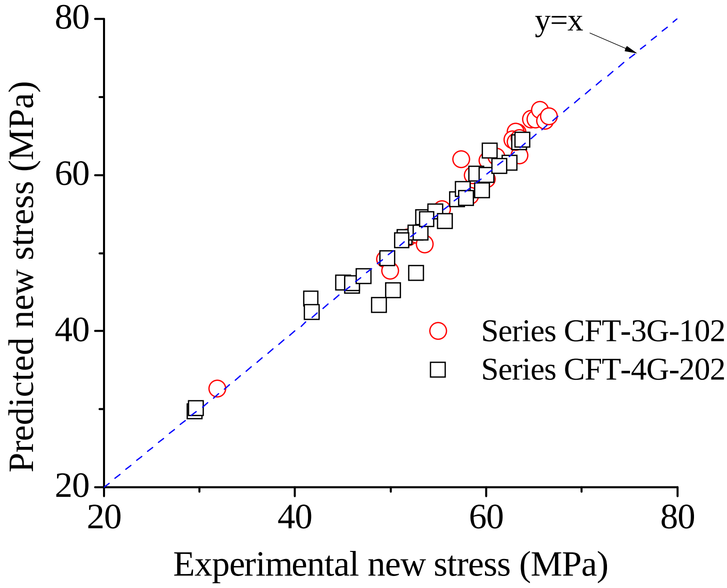


(b) New stress

Figure 6.12 Comparison of test and predicted plastic strains and new stresses

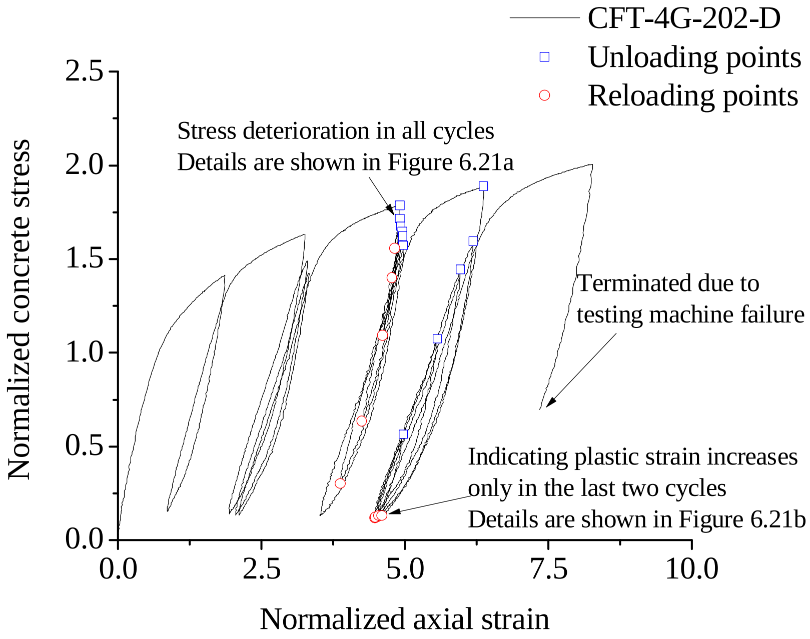


Figure 6.13 Partially unloading/reloading cycles in specimen CFT-4G-202-D

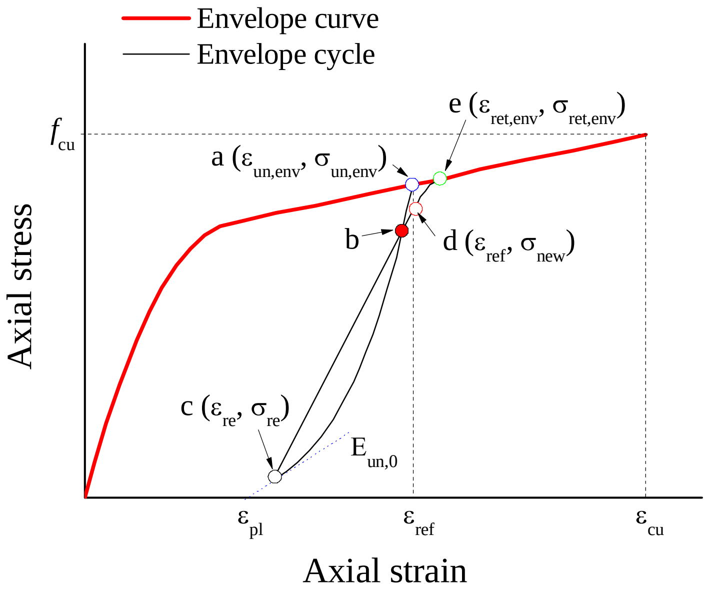


(a) Envelope cycle

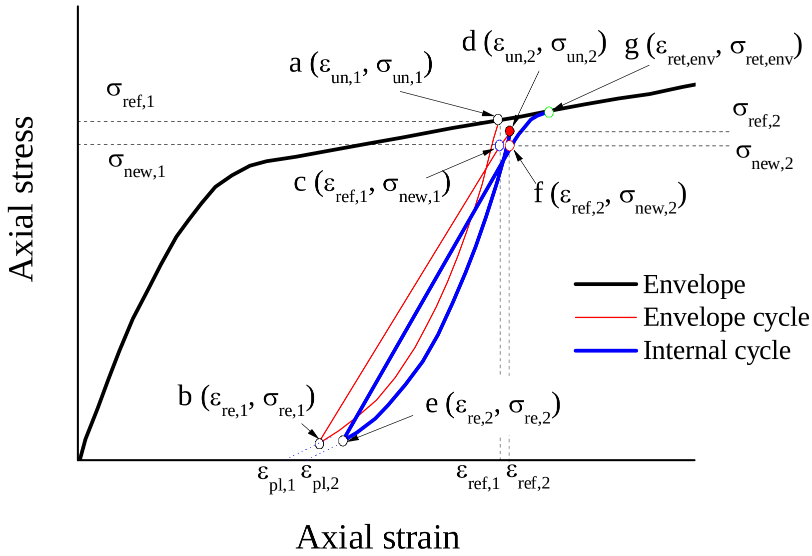


(b) Internal cycles

Figure 6.14 Key parameters of cyclic stress-strain curves of confined concrete [After Lam and Teng (2009)]

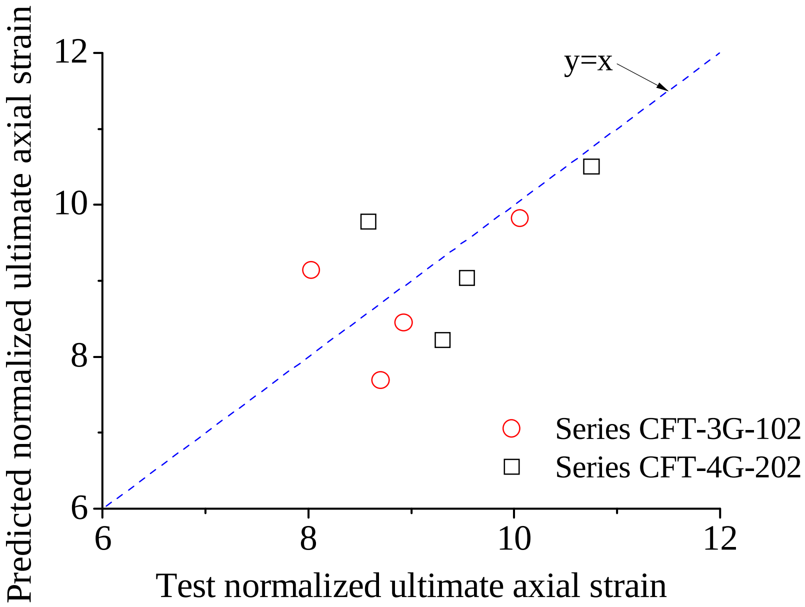


Figure 6.15 Comparison of the predicted and test normalized ultimate axial strain

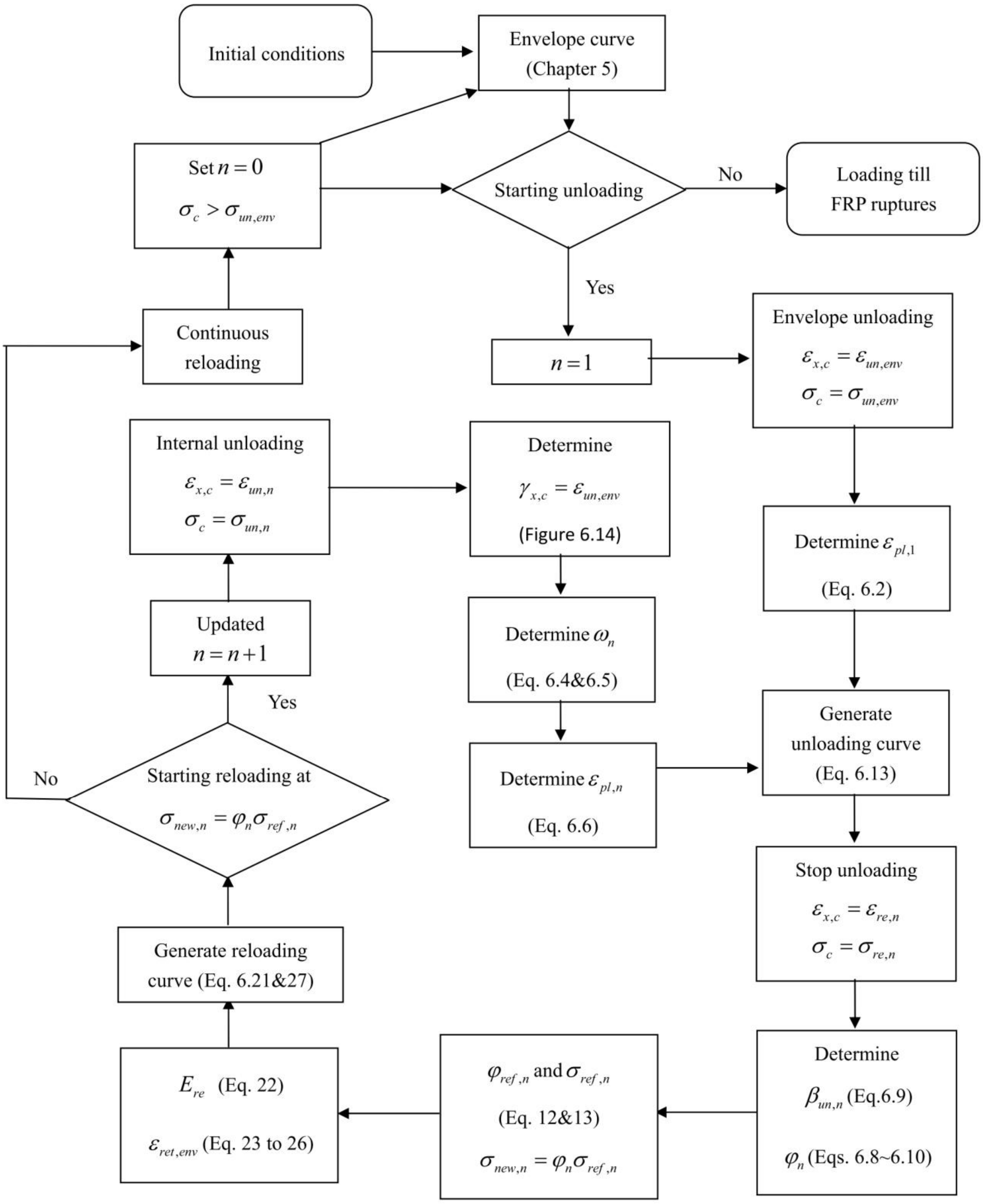


Figure 6.16 Generation of cyclic stress-strain curves

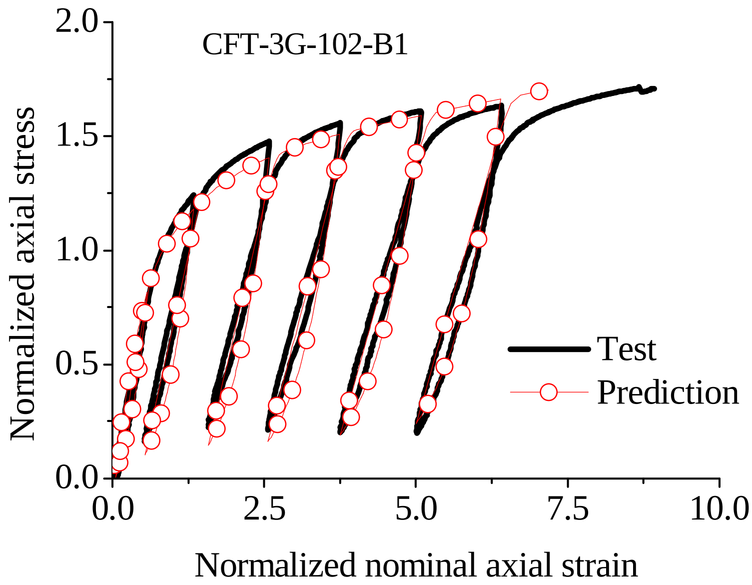


(a) CFT-3G-102-B1

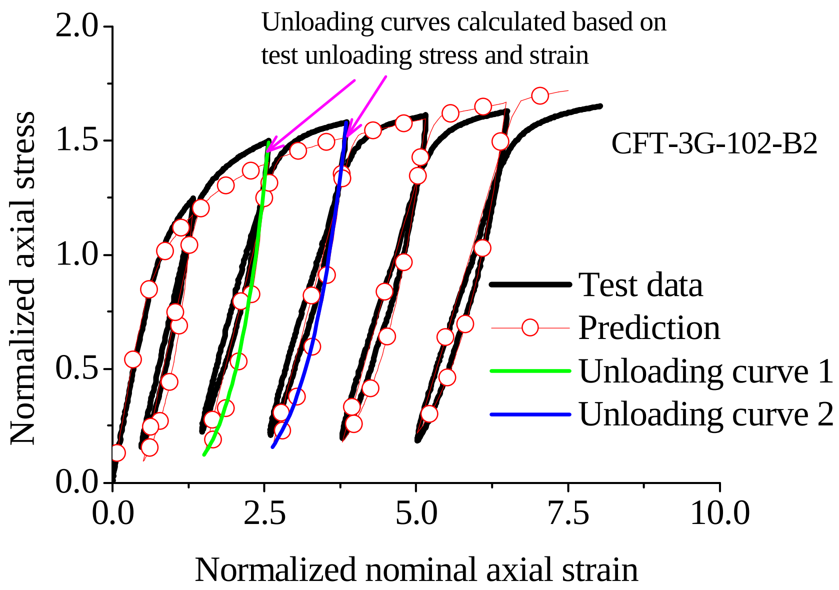


(b) CFT-3G-102-B2

Figure 6.17 Comparison of concrete stress-strain curves for series 102

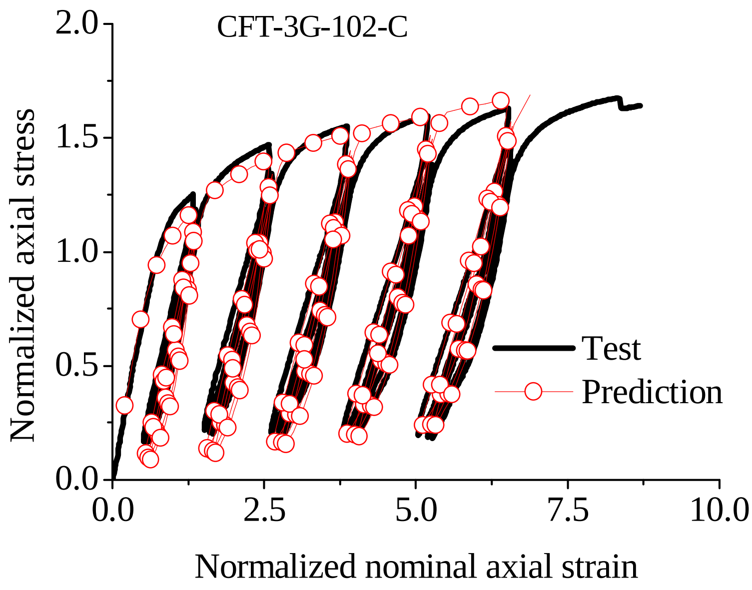


(c) CFT-3G-102-C

Figure 6.17 Comparison of concrete stress-strain curves for series 102 (continued)

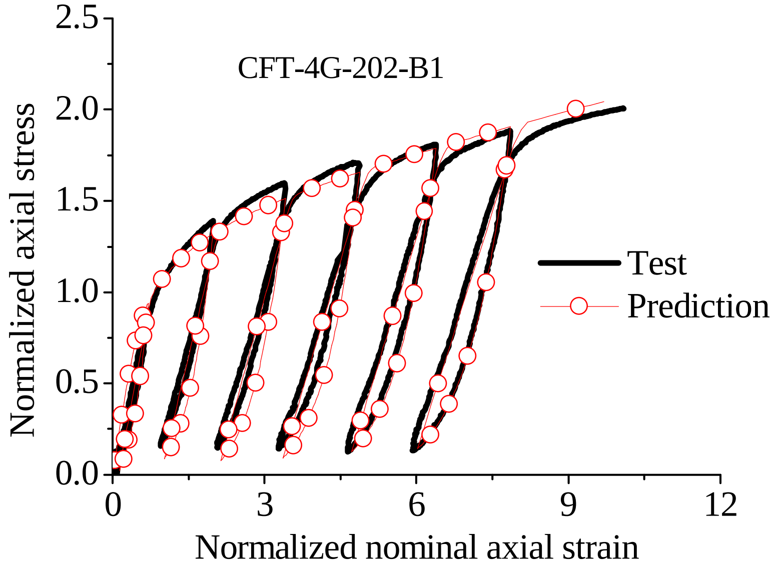


(a) CFT-4G-202-B1

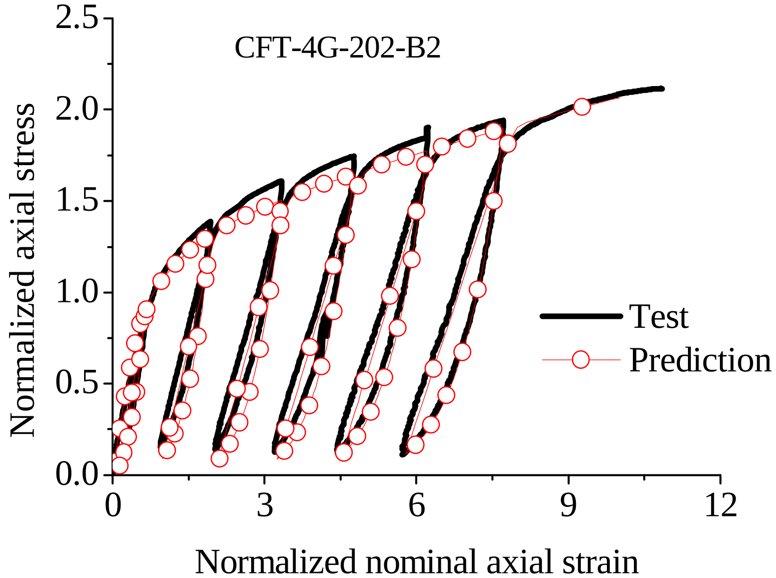


(b) CFT-4G-202-B2

Figure 6.18 Comparison of concrete stress-strain curves for series 202

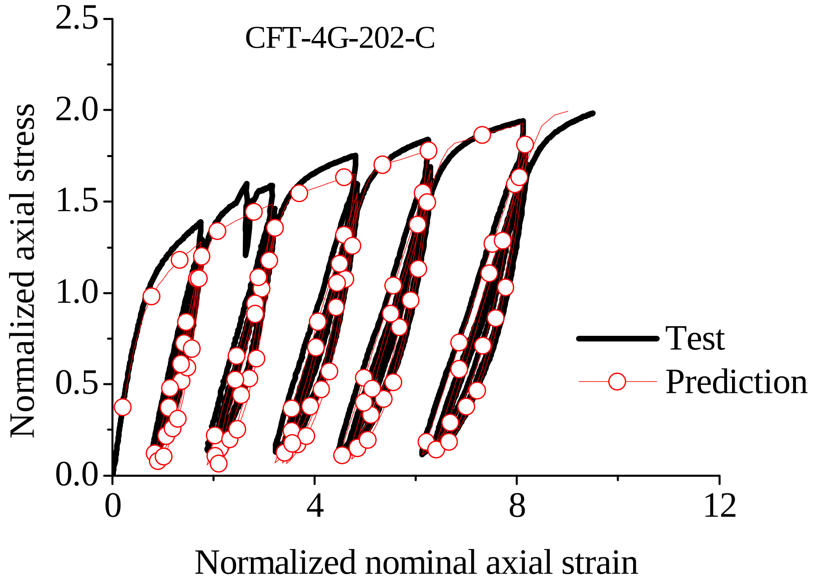


(c) CFT-4G-202-C

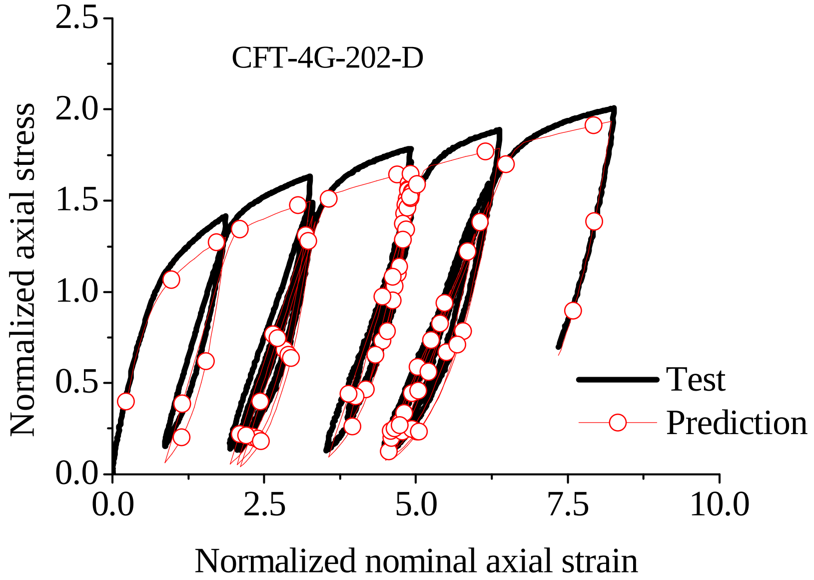


(d) CFT-4G-202-D

Figure 6.18 Comparison of concrete stress-strain curves for series 202 (continued)

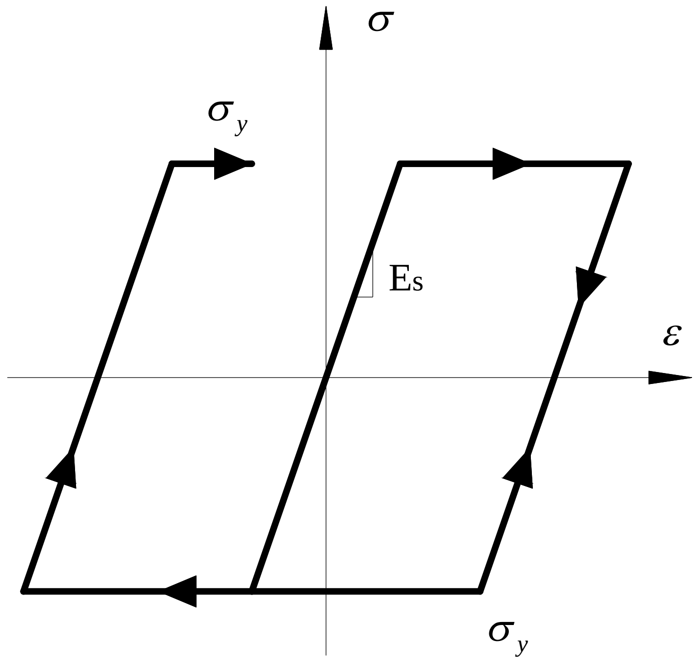


Figure 6.19 Bilinear steel hysteretic model

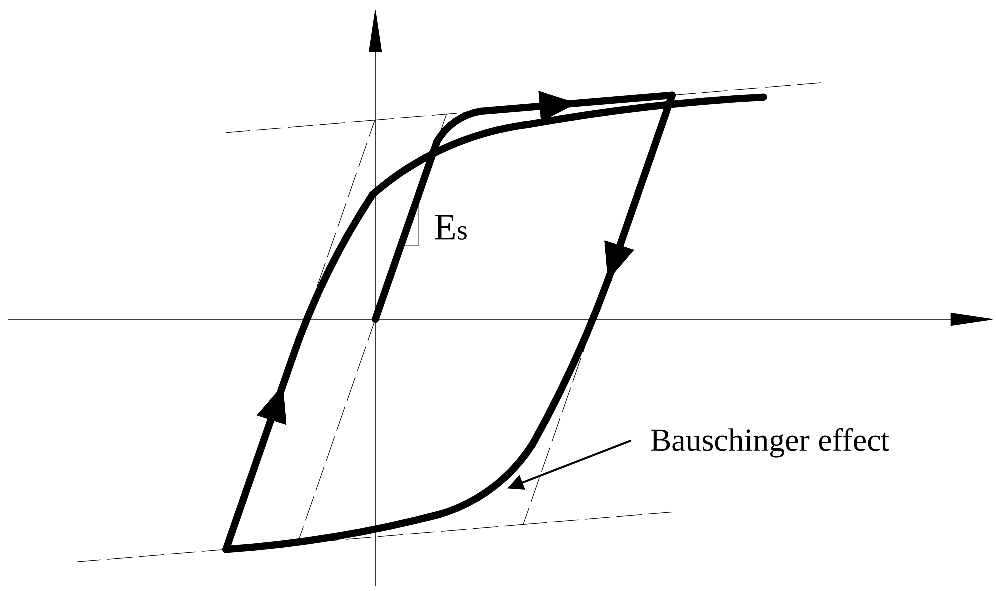


Figure 6.20 Typical steel hysteretic behaviour

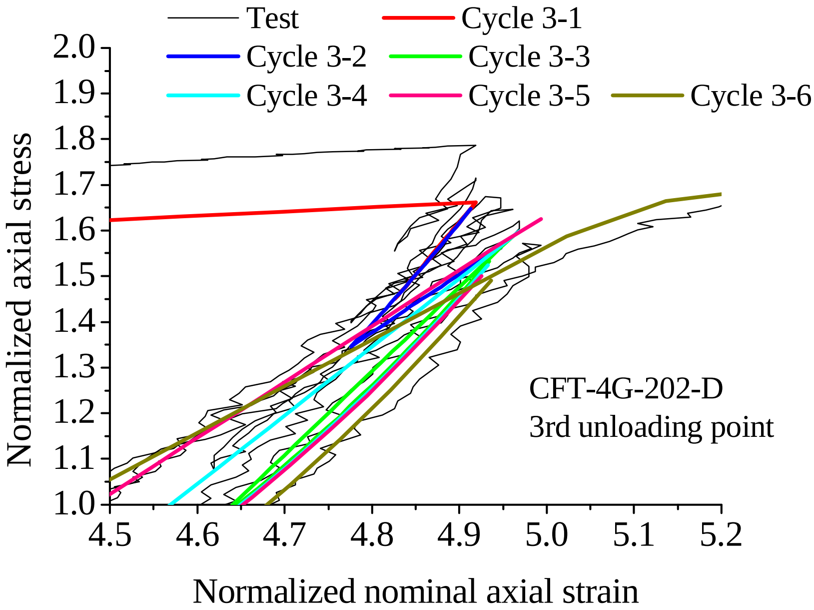


(a) Stress degradation

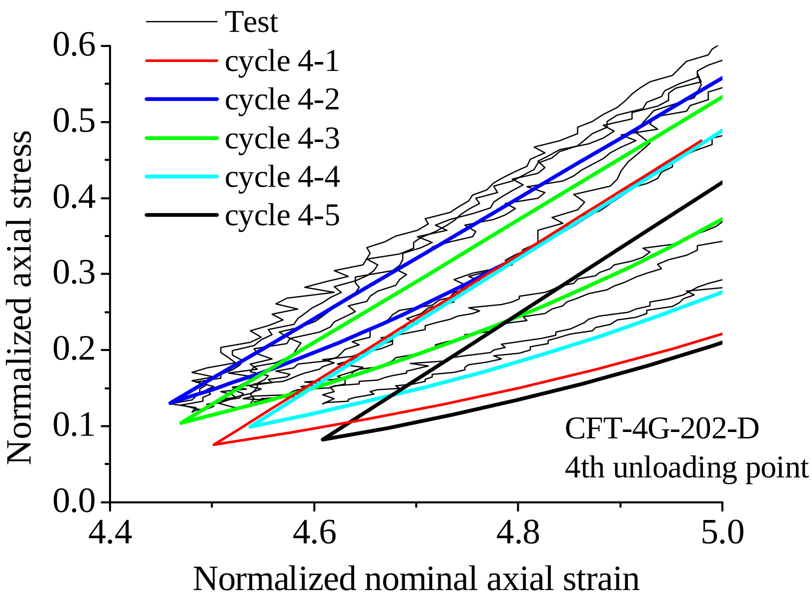


(b) Plastic strain accumulation

Figure 6.21 Cumulative effects of repeated loading

# CHAPTER 7

# BEHAVIOUR OF FRP-CONFINED CIRCULAR CONCRETE-FILLED STEEL TUBULAR COLUMNS SUBJECTED TO COMBINED AXIAL AND CYCLIC LATERAL LOADS

## 7.1 INTRODUCTION

In practice, columns are normally subjected to not only axial compression but also lateral loads, such as the wind and seismic loads. Extensive studies have been conducted on concrete-filled steel tubular (CFT) columns under combined axial and lateral loads (Ichinohe et al. 1991; Sugano and Nagashima 1992; Prion and Boehme 1994; Boyd et al. 1995; Toshiyuki et al. 1996; Elremaily and Azizinamini 2002; Fam et al. 2004; Inai et al. 2004; Han and Yang 2005; Lee 2007; Lu et al. 2009; Valipour and Foster 2010). In such columns, the critical regions are the ends of the column where the moments are the largest; failure is often initiated by the degradation in the strength and ductility of the steel tube in the critical regions as a result of inelastic outward local buckling of the steel tube. Under seismic loading, large plastic rotations without significant degradation in stiffness and strength are demanded at these critical regions.

Xiao (2004) recently proposed the use of FRP jackets for the confinement of the critical regions of concrete-filled steel tubes, and Xiao et al. (2005) presented results from a few preliminary tests which demonstrated the expected advantages of FRP-confined CFT (CCFT) columns under combined axial and cyclic lateral loads.

The behaviour of FRP-confined CFT columns under both monotonic and cyclic axial compression has been examined in Chapters 4 to 6. The advantages of FRP jacketing of CFT columns with a thin steel tube have been clearly shown in these chapters. In this chapter, a series of large-scale cantilever column tests are presented, where CFT columns with or without FRP jacketing at the column end were tested under combined constant axial compression and monotonic or cyclic lateral loading. The test programme was designed to develop a good understanding the behaviour of such CCFTs, and to examine the effects of two important test parameters, namely, the stiffness of the FRP jacket and the loading scenarios (i.e. monotonic lateral loading and cyclic lateral loading). To the best knowledge of the author, these test parameters have not been examined in any existing studies. In this chapter, details of the specimens and the test set-up are first presented, followed by the presentation and discussion of the test observations and results.

## 7.2 EXPERIMENTAL PROGRAMME

### 7.2.1 Details of Specimens

In total five large-scale columns were prepared and tested, among which two were tested under combined axial compression and monotonic lateral loading (referred to as type E loading hereafter), while the other three were tested under combined axial compression and cyclic lateral loading (referred to as type F loading hereafter). The two columns tested under type E loading included one CFT specimen as the control specimen and one CCFT specimen with a five-ply GFRP jacket. The three columns under type F loading included two specimens which were nominally identical to the two tested under type E loading so that the effect of loading scenarios can be examined; they also included an additional CCFT specimen with a six-ply CFRP jacket so that the effect of FRP jacket stiffness can be examined. All the five columns had a circular section with a diameter of 318 mm, and a height of 1625 mm from the point of lateral loading to the top of the stiff reinforced concrete (RC) footing which was 1500 mm long, 1400 mm wide and 550 mm thick. The steel tubes used in all the specimens had a thickness of 3 mm, leading to a $D_{outer} / t_s$ ratio of 106. For the three CCFT specimens, an FRP jacket was applied to provide additional confinement to the potential hinge region which was assumed to be 500 mm from the column footing. The details of all specimens are summarized in Table 7.1.

### 7.2.2 Preparation of Specimens

All specimens were constructed at the Structural Engineering Research Laboratory of The Hong Kong Polytechnic University. Each specimen consisted of a CFT or a CCFT column with one end embedded in a stiff RC footing. In the preparation process, the steel tube of the column was connected to the steel reinforcement embedded in the RC footing in the following way: (1) the steel tube was first welded to a bottom steel plate which was 700 mm long, 500 wide and 25 mm thick; the steel tube was placed at the middle of the steel plate and the welding seam of the steel tube was placed at the middle of the longer side (700 mm) of the bottom plate; (2) six vertical stiffeners were then welded to the embedded part of the steel tube (i.e. the part within the RC footing); each stiffener had a radial width of 120 mm, a thickness of 20 mm and a height of 480 mm ; (3) a 20 mm thick and 100 mm wide steel ring which was formed from two halves was then placed onto the stiffeners and welded to the steel tube; the steel ring was used to ensure a uniform stress distribution at the end of the column (i.e. the part above the footing). The steel tube integrated with the embedded steel reinforcement is shown in Figure 7.1. The steel assembly was next enclosed in a wooden formwork for the casting of concrete to form the footing which was heavily reinforced to ensure a sufficiently large stiffness/strength (Figure 7.2). Afterwards, commercially available concrete was cast both in the steel tube and to form the footing. One week later, a thin layer of gypsum was applied on the top surface of the concrete in the steel tube to eliminate the gap caused by the shrinkage of concrete between the top surface of the concrete and the top end of the steel tube, so that the two components can be axially-loaded simultaneously in the test.

The FRP jacket was formed via a wet lay-up process, and each ply consisted of a single lap of a fibre sheet impregnated with an epoxy resin. A continuous fibre sheet was wrapped around the steel tube to form a jacket with the required number of plies, with the finishing end of the fibre sheet overlapping its starting end by 150 mm to ensure circumferential stress transfer. Before the wrapping of the FRP jacket, the surface of the steel tube was properly cleaned using alcohol. The height of the FRP jacket was finally 490 mm instead of the designed 500 mm for ease of installing transducers (see Section 7.2.4).

### 7.2.3 Material Properties

Three concrete cylinders were prepared for each column according to ASTM C192 (2007) and tested according to ASTM C39 (2009) in order to determine the cylinder strength, the axial strain at peak axial stress, and the elastic modulus of concrete. The so-obtained concrete properties are summarized in Table 7.2. Three steel coupons were cut from a steel tube which was exactly the same as those in the columns and tested according to BS 18 (1987). The stress-strain curves obtained from the steel coupon tests are shown in Figure 7.3. The steel had an elastic modulus of 203 GPa, a yield stress of 271 MPa, and an ultimate stress of 353 MPa. The GFRP jacket used had an elastic modulus of 80.1 GPa and an ultimate strain of 2.28%, based on a nominal thickness of 0.17 mm per ply. These GFRP material properties are taken from the coupon tests presented in Chapter 3. The CFRP jacket used had an elastic modulus of 237.8 GPa and an ultimate strain of 0.85%, based on a nominal thickness of 0.34 mm per ply as obtained from five tensile coupon tests. The adhesive had an elastic modulus of 1.7 GPa and an ultimate tensile stress of 55 MPa according to the manufacturer.

### 7.2.4 Instrumentation

In order to monitor the behaviour of the column, extensive strain gauging and many transducers were employed in the test of each column as summarized below.

A number of bi-directional strain gauges were used to measure the axial and hoop strain distributions of the column at five different column heights, namely, the circumferences at 20 mm, 150 mm, 325 mm, 470 mm and 850 mm from the column footing top surface respectively. For each of the three lower heights, eight strain gauges were evenly installed around the circumference. The other two heights (i.e. at 470 mm and 850 mm) were expected to be outside the plastic hinge region, so a smaller number (i.e. four) of strain gauges were used for each circumference and there were placed at 90 degrees apart from each other. The gauge length of the strain gauges attached to the steel tubes was 10 mm while that of the strain gauges attached onto the FRP jackets was 20 mm. The layout of the strain gauges is shown in Figure 7.4.

Eight pairs of linear variable displacement transducers (LVDTs) were installed on the two sides of the loading plane (i.e. the western side and the eastern side, see Figure 7.5) of the column at intervals of 100 mm starting from the column end (i.e. the top surface of the footing). These LVDTs were installed on the column surface through pre-fixed nuts (Figure 7.6). In addition, two pairs of LVDTs (each pair consisted of one vertical and one horizontal transducer) were used on the two sides of the foundation to monitor the movement it could experience during the test. Two LVDTs were installed at the column head to measure the lateral displacement. The rotation of the column head and the shortening of the column were also measured by LVDTs. The layout of the LVDTs is shown in Figure 7.5.

### 7.2.5 Testing Frame

All the tests were conducted using a testing frame which is capable of testing large-scale structural members and sub-assemblies at the Structural Engineering Research Laboratory of The Hong Kong Polytechnic University. Figure 7.7 shows a photo of the testing frame while Figure 7.8 shows a schematic diagram of the test set-up for the present columns. The testing frame (Figure 7.7 & 7.8) includes a vertical actuator (capacity: 10,000 kN) connected to a relatively large plate (i.e. top plate) and a hinge joint connected to a relatively small plate (i.e. bottom plate);

rollers are provided between the top plate and the bottom plate so that during the test the horizontal locations of the actuator and the hinge can be adjusted. In addition, a horizontal actuator (capacity: 1,000 kN in tension and 1,500 kN in compression) is provided which can apply horizontal loading through a hinge joint. The positions of both actuators can be controlled manually. Both actuators can apply not only compression but also tension forces. In the test, the specimen was fixed to a strong floor using eight sets of screws (80 mm in diameter) and nuts. Both hinges were lubricated in advance so that they could rotate freely during the test.

In the test, significant frictional forces were induced between the top and the bottom plates (see Figure 7.8) because of the large axial load applied to the column and the relative movement between the two plates when the column was horizontally pulled or pushed. These frictional forces need to be deducted from the load applied by the horizontal actuator to obtain the horizontal load actually resisted by the column. In the present study, the frictional forces were determined in the following way: (1) a certain displacement was applied to the column head while the position of the axial actuator was held; in this process, the direction of frictional forces acting on the column was opposite to that of the applied displacement; (2) an equal displacement was applied to the axial actuator while the position of column head was held; in this process, the direction of frictional forces acting on the column was the same as that of the applied displacement. This change of direction of the frictional forces led to changes in the load readings from the horizontal actuator. The magnitude of the frictional forces was therefore taken to be half of the difference between the load readings of process (1) and process (2). In each column test, many pairs of processes (1) and (2) were executed, and the frictional forces during each test were averaged from the values found from the many pairs of processes (1) and (2). The so-obtained frictional forces for all column tests are summarized in Table 7.3. The frictional coefficients for different specimens are seen to be similar (Table 7.3), indirectly confirming the reliability of these results. The average frictional coefficient is 0.00527.

### 7.2.6 Loading Scheme

A constant axial load $N_{35}$ which is equal to 35% of the column squash load $N_{sq}$ was applied to each column. $N_{35}$ is given by the following equation:

$$N_{35} = 0.35N_{sq} = 0.35(f_y A_s + f'_{co} A_c) \tag{7.1}$$

where $f_y$ and $A_s$ are the yield stress and the cross-sectional area of the steel tube respectively; $f'_{co}$ is the cylinder compressive strength of concrete; and $A_c$ is the cross-sectional area of the concrete core. It should be noted that for different columns, the concrete strengths were slightly different (Table 7.2), so the magnitudes of the applied constant axial load were also slightly different (Table 7.3).

Following the practice of many existing studies (Boyd et al. 1995; Hsu and Chang 2001; Elremaily and Azizinamini 2002; Yamao et al. 2002; Cheng et al. 2003; Iacobucci et al. 2003; Kitada et al. 2003; Galal et al. 2005; Susantha et al. 2006; Bae and Bayrak 2008; Susantha et al. 2008), the lateral loading was applied step by step based on the yield displacement of the column. The yield displacement of the column was defined in the following way which was suggested as by Priestly and Park (1987): (1) load the column to a level which is 0.75 times the maximum lateral load $H_{peak}$; $H_{peak}$ was estimated through a sectional analysis method adopting the stress-strain model developed in Chapter 5 for the confined concrete and a column analysis method for evaluating the column behaviour (Chen and Atsuta 1976); (2) the yield displacement $\delta_y$ is defined as the elastic limit of an equivalent elastic-perfectly plastic curve with a reduced stiffness being equal to the secant stiffness at 75% of the peak lateral load (i.e. $0.75H_{peak}$; see Figure 7.9). For all the columns, the loading rate applied had a maximum value of 5mm/min. For the columns subjected to cyclic lateral loading, the yield displacement was averaged from the two values found using the method above for the pull direction and the push direction respectively. The so-obtained yield displacements are summarized in Table 7.4. The cyclic loading schemes were based on these in-situ determined yield displacements and consisted of two cycles at displacement levels of $\pm\delta_y$ ; $\pm 2\delta_y$ ; $\pm 3\delta_y$ ; $\pm 5\delta_y$ ; $\pm 7\delta_y$ ; $\pm 9\delta_y$ and one cycle at displacement levels of $\pm 11\delta_y$ (Figure 7.10), except for specimen LCFT-0-106-F where the second cycle at $\pm 9\delta_y$ was skipped due to time limitation. It should be noted that in the above descriptions the term "displacement" or "lateral displacement" refers to the lateral displacement at the column head. This simplification in terminology is also used elsewhere in this chapter unless otherwise specified.

In the present study, no fatal brittle failure occurred in all the cantilever tests, even though the FRP jacket ruptured and the steel tube fractured in specimen LCFT-5G-106-F. Hence, the two monotonic loading tests were terminated when the lateral resistance of the column was reduced to a reasonably low level; for the other columns which were loaded cyclically, the tests were terminated after the pre-determined loading scheme had been completed (Figure 7.10). At such a large final lateral displacement (i.e. $\pm 11\delta_y$), the lateral resistance of the column was reduced significantly.

## 7.3 EXPERIMENTAL OBSERVATIONS AND RESULTS

### 7.3.1 General

The experimental observations and results are presented in this section for each column. For clarity of presentation, the push direction (i.e. western direction) is defined to be the positive direction while the pull direction (i.e. eastern direction) is defined to be the negative direction (Figure 7.8); compressive stresses/strains are defined to be negative while tensile strains/stresses are defined to be positive. These definitions are adopted throughout this chapter unless otherwise specified. Therefore, for example, the western side of a column is in compression and the eastern side is in tension when a column is loaded in the push (positive) direction. For ease of reference, the five cross-sections where strain gauges were attached are defined as Sections A to E (Figure 7.4) from the column bottom end (i.e. column base) while the eight segments over which LVDTs were installed are defined as the first to the eighth segments from the column base.

### 7.3.2 Column LCFT-0-106-E

#### *7.3.2.1 Observations*

At a lateral displacement of 25 mm, a bulge which was located at a height of around 60 mm from the column base could be felt by hand on the compression side of the steel tube, indicating that significant localized outward deformation occurred by then. With further increases of the lateral displacement, the bulge became more and more severe and obvious. When the lateral displacement reached around 70 mm, another smaller bulge was noticed at a height of 250 mm from the column base. With the development of these bulges, localized deformation of concrete at the same locations can be expected because of the local degradation of steel confinement; relative slips between the concrete and the steel tube may also have occurred in these regions. The test stopped at a lateral displacement of 125 mm and the specimen after test is shown in Figure 7.11.

#### *7.3.2.2 Strain distributions*

Figure 7.12 shows the distributions of axial strains along both the western and the eastern sides (i.e. the extreme compression fibre and extreme tension fibre) of the column where the axial strains were found from the LVDT readings. The different curves in Figure 7.12 represent strain distributions at different lateral displacement levels. It is easy to understand that the axial strains at lower sections are generally larger because of the existence of a moment gradient along the column height. Figure 7.12 also shows clearly that localized compressive strain concentration exists in the first segment and the third segment where bulges of the steel tube occurred during the test. As a result, the compressive strains of the second segment are seen to be much smaller in comparison. It should be noted that the LVDTs were installed on the surface of the steel tube or the FRP jacket (for CCFT columns) (see Figure 7.6), so the LVDT readings reflected only the deformation of the steel tube but not closely the deformation of the concrete because of possible slips between them especially after the appearance local bulges on the steel tube. The compressive strains of the concrete in the second segment may actually be significantly larger than those shown in Figure 7.12.

Figure 7.12 also shows that the tensile strains of the first two segments are generally similar and in the final stage the tensile strain of the second segment is even larger, despite the fact that the moment in the first segment was larger. This phenomenon may be attributed to the local bulge of the steel tube on the compression side and the tension shift effect which arises from the transfer of compressive stresses directly to the column base by adequately inclined struts between flexural-shear cracks. This tension shift phenomenon has been well recognised in studies on RC columns (Hines et al. 2004). It is also noted that the phenomenon of “strain penetration” commonly observed in RC columns (Priestley and Park 1987), which generally leads to large recorded tensile strains at the bottom segment, did not occur in the test. This is believed to be due to the detailing of the test specimen within the RC footing (Figure 7.1), which made it difficult for the tensile forces to be transferred to the part of the steel tube embedded in the footing.

The axial strain distributions obtained from the axial strain gauge readings are shown in Figure 7.13 for the five sections. For each section, several curves representing strain distributions at different lateral displacement levels are shown. Figure 7.13 shows that the strain distributions of the two upper sections (i.e. Sections D and E) remain approximately linear, indicating that the plane section assumption applies here. For the lower sections, the strain distributions are approximately linear at lower displacement levels, but become significantly nonlinear afterwards. For example, for the first section, the strains at the extreme compressive fibre remain nearly constant after a certain displacement level (Figure 7.13a), which is believed to be due to the existence of significant localized buckling deformation (i.e. bulges) outside the region covered by the strain gauge.

Similarly, the deviation of other strain values from a linear strain distribution is believed to be due also to the same reason (i.e. localized buckling deformation). For the other four columns, a similar conclusion can also be reached: the plane section assumption is valid for the higher sections and/or at lower displacement levels, but significant deviation from this assumption can be found in the lower sections at high displacement levels, when the strain distributions were significantly affected by localized deformations in the steel tube such as cracks on the tension side and bulges on the compression side of the steel tube. Therefore, for the other four columns, the axial strain distributions obtained from the axial strain gauge readings are shown in Appendix (Figure A.1-A.4) and are not further discussed in the following sections.

The distributions of hoop strains at a lateral displacement of 125 mm are shown in Figure 7.14 for Sections A-C (see Figure 7.4). As expected, the largest hoop strain of a section is always found on the compression side because of the expansion of concrete under compression. The hoop strains on the tension side are shown to be very small (Figure 7.14). It is also evident from Figure 7.14 that the hoop strains at the first section are smaller than those at the other two sections, which is at least partial due to the constraint from the column footing. In addition, the localized buckling deformation could also affect the hoop strain distributions shown in Figure 7.14.

#### *7.3.2.3 Curvature distributions*

The curvature of a section is commonly found from strains at different locations of the section. In the present study, the strains obtained from the LVDT readings were used instead of those obtained from the axial strain gauges as the latter cover only a small vertical distance (i.e. 20 mm or 10mm) and their readings were more easily affected by localized deformations. With the LVDT readings, the average curvature of a segment is given by:

$$\phi_{\Delta} = \frac{(\Delta_1 - \Delta_2)}{D' l_{seg}} \tag{7.2}$$

where $\phi_\Delta$ is the average curvature of the segment based on LVDT readings; $l_{seg}$ is the length of the segment; $\Delta_1$ and $\Delta_2$ are the LVDT readings on the western and eastern sides of the segment respectively; and $D'$ is the horizontal distance between the tips of the two transducers and is slightly larger than the diameter of the column.

The curvatures calculated using Eq. 7.2 are shown in Figure 7.15 for different lateral displacement levels. In Figure 7.15, the curvatures calculated for each segment are shown at the mi-height of the segment and the curvatures at the same displacement level are connected by straight lines to represent an approximate variation of the curvature along the column height. It is not surprising to find that larger curvatures always occur adjacent to the column base and above a certain height (i.e. 300 mm as shown in Figure 7.15); the curvatures above 300 mm remain very small during the loading process.

The curvatures of the first and the third segments are very large; the latter is even larger than that of the second segment which should have experienced a larger moment. This unexpected observation is believed to be due to the way adopted to calculate the curvatures (i.e. Eq. 7.2): the use of Eq. 7.2 implies that the deformations of the hybrid section follow the plane section assumption but the localized deformation (i.e. steel bulges) occurring in the first and third segments caused significant slips between the steel tube and the concrete (i.e. the deformation of concrete in these two segments may be smaller than that of steel the tube). Therefore, the use of LVDT readings which only reflect the deformation of the steel tube may lead to an overestimation of the curvatures of the first and the third segments but an underestimation of their adjacent segment (i.e. the second segment).

*7.3.2.4 Moment-curvature curves*

The moment-curvature curves of different sections are shown in Figure 7.16, where the curvatures were calculated using Eq. 7.2 while the moments were calculated using the lateral load and the axial load (i.e. considering the second-order effect), with the assumption that the lateral displacement of the bottom eight segments was minor and can be ignored. This assumption has only a small effect on the curves shown in Figure 7.16.

Figure 7.16 shows that the peak moments of different sections are different, and generally decrease as the distance from the column end increases. The larger moment capacities of the lower sections were caused by the constraint from the column footing which provided additional confinement to the steel tube and the concrete. This is also one of the main reasons for the existence of a certain length of plastic hinge which should otherwise be only a single point. The initial slopes of all these curves are seen to be almost identical, but the slopes of the curves of the first and the third segments become smaller than those of the other sections after a certain load level, which is believed to be at least partially due to the overestimation of the curvature by Eq. 7.2, as discussed earlier. Figure 7.16 also indicates that significant plastic deformation only occurred in the bottom three segments. Examined together with Figure 7.15, it may be concluded that the plastic hinge length of this column was approximately 300 mm.

The points corresponding to the occurrence of the two bulges on the steel tube are also marked on the moment-curvature curves. There is no evidence that these bulges led to a significant rapid/sudden reduction in the moment capacity of the section. Instead, good ductility is seen in Figure 7.16 for all the sections.

*7.3.2.5 Lateral load-lateral displacement curve*

The lateral load-lateral displacement curve of the column is shown in Figure 7.17 where the lateral displacement was averaged from the readings of the two LVDTs installed at the column head (Figure 7.5). The point corresponding to the peak moment of the first segment is also marked on the curve, and it is seen to be on the descending branch (i.e. post-peak branch) of the curve. This suggests that the member behaviour of the column was significantly affected by the second-order effect caused by the large axial load acting on the column. The large axial load also caused a relatively steep descending branch of the curve, despite the good ductility of the section as shown in Figure 7.16.

### 7.3.3 Column LCFT-5G-106-E

#### *7.3.3.1 Observations*

The physical conditions of the column at different stages of loading are shown in Figure 7.18. At a displacement of around 18 mm, the first two flexural cracks were noticed at heights of around 60 mm and 140 mm from the column base on the tension side of the FRP jacket. With further increases of the lateral displacement, these two cracks widened and propagated horizontally; new cracks also appeared at higher levels (i.e. 225 mm and 295 mm from the column base at displacements of 40 mm and 60 mm respectively). A bulge on the compression side of the steel tube at a height of 30 mm from the column base could be felt by fingers at a lateral displacement of 80 mm. There was no FRP rupture during the whole loading process.

#### *7.3.3.2 Strain distributions*

Figure 7.19 shows the distributions of axial strains along both the western and the eastern sides where the axial strains were found from the LVDT readings. Similar to column LCFT-0-106-E, the "tension shift" phenomenon is obvious in Figure 7.19. The compressive strain of the first segment is also seen to be significantly larger than that of the second segment especially at higher displacement levels, partially because of the existence of a steel bulge in the first segment. However, because of the confinement from the FRP jacket, the bulge was effectively controlled, so the strain concentration seen in Figure 7.19 is not as severe as in column LCFT-0-106-E in which no FRP jacket was provided (Figure 7.12).

The distributions of hoop strains at the lateral displacement of 125 mm are shown in Figure 7.20 for Sections A to C. Compared with column LCFT-0-106-E (Figure

7.14), Figure 7.20 also shows large hoop strains on the compression side and very small hoop strains on the tension side. However, the differences between the largest hoop strains of the three sections are much smaller; in particular, large hoop strains also exist in Section A which should have been subjected to strong constraint from the footing. Further examination of the column revealed that this is because of the locations of steel bulges: in column LCFT-0-106-E, the lowest steel bulge was at a height of 60 mm away from the column base, but in the present column the steel bulge moved down to a height of around 30 mm because of the confinement from the FRP jacket; this lower steel bulge effectively enlarged the hoop strain of Section A which is located 20 mm from the column base.

*7.3.3.3* *Curvature distributions*

The curvature distributions obtained using Eq. 7.2 are shown in Figure 7.21 for different lateral displacement levels. Figure 7.21 shows that the curvatures at lower sections are generally larger because of the moment gradient along the column height. However, the curvature of the bottom segment is seen to be smaller than that of the second segment at higher levels of displacement, which is believed to due to: (1) the compressive strain concentration in the first segment being unpronounced because of the confinement from the FRP jacket; (2) the existence of a larger tensile strain in the second segment which is due to the "tension shift" mechanism and the local bulge of the steel tube on the compression side (see Figure 7.19).

*7.3.3.4* *Moment-curvature curves*

The moment-curvature curves of different sections are shown in Figure 7.22, where the moments and the curvatures were obtained in the same way as those in Figure 7.16. Similar to column LCFT-0-106-E, the lower sections also have a larger moment capacities due to the constraint from the column footing, but the differences between different sections are smaller because of the additional confinement from the FRP jacket. The point corresponding to the occurrence of the bulges on the steel tube is also marked on the moment-curvature curves, and it is seen that the bulges had little effect on the moment capacity of the section.

*7.3.3.5 Load-displacement curve*

The lateral load-lateral displacement curve of the column is shown in Figure 7.23, with the point corresponding to the peak moment of the first segment marked on the curve. Similar to column LCFT-0-106-E, the member behaviour of the column is seen to be significantly affected by the second-order effect caused by the large axial load acting on the column.

7.3.4 Column LCFT-0-106-F

*7.3.4.1 Observations*

A bulge appeared (i.e. could be felt by hand) on the western side of the steel tube at a height of 60 mm when the column was loaded close to the end of the first excursion to $2\delta_y$ (i.e. 19.6 mm). Similarly, a bulge on the eastern side appeared at a height of 55 mm when the column was loaded close to the end of the first excursion to $-2\delta_y$ (i.e. -19.6 mm). In the subsequent cyclic loading process, the bulge could be re-straightened when the column was loaded in the opposite direction, with another bulge formed on the opposite side. With the increase of lateral displacement in both directions, the bulges on both sides of the steel tube became more and more severe and formed a ring around the column as illustrated in Figure 7.24 which shows the specimen at a lateral displacement of $9\delta_y$ (i.e. 88.2 mm). At the same time, obvious concrete dilation was observed close to the column base (i.e. within a region of 300 mm from the column base). Another bulge at a height of 250 mm was noticed on the western side when the column was loaded in the first cycle to $5\delta_y$ (i.e. 49 mm). With further loading, this bulge also became more obvious. On the contrary, no additional bulge was formed on the eastern side till the termination of the experiment. The conditions of the column at lateral displacements of $\pm 11\delta_y$ are shown in Figure 7.25 & 7.26

respectively.

*7.3.4.2 Strain distributions*

Figure 7.27 shows the distributions of axial strains along both the western and the eastern sides of the column where the axial strains were found from the LVDT readings. An obvious observation from Figure 7.27 is that the axial strains on the compression side of the second segment became tensile strains after a certain lateral displacement level. This is believed to be due to the significant compressive strain concentration in the first segment because of the existence of a steel bulge. As a result of this strain concentration, only limited compressive strains were developed on the compression side of the second segment, but when the column was loaded in the opposite direction in a loading cycle, significantly larger tensile strains were developed in the same region; the cumulative effects of several loading cycles led to the strain distributions shown in Figure 7.27. It should again be mentioned that the axial strains shown in Figure 7.27 were obtained from readings of the LVDTs which were installed on the surface of the steel tube, and do not closely reflect the deformation of the concrete inside; the concrete on the compression side of the second segment should have been subjected to compressive strains instead of tensile strains shown in Figure 7.27. It is also noted from Figure 7.27 that while the tensile strains of the first two segments are similar when the lateral displacement is relatively small (i.e. tension shift), that of the first segment becomes significantly larger when the lateral displacement is large, indicating that in the final stage of loading both tensile and compressive deformations were highly localized in the first segment, probably because of the more severe damage of concrete in this region.

The hoop strains at the extreme compression fibre on the western side of the five sections are shown against the lateral displacement in Figure 7.28. The hoop strains are seen to be higher for a lower section where the moment was larger, except for Section A where only limited hoop strains were developed because of the constraint from the column base. It is also obvious from Figure 7.28 that significant hoop strains were only developed below Section C (i.e. at a height of

300 mm).

*7.3.4.3* *Curvature distributions*

The curvature distributions obtained using Eq. 7.2 are shown in Figure 7.29 for different lateral displacement levels. On the western side, the larger curvature of the third bottom segment is due to the formation of a bulge in the steel tube at the height of 250 mm, while the negative curvature of the second segment is due to the formation of a bulge in steel tube within the first segment; the curvatures at both locations shown in Figure 7.29 may not represent closely the real curvatures of the column because of the error introduced by the method adopted to obtain Figure 7.29, as discussed earlier. Despite the possible errors in the method, the significant difference between the curvature distributions of the two loading directions (i.e. a larger curvature in the third segment for the positive direction and a larger curvature in the first segment for the negative direction) clearly illustrates the effect of localized deformation.

*7.3.4.4* *Moment-curvature curves*

The envelope moment-curvature curves in both directions are shown in Figure 7.30 for the first segment, where the moments and the curvatures were obtained in the same way as those in Figure 7.16. It is evident that while the two curves coincide well before the peak moment, they become significantly different afterwards.

*7.3.4.5* *Load-displacement curves*

The load-displacement curve is shown in Figure 7.31 with the points corresponding to the peak moment of the first segment in both directions marked on the curve. Again, it is shown that the member behaviour of the column was significantly affected by the second-order effect from the large axial load acting on the column. The envelope curves in both directions are compared in Figure 7.32, and are shown to agree well with each other despite the different curvature distributions (Figure 7.29).

Two main characteristics, which have been reported by other researchers (Boyd et al. 1995), can also be identified from the hysteretic curve shown in Figure 7.31: (1) strength degradation; and (2) the pinching effect. Strength degradation refers to the observation that the lateral load that can be resisted by the column at the same lateral displacement reduces after cyclic loading (Figure 7.31). Strength degradation is seen to be more severe at a higher lateral displacement level. Such degradation of column resistance is due to strength deterioration of both the concrete and the steel tube. The strength deterioration of concrete in CCFTs has been discussed in Chapter 6.

The pinching effect can be identified by examining the shape of the load-displacement curve when the lateral displacement is close to zero. In the present column, the pinching effect becomes obvious after the ring-shaped bulge was formed in the steel tube (i.e. after the first excursion of the $\pm 5\delta_y$ cycle). Due to the existence of a bulge on both sides when the lateral displacement was close to zero, the steel tube could hardly contribute any tensile forces with a further increment of the lateral displacement. Therefore, the flexural stiffness of the column was very small at that moment. However, with further loading, the bulge was re-straightened which allowed the steel tube to provide tensile resistance again. As a result, the flexural stiffness started to increase only after a certain lateral displacement.

### 7.3.5 Column LCFT-5G-106-F

#### *7.3.5.1 Observations*

When the column was loaded close to the end of the first excursion to $2\delta_y$, noise was heard which signified the initiation of flexural tensile cracks. The first visible tensile crack appeared when the column was in the first excursion to $3\delta_y$, at a height of 95 mm on the eastern side of the column. In the subsequent excursion in the opposite direction, two cracks at 70 mm and 150 mm respectively from the column base appeared simultaneously on the western side. With further cyclic lateral loading, these cracks widened and new cracks appeared. Most of the new cracks were within a small region (i.e. within 70 mm) of the column base. When the column was loaded in the first cycle of $\pm 5\delta_y$, bulges of the steel tube appeared (i.e. could be felt by hand) at a height of 30 to 40 mm on both sides. At approximately the same location of a bulge, flexural cracks were commonly induced when the column was loaded in the opposite direction, probably because of the local damage introduced by the previous bulge which weakened the section. These flexural cracks, however, could not be closed in the subsequent loading cycle because of the localized lateral expansion caused by the previous bulge. Consequently, damage of the GFRP jacket in this region became increasingly severe as the loading process continued, and led to the hoop tensile rupture of the jacket when the column was in the second cycle of $\pm 5\delta_y$. With further loading, the steel bulges became more and more obvious where the GFRP ruptured, because of the loss of confinement. The steel tube fractured horizontally on the western side when the lateral displacement was close to $-11\delta_y$. The column after test is shown in Figure 7.33.

*7.3.5.2 Strain distributions*

Figure 7.34 shows the distributions of axial strains along both the western and the eastern sides of the column, where the axial strains were found from the LVDT readings. It is evident from Figure 7.34 that the axial deformations on both sides are highly concentrated in the first segment where the local bugles in the steel tube and GFRP rupture occurred. This is consistent with the test observation presented earlier.

The hoop strains at the extreme compressive fibre on the western side of the five sections are shown against the lateral displacement in Figure 7.35. The trend shown in Figure 7.35 is basically the same as that in Figure 7.28 for column LCFT-0-106-F except that the largest hoop strain occurred in Section A (i.e. 20

mm from the column base) which was significantly affected by the localized bulge in the steel tube (being 30mm to 40mm from the column base). The strain gauge at Section A was damaged at the rupture of the GFRP jacket, so its readings are not available thereafter.

#### *7.3.5.3 Curvature distributions*

The curvature distributions obtained using Eq. 7.2 are shown in Figure 7.36 for different lateral displacement levels. It is easy to understand that the curvature is also highly localized at the lowest segment. It may be noted that the curvature distribution shown in Figure 7.36 is significantly different from that shown in Figure 7.21 for a nominally identical specimen subjected to monotonic lateral loading. The difference is mainly due to the loss of GFRP confinement in the first segment of the cyclically-loaded specimen because of the cumulative localized damage in the lowest segment. This also suggests that cyclic loading can lead to more localized deformation.

#### *7.3.5.4 Moment-curvature curves*

The envelope moment-curvature curves in both directions are shown in Figure 7.37 for the first segment, where the moments and the curvatures were obtained in the same way as those in Figure 7.16. The points corresponding to the rupture of GFRP jacket are also marked on the curves. It is evident that the two curves coincide well before the GFRP rupture, but become significantly different afterwards. It is also noted that there is a sudden load drop on the curve for the negative direction, which is because of the steel fracture on the tension side as described earlier.

After the rupture of the GFRP jacket, in the positive direction, the moment-curvature curve is close to that of column LCFT-0-106-E, indicating the loss of confinement due to the GFRP rupture. On the contrary, the moment-curvature curve in the negative direction is closer to that of column LCFT-5G-106-E, although the GFRP jacket also ruptured at the same displacement level. It should be noted that the local region of GFRP rupture could still be subjected to confinement from the adjacent GFRP jacket, and the damage in the steel tube and the concrete of this local region depended on the level of the supplementary confinement it received. Therefore, it can be expected that the behaviour of the section with GFRP rupture lies between that of a bare CFT section and that of an intact GFRP-confined section. The different behaviours in the two directions may be due to the different supplementary confinement levels, which could result from the different extents of GFRP damage in the two directions. It should also be noted that the fracture of steel tube occurred also only on the western side, implying the different level of damage on the two sides.

#### *7.3.5.5 Load-displacement curve*

The hysteretic load-displacement curve is shown in Figure 7.38 while the envelope curves in the two directions are shown in Figure 7.39. The points corresponding to the peak moment of the first segment and the rupture of the GFRP jacket are also marked on the curves. The column behaviour is again shown to be significantly affected by the second-order effect. The two envelope curves are seen to agree well with each other until the rupture of the GFRP jacket which caused the asymmetric behaviour of the column.

The strength degradation at the same lateral displacement after cyclic loading is clearly seen in Figure 7.38. However, the pinching effect was well controlled before the GFRP rupture as the steel bulges were constrained by the confinement provided by the GFRP jacket. After the rupture of the GFRP jacket, the pinching effect appeared with the formation of localized bulges in the steel tube.

### 7.3.6 Column LCFT-6C-106-F

#### *7.3.6.1 Observations*

When the column was in the first excursion to $3\delta_y$, the first two visible flexural cracks appeared on the eastern side at heights of 60 mm and 210 mm from the column base. The first visible flexural crack on the western side appeared at a height of 230 mm when the column was in the first excursion to $-5\delta_y$. With further cyclic lateral loading, these cracks widened and no additional cracks were observed.

Local bulges of the steel tube appeared (i.e. could be felt by hand) at a height of 30 mm on both sides when the column was loaded in the first cycle of $\pm 5\delta_y$. When the column was loaded close to $7\delta_y$ and $-7\delta_y$, steel bulges appeared at a height of around 510 mm from the column base (i.e. above the CFRP-jacketed zone) on both sides of the column; the bulge on the western side was more obvious. With further cyclic loading, the bulges above the CFRP-jacketed zone became more and more severe. No rupture of the CFRP jacket was found after the test. The column at the end of test is shown in Figure 7.40.

*7.3.6.2 Strain distributions*

Figure 7.41 shows the distributions of axial strains along both the western and the eastern sides of the column where the axial strains were found from the LVDT readings. The readings for the fifth and sixth segments are not available after the cycle of $\pm 7\delta_y$ because the LVDTs there stopped functioning as a result of the large outward deformation of the steel tube which displaced excessively some of the nuts for installing the LVDTs. An obvious difference between the axial strain distributions shown in Figure 7.41 (especially Figure 7.41a) and those shown in Figure 7.27 & 7.34 (i.e. those for the CFT and the CCFT with a weak FRP jacket respectively) is that the compressive strain concentration in the first segment is much less pronounced. This is because: (1) the bulge of the steel tube in the first segment was well controlled by the strong CFRP jacket; and (2) an additional bulge occurred above the CFRP jacket, which attracted a large amount of axial deformation there (this also explains the difference between Figure 7.41a & b as when loaded in the positive direction, this additional bulge was found to be more severe).

*7.3.6.3* *Curvature distributions*

The curvature distributions obtained using Eq. 7.2 are shown in Figure 7.43 for different lateral displacement levels. Again, the curvatures for the fifth and sixth segments are not available after the cycle of $\pm 7\delta_y$ because the LVDTs there stopped functioning. It can however be expected that the curvatures in these two segments were large because of the localized deformations in the steel tube (i.e. the local bulges in the steel tube, see Figure 7.42).

Similar to the observation from Figure 7.41 for the axial strain distributions, the localization of curvature in the first segment of this column is seen to be less pronounced than that of the other two columns subjected to cyclic loading (i.e. a CFT column and a CCFT column with a weak GFRP jacket). The curvature distribution when the column was loaded in the positive direction and that for the loading in the negative direction are also seen to be different especially after the cycle of $\pm 7\delta_y$ (Figure 7.43) when local bulges in the tube appeared above the CFRP jacket. As described earlier, the local bulge on the western side (i.e. when loaded in the positive direction) was more severe than that on the eastern side. As a result, at the same lateral displacement level, for the loading in the positive direction, a larger curvature was induced in the segment where steel tube bulges above the CFRP jacket occurred; this reduced curvature localization in the bottom segments and made the deformation more distributed along the column height. A more direct comparison between the curvature distributions for the loading in the two directions is shown in Figure 7.44, where the absolute values of the curvatures are shown.

*7.3.6.4* *Moment-curvature curves*

The envelope moment-curvature curves in both directions are shown in Figure 7.45 for the bottom segment, where the moments and the curvatures were obtained in the same way as those in Figure 7.16. Although small bulges in the steel tube were observed during the test, no degradation of the flexural strength occurred as seen from Figure 7.45. Instead, the moment continued to increase with the curvature (and also the lateral displacement) until a level when the steel bulges above the CFRP jacket occurred. With the development of these steel bulges, the moments due to loading in the negative direction kept increasing but those due to loading in the positive direction slightly decreased, as a more severe bulge was formed in the latter case (see Figure 7.40).

While the different results (e.g. curvature distributions; moment-curvature curves) for the two loading directions were most likely caused by the imperfection of the column test (e.g. the asymmetry of material property distributions and/or geometry of the column, and/or that of loading), they allow the following conclusions to be made : (1) when the FRP jacket is strong enough, significant degradation of the steel section above the FRP jacket may control the behaviour of the column; in this case, the deformation is more distributed along the column height which makes the determination of the plastic hinge length more involved; (2) when a sufficiently strong FRP jacket covers a sufficient length of the column, the moment resisted by the critical section can keep increasing and the column failure is controlled by the second-order effect. The design of CCFTs needs to appropriately consider the above two conditions to reach an optimal design.

#### *7.3.6.5 Load-displacement curve*

The hysteretic load-displacement curve is shown in Figure 7.46 while the envelope curves in the two directions are shown in Figure 7.47. The column behaviour is again shown to be significantly affected by the second-order effect. The two envelope curves are seen to agree well with each other until the peak load after which the column behaviour became asymmetrical. The strength degradation at the same lateral displacement after cyclic loading is also clearly seen in Figure 7.46. The pinching effect was well controlled before the bulges appeared above the CFRP jacket but became obvious after that.

## 7.4 DISCUSSION OF TEST RESULTS

### 7.4.1 General Considerations

The concrete strengths of the different columns are different (see Table 7.2). To eliminate (or minimize) the effect of these differences in concrete strength, the test results of different columns were normalized before being compared. Table 7.2 shows that columns LCFT-0-106-E and LCFT-5G-106-F (referred to as group I) had approximately the same concrete strength while the concrete strengths of columns LCFT-5G-106-E, LCFT-0-106-F and LCFT-6C-106-F (referred to as group II) were very close. In the present study, the bending moments resisted by a column are normalized by the peak moment of the CFT column of the same group. The normalized moment-curvature curves of the first segment (i.e. bottom segment) are shown in Figure 7.48 for all the columns. For the cyclically-loaded columns, two normalized moment-curvature curves are given for loading in both directions. It should be noted that the curvature of a column section may also be affected by the different concrete properties, but this effect is expected to be minor, as also indicated by the very similar initial slopes of the curves shown in Figure 7.48.

Besides the concrete strength, the lateral load resisted by a column is affected by the magnitude of the applied axial load (including the second-order effect). In the present study, the axial load applied to a column was equal to 35% of its squash load (Eq. 7.1) which is also dependent on the concrete strength and is different from one column to another (see Table 7.3). The second-order effect induced by the applied axial load is therefore also different for different columns. To eliminate this second-order effect on the lateral load-displacement behaviour of the columns, the lateral loads resisted by all the columns were adjusted using the following equation:

$$P_{adj} = P_{ori} + P_{\mathrm{mod}} = P_{ori} + \frac{\left(N_{app} - 1134\right)\delta}{l_{col}} \tag{7.4}$$

in which, $P_{adj}$ is the adjusted lateral load; $P_{ori}$ is original lateral load from the test readings; $N_{app}$ is the applied axial load; $P_{\mathrm{mod}}$ is a value used to consider the different second-order effects in different columns and is equal to zero for column LCFT-0-106-E for which the applied axial load is equal to 1134 kN; $l_{col}$ is the effective length of the column (from the point of loading to the fixed end); and $\delta$ is the lateral displacement. The adjusted lateral loads are then normalized by the load $P_{nor}$ which corresponds to the moment used to normalize the bending moments:

$$P_{nor} = \frac{M_{co}}{l_{col}} \tag{7.5}$$

in which $M_{co}$ is the peak moment of the CFT column of the same group. The normalized load-normalized displacement curves using the above method are shown in Figure 7.49 for all the columns, where the lateral displacement is normalized by the column length.

### 7.4.2 Effect of Loading Scenarios

The effect of loading scenarios is obvious from the failure modes of the two CCFTs with a GFRP jacket but subjected to monotonic lateral loading and cyclic lateral loading respectively. As described earlier, in the column subjected to monotonic lateral loading (i.e. column LCFT-5G-106-E), the local buckling of the steel tube was significantly delayed and no FRP rupture on the compression side occurred at the end of test. However, in the column subjected to cyclic lateral loading (i.e. column LCFT-5G-106-F), the FRP jacket ruptured on both sides and severe local bulking of the steel tube occurred at the location of FRP rupture. The rupture of the FRP jacket in the cyclically-loaded column was due to the combined effects of the formation of flexural cracks which could not be closed in the subsequent reverse loading process and the consequent local loss of confinement which led to severe localized outward deformation of the steel tube. This suggests that cyclic loading tends to produce more localized deformation near the column end and FRP jacketing may be less effective. However, it should be noted that although this local FRP rupture is a direct consequence of cyclic lateral loading, it can be avoided when the stiffness/strength of the FRP jacket is sufficiently large, as seen from the test results of column LCFT-6C-106-F.

The more severe localized deformation is clearly illustrated in Figure 7.50 where the development of axial strains in the first two segments of the two CCFT columns (i.e. columns LCFT-5G-106-E and LCFT-5G-106-F) is shown, and in Figure 7.51 where the curvature distributions of the two columns at several displacement levels are compared. It is clear from these figures that at the same displacement level, the axial strain and the curvature are more localized in the first segment (i.e. bottom segment) for the cyclically-loaded column. In the later stage of loading, the axial strain on the compression side of the second segment in the cyclically-loaded column became positive (i.e. tensile strain), which is also a result of the strain concentration in the first segment, as discussed earlier in Section 7.3.4.2.

Similarly, more severe localized deformation near the column end was also found in column LCFT-0-106-F (i.e. CFT column) when compared with its counterpart subjected to monotonic lateral loading (i.e. column LCFT-0-106-E), as shown in Figure 7.52 (i.e. axial strain development) and Figure 7.53 (i.e. curvature distribution). Figure 7.52 & 7.53, however, also show that the difference in the localized deformation between the two CFT columns is not as significant as that between the two CCFT columns (Figure 7.50 & 7.51). This is believed to be due to the fact that in the cyclically-loaded CCFT column (i.e. column LCFT-5G-106-F), the local FRP rupture led to a significant loss of the section capacity, which exacerbated deformation localization.

The more localized deformation in a cyclically-loaded column is due to the cumulative damage in its bottom segment during cyclic loading; the cumulative damage weakens the bottom segment and thus leads to further localization of deformation in this segment. At the same displacement level, for a cyclically-loaded column, the curvature in the bottom segment is larger which generally means more severe damage in this segment and more pronounced degradation in the section capacity. Therefore, it can be expected that the descending branch of the moment-lateral displacement curve is steeper for a cyclically-loaded column. Figure 7.54 compares the normalized moment-lateral displacement curves of the two pairs of columns discussed above and indicates that the moment generally decreases more rapidly as the displacement increases for cyclically-loaded columns. However, for the two CFT columns, the effect of cyclic loading on the curves is seen to be small (Figure 7.54). This is believed to be due to the very good ductility of the CFT section as shown in Figure 7.16, which means the moment decreases only slowly as the curvature increases. For the two CCFT columns, the effect of cyclic loading is particularly obvious as seen from the curve for the loading in the positive direction (column LCFT-5G-106-F, see Figure 7.54). This more obvious effect of cyclic loading is due to the rapid degradation of section capacity after the rupture of the FRP jacket, compared to the original FRP-confined section, as seen from Figure 7.48. The normalized lateral load-lateral displacement curves of the two pairs of columns are shown in Figure 7.55 and similar observations can be made.

Based on the foregoing discussions, it can be expected that the effect of cyclic loading on the moment-lateral displacement curve (or the lateral load-lateral displacement curve) of a column is more pronounced when the moment-curvature curve of its cross-section has a steeper descending branch. It can therefore be expected that for CFT columns with a thinner steel tube, the effect of cyclic loading is more significant. On the other hand, when a weak FRP jacket is used, it is likely to be damaged locally because of cyclic loading and thus has little contribution to the performance of the CFT column, although it may improve the column behaviour under monotonic loading.

### 7.4.3 Effect of FRP Confinement

It is shown in Section 7.3 that the FRP jacket can effectively delay (when a 5-ply GFRP jacket was used in the present study) or even prevent (when a 6-ply CFRP jacket was used in the present study) an elephant's foot local buckling failure at the end of a cantilevered CFT column when the column is subjected to both constant axial compression and cyclic lateral loading. In columns with a relatively thick FRP jacket (e.g. 6-ply CFRP jacket in the present study), the buckling deformations can be forced by FRP jacketing to appear above the FRP jacketed region (Figure 7.40 & 7.42). As a result, the curvature distribution in a CFT column with FRP confinement can be quite different from that in a bare CFT column. Figure 7.56 & 7.57 compare the curvature distributions for the two monotonically-loaded columns and the three cyclically-loaded columns respectively. These figures generally reveal that with FRP confinement, the localization of curvature is less pronounced. For column LCFT-6C-106-F, significant localization of deformation occurred above the FRP jacketed region because of the bulges developed there, which apparently affected the curvature distributions (see also Section 7.3.6 for details).

The normalized moment-curvature curves and the normalized moment-lateral displacement curves are shown in Figure 7.48 & 7.58 respectively for all the columns. It is evident from the two figures that the flexural strength (i.e. moment capacity) of the CFT section can be significantly enhanced by FRP confinement. The enhancement increases with an increase in the stiffness/strength of the FRP jacket. It is also shown that the moment-curvature curves of the CFT section have a descending branch after the peak moment, but with FRP confinement, the moment resisted by the section can continuously increase with the curvature.

The normalized envelope lateral load-lateral displacement curves are shown in Figure 7.49 for all the columns. The peak lateral load is also seen to be enhanced with FRP confinement (Figure 7.49). In addition, the slope of the descending branch of the curve becomes smaller (i.e. slower rate of decrease in the load) when FRP jacketing is provided. As expected, the effect of FRP jacketing becomes more obvious when the stiffness/strength of the jacket is larger.

The effect of FRP confinement is also examined in terms of the ductility of the columns. The ductility of a member is defined as its ability to sustain inelastic deformations prior to collapse, without a substantial loss of strength. The ductility of a column is generally defined based on the deformation capacity or energy dissipation capacity. The most commonly used parameter appears to be the ductility parameter $\mu_\delta$ defined by the following equation (Park 1989; Mirmiran et al. 1999; Wu et al. 2006 and see Chapter 2):

$$\mu_\delta = \frac{\delta_u}{\delta_y} \tag{7.6}$$

where $\delta_y$ and $\delta_u$ are the yield and ultimate displacements of the column. Various definitions of the yield and ultimate displacements of a column have been proposed by different researchers, as reviewed in Chapter 2. In the present study, the yield displacement is defined as the elastic limit of an equivalent elastic-perfectly plastic curve with a reduced stiffness being equal to the secant stiffness at 75% of the peak load (Figure 7.9). The ultimate displacement is defined as the displacement where the load carried by the column has undergone a 20 percent reduction, following the practice of many previous studies (Priestley and Park 1987; Iacobucci et al. 2003).

The values of the ductility parameter based on the above definition are summarized in Table 7.9 for all the columns. It is evident that the ductility parameter generally increases with the provision of an FRP jacket, especially when a strong jacket (e.g. 6-ply CFRP jacket) is provided. In particular, the ductility parameter can be enhanced from around 5.55 for the bare CFT column (i.e. LCFT-0-106-F) to 8.86 for column LCFT-6C-106-F when loaded in the negative direction. It may also be noted that the ductility parameter values for the same column can be quite different when they are calculated based on the envelope load-displacement curves in the two different directions (i.e. positive direction and negative direction). This is due to the asymmetric deformation of the columns: for column LCFT-5G-106-F, the smaller ductility parameter for the positive direction is due to the more severe degradation of FRP confinement near the column end as discussed in section 7.3.5.4; for column LCFT-6C-106-F, the smaller ductility parameter for the positive direction is due to the more severe local bulge developed in the steel tube above the FRP jacketed region. While these differences were caused by unintended asymmetry of the column tests (e.g. asymmetry in geometry, material properties and load application), the results suggest that if local FRP rupture and local bulges in the steel tube above the FRP jacketed region can be avoided, the ductility of a CFT column can be significantly enhanced by strong FRP jacketing. In practice, local FRP rupture near the column end can be avoided by using a stiffer FRP jacket (e.g. using a 6-ply CFRP jacket for the CFT column examined in the present study), while local bulges above the FRP jacketed region can be delayed by extending the FRP jacket vertically to cover a longer region.

Besides a larger value of the ductility parameter, it should also be noted that the conditions of CFT columns with and without FRP jacketing can be quite different when the load reduction has reached 20% of the peak load. The structural integrity of the FRP-jacketed column may be much better as damage in the steel tube is much less severe and the concrete is still being well confined, as seen from the present tests.

Besides the ductility parameter defined by Eq. 7.6, some researchers (Gosain et al. 1977; Banon et al. 1981; Darwin and Nmai 1986; Nmai and Darwin 1986; Iacobucci et al. 2003; Shim et al. 2008) have also used the total cumulative dissipated energy to assess column behaviour. The total dissipated energy of a column can generally be represented by the area enclosed by the load-displacement curve. From Figure 7.49, it is not difficult to find that the capability of energy dissipation of a CFT column can also be significantly increased with FRP confinement.

## 7.5 CONCLUSIONS

This chapter has presented a series of large-scale column tests, where CFT columns with or without FRP jacketing at the column end were tested under combined constant axial compression and monotonic or cyclic lateral loading. The results and discussions presented in this chapter allow the following conclusions to be made:

1. The FRP jacket can effectively delay or even prevent an elephant's foot local buckling failure at the end of a cantilevered CFT column when the column is subjected to both constant axial compression and cyclic lateral loading. In columns with a relatively thick FRP jacket, the buckling deformations may be forced by FRP jacketing to appear above the FRP jacketed region.

2. The performance of a CFT column can be significantly improved by FRP jacketing. Because of FRP confinement, both the flexural strength of a CFT section and the lateral load-carrying capacity of a CFT column can be significantly enhanced. The ductility and the energy-dissipation capacity of the column, although significantly affected by the second-order effect due to the applied axial load, can also be enhanced with FRP confinement.

3. Cyclic lateral loading introduces more severe localized deformation near the column end and may lead to earlier FRP rupture within that region. The performance of a CCFT column subjected to cyclic lateral loading may not be as good as found from a monotonic lateral loading test.

It should also be noted that the CFT columns tested in the present study already possessed good ductility before FRP jacketing. The effect of FRP jacketing can be expected to be more pronounced when weaker sections (i.e. CFTs with a thinner steel tube) are considered, where the confinement from the steel tube is smaller and the local buckling problem is more pronounced. Apparently, FRP jacketing is a promising approach for improving the performance of CFT columns, especially for those with an economical thin tube.

Table 7.1 Details of large-scale CCFT specimens

| ***Specimen*** | $D_{outer}$ ***(mm)*** | $t_s$ ***(mm)*** | $D_{outer}/t_s$ | $t_{frp}$ ***(mm)*** | ***FRP type*** | $N_{app}/N_{sq}$ | $N_{app}$ ***(kN)*** | $h_{frp}$ ***(mm)*** |
|---|---|---|---|---|---|---|---|---|
| **LCFT-0-106-E** | 318 | 3.0 | 106 | N/A | N/A | 0.35 | 1134 | N/A |
| **LCFT-5G-106-E** | | | | 0.85 | GFRP | | 1313 | 490 |
| **LCFT-0-106-F** | | | | N/A | N/A | | 1234 | N/A |
| **LCFT-5G-106-F** | | | | 0.85 | GFRP | | 1125 | 490 |
| **LCFT-6C-106-F** | | | | 2.04 | CFRP | | 1260 | 490 |

Table 7.2 Concrete properties

| ***Specimen*** | $f'_{co}$ ***(MPa)*** | $\varepsilon_{co}$ | $E_c$ ***(GPa)*** |
|---|---|---|---|
| **LCFT-0-106-E** | 31.7 | 0.0027 | 21.70 |
| **LCFT-5G-106-E** | 36.96 | 0.0030 | 23.34 |
| **LCFT-0-106-F** | 35.63 | 0.0026 | 23.41 |
| **LCFT-5G-106-F** | 31.06 | 0.0026 | 21.92 |
| **LCFT-6C-106-F** | 36.56 | 0.0026 | 22.46 |

Table 7.3 Applied axial loads and calculated rolling frictional forces

| ***Specimens*** | $N_{app}$ ***(kN)*** | ***Calculated friction (kN)*** | ***Frictional coefficient*** |
|---|---|---|---|
| **LCFT-0-106-E** | 1134 | 5.95 | 0.00525 |
| **LCFT-5G-106-E** | 1313 | 6.95 | 0.00529 |
| **LCFT-0-106-F** | 1234 | 6.37 | 0.00516 |
| **LCFT-5G-106-F** | 1125 | 6.08 | 0.00540 |
| **LCFT-6C-106-F** | 1260 | 6.61 | 0.00525 |
| | | ***Mean*** | 0.00527 |

Table 7.4 In-situ determined yield displacements

| ***Specimen*** | $\delta_{y1}$ ***(mm)*** | $\delta_{y2}$ ***(mm)*** | $\delta_{y}$ ***(mm)*** |
|---|---|---|---|
| **LCFT-0-106-F** | 10.1 | 9.5 | 9.8 |
| **LCFT-5G-106-F** | 8.3 | 7.4 | 10.5 |
| **LCFT-6C-106-F** | 11.3 | 10.5 | 10.9 |

Table 7.5 Ductility ratios based on displacements

| ***Specimen*** | $\delta_{y+}$ | $\delta_{u+}$ | $\mu_{\delta+}$ | $\delta_{y-}$ | $\delta_{u-}$ | $\mu_{\delta-}$ |
|---|---|---|---|---|---|---|
| **CFT-0-106-E** | 10.20 | 48.67 | 4.77 | N/A | N/A | N/A |
| **LCFT-5G-106-E** | 11.70 | 65.83 | 5.63 | N/A | N/A | N/A |
| **LCFT-0-106-F** | 10.27 | 55.90 | 5.44 | 11.08 | 62.61 | 5.65 |
| **LCFT-5G-106-F** | 10.91 | 58.45 | 5.35 | 10.33 | 66.07 | 6.39 |
| **LCFT-6C-106-F** | 11.29 | 70.98 | 6.29 | 10.93 | 96.88 | 8.86 |

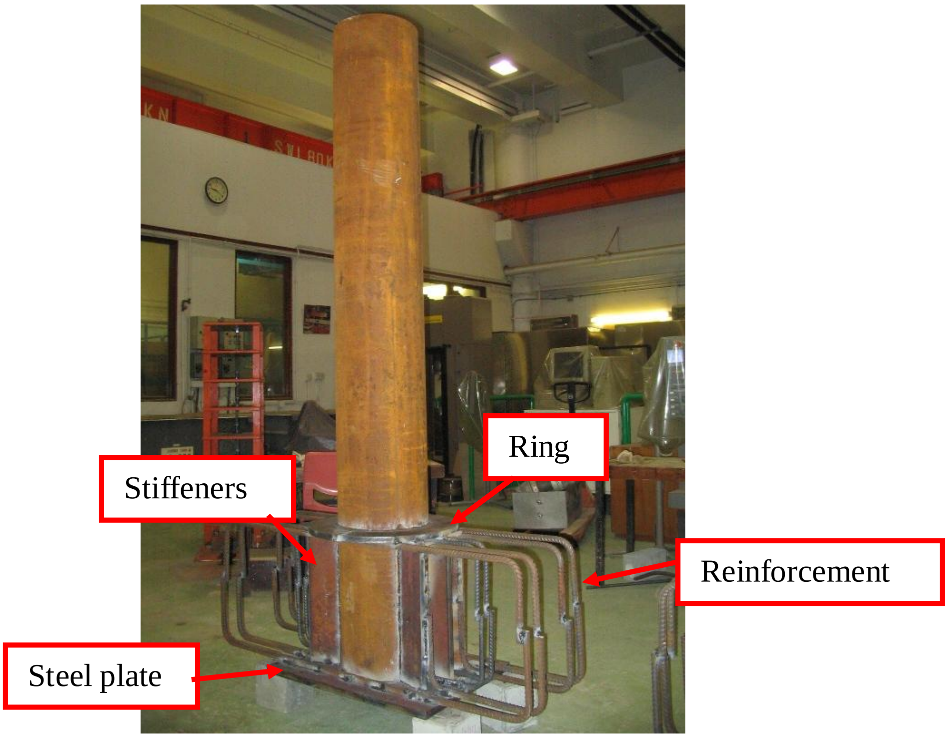


Figure 7.1 Steel tube integrated with steel plate, stiffeners, ring and part of the steel reinforcement.

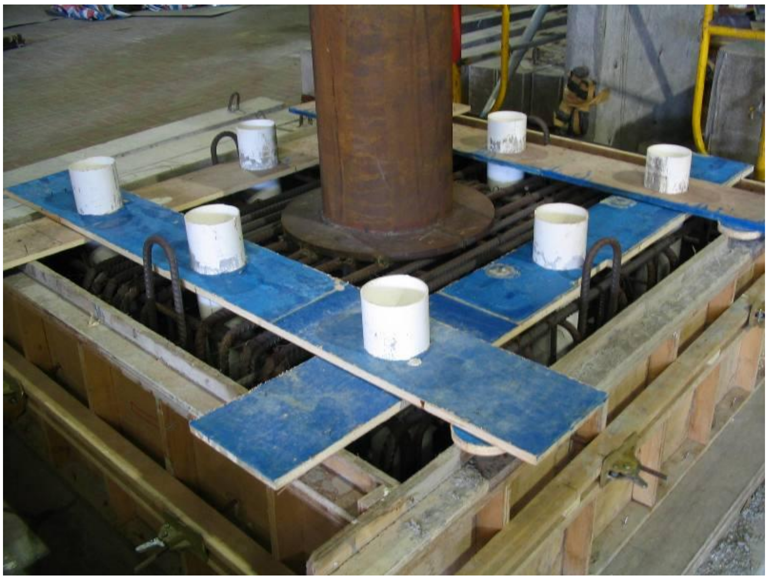

Figure 7.2 Specimen ready for concrete casting.

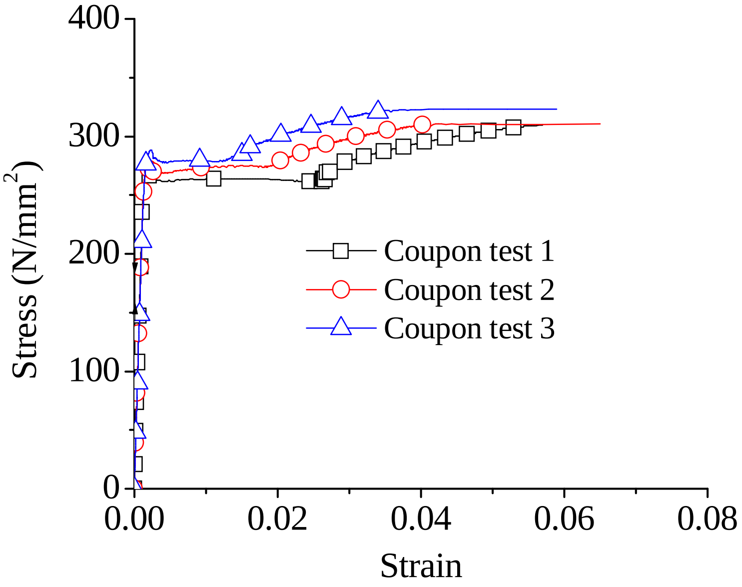


Figure 7.3 Steel coupon test results

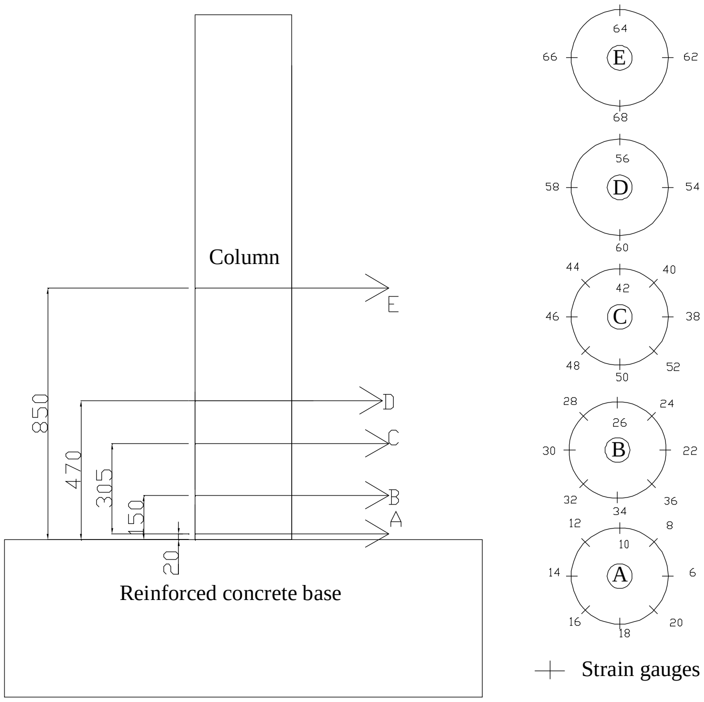


Figure 7.4 Layout of strain gauges

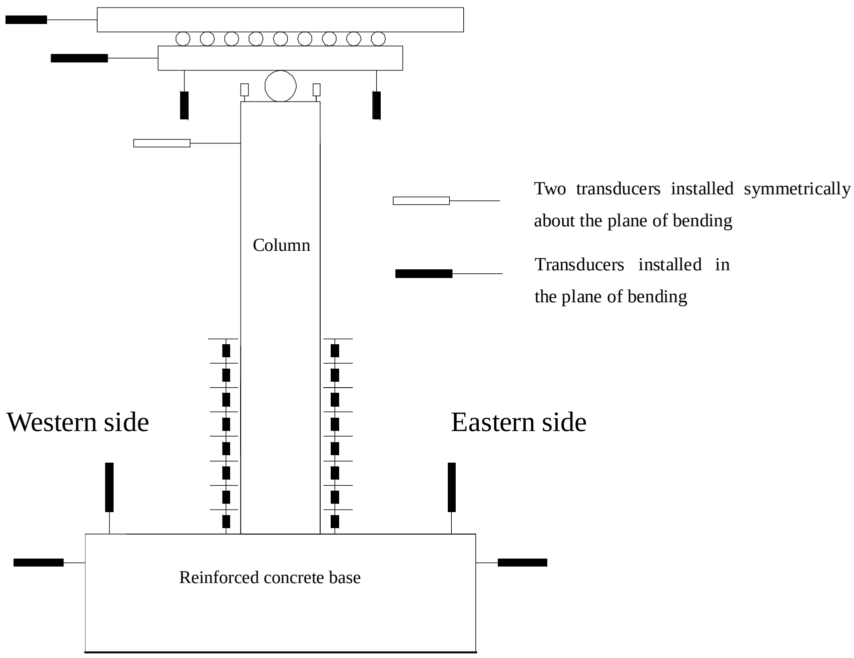


Figure 7.5 Layout of transducers

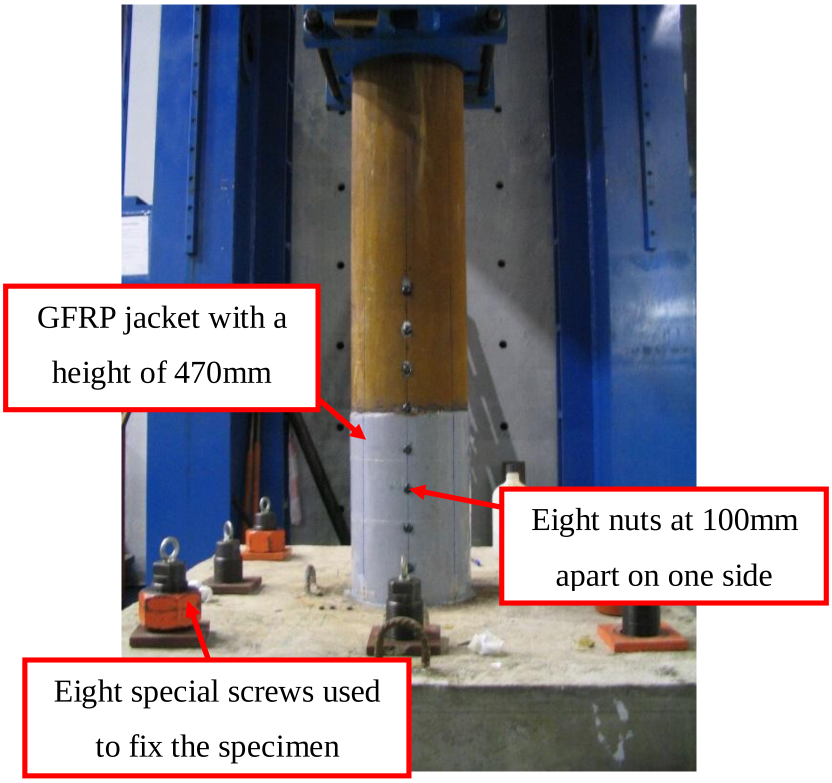


Figure 7.6 Column wrapped with a GFRP jacket and installed with nuts

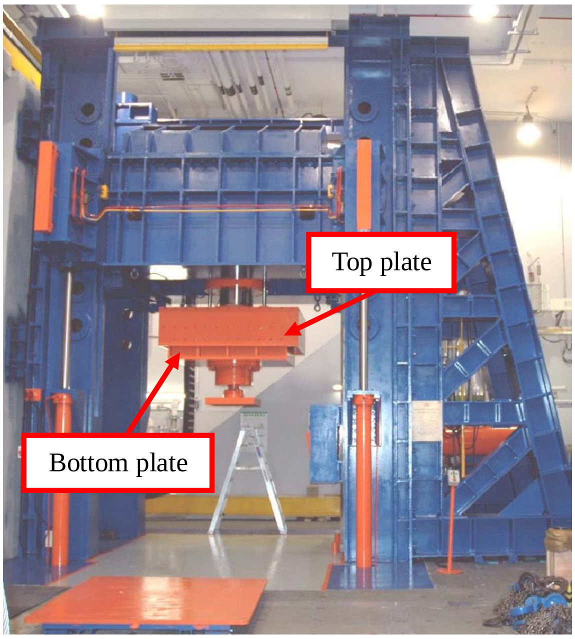


Figure 7.7 Testing frame

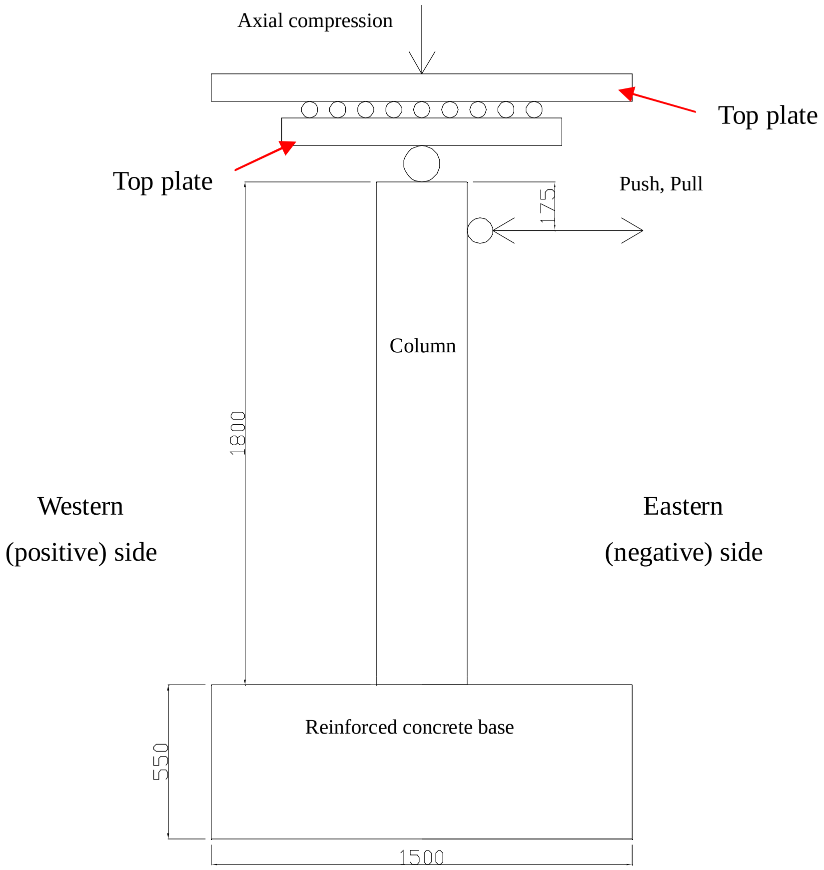


Figure 7.8 Schematic diagram of test set-up

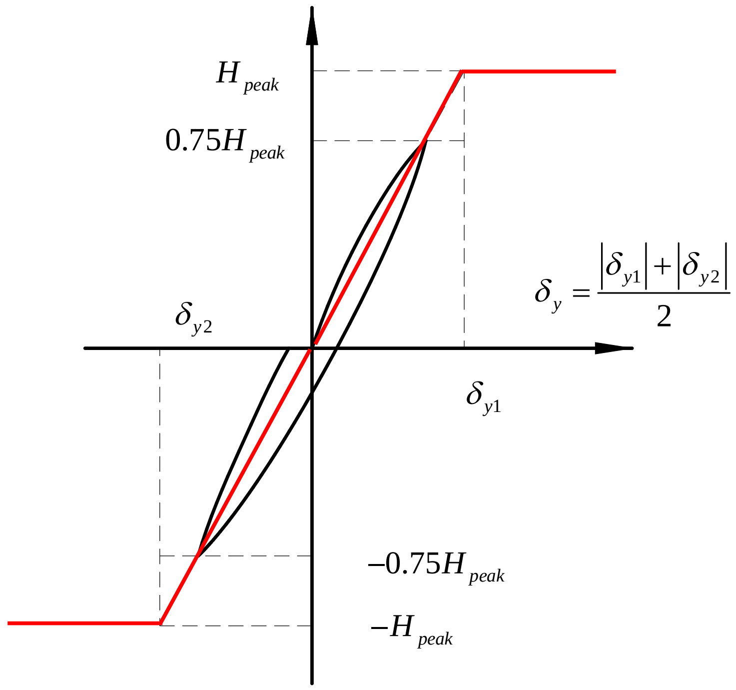


Figure 7.9 Experimental definition of yield displacement

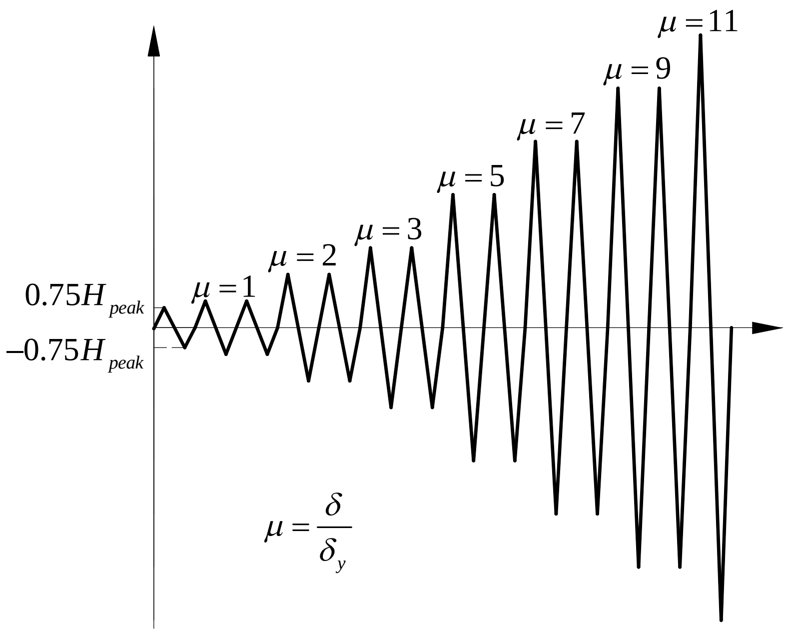


Figure 7.10 Applied lateral displacement history


Figure 7.11 Failure mode of column LCFT-0-106-E on the compression side

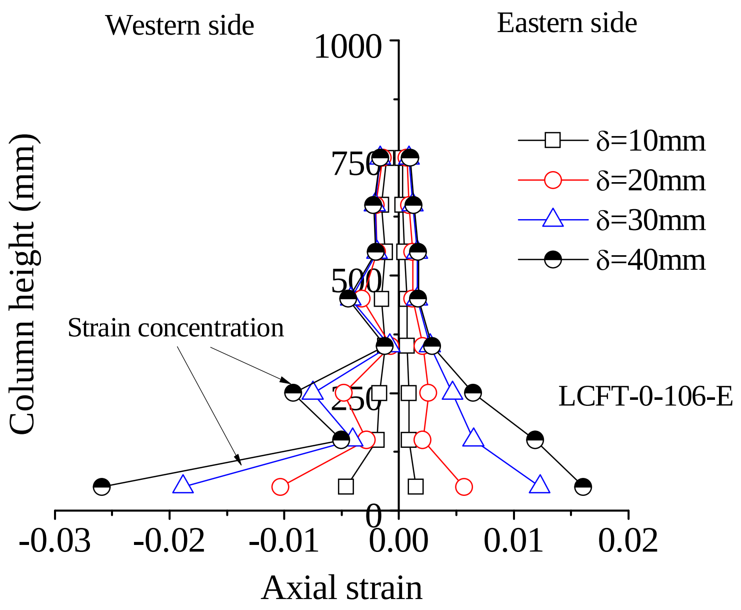


(a) Before and at $\delta$ =40mm

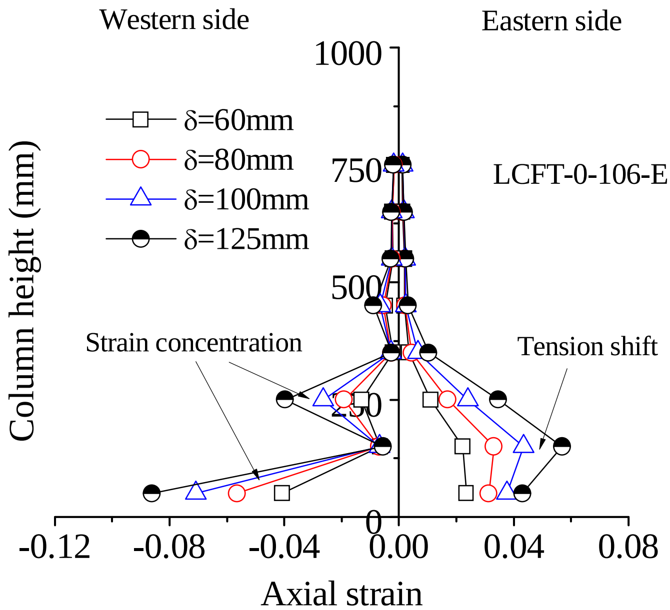


(b) At and after $\delta$ =60mm

Figure 7.12 Axial strain distributions along the height of column LCFT-0-106-E

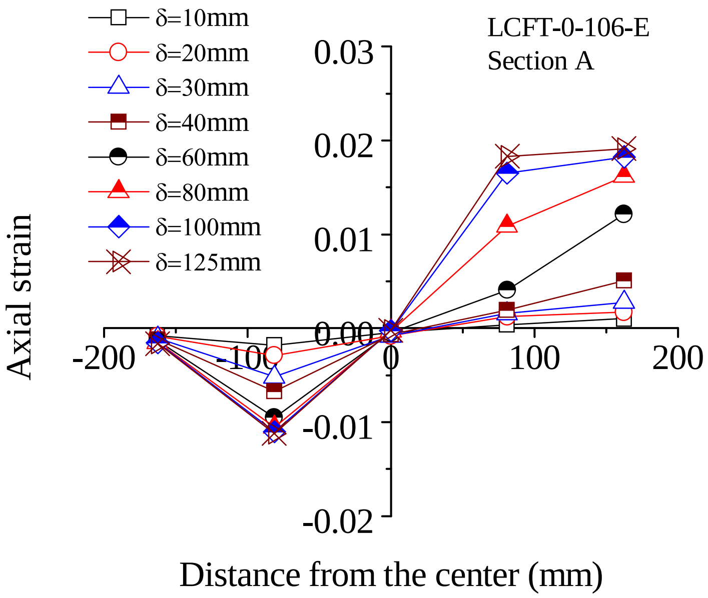


(a) Section A

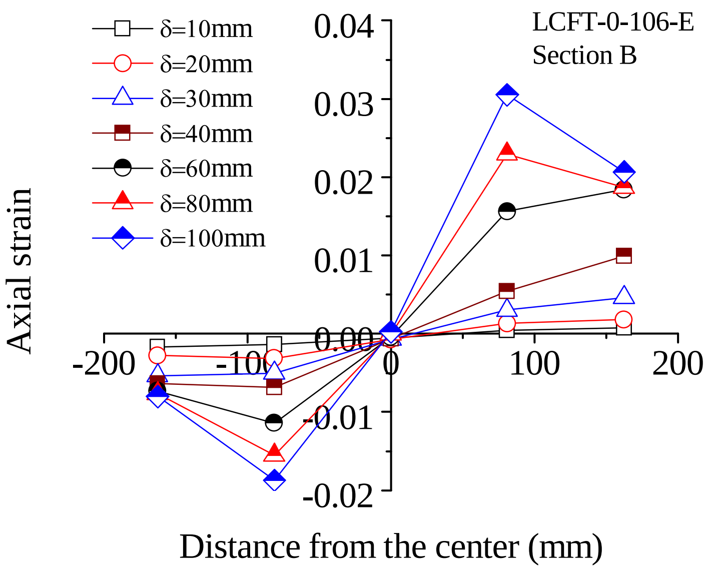


(b) Section B

Figure 7.13 Axial strain distributions on examined sections of column LCFT-0-106-E

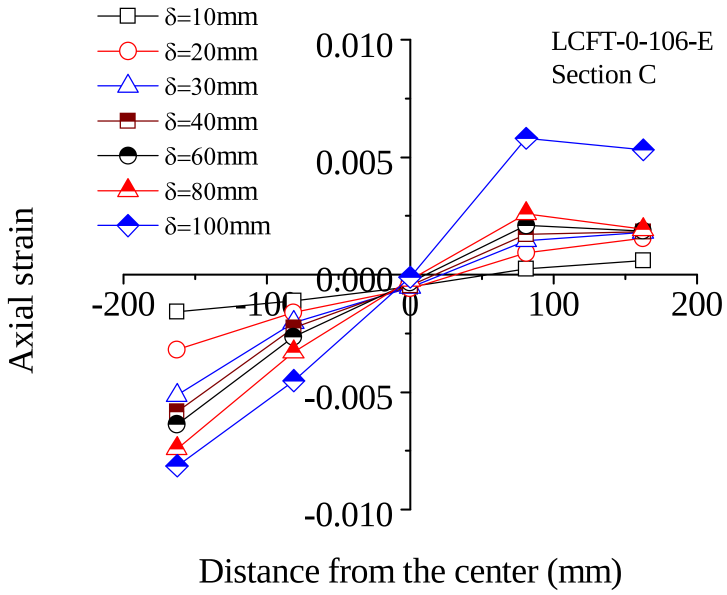


(c) Section C

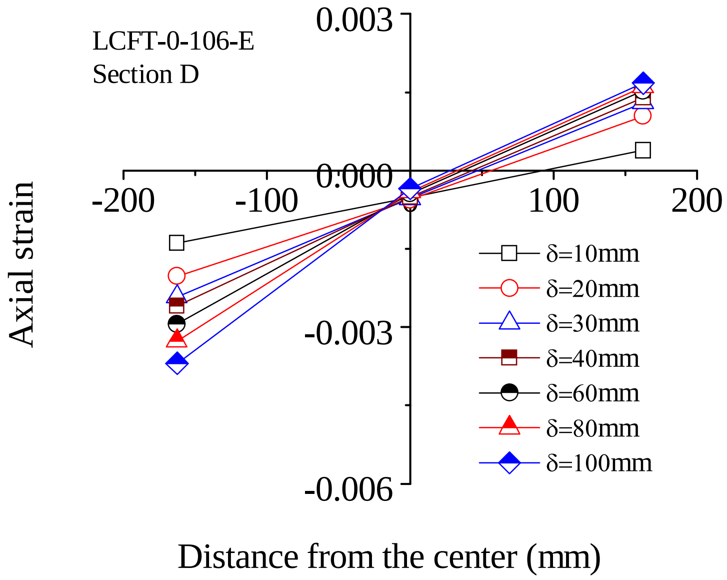


(d) Section D

Figure 7.13 Axial strain distributions on examined sections of column LCFT-0-106-E (continued)

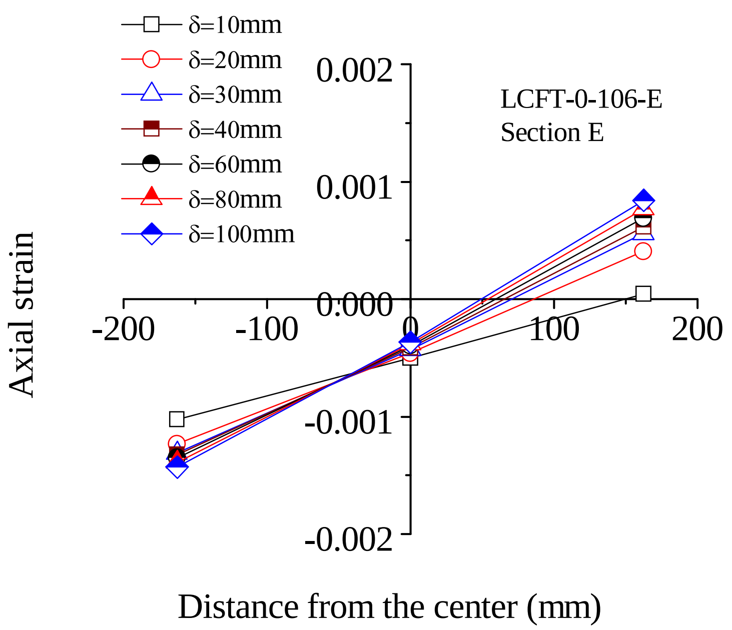


(e) Section E

Figure 7.13 Axial strain distributions on examined sections of column LCFT-0-106-E (continued)

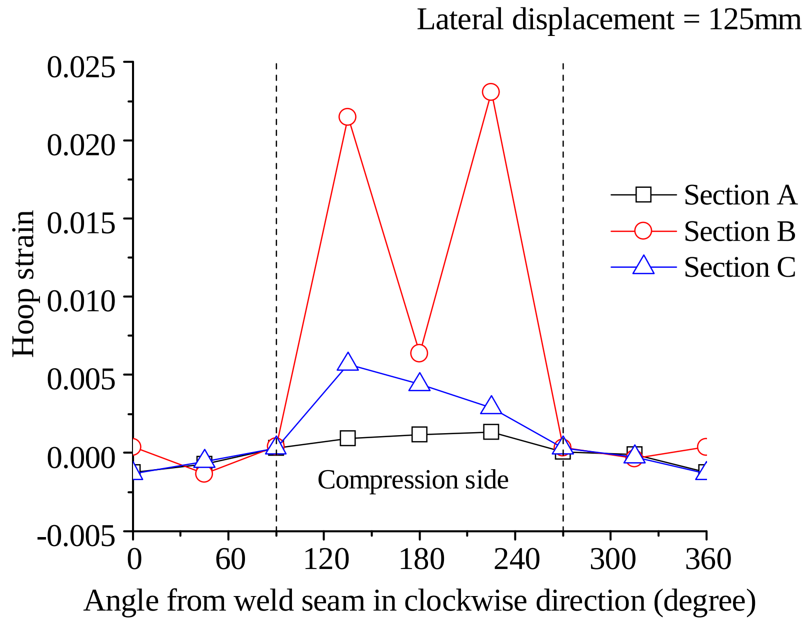


Figure 7.14 Hoop strain distributions on the bottom three sections of column LCFT-0-106-E

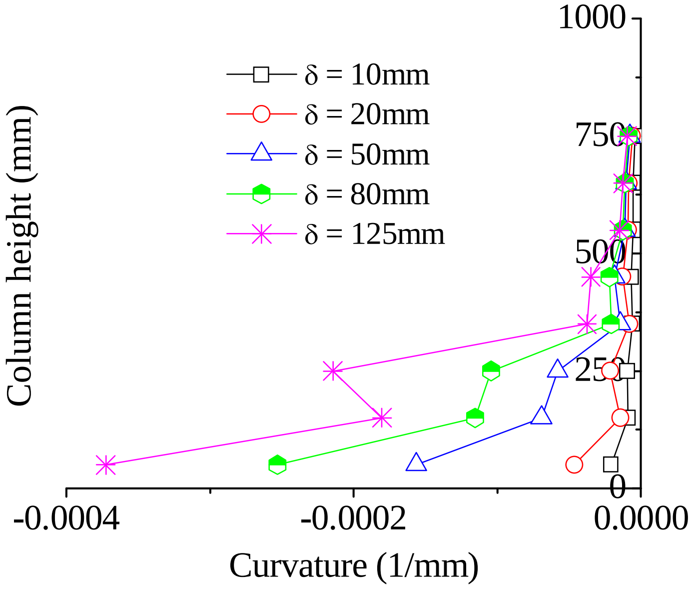


Figure 7.15 Curvature distributions along the height of column LCFT-0-106-E

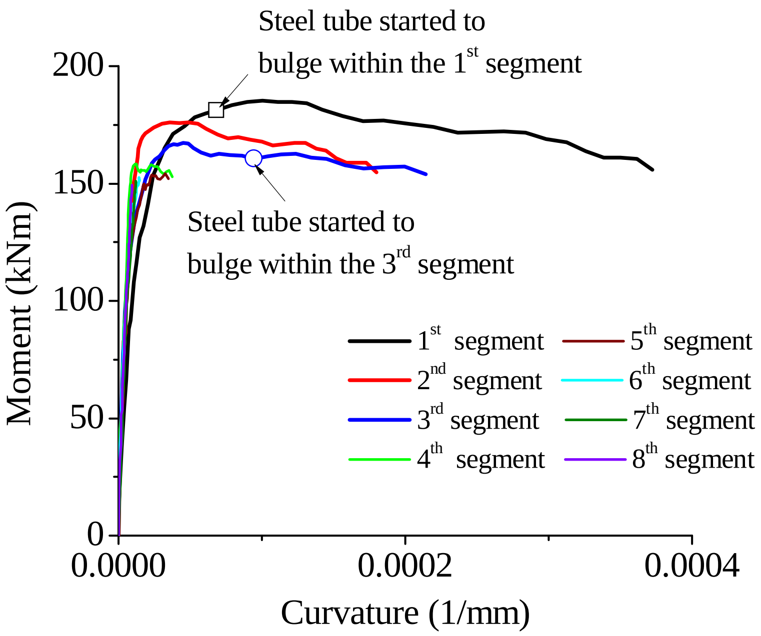


Figure 7.16 Moment-curvature curves of different segments of column LCFT-0-106-E

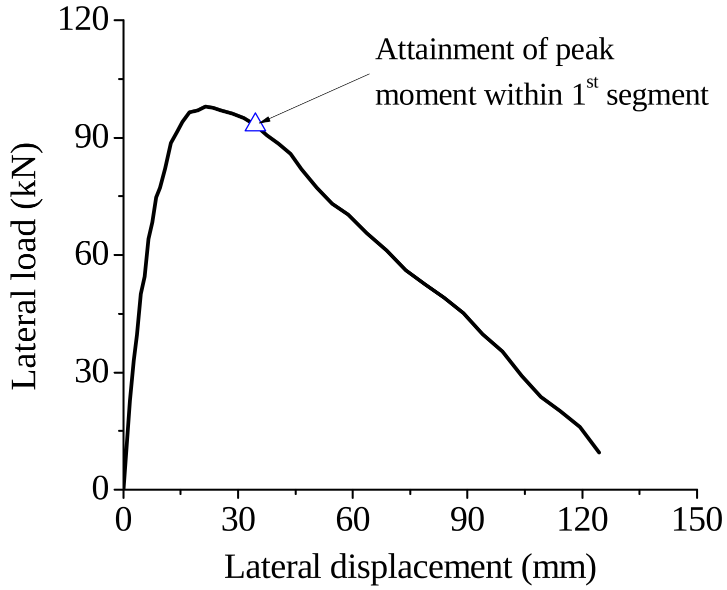


Figure 7.17 Lateral load-displacement curve of column LCFT-0-106-E

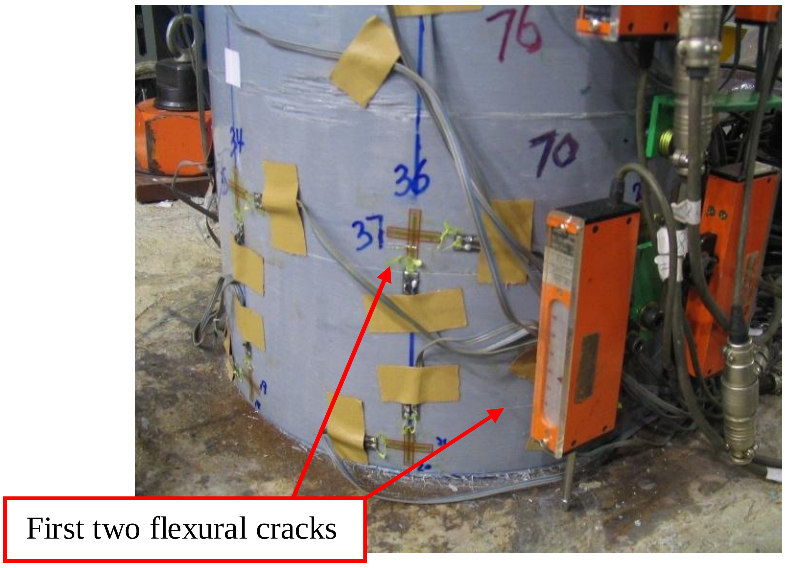


(a) $\delta$ =18mm

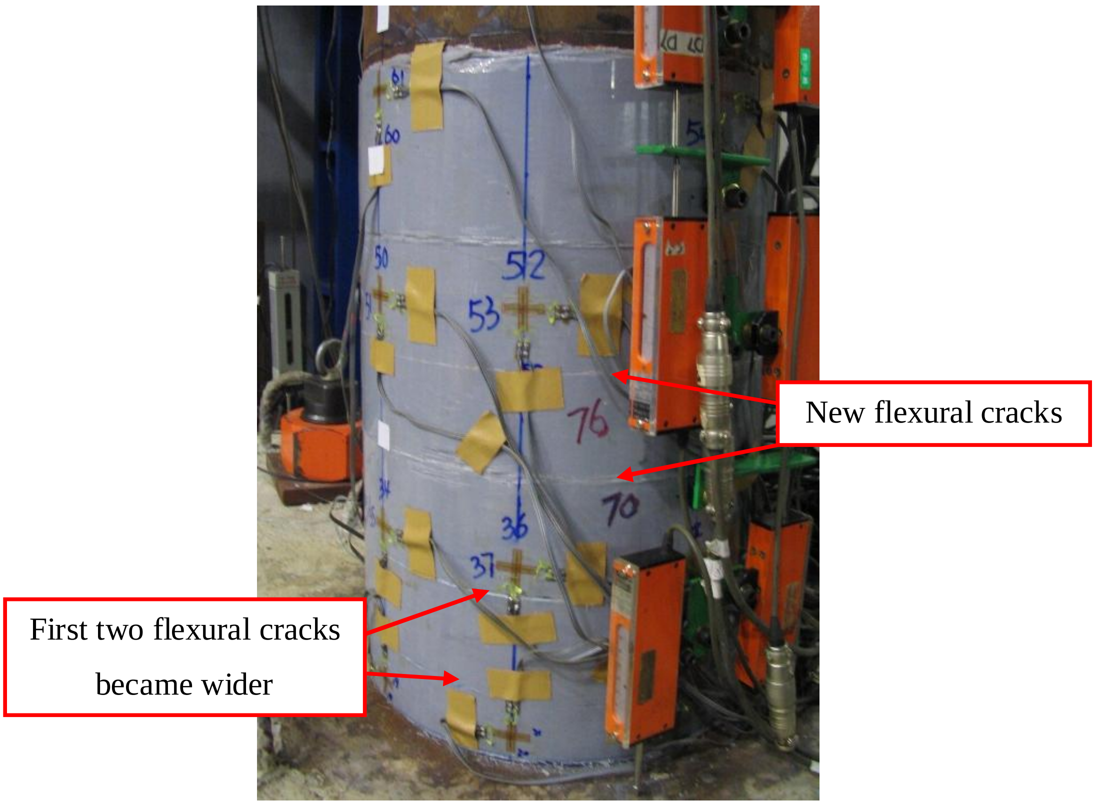


(b) $\delta$ =43mm

Figure 7.18 Column LCFT-5G-106-E at different lateral displacement levels


(c) $\delta$ =125mm

Figure 7.18 Column LCFT-5G-106-E at different lateral displacement levels (continued)

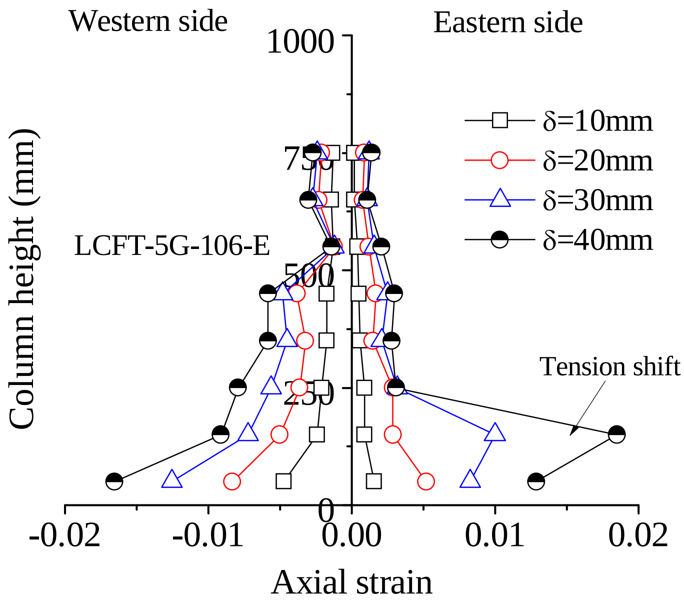


(a) Before and at $\delta$ =40mm

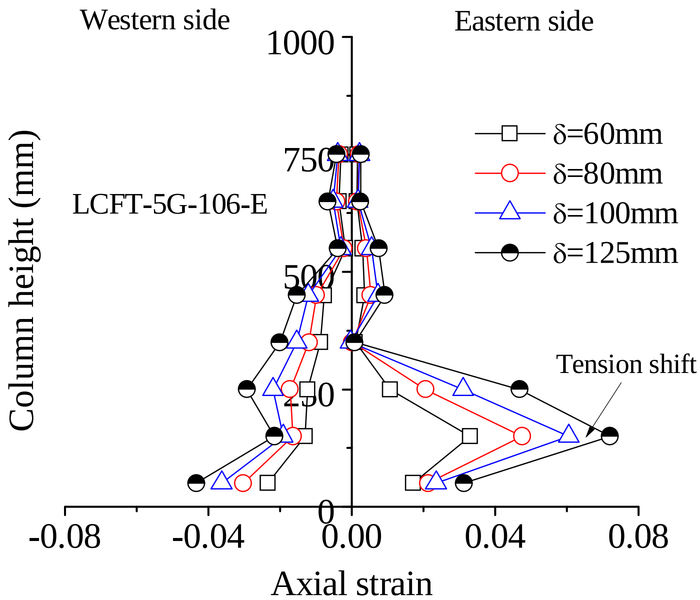


(b) At and after $\delta$ =60mm

Figure 7.19 Extreme fibre axial strain distributions of column LCFT-5G-106-E

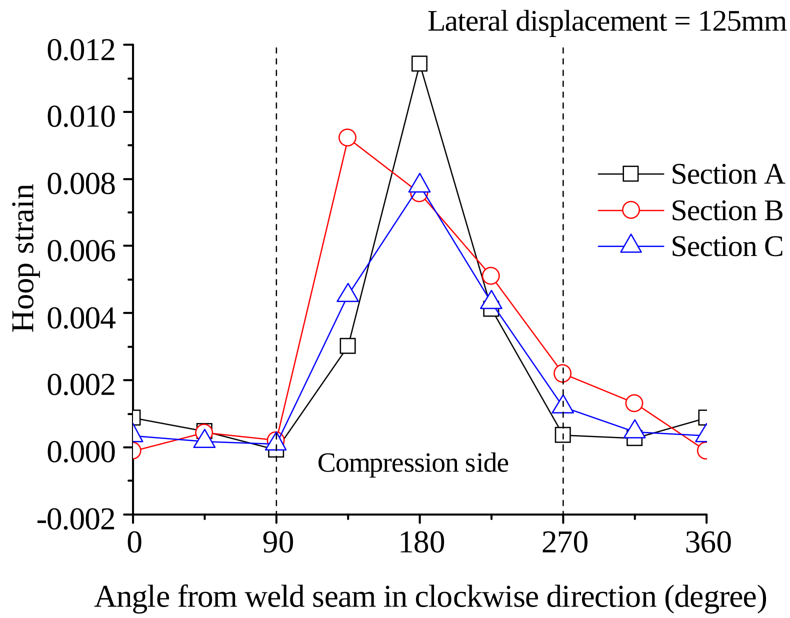


Figure 7.20 Hoop strain distributions on the bottom three sections of column LCFT-0-106-E

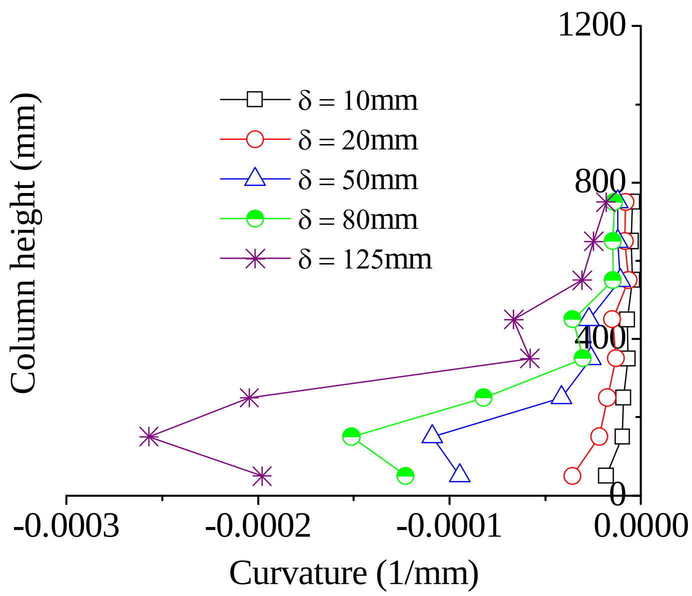


Figure 7.21 Curvature distributions along the height of column LCFT-5G-106-E

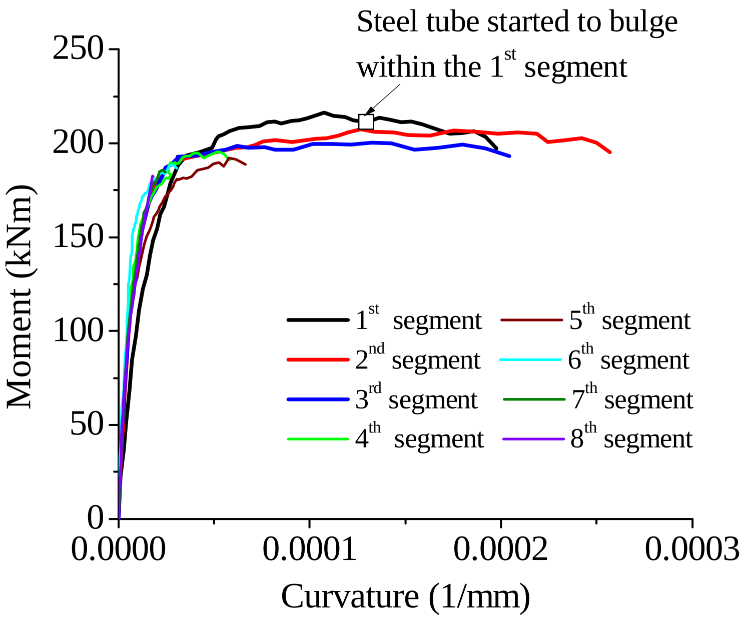


Figure 7.22 Moment-curvature curves of different segments of column LCFT-5G-106-E

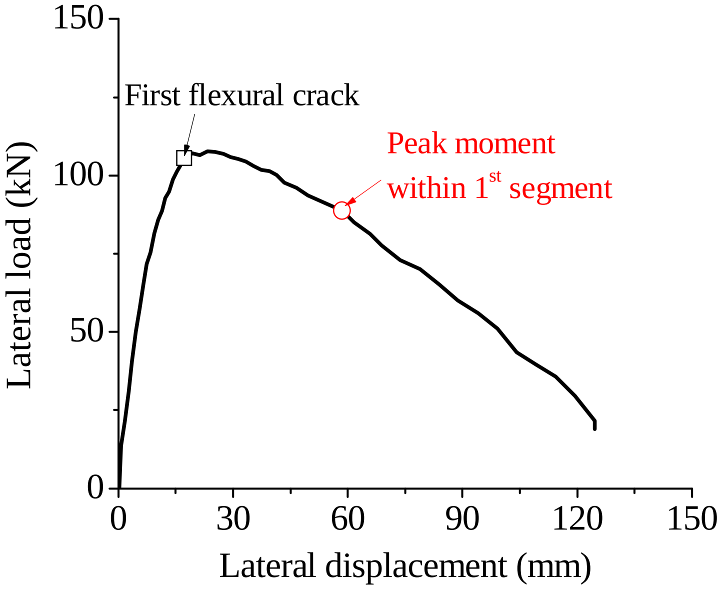


Figure 7.23 Load-displacement curve of column LCFT-5G-106-E

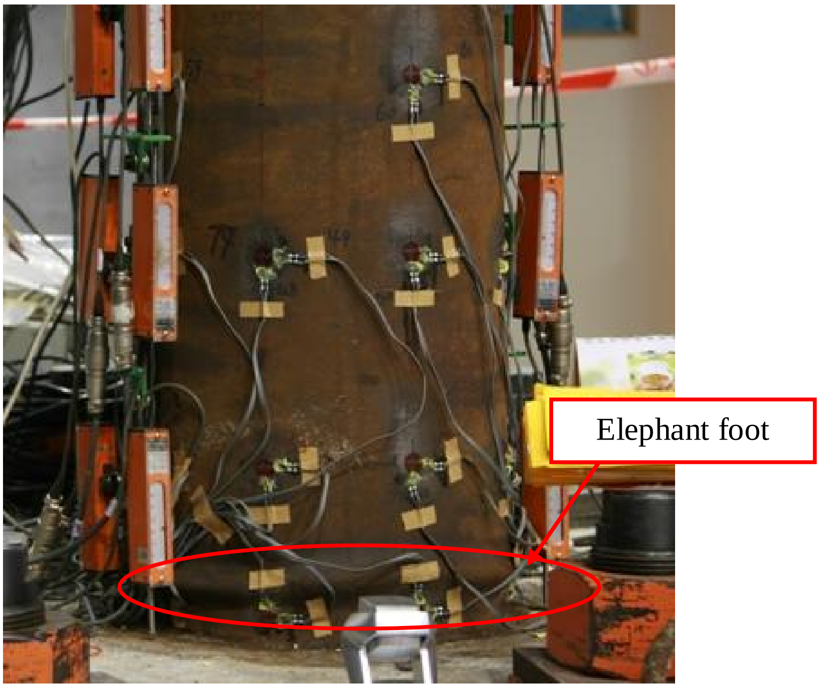


Figure 7.24 Buckling deformation near the end at $9\delta_y$ of column LCFT-0-106-F

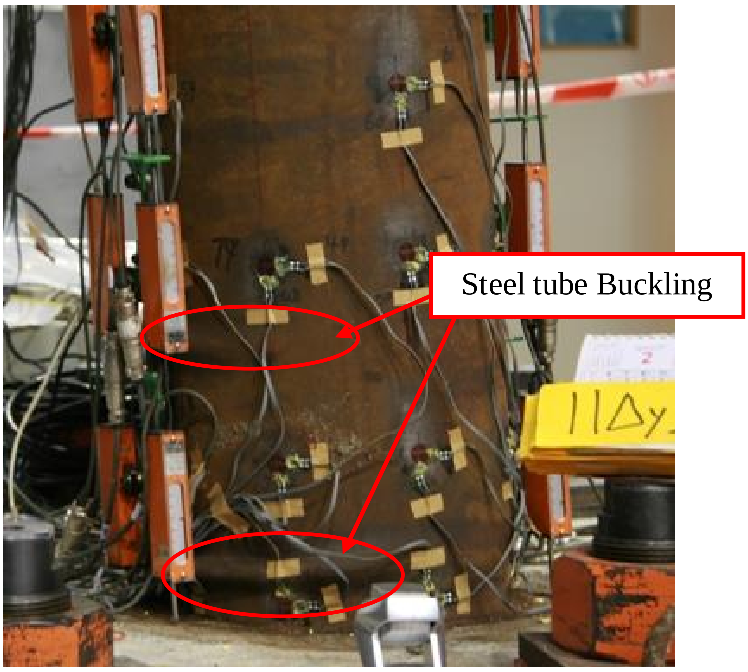


Figure 7.25 Column LCFT-0-106-F at $11\delta_y$

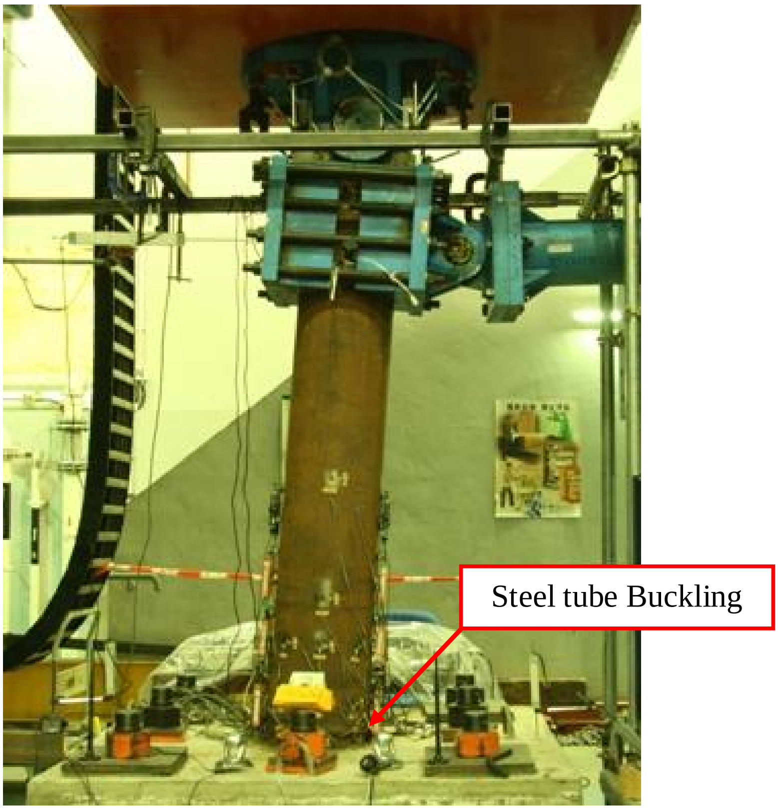


Figure 7.26 Column LCFT-0-106-F at $-11\delta_y$

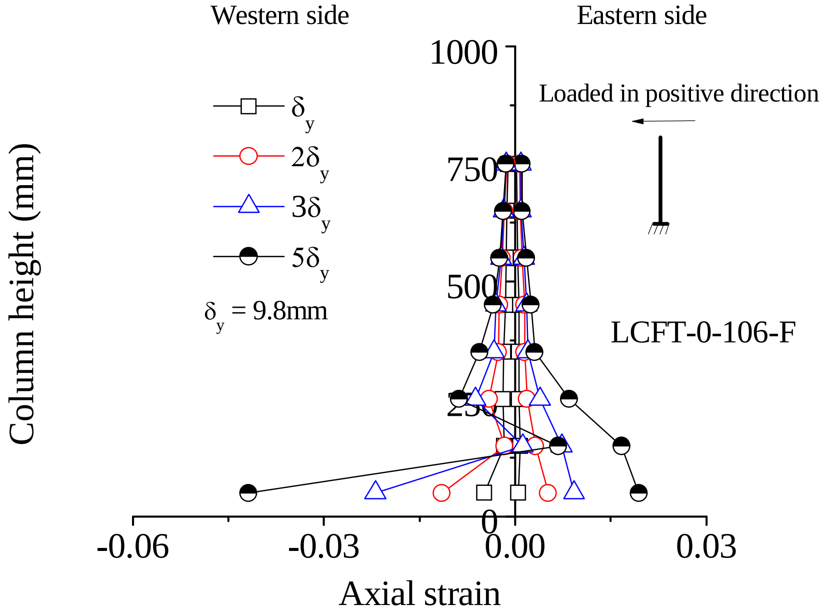


(a) Before and at $5\delta_y$

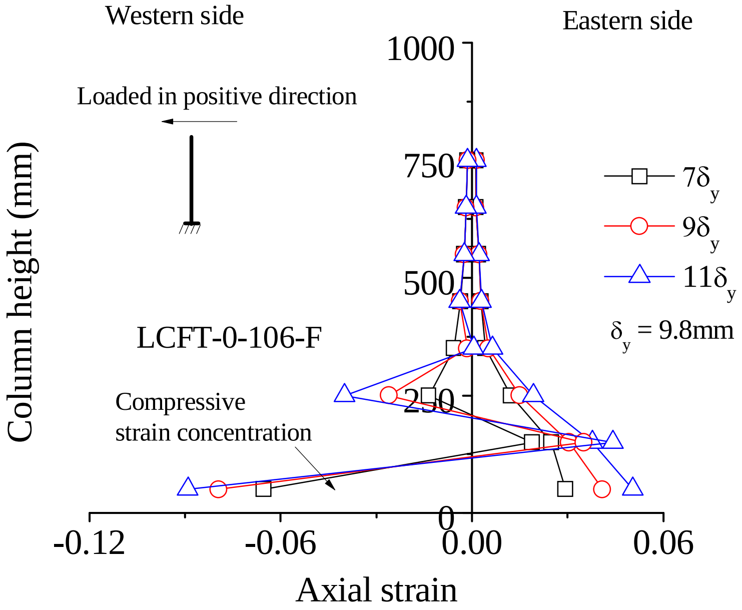


(b) At and after $7\delta_y$

Figure 7.27 Axial strain distributions along the height of column LCFT-0-106-F

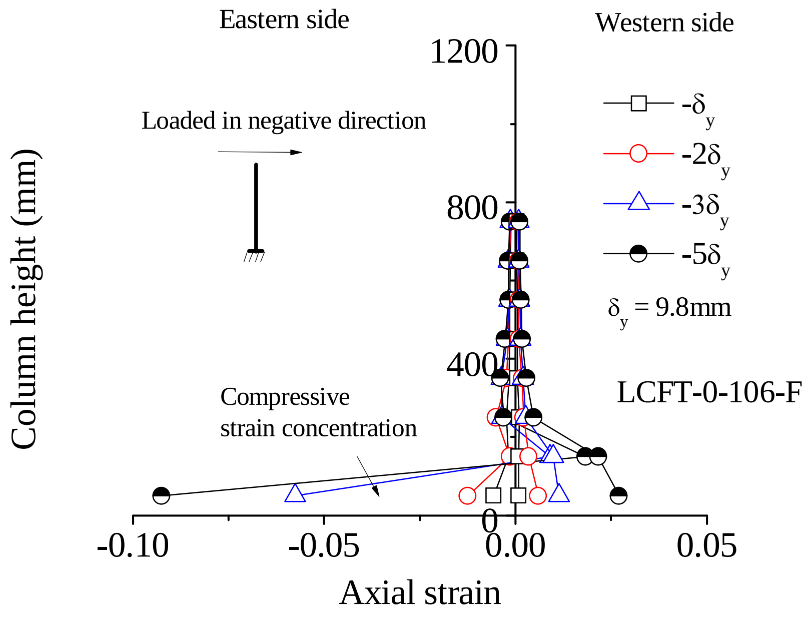


(c) Before and at $-5\delta_y$

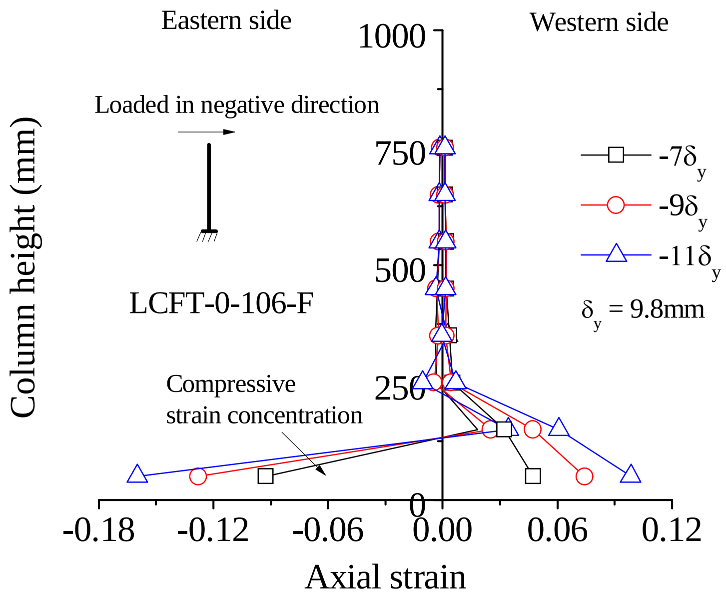


(d) At and after $-7\delta_y$

Figure 7.27 Axial strain distributions along the height of column LCFT-0-106-F (continued)

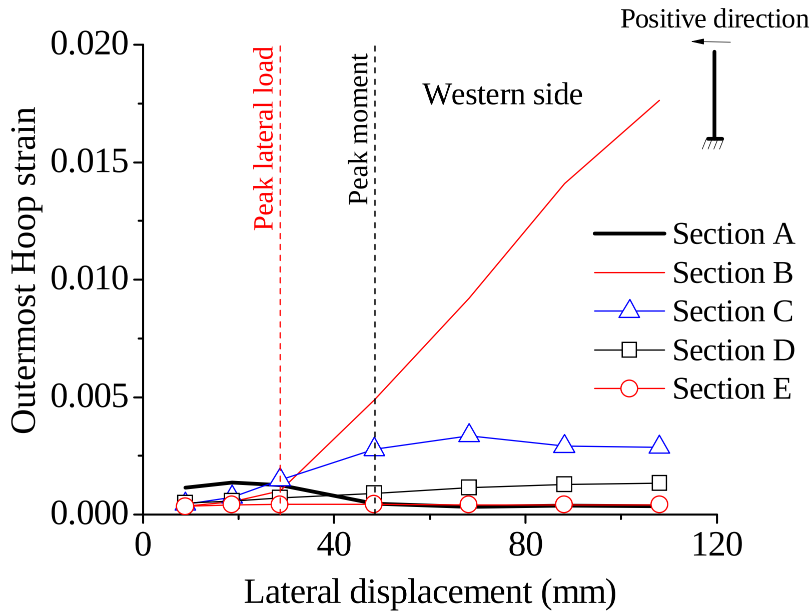


Figure 7.28 Extreme compression fibre lateral strain histories of column LCFT-0-106-F on the western side

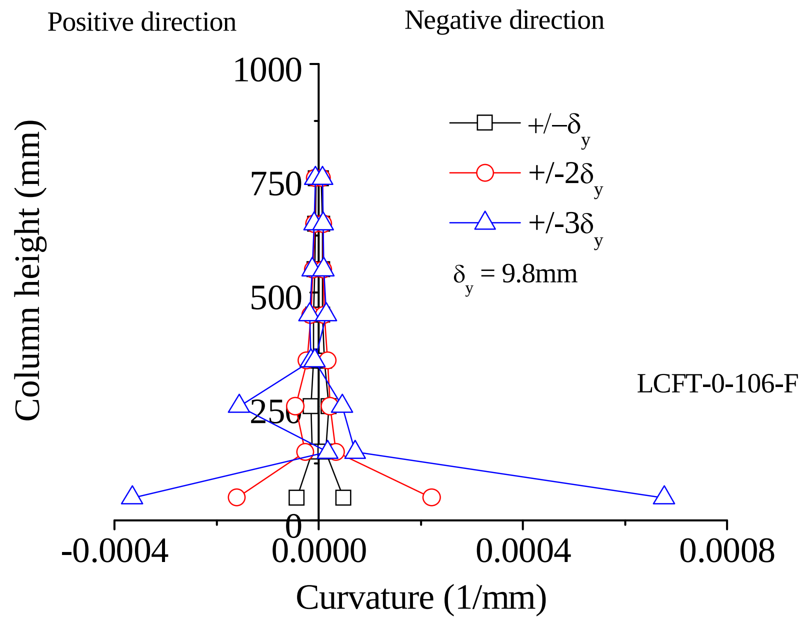


(a) Before and at $\pm 3\delta_y$

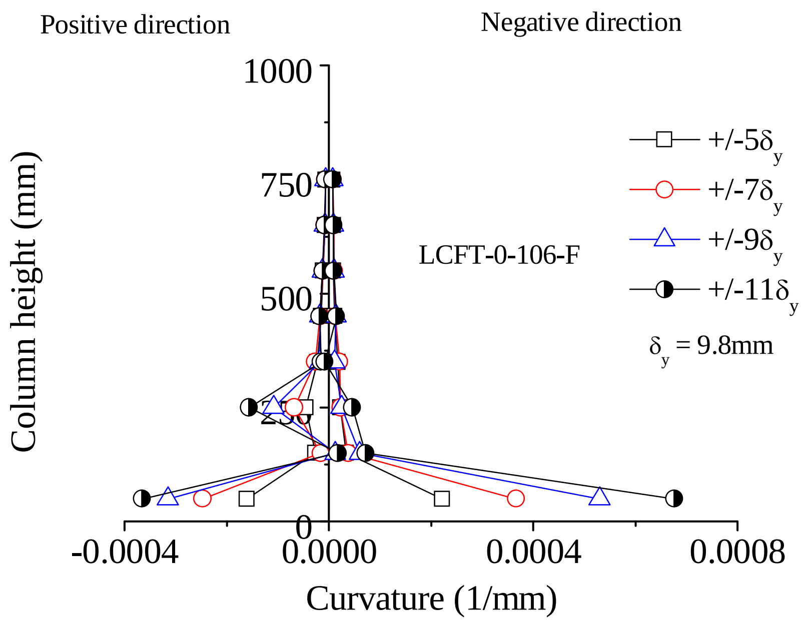


(b) At and after $\pm 5\delta_y$

Figure 7.29 Curvature distributions along the height of column LCFT-0-106-F

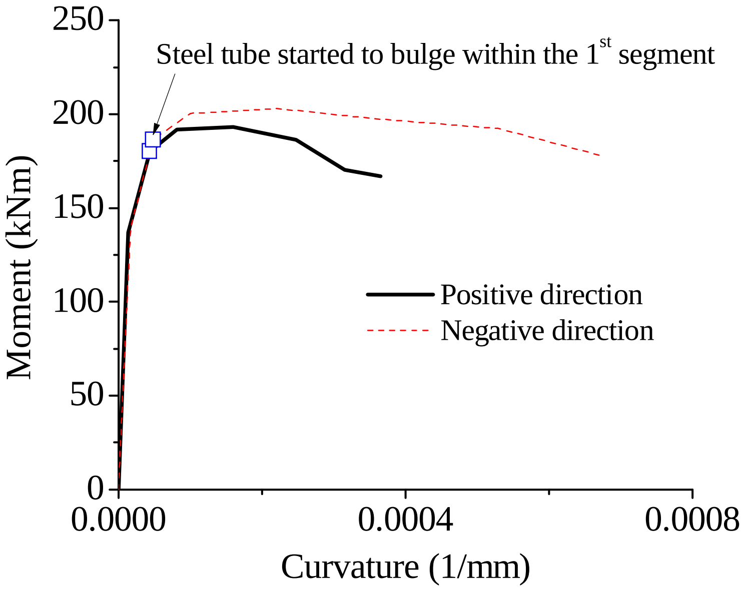


Figure 7.30 Envelope moment-curvature curves of column LCFT-0-106-F

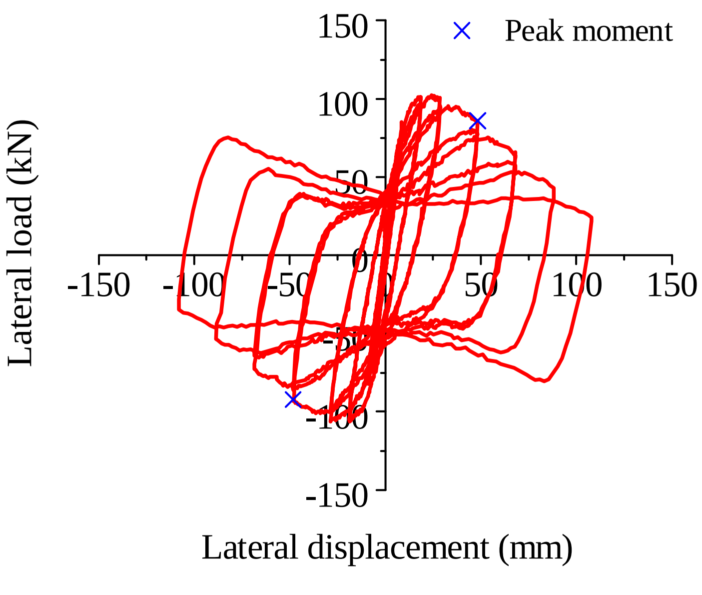


Figure 7.31 Lateral load-displacement curve of column LCFT-0-106-F

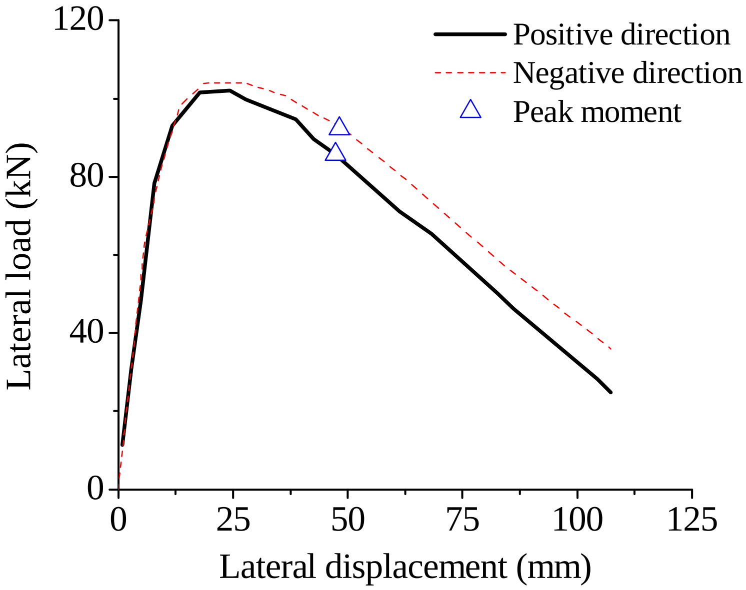


Figure 7.32 Envelope lateral load-displacement curves of column LCFT-0-106-F

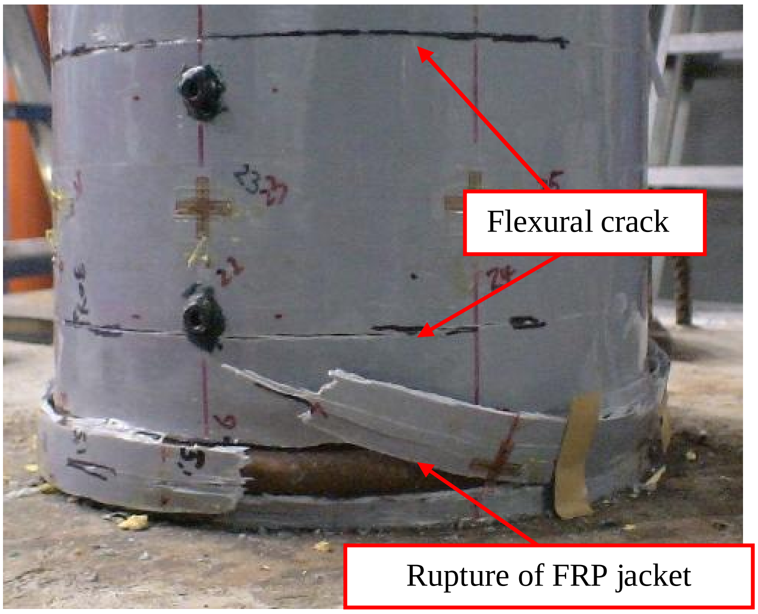


(a) Eastern side

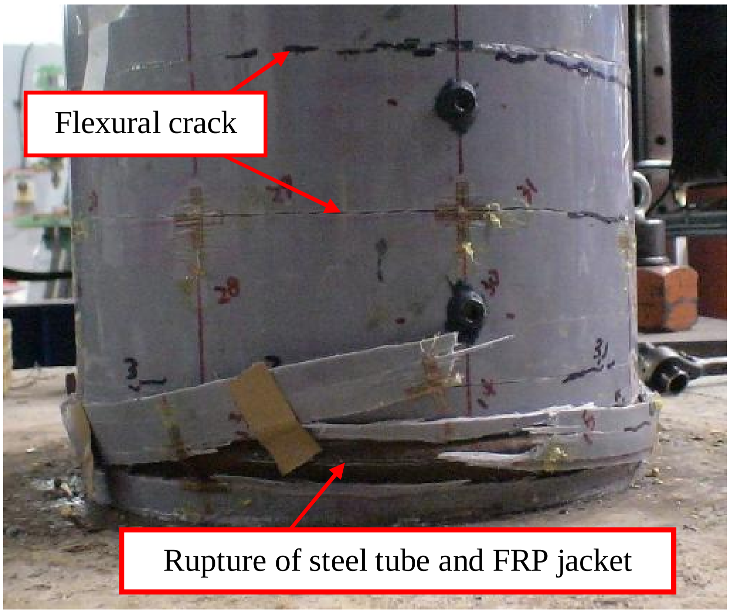


(b) Western side

Figure 7.33 Column LCFT-5G-106-F after test

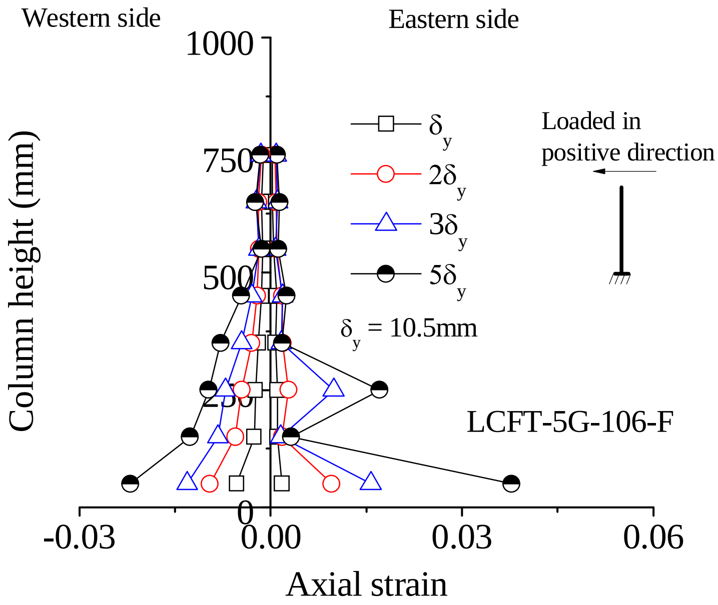


(a) Before and at $5\delta_y$

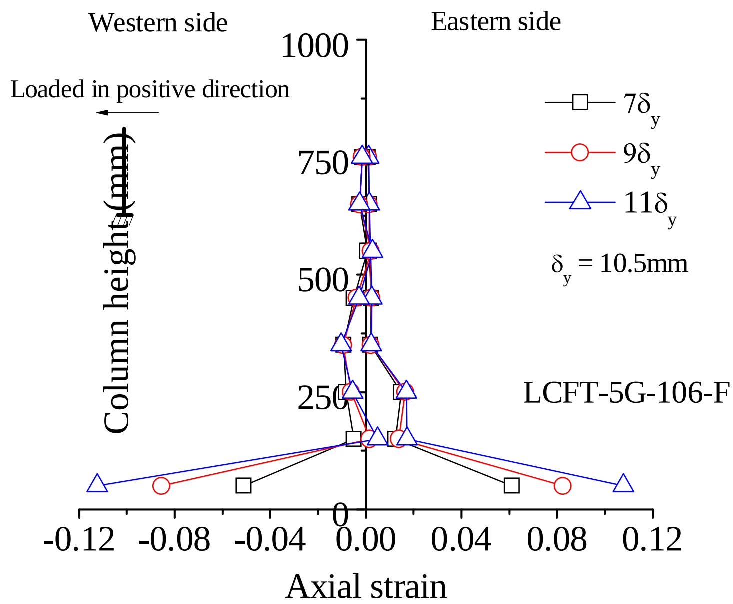


(b) At and after $7\delta_y$

Figure 7.34 Axial strain distributions along the height of column LCFT-5G-106-F

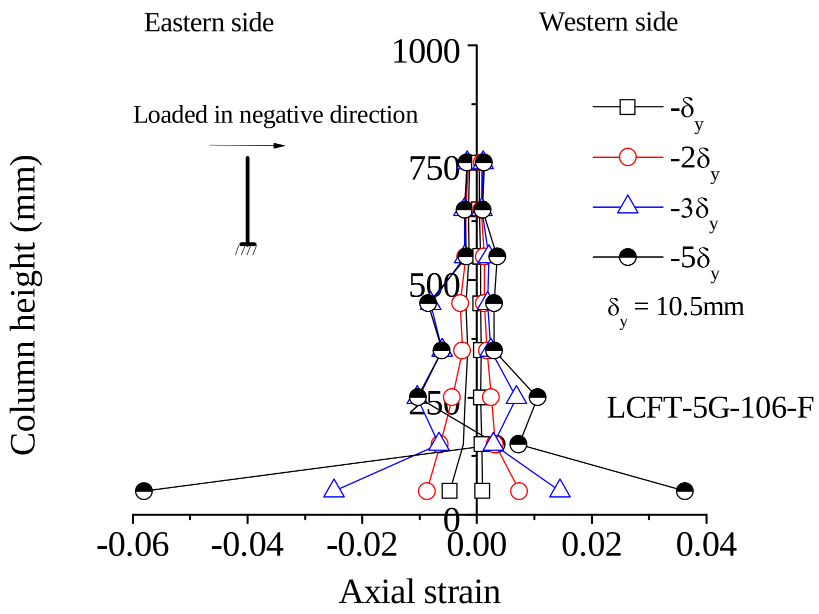


(c) Before and at $-5\delta_y$

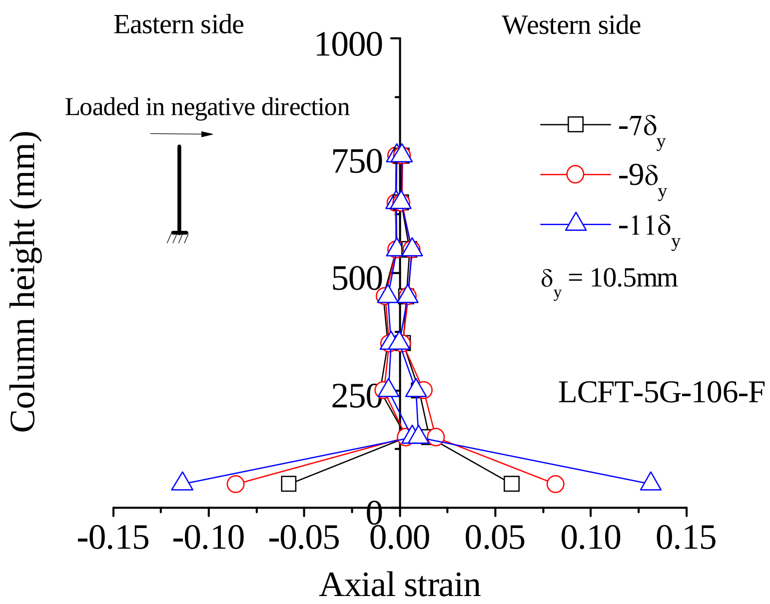


(d) At and after $-7\delta_y$

Figure 7.34 Axial strain distributions along the height of column LCFT-5G-106-F (continued)

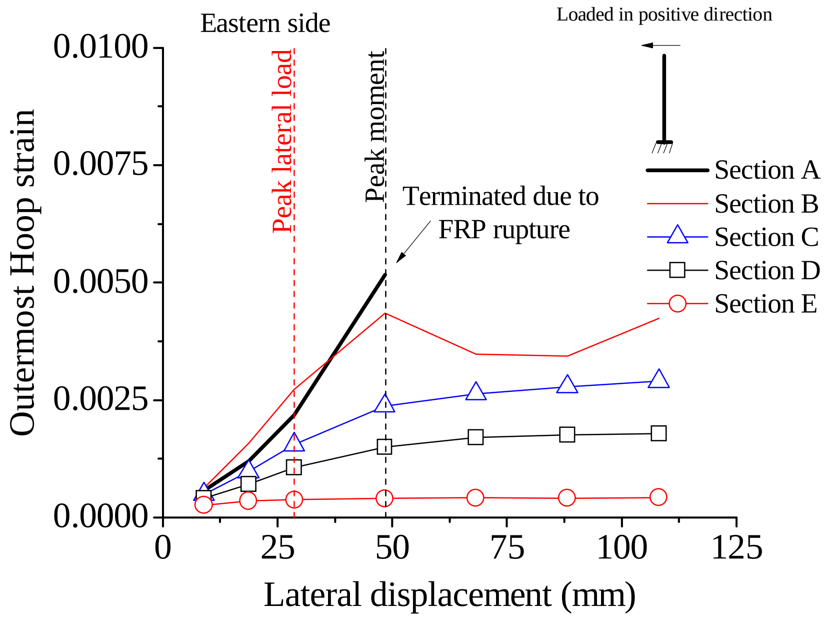


Figure 7.35 Extreme compression fibre lateral strain histories of column LCFT-5G-106-F on the eastern side

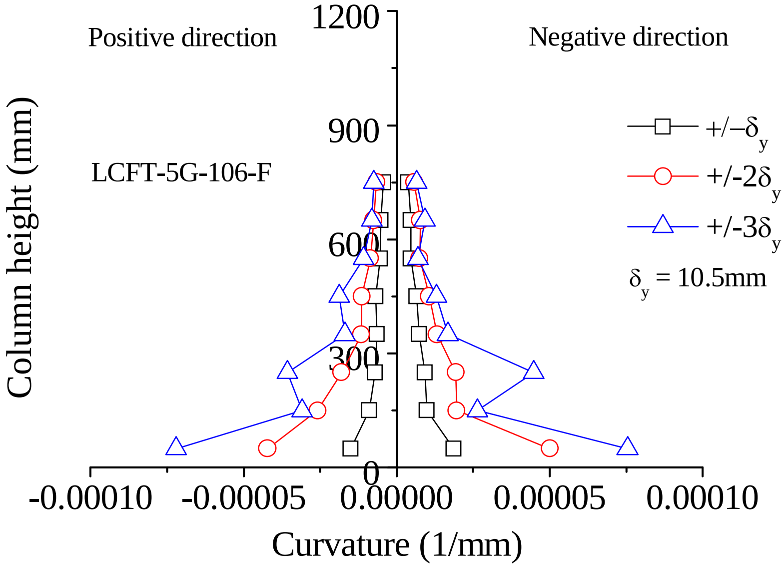


(a) Before and at $\pm 3\delta_y$

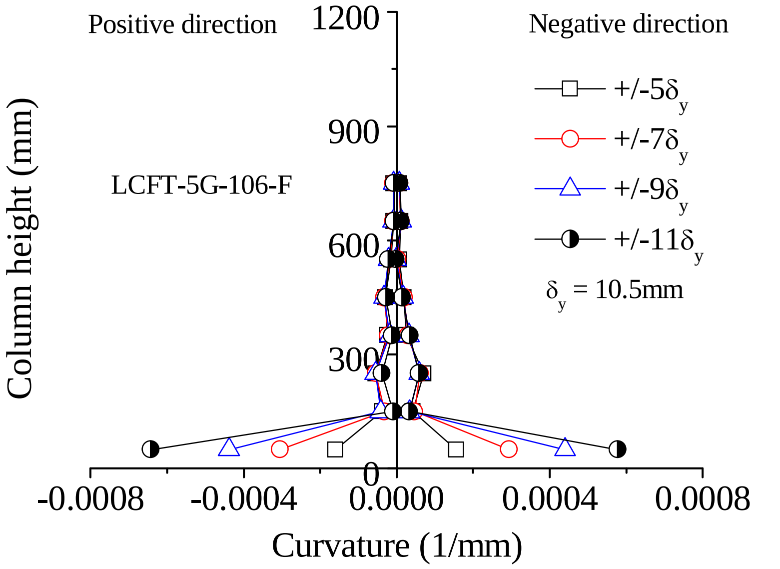


(b) At and after $\pm 5\delta_y$

Figure 7.36 Curvature distributions along the height of column LCFT-5G-106-F

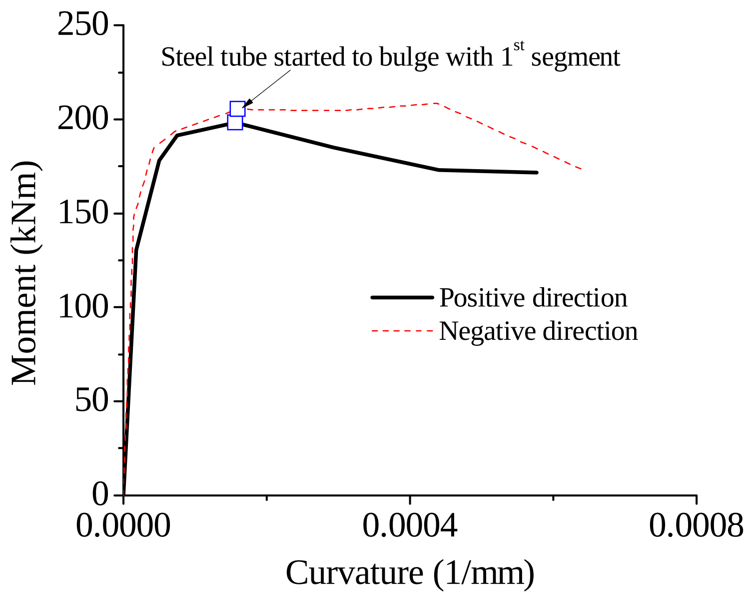


Figure 7.37 Envelope moment-curvature curves of column LCFT-5G-106-F

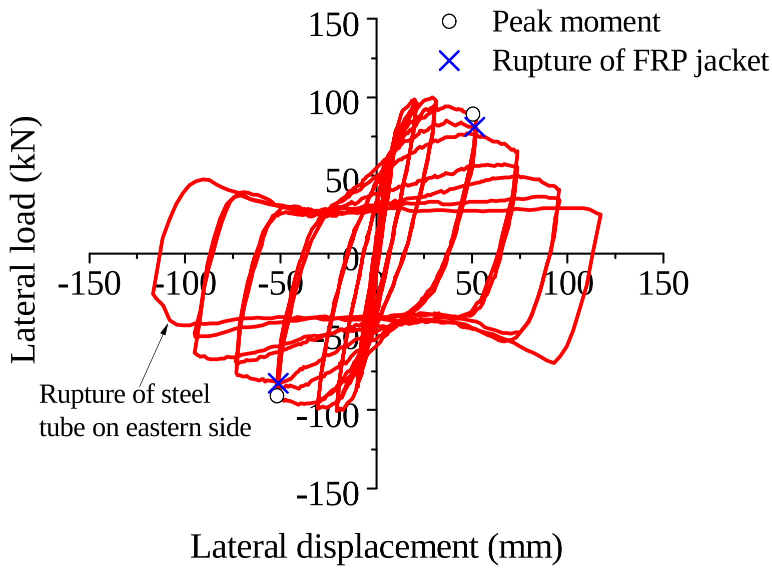


Figure 7.38 Lateral load-displacement curve of column LCFT-5G-106-F

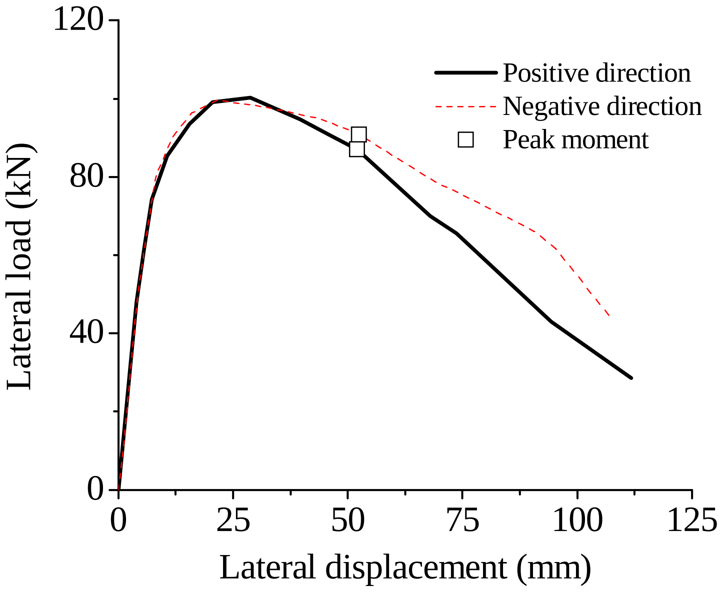


Figure 7.39 Envelope lateral load-displacement curves of column LCFT-5G-106-F

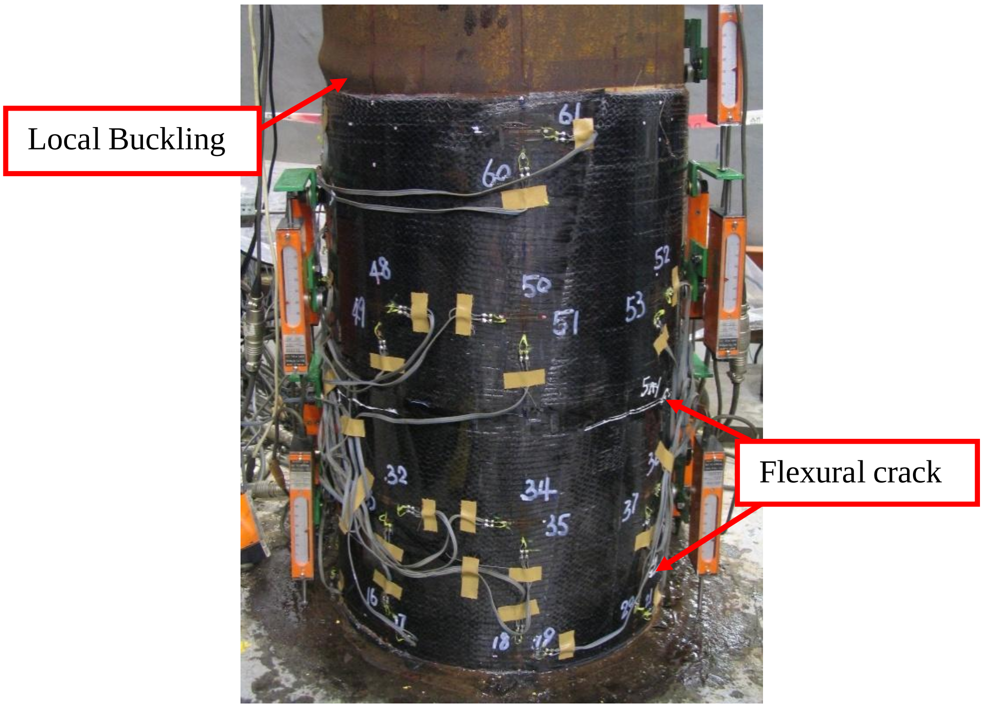


(a) $11\delta_y$

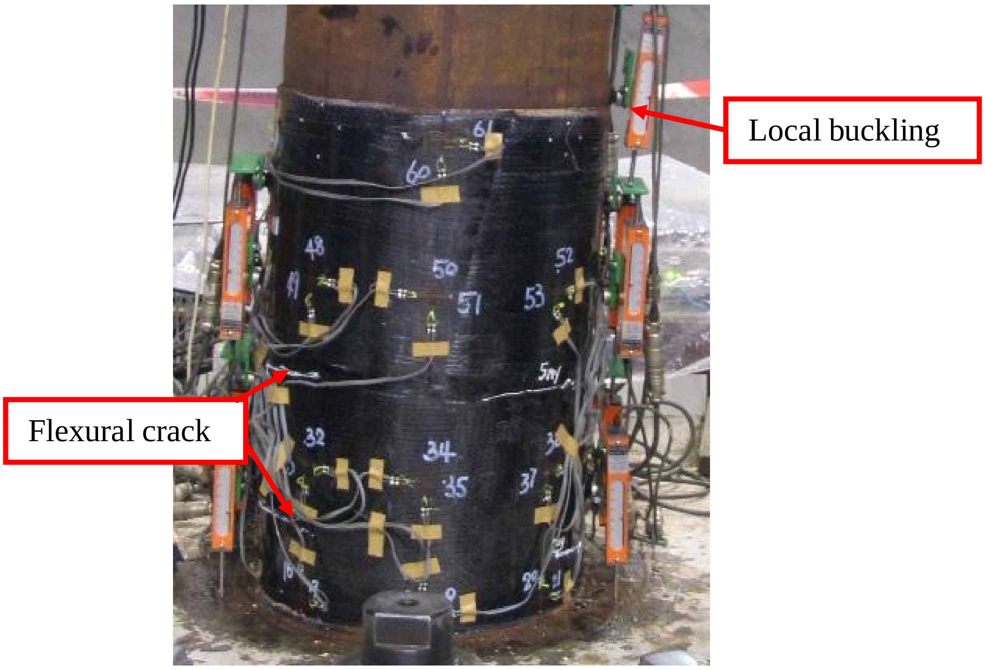


(b) $-11\delta_y$

Figure 7.40 Column LCFT-6C-106-F after test

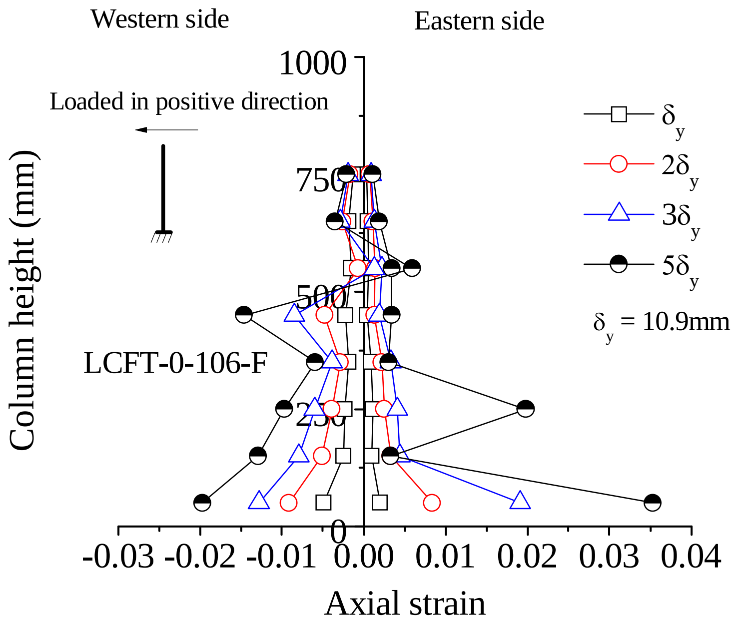


(a) Before and at $5\delta_y$

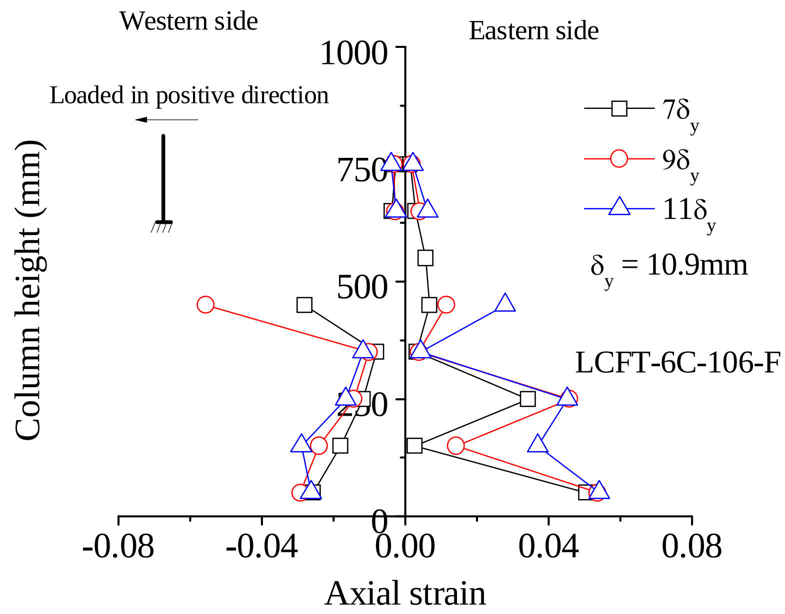


(b) At and after $7\delta_y$

Figure 7.41 Axial strain distributions along the height of column LCFT-6C-106-F

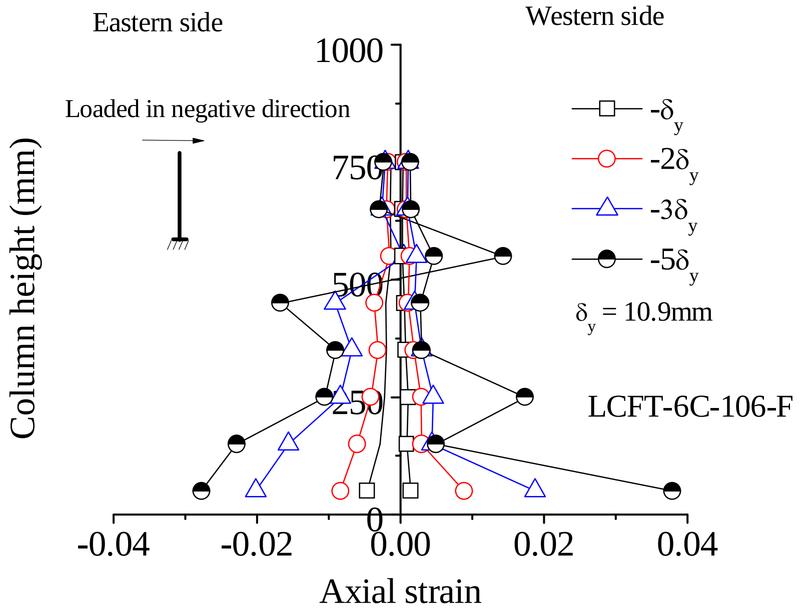


(c) Before and at $-5\delta_y$

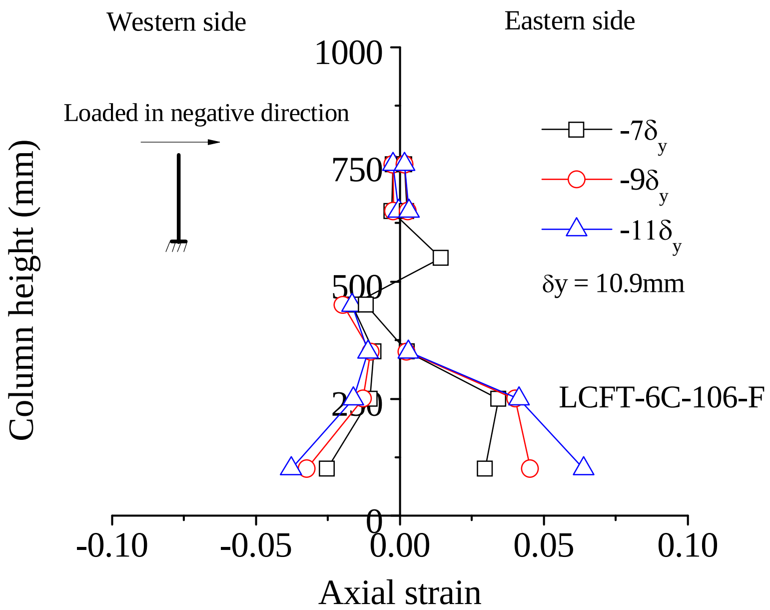


(d) At and after $-7\delta_y$

Figure 7.41 Axial strain distributions along the height of column LCFT-6C-106-F (continued)


Figure 7.42 Inactivation of LVDTs due to bulging

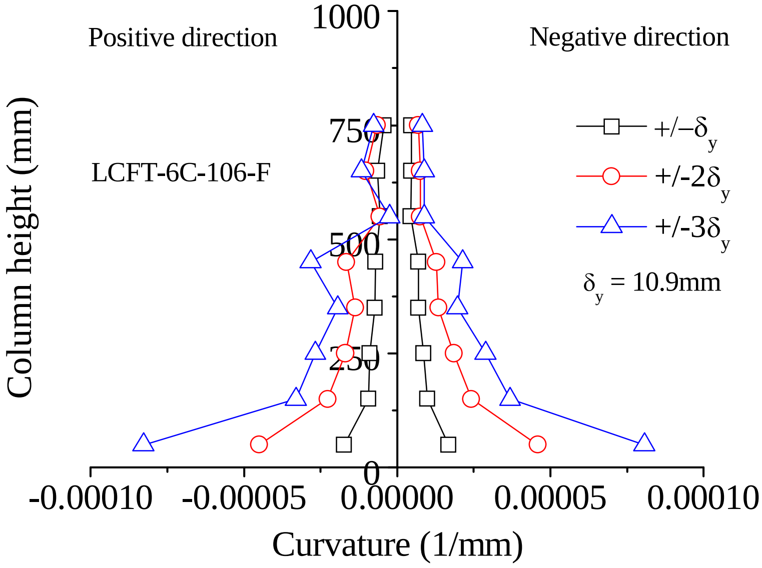


(a) Before and at $\pm 3\delta_y$

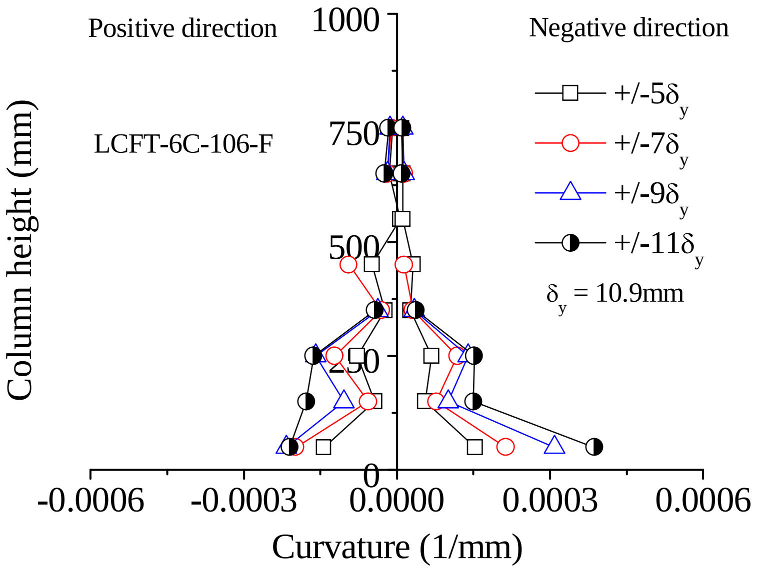


(b) At and after $\pm 5\delta_y$

Figure 7.43 Curvature distributions along the height of column LCFT-6C-106-F

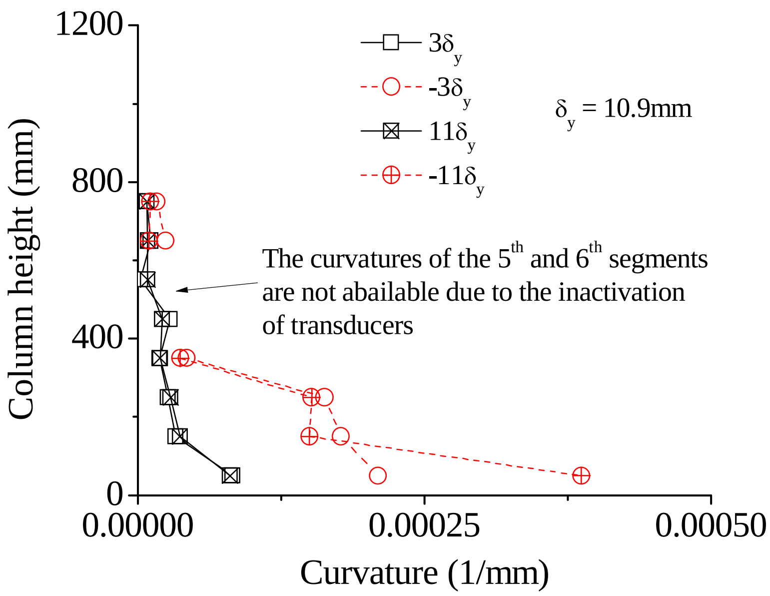


Figure 7.44 Comparison of curvature distributions between the two sides of column LCFT-5G-106-F

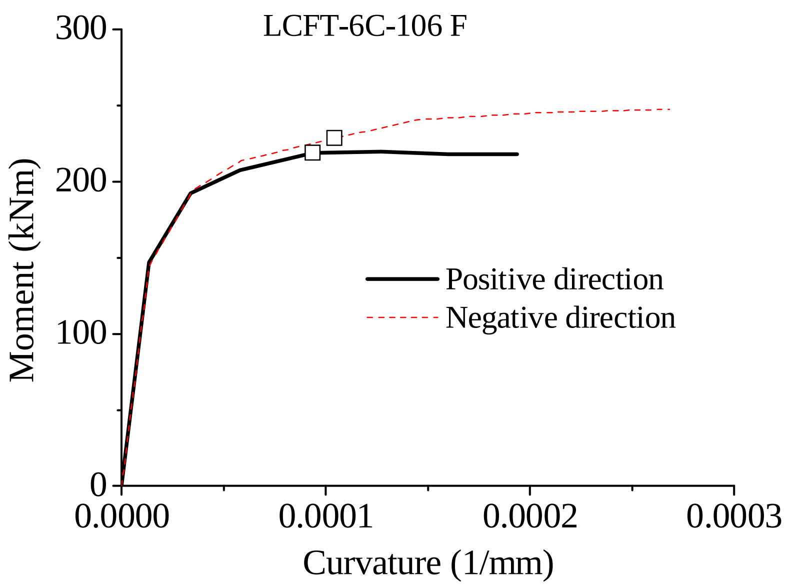


Figure 7.45 Envelope moment-curvature curves of column LCFT-6C-106-F

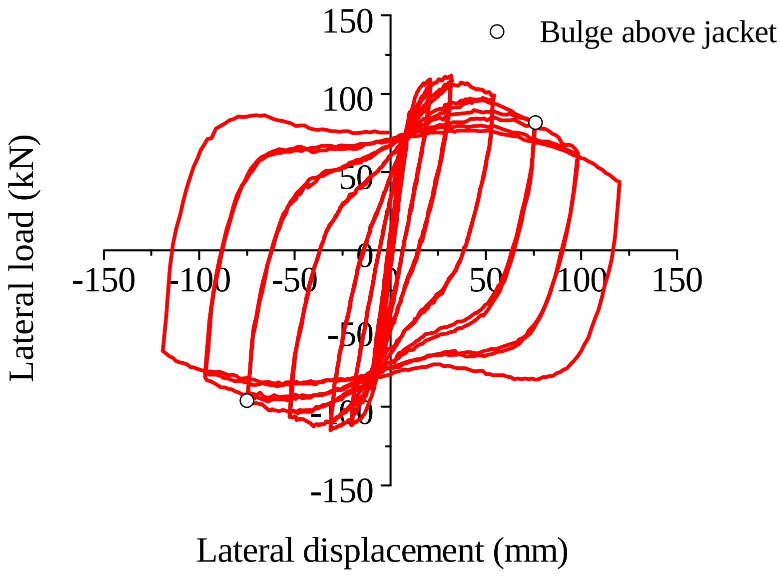


Figure 7.46 Lateral load-displacement curve of column LCFT-6C-106-F

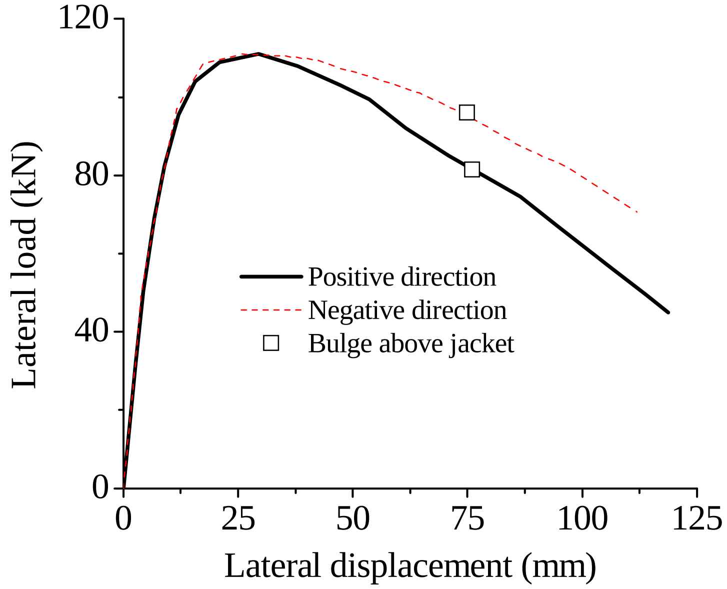


Figure 7.47 Envelope lateral load-displacement curves of column LCFT-6C-106-F

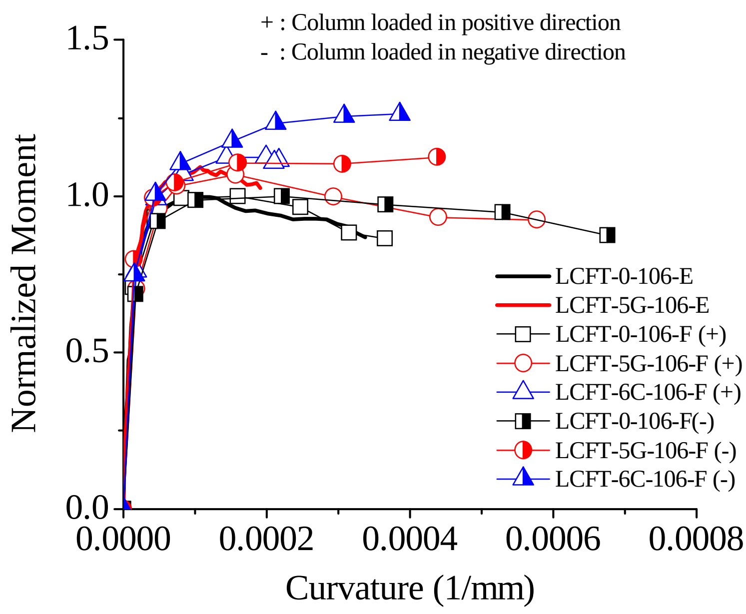


Figure 7.48 Normalized moment-curvature curves of all specimens

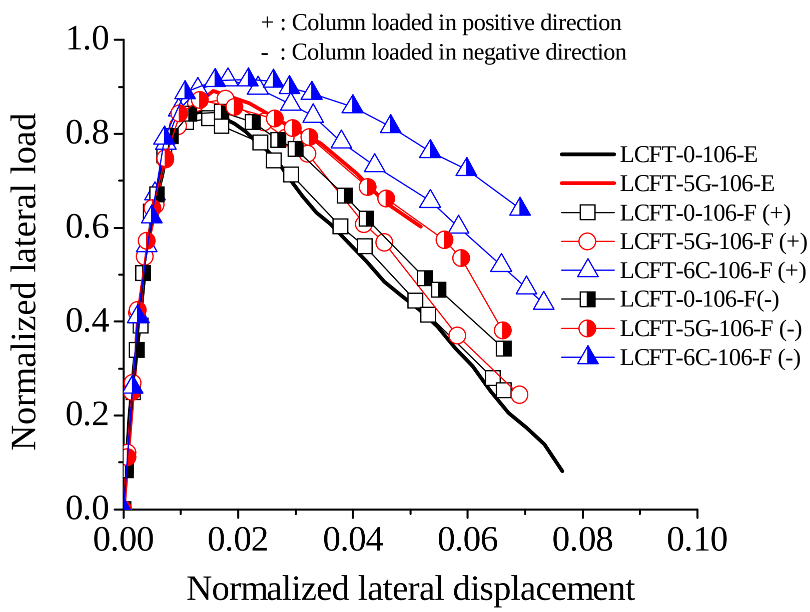


Figure 7.49 Normalized load-displacement curves of all specimens

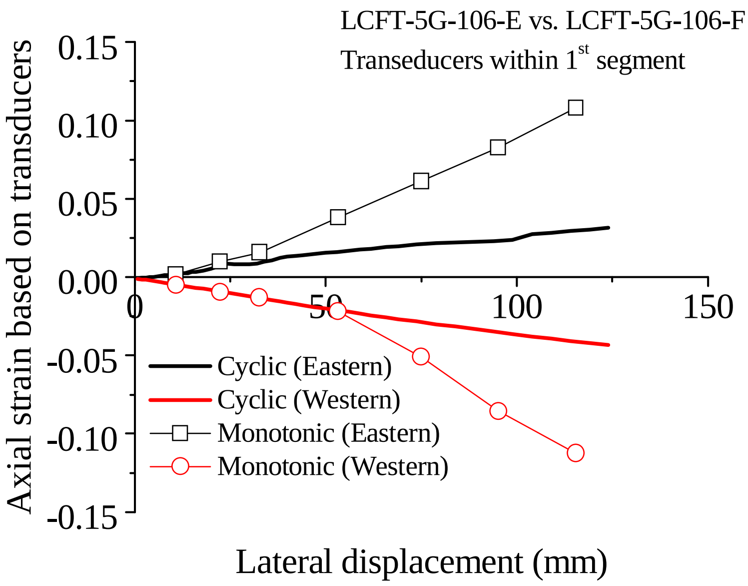


(a) First segment

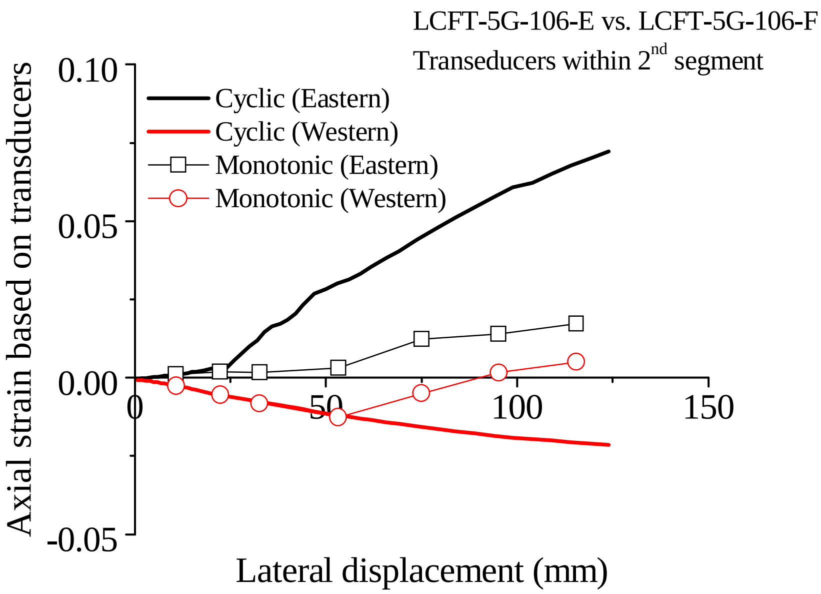


(b) Second segment

Figure 7.50 Transducer readings of GFRP-confined columns under different loading scenarios

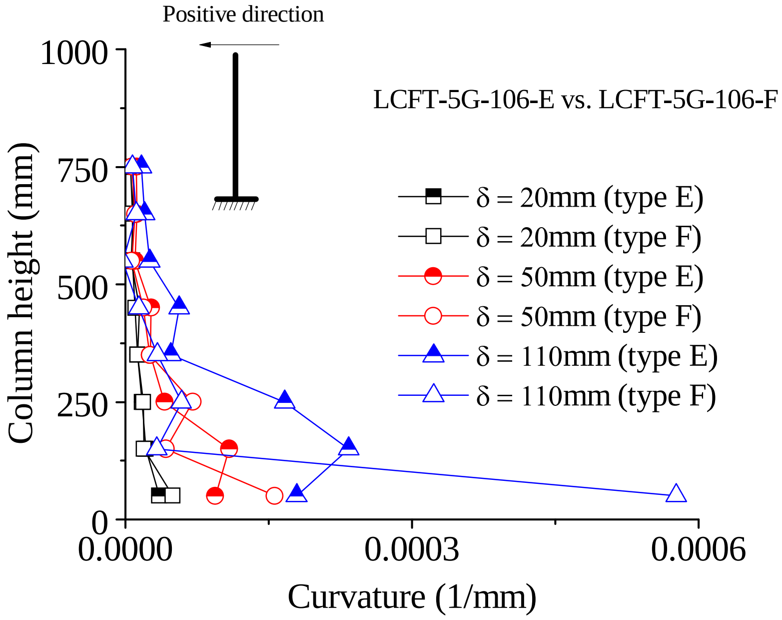


Figure 7.51 Curvature distributions of GFRP-confined columns under different loading scenarios

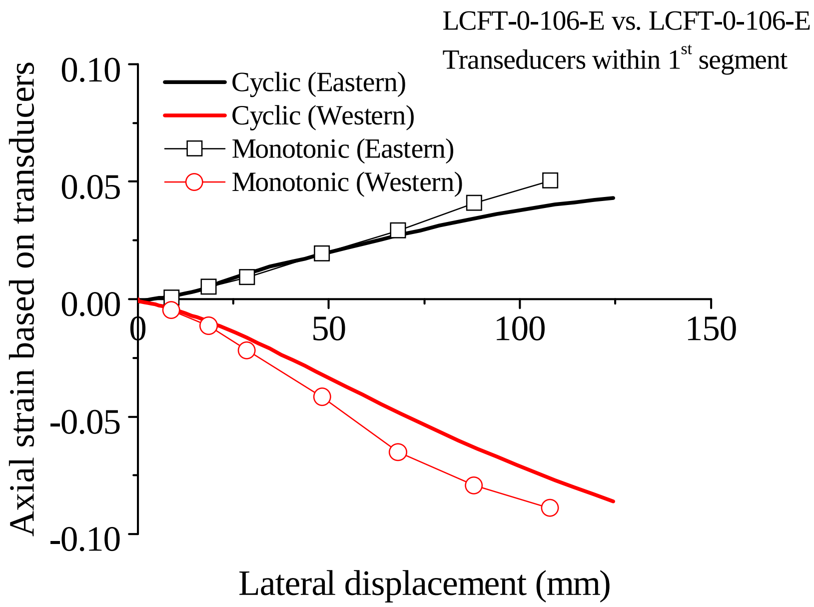


(a) First segment

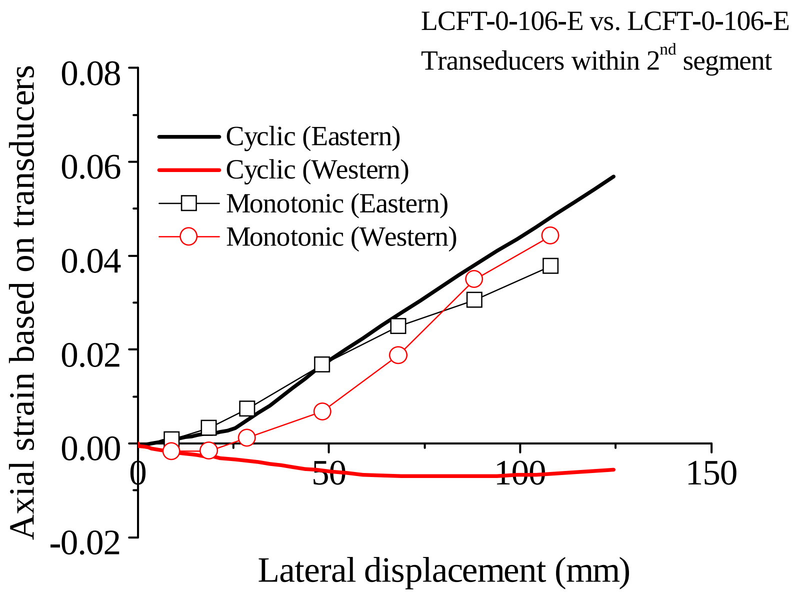


(b) Second segment

Figure 7.52 Transducer readings of unconfined columns under different loading scenarios

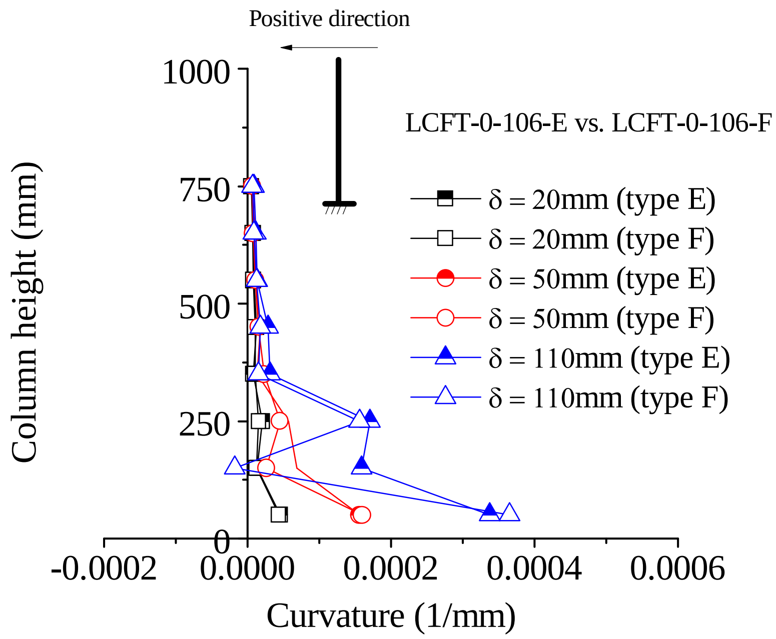


Figure 7.53 Curvature distributions of unconfined columns under different loading scenarios

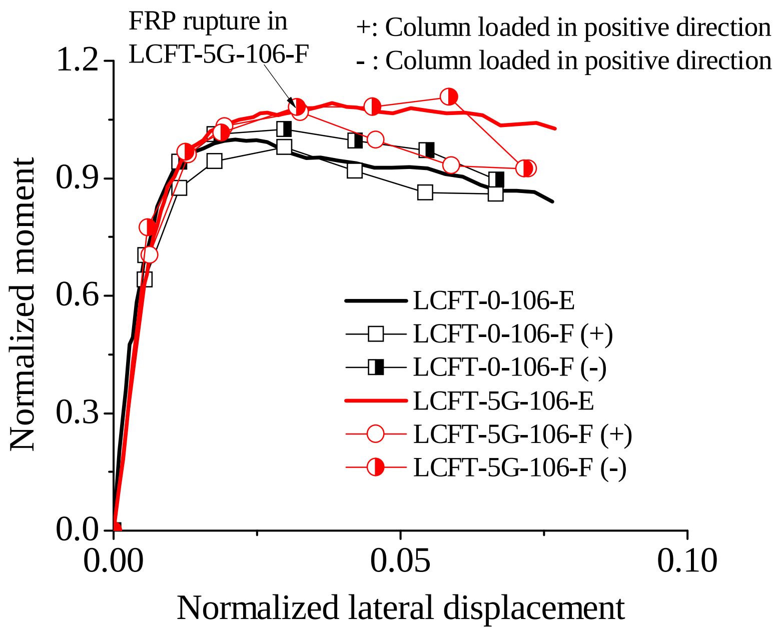


Figure 7.54 Normalized moment-displacement curves under different loading scenarios

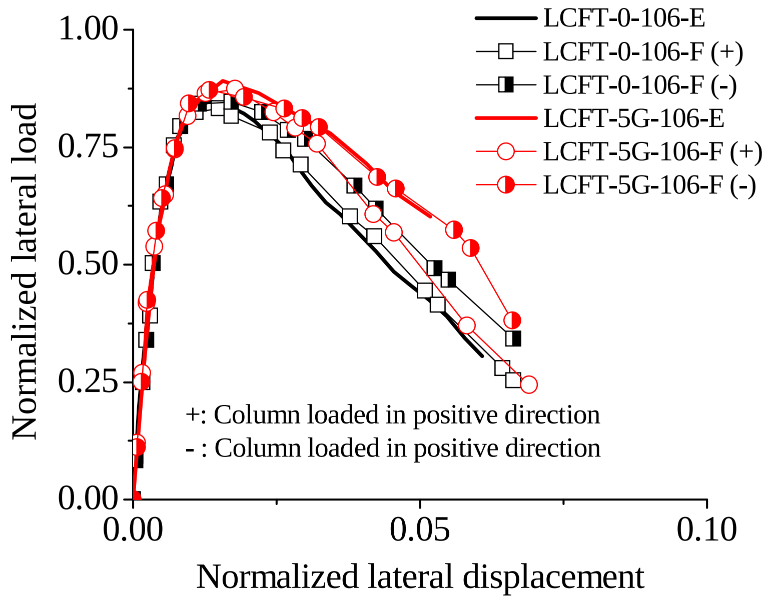


Figure 7.55 Normalized lateral load-displacement curves under different loading scenarios

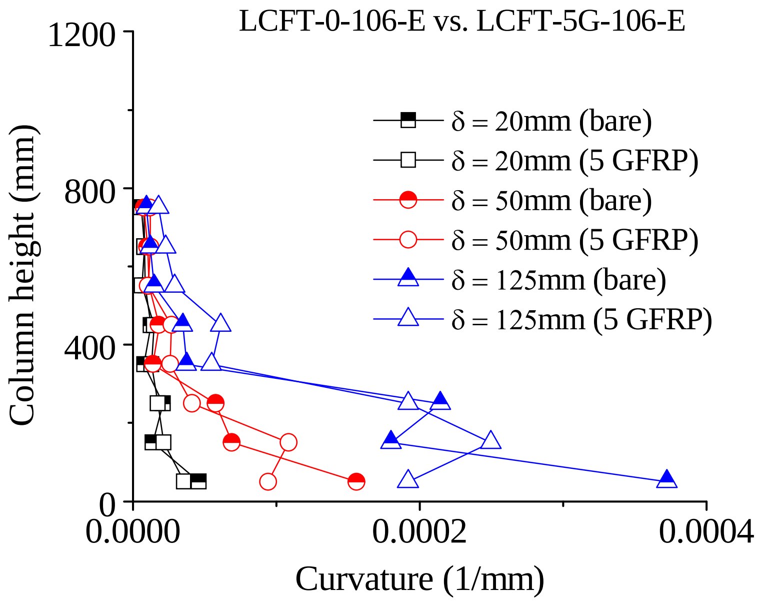


Figure 7.56 Curvature distributions of columns under monotonic lateral loading

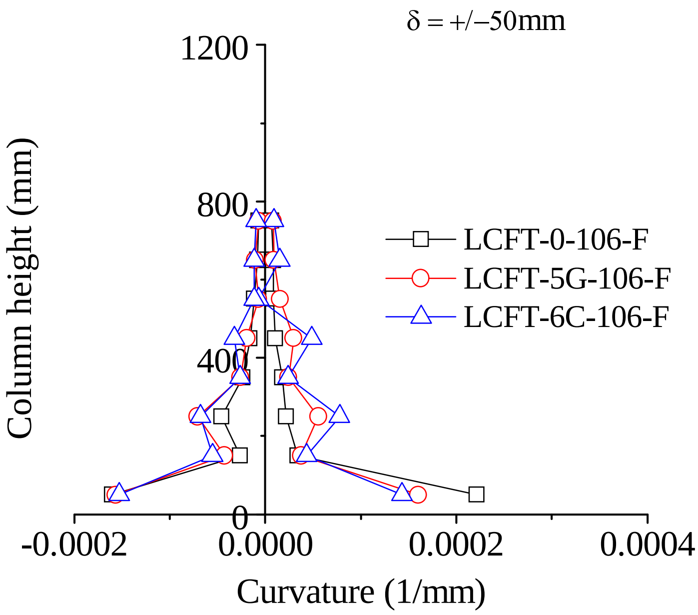


(a) $\delta$ =+/-50mm

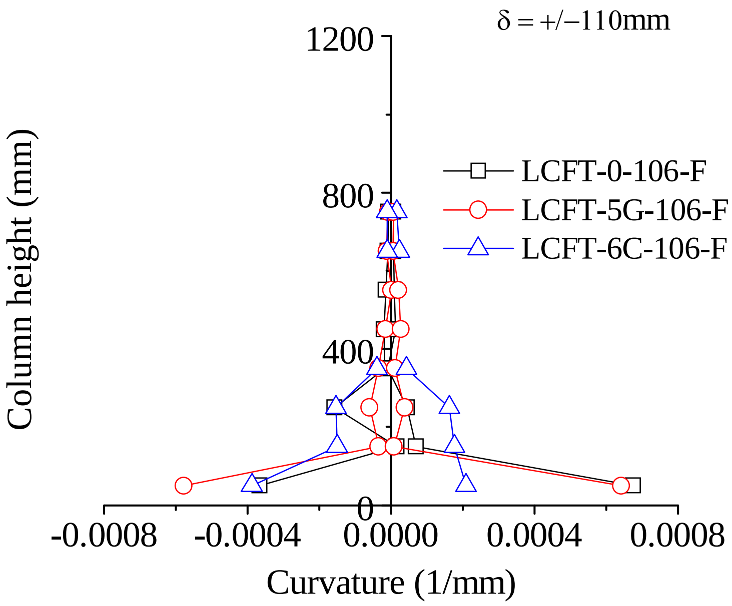


(b) $\delta$ =+/-110mm

Figure 7.57 Curvature distributions of columns under cyclic lateral loading

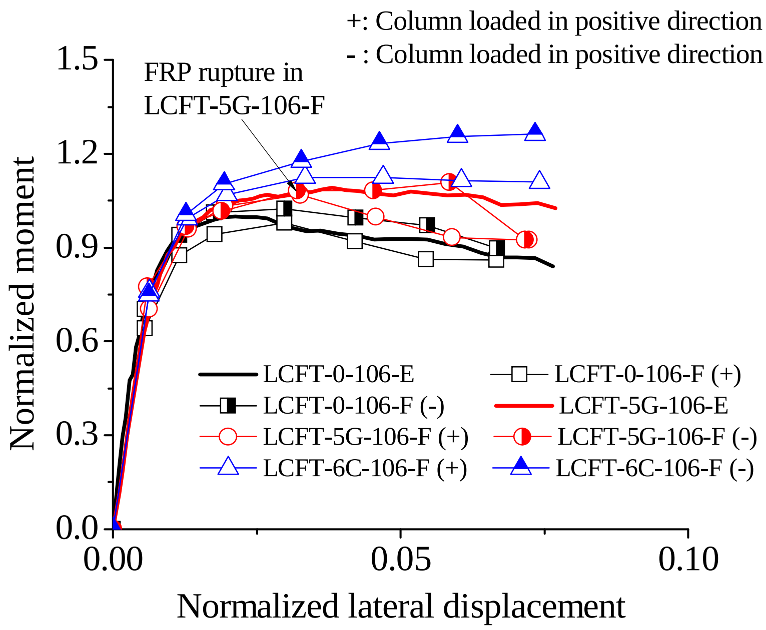


Figure 7.58 Normalized moment-displacement curves of all the columns

# CHAPTER 8

# CONCLUSIONS

## 8.1 INTRODUCTION

This thesis has presented a combined experimental and theoretical study into the structural behaviour and modelling of FRP-confined circular hollow steel tubes and FRP-confined concrete-filled steel tubes (CCFTs). The use of FRP jackets to provide external confinement to hollow and concrete-filled steel tubes is for the suppression of local bulking in such tubular columns when subjected to axial compression alone or in combination with monotonic/cyclic lateral loading.

A large amount of experimental work has been presented in this thesis, including monotonic axial compression tests on FRP-confined circular hollow steel tubes and CCFTs, cyclic axial compression tests on CCFTs and lateral loading tests on large-scale CCFTs with the FRP jacket only provided in the critical region near the column end. The FRP jacket has been shown to significantly enhance the performance of hollow and concrete-filled steel tubes by delaying or even suppressing local buckling in the steel tube and providing additional confinement to the concrete in CCFTs. A good understanding of the confining mechanism for the concrete in CCFTs has also been gained through the experimental work. These test results have provided not only a direct insight into the structural behaviour of the two types of tubular columns but also the means for verifying theoretical models.

Apart from the experimental work, theoretical modelling of the behaviour of FRP-confined circular hollow steel tubes and CCFTs has also been presented. A finite element (FE) model for predicting the behaviour of FRP-confined circular hollow steel tubes was presented and verified with test results. An analysis-oriented stress-strain model for concrete in CCFTs under monotonic axial compression was also developed. Using this monotonic stress-strain model to predict the envelope curve, a cyclic stress-strain model was also established and verified with the cyclic axial compression test results.

## 8.2 AXIAL COMPRESSIVE BEHAVIOUR OF FRP-CONFINED CIRCULAR HOLLOW STEEL TUBES

The use of FRP jackets to enhance the ductility and hence the seismic resistance of circular hollow steel tubes has been explored in Chapter 3. A series of axial compression tests has been presented to demonstrate the effectiveness of FRP confinement of hollow steel tubes whose ductility is otherwise limited by the development of the elephant's foot buckling mode. An FE model for predicting the behaviour of these FRP-confined tubes has also been presented. The FE model was also used to explore the use of FRP jackets to strengthen thin steel cylindrical shells (e.g. tanks and silos) against local elephant's foot buckling failure at the base. Based on the test and the FE results, the following conclusions were drawn:

1. The ductility of the steel tube can be greatly enhanced with the provision of a thin FRP jacket.
2. When the jacket thickness reaches a threshold value for which inward buckling deformations dominate the behaviour, further increases in the jacket thickness do not lead to significant additional benefits as the jacket provides little resistance to inward buckling deformations.
3. FRP confinement of steel tubes leads to large increases in ductility but limited increases in the ultimate load, which is desirable in seismic retrofit so that the retrofitted tube will not attract forces which are so high that adjacent members may be put in danger.

4. Both the load-axial shortening curves and the failure modes from the finite element model are in close agreement with those from the tests, although the degree of accuracy depends significantly on the geometric imperfection included in the finite element model.
5. The numerical results for a thin cylindrical shell subjected to axial compression in combination with internal pressure indicate that the FRP jacketing method leads to significant increases of the ultimate load. The FRP jacketing of steel cylindrical shells can also be used in the construction of new tanks and silos to enhance their performance.

## 8.3 BEHAVIOUR OF CCFTS UNDER MONOTONIC AXIAL COMPRESSION

The behaviour of CCFTs under monotonic axial compression has been studied both experimentally and theoretically. Chapter 4 presented results from three series of monotonic axial compression tests and Chapter 5 presented a theoretical model for the behaviour of circular CCFTs, with the focus being on the stress-strain behaviour of the confined concrete. An analysis-oriented model was developed which explicitly considers interactions between the three components (i.e. the concrete, the steel tube and the FRP jacket) in a CCFT and has been shown to provide reasonably accurate predictions of test results. The results presented in Chapters 4 and 5 allow the following conclusions to be drawn:

1 The FRP jacket is very effective in improving the monotonic axial compressive behaviour of concrete-filled thin steel tubes, in terms of both the load-carrying capacity and the ductility. All specimens failed by the explosive rupture of FRP in the mid-height region because of the lateral expansion of concrete.
2 The local buckling of a steel tube in a CFT column can be either much delayed or even prevented by the FRP jacket, and the strength and the strain capacity of the concrete can be significantly enhanced with the additional confinement

from the FRP jacket. The effect of FRP jacketing appears to be more pronounced for CFT columns with a thinner steel tube.

3 The axial stress-strain behaviour of the concrete, as a direct result of the interactions between the three components, has three distinctive stages including a first stage similar to that of unconfined concrete, a second stage where the stress increases rapidly resulting from a rapidly increasing confining pressure provided by both the steel tube and the FRP jacket, and a third stage where the confinement provided by the FRP jacket dominates its behaviour.

4 The lateral equation proposed by Teng et al. (2007) based on results from FRP-confined concrete and actively-confined concrete underestimates the lateral dilation of concrete in CCFTs. A new lateral strain equation was proposed based on test results from the present study, which forms an important component of the proposed analysis-oriented stress-strain model for confined concrete in CCFTs.

5 The proposed analysis-oriented model not only provides very accurate predictions of the test results presented in Chapter 4, but also provides reasonably accurate predictions of the test results reported by other researchers.

## 8.4 BEHAVIOUR OF CCFTS UNDER CYCLIC AXIAL COMPRESSION

The behaviour of CCFTs under cyclic axial compression has also been studied both experimentally and theoretically. Chapter 6 presented results from two series of cyclic axial compression tests and a cyclic stress-strain model for confined concrete in CCFTs. The following conclusions were drawn from the results presented in Chapter 6:

1 CCFTs have very good ductility when subjected to cyclic axial compression. The failure of such CCFTs is controlled by the explosive rupture of the FRP jacket in the mid-height region, in a manner similar to that of CCFTs subjected to monotonic axial compression.

2 The stress-strain curve of confined concrete in a CCFT under monotonic axial compression can be used as the envelope curve for the stress-strain history of confined concrete in an identical specimen subjected to cyclic axial compression.

3 For a CCFT column subjected to cyclic axial compression, when the axial load carried by the CCFT column is reduced to zero, the nominal axial strain of the column is generally larger than the plastic strain of the concrete and is always smaller than the plastic strain of the steel tube.

4 Repeated unloading/reloading cycles have a cumulative effect on the plastic strain and stress deterioration of concrete in CCFTs, so the uniqueness concept of cyclic stress-strain responses is invalid.

5 The proposed cyclic stress-strain model can provide accurate predictions of the envelope stress-strain curve, unloading/reloading responses and plastic strain of concrete in CCFTs.

## 8.5 BEHAVIOUR OF CCFTS UNDER COMBINED AXIAL COMPRESSION AND CYCLIC LATERAL LOADING

Chapter 7 presented a series of large-scale tests on CFT and CCFT columns subjected to combined constant axial compression and monotonic or cyclic lateral loading. The FRP jacket provided near the end of CCFT columns is to offer additional confinement to the potential plastic hinge region so that the seismic behaviour of the column can be enhanced. Based on the test results presented in Chapter 7, the following conclusions can be drawn:

1. The FRP jacket can effectively delay or even prevent an elephant’s foot local buckling failure at the end of a cantilevered CFT when the column is subjected to both constant axial compression and cyclic lateral loading. In columns with a relatively thick FRP jacket, the buckling deformations may be forced by the FRP jacket to appear above the FRP-jacketed region.
2. The performance of a CFT column can be significantly improved by FRP

jacketing. Because of FRP confinement, both the flexural strength of a CFT section and the lateral load-carrying capacity of a CFT column can be significantly enhanced. The ductility and the energy-dissipation capacity of the column, although significantly affected by the second-order effect caused by the applied axial load, can also be enhanced with FRP confinement.

3. Cyclic lateral loading introduces more severe localized deformation near the column end and may lead to earlier FRP rupture within that region. The performance of a CCFT column subjected to cyclic lateral loading may not be as good as seen in a monotonic loading test, especially when a weak FRP jacket is used.
4. The steel tube used in the present column tests all had a diameter-to-thickness ratio of around 100. With such a steel tube, the CFT sections still possessed good ductility. The effect of FRP jacketing can be more pronounced than indicated by the present test results when CFTs with a thinner steel tube are examined, where the confinement from the steel tube is smaller and the local buckling problem is more pronounced.

## 8.6 FURTHER RESEARCH

This thesis has been concerned with the structural behaviour and modelling of FRP-confined circular hollow steel tubes and CCFTs. This research has led to a good understanding of the axial compressive behaviour of FRP-confined circular hollow steel tubes and the behaviour of CCFTs under monotonic and cyclic axial compression as well as combined axial compression and cyclic lateral loading. A finite element model has been developed for predicting the behaviour of FRP-confined circular hollow steel tubes under axial compression, and both monotonic and cyclic stress-strain models have been developed for the confined concrete in CCFTs. All these models have been verified with test results. The results presented in this thesis represent significant advancements of existing knowledge for the two structural forms and facilitate further research on the following issues.

1 Experiments on FRP-confined circular hollow steel tubes have so far been limited to axial compression tests on small-scale specimens. Testing of large or full-scale specimens under different loading conditions (e.g. cyclic axial compression or combined axial compression and cyclic lateral loading) should be carried out in the future to gain a fuller understanding of the structural behaviour of FRP-confined circular hollow steel tubes.

2 While the proposed analysis-oriented stress-strain model for confined concrete in CCFTs has been shown to provide close predictions of test results, the lateral strain equation used in this model was based only on limited test results. Further research is needed to verify/refine this equation when a larger test database becomes available. The analysis-oriented model does not consider the effect of strain hardening of steel which may become important when the steel tube used in CCFTs does not have or has only a short plastic plateau, and/or when a relatively thick FRP jacket is used (i.e. the CCFT has a large ultimate axial strain). Further development of the analysis-oriented model is necessary to account for this factor.

3 The analysis-oriented model proposed in the present study requires an incremental procedure to produce the stress-strain curve. While it clearly reflects the confining mechanism for the concrete in CCFTs, the direct use of this model in design is difficult due to its relatively complex analysis process. A design-oriented stress-strain model in closed-form expressions should be developed in the future. A parametric study using the proposed analysis-oriented model can be conducted in the future to generate a large database for the development of such a design-oriented model.

4 Theoretical modelling of the behaviour of CCFTs under combined axial compression and monotonic or cyclic lateral loading should be carried out in the future. The theoretical modelling work can be conducted through the development of a finite element model employing beam-column elements in conjunction with the fibre model for section analysis; the confined concrete and the steel can be modelled using the cyclic stress-strain model developed in the present study and a cyclic stress-strain model for steel which appropriately

considers the Bauchinger effect. The effect of local buckling on the behaviour of the steel tube should also be duly accounted for. Results from the large-scale column tests presented in this thesis can be used to verify/refine such a theoretical model.

# REFERENCES

ABAQUS. (2003). *ABAQUS/Standard User's Manual*, ABAQUS Inc.

ACI 318. (2008). *Building Code Requirements for Structural Concrete and Commentary,* ACI Committee318, American Concrete Institute.

ACI 440. (2002). *Guide for the Design and Construction of Externally Bonded FRP Systems for Strengthening Concrete Structures*, ACI Committee 440, American Concrete Institute.

Ahmad, S.H., and Shah, S.P. (1982). "Stress-strain curves of concrete confined by spiral reinforcement." *Journal of the American Concrete Institute*, 79(6), 484-490.

AISC 360. (2005). *Specification for Structural Steel Buildings*, American Institution of Steel Construction.

Arivalagan, S., and Kandasamy, S. (2010). "Finite element analysis on the flexural behaviour of concrete filled steel tube beams." *Journal of Theoretical and Applied Mechanics*, 48(2), 505-516.

AS 4100. (1998). *Steel Structures*, Standards Australia.

ASTM 3039. (2000). *Standard Test Method for Tensile Properties of Polymer Matrix Composite Materials*, American Society for Testing of Materials, Philadelphia, USA.

ASTM C39. (2009). *Standard Test Method for Compressive Strength of*

*Cylindrical Concrete Specimens*, American Society for Testing and Materials, Philadelphia, USA.

ASTM C192. (2007). *Standard Practice for Making and Curing Concrete Test Specimens in the Laboratory*, American Society for Testing and Materials, Philadelphia, USA.

Bae, S., and Bayrak, O. (2008). "Seismic performance of full-scale reinforced concrete columns." *ACI Structural Journal*, 105(2), 123-133.

Bahn, B.Y., and Hsu, C.T.T. (1998). "Stress-strain behaviour of concrete under cyclic loading." *ACI Materials Journal*, 95(2), 178-193.

Banon, H., Biggs, J.M., and Irvine, H.M. (1981). "Seismic damage in reinforced-concrete frames." *Journal of the Structural Division*, ASCE, 107(9), 1713-1729.

Bazant, Z.P., Cedolin, L., and Tabbara, M.R. (1991). "New method of analysis for slender columns." *ACI Structural Journal*, 88(4), 391-401.

Binici, B. (2005). "An analytical model for stress-strain behavior of confined concrete." *Engineering Structures*, 27(7), 1040-1051.

Boyd, P.F., Cofer, W.F., and McLean, D.I. (1995). "Seismic performance of steel-encased concrete columns under flexural loading." *ACI Structural Journal*, 92(3), 355-364.

Broderick, B.M., Goggins, J.M., and Elghazouli, A.Y. (2005). "Cyclic performance of steel and composite bracing members." *Journal of Constructional Steel Research*, 61(4), 493-514.

BS 18. (1987). *British Standard Method for Tensile Testing of Metals*, British Standard Institution.

BS 5400. (2005). *Steel, Concrete and Composite Bridges, Part 5, Code of Practice for the Design of Composite Bridges*, British Standard Institution.

BS 5950. (2000). *Structural Use of Steel Work in Building*, British Standard Institution.

Calladine, C.R. (1985). *Plasticity for Engineers*, Chichrster, West Sussex, England: Ellis Worwood; New York: Halsted Press.

Carreira, D.J., and Chu, K.H. (1985). "Stress-strain relationship for plain concrete in compression." *ACI Materials Journal*, 83(6), 797-804.

Castellani, A., Scirocco, F., and Boffi, G. (1993). "Reinforced-concrete columns under cyclic axial compressive forces." *Journal of Structural Engineering*, ASCE, 119(11), 3426-3433.

Chai, Y.H., Priestley, M.J.N., and Seible, F. (1994). "Analytical model for steel-jacketed RC circular bridge columns." *Journal of Structural Engineering*, ASCE, 120(8), 2358-2376.

Chapman, H.E., and Park, R. (1991) "Seismic retrofitting of bridges." *Proceedings, International Workshop on Seismic Design and Retrofiting of Reinforced Concrete Bridges*, Bormio, Italy.

Chen, W.F., and Atsuta, T. (1976). *Theory of Beam Columns*, McGraw-Hill, New York.

Cheng, C.T., Yang, J.C., Yeh, Y.K., and Chen, S.E. (2003). "Seismic performance of repaired hollow-bridge piers." *Construction and Building Materials*, 17(5), 339-351.

Chitawadagi, M.V., and Narasimhan, M.C. (2009). "Strength deformation behaviour of circular concrete filled steel tubes subjected to pure bending."

*Journal of Constructional Steel Research*, 65(8-9), 1836-1845.

Choi, K.K., and Xiao, Y. (2010a). "Analytical model of circular CFRP confined concrete-filled steel tubular columns under axial compression." *Journal of Composites for Construction*, ASCE, 14(1), 125-133.

Choi, K.K., and Xiao, Y. (2010b). "Analytical studies of concrete-filled circular steel tubes under axial compression." *Journal of structural Engineering*, ASCE, 136(5), 565-573.

Choo, C.C., Harik, I.E., and Gesund, H. (2006). "Strength of rectangular concrete columns reinforced with fiber-reinforced polymer bars." *ACI Structural Journal*, 103(3), 452-459.

Chung, K.S., Park, S., and Choi, S. (2009). "Fire resistance of concrete filled square steel tube columns subjected to eccentric axial load." *International Journal of Steel Structures*, 9(1), 69-76.

Concrete Society. (2004). *Design Guidance for Strengthening Concrete Structures with Fibre Composite Materials*, Second Edition, Concrete Society Technical Report No. 55, Crowthorne, Berkshire, UK.

Cranston, W.B. (1972). *Analysis and Design of Reinforced Concrete Columns*, Research Report 20, Cement and Concrete Association, UK

Dai, X., and Lam, D. (2010). "Numerical modelling of the axial compressive behaviour of short concrete-filled elliptical steel columns." *Journal of Constructional Steel Research*, 66(7), 931-942.

Darwin, D., and Nmai, C.K. (1986). "Energy-dissipation in RC beams under cyclic load." *Journal of Structural Engineering*, ASCE, 112(8), 1829-1846.

De Nardin, S., and El Debs, A.L.H.C. (2007). "Axial load behaviour of concrete-filled steel tubular columns." *Proceedings of the Institution of Civil Engineers-Structures and Buildings*, 160(1), 13-22.

De Oliveira, W.L.A., De Nardin, S., El Debs, A.L.H.D., and El Debs, M.K. (2010). "Evaluation of passive confinement in CFT columns." *Journal of Constructional Steel Research*, 66(4), 487-495.

EC 4. (2004). *Design of Composite Steel and Concrete Structures*, European Committee for standardization.

Elchalakani, M., Zhao, X.L., and Grzebieta, R.H. (2001). "Concrete-filled circular steel tubes subjected to pure bending." *Journal of Constructional Steel Research*, 57(11), 1141-1168.

Elchalakani, M., Zhao, X.L., and Grzebieta, R.H. (2004). "Concrete-filled steel circular tubes subjected to constant amplitude cyclic pure bending." *Engineering Structures*, 26(14), 2125-2135.

Elremaily, A., and Azizinamini, A. (2002). "Behavior and strength of circular concrete-filled tube columns." *Journal of Constructional Steel Research*, 58(12), 1567-1591.

Elsanadedy, H.M. (2002). *Seismic Performance and Analysis of Ductile Composite-Jacketed Reinforced Concrete Bridge Columns*, PhD Thesis, University of California, Irvine.

Fam, A., Qie, F.S., and Rizkalla, S.H. (2004). "Concrete-filled steel tubes subjected to axial compression and lateral cyclic loads." *Journal of Structural Engineering*, ASCE, 130(4), 631-640.

Fam, A.Z., and Rizkalla, S.H. (2001). "Confinement model for axially loaded concrete confined by circular fiber-reinforced polymer tubes." *ACI*

*Structural Journal*, 98(4), 451-461.

fib. (2001). *Externally Bonded FRP Reinforcement for RC Structures*, International Federation for Structural Concrete, Lausanne, Switzerland.

Furlong, R.W. (1967). "Strength of steel-encased concrete beam columns." *Journal of Structural Division*, ASCE, 96(ST5), 113-124.

Galal, K., Arafa, A., and Ghobarah, A. (2005). "Retrofit of RC square short columns." *Engineering Structures*, 27(5), 801-813.

Gardner, N.J., and Jacobson, E.R. (1967). "Structural behavior of concrete-filled steel tubes." *ACI Structural Journal*, 64(7), 404-412.

Giakoumelis, G., and Lam, D. (2004). "Axial capacity of circular concrete-filled tube columns." *Journal of Constructional Steel Research*, 60(7), 1049-1068.

Gomes, A., and Appleton, J. (1997). "Nonlinear cyclic stress-strain relationship of reinforcing bars including buckling." *Engineering Structures*, 19(10), 822-826.

Gosain, N.K., Brown, R.H., and Jirsa, J.O. (1977). "Shear requirements for load reversals on RC members." *Journal of the Structural Division*, ASCE, 103(7), 1461-1475.

Gourley, B.C., Tort, C., Hajjar, J.F., and Schiller, P.H. (2001). *A Synopsis of Studies of the Monotonic and Cyclic Behavior of Concrete-Filled Steel Tube Beam Columns*, Structural Engineering Report No. ST-01-4, Department of Civil Engineering, University of Minnesota.

Gu, W., Guan, C.W., Zhao, Y.H., and Cao, H. (2004). "Experimental study on concentrically-compressed circular concrete filled CFRP-steel composite tubular short columns." *Journal of Shenyang Architecture and Civil Engineering University*, 20(2), 118-120, (in Chinese).

Hajjar, J.F. (2000). "Concrete-filled steel tube columns under earthquake loads." *Progress in Structural Engineering and Materials*, 2, 72-81.

Hajjar, J.F., and Gourley, B.C. (1996). "Representation of concrete-filled steel tube cross-section strength." *Journal of Structural Engineering*, ASCE, 122(11), 1327-1336.

Han, L.H., Huang, H., Tao, Z., and Zhao, X.L. (2006). "Concrete-filled double skin steel tubular (CFDST) beam-columns subjected to cyclic bending." *Engineering Structures*, 28(12), 1698-1714.

Han, L.H., Tao, Z., and Yao, G.H. (2008). "Behaviour of concrete-filled steel tubular members subjected to shear and constant axial compression." *Thin-Walled Structures*, 46(7-9), 765-780.

Han, L.H., and Yang, Y.F. (2005). "Cyclic performance of concrete-filled steel CHS columns under flexural loading." *Journal of Constructional Steel Research*, 61(4), 423-452.

Han, L.H., Yao, G.H., and Zhao, X.L. (2004). "Behavior and calculation on concrete-filled steel CHS (circular hollow section) beam-columns." *Steel and Composite Structures*, 4(3), 169-188.

Haroun, M.A., Elsanadedy, H.M., and Elbahar, M.R. (2002). "Design evaluation of seismically retrofitted reinforced concrete bridge column bents by infill walls." *Proceedings, Seventh US National Conference on Earthquake Engineering*, Boston, USA.

Hatzigeorgiou, G.D. (2008). "Numerical model for the behavior and capacity of circular CFT columns, Part I: Theory." *Engineering Structures*, 30(6), 1573-1578.

Hines, E.M., Restrepo, J.I., and Seible, F. (2004). "Force-displacement characterization of well-confined bridge piers." *ACI Structural Journal*, 101(4), 537-548.

Hollaway, L.C., and Cadei, J. (2002). "Progress in the technique of upgrading metallic structures with advanced polymer composites." *Progress in Structural Engineering and Materials*, 4, 131-148.

Hong, S.D., and Varma, A.H. (2009). "Analytical modeling of the standard fire behavior of loaded CFT columns." *Journal of Constructional Steel Research*, 65(1), 54-69.

Hsu, H.L., and Chang, D.L. (2001). "Upgrading the performance of steel box piers subjected to earthquakes." *Journal of Constructional Steel Research*, 57(9), 945-958.

Hu, H.T., Huang, C.S., and Chen, Z.L. (2005). "Finite element analysis of CFT columns subjected to an axial compressive force and bending moment in combination." *Journal of Constructional Steel Research*, 61(12), 1692-1712.

Hu, H.T., Huang, C.S., Wu, M.H., and Wu, Y.M. (2003). "Nonlinear analysis of axially loaded concrete-filled tube columns with confinement effect." *Journal of Structural Engineering*, ASCE, 129(10), 1322-1329.

Iacobucci, R.D., Sheikh, S.A., and Bayrak, O. (2003). "Retrofit of square concrete columns with carbon fiber-reinforced polymer for seismic resistance." *ACI Structural Journal*, 100(6), 785-794.

Ichinohe, Y., Matsutani, T., Nakajima, M., Ueda, H., and Takada, K. (1991) "Elasto-plastic behavior of concrete filled steel circular columns."

*Proceedings, Third International Conference on Steel-Concrete Composite Structures*, Fukuoka, Japan, 131-136.

Ilki, A., and Kumbasar, N. (2002). "Behavior of damaged and undamaged concrete strengthened by carbon fiber composite sheets." *Structural Engineering and Mechanics*, 13(1), 75-90.

Inai, E., Mukai, A., Kai, M., Tokinoya, H., Fukumoto, T., and Mori, K. (2004). "Behavior of concrete-filled steel tube beam columns." *Journal of Structural Engineering*, ASCE, 130(2), 189-202.

Jiang, T. (2008). *FRP-Confined RC Columns: Analysis, Behavior, and Design*, PhD Thesis, The Hong Kong Polytechnic University, Hong Kong.

Jiang, T., and Teng, J.G. (2007). "Analysis-oriented stress-strain models for FRP-confined concrete." *Engineering Structures*, 29(11), 2968-2986.

Johansson, M. (2002). "The efficiency of passive confinement in CFT columns." *Steel and Composite Structures*, 2(5), 379-396.

Johansson, M., and Gylltoft, K. (2002). "Mechanical behavior of circular steel-concrete composite stub columns." *Journal of Structural Engineering*, ASCE 128(8), 1073-1081.

Julio, E., and Branco, F.A.B. (2008). "Reinforced concrete jacketing - interface influence on cyclic loading response." *ACI Structural Journal*, 105(4), 471-477.

Karsan, I.D., and Jirsa, J.O. (1969). "Behavior of concrete under compressive loadings." *Journal of Structural Engineering Division*, ASCE, 95(ST12), 2543-2563.

Kawano, A., and Matsui, C. (1988) "An experimental study on hysteretic behavior of concrete filled tubular members under repeated axial loading." *Proceedings, The Ninth World Conference on Earthquake Engineering*, Tokyo-Kyoto, Japan.

Kitada, T. (1998). "Ultimate strength and ductility of state-of-the-art concrete-filled steel bridge piers in Japan." *Engineering Structures*, 20(4-6), 347-354.

Kitada, T., Matsumura, M., and Otoguro, Y. (2003). "Seismic retrofitting techniques using an energy absorption segment for steel bridge piers." *Engineering Structures*, 25(5), 621-635.

Kitada, T., Yamaguchi, T., Matsumura, M., Okada, J., Ono, K., and Ochi, N. (2002). "New technologies of steel bridges in Japan." *Journal of Constructional Steel Research*, 58(1), 21-70.

Knowles, R.B., and Park, R. (1969). "Strength of concrete filled steel tubular columns." *Journal of Structural Division*, ASCE, 95(ST12), 2565-2587.

Lam, L., and Teng, J.G. (2003). "Design-oriented stress-strain model for FRP-confined concrete." *Construction and Building Materials*, 17(6-7), 471-489.

Lam, L., and Teng, J.G. (2004). "Ultimate condition of fiber reinforced polymer-confined concrete." *Journal of Composites for Construction*, ASCE 8(6), 539-548.

Lam, L., and Teng, J.G. (2009). "Stress-strain model for FRP-confined concrete under cyclic axial compression." *Engineering Structures*, 31(2), 308-321.

Lam, L., Teng, J.G., Cheung, C.H., and Xiao, Y. (2006). "FRP-confined concrete under axial cyclic compression." *Cement & Concrete Composites*, 28(10), 949-958.

Lee, S.J. (2007). "Capacity and the moment-curvature relationship of high-strength concrete filled steel tube columns under eccentric loads." *Steel and Composite Structures*, 7(2), 135-160.

Liu, L., and Lu, Y.Y. (2010). "Axial bearing bapacity of short FRP confined concrete-filled steel tubular columns." *Journal of Wuhan University of Technology-Materials Science Edition*, 25(3), 454-458.

Liu, Z.Y., and Goel, S.C. (1988). "Cyclic load behavior of concrete-filled tubular braces." *Journal of Structural Engineering*, ASCE, 114(7), 1488-1506.

Lu, H., Han, L.H., and Zhao, X.L. (2009). "Analytical behavior of circular concrete-filled thin-walled steel tubes subjected to bending." *Thin-Walled Structures*, 47(3), 346-358.

Lu, H., Han, L.H., and Zhao, X.L. (2010). "Fire performance of self-consolidating concrete filled double skin steel tubular columns: Experiments." *Fire Safety Journal*, 45(2), 106-115.

Lu, Y.Q., and Kennedy, D.J.L. (1994). "The flexural behavior of concrete-filled hollow structural sections." *Canadian Journal of Civil Engineering*, 21(1), 111-130.

Mahin, S.A., and Bertero, V.V. (1976) "Probelms in establishing and predicting ductility in structural design." *Proceedings, International Symposium on Earthquake Structural Engineering*, 613-628.

Mander, J.B., Priestley, M.J.N., and Park, R. (1984). *Seismic Design of Bridge Piers*, Research report No. 84-2, University of Canterbury, New Zealand.

Mander, J.B., Priestley, M.J.N., and Park, R. (1988). "Theoretical stress-strain model for confined concrete." *Journal of Structural Engineering*, ASCE, 114(8), 1804-1826.

Manos, G.C., and Clough, R.W. (1985). "Tank damage during the Coalinga earthquake." *Earthquake Engineering and Structural Dynamics*, 13(4), 449-466.

Mao, X.Y., and Xiao, Y. (2006). "Seismic behavior of confined square CFT columns." *Engineering Structures*, 28(10), 1378-1386.

Martinez-Rueda, J.E., and Elnashai, A.S. (1997). "Confined concrete model under cyclic load." *Materials and Structures,* 30(197), 139-147.

Mirmiran, A., and Shahawy, M. (1996). "A new concrete-filled hollow FRP composite column." *Composites Part B: Engineering*, 27(3-4), 263-268.

Mirmiran, A., Shahawy, M., and Samaan, M. (1999). "Strength and ductility of hybrid FRP-concrete beam-columns." *Journal of Structural Engineering*, ASCE, 125(10), 1085-1093.

Monti, G., and Nuti, C. (1992). "Nolinear cyclic behavior of reinforcing bars including buckling." *Journal of structural Engineering*, ASCE, 118(12), 3268-3284.

Naaman, A., and Jeong, S. (1995) "Structural ductility of concrete beams prestressed with FRP tendons." *Proceedings, Second International RILEM symposium (FRPRCS-2)*, Cachan, France, 379-384.

Neogi, P.K., Sen, H.K., and Chapman, J.C. (1969). "Concrete-filled tubular steel columns under eccentric loading." *The Structural Engineer*, 47(5), 187-195.

Newmark, N.M. (1943). "Numerical rocedure for computing deflections, moments, and buckling loads." *ASCE Transactions*, 108, 1161-1234.

Nishikawa, K., Yamamoto, S., Natori, T., Terao, K., Yasunami, H., and Terada, M.

(1998). "Retrofitting for seismic upgrading of steel bridge columns." *Engineering Structures*, 20(4-6), 540-551.

Nishino, T., and Furukawa, T. (2004) "Strength and deformation capacities of circular hollow section steel member reinforced with carbon fiber." *Proceedings, Seventh Pacific Structural Steel Conference*.

Nmai, C.K., and Darwin, D. (1986). "Lightly reinforced concrete beams under cyclic load." *ACI Structural Journal*, 83(5), 777-783.

O'Shea, M.D., and Bridge, R.Q. (1997). *Tests on Circular Thin-Walled Steel Tubes Filled With Medium and High Strength Concrete*, School of civil engineering, University of Sydney, Sydney.

O'Shea, M.D., and Bridge, R.Q. (1999) "The effects of local buckling and confinement in concrete filled circular steel tubes." *Proceedings, Mechanics of structures and materials*, Sydney, New South Wales, Australia, 8-10 December, 321-326.

Oehlers, D.J., and Bradford, M.A. (1995). *Composite Steel and Concrete Structural Members*, Pergamon Press, Oxford.

Park, J.W., Hong, Y.K., and Choi, S.M. (2010). "Behaviors of concrete filled square steel tubes confined by carbon fiber sheets (CFS) under compression and cyclic loads." *Steel and Composite Structures*, 10(2), 187-205.

Park, R. (1989). "Evaluation of ductility of structures and structural assemblages for laboratory testing." *Bulletin of the New Zealand National Society for Earthquake Engineering*, 22(3), 155-166.

Park, R., and Paulay, T. (1975). *Reinforced Concrete Structures*, John Wiley & Sons, Inc.

Park, Y.J., and Ang, A.H.S. (1985). "Mechanistic seismic damage model for reinforced-concrete." *Journal of Structural Engineering*, ASCE, 111(4), 722-739.

Park, Y.J., Ang, A.H.S., and Wen, Y.K. (1987). "Seismic damage analysis of reinforced concrete buildings." *Journal of structural Engineering*, ASCE, 111(ST4), 740-757.

Pessiki, S., Harries, K.A., Kestner, J.T., Sause, R., and Ricles, J.M. (2001). "Axial behavior of reinforced concrete columns confined with FRP jackets." *Journal of Composites for Construction*, ASCE 5(4), 237-245.

Popovics, S. (1973). "Numerical approach to the complete stress-strain relation for concrete." *Cement and Concrete Research*, 3(5), 583-599.

Priestley, M.J.N., and Park, R. (1987). "Strength and ductility of concrete bridge columns under seismic loading." *ACI Structural Journal*, 84(1), 61-76.

Priestley, M.J.N., Seible, F., and Chai, Y.H. (1992). "Seismic retrofit of bridge columns using steel jackets." *Proceedings, Tenth World Conference on Earthquake Engineering*, 1-10, 5285-5290.

Prion, H.G.L., and Boehme, J. (1994). "Beam-column behavior of steel tubes filled with high-strength concrete." *Canadian Journal of Civil Engineering*, 21(2), 207-218.

Quach, W.M., Teng, J.G., and Chung, K.F. (2004). "Residual stresses in steel sheets due to coiling and uncoiling: a closed-form analytical solution." *Engineering Structures*, 26(9), 1249-1259.

Richart, F.E., Brandtzaeg, A., and Brown, R.L. (1929). *The Failure of Plain and Spirally Reinforced Concrete in Compression*, University of Illinois, Engineering Experimental Station, Illinois, USA.

Rodriguez, M.E., and Park, R. (1994). "Seismic load tests on reinforced concrete columns strengthened by jacketing." *ACI Structural Journal*, 91(2), 150-159.

Roeder, C.W. (1998). "Overview of hybrid and composite systems for seismic design in the United States." *Engineering Structures*, 20(4-6), 355-363.

Romero, M.L., Bonet, J.L., and Ivorra, S. (2005). "A review of Nonlinear analysis models for concrete filled tubular columns." *Innovation in Civil and Structural Engineering Computing*, 119-142.

Rotter, J.M. (1990). "Local collapse of axially compressed pressurized thin steel cylinders." *Journal of Structural Engineering-ASCE*, 116(7), 1955-1970.

Rotter, J.M. (2004). "Chapter 2: Cylindrical shells under axial compression." *Buckling of Thin Metal Shells*, J.G. Teng and J.M. Rotter, eds., Spon Press, UK, 42-87.

Roufaiel, M.S.L., and Meyer, C. (1987). "Analytical modeling of hysteretic behavior of R/C frames." *Journal of Structural Engineering*, ASCE, 113(3), 429-444.

Rousakis, T. (2001). *Experimental Investigation of Concrete Cyclinders Confined by Carbon FRP Sheets, under Monotonic and Cyclic Axial Compression Load*, Research Report. Publication 01:2, Division of Building Technology, Chalmers University of Technology.

Saadatmanesh, H., Ehsani, M.R., and Jin, L.L. (1997). "Repair of earthquake-damaged RC columns with FRP wraps." *ACI Structural Journal*, 94(2), 206-215.

Saadatmanesh, H., Ehsani, M.R., and Li, M.W. (1994). "Strength and ductility of concrete columns externally reinforced with fiber-composite straps." *ACI*

*Structural Journal*, 91(4), 434-447.

Sakai, J., and Kawashima, K. (2006). "Unloading and reloading stress-strain model for confined concrete." *Journal of Structural Engineering*, ASCE, 132(1), 112-122.

Sakino, K., Nakahara, H., Morino, S., and Nishiyama, A. (2004). "Behavior of centrally loaded concrete-filled steel-tube short columns." *Journal of Structural Engineering*, ASCE, 130(2), 180-188.

Schneider, S.P. (1998). "Axially loaded concrete-filled steel tubes." *Journal of Structural Engineering*, ASCE, 124(10), 1125-1138.

Seible, F., Priestley, M.J.N., Hegemier, G.A., and Innamorato, D. (1997). "Seismic retrofit of RC columns with continous carbon fiber jackets." *Journal of Composites for Construction*, ASCE, 1(2), 52-62.

Shaat, A., and Fam, A. (2004). "Strengthening of short HSS steel columns using FRP sheets." *Proceedings, Fourth International Conference on Advanced Composite Materials in Bridges and Structures*, Galgary, Alberta, Cannda.

Shah, S.P., Fafitis, A., and Arnold, R. (1983). "Cylic loading of spirally reinforced concrete." *Journal of Structural Engineering*, ASCE, 109(7), 1695-1710.

Shakir-Khalil, H., and Zeghiche, J. (1989). "Experimental behavior of concrete-filled rolled rectangular hollow-section columns." *The Structural Engineer*, 67(19), 346-353.

Shams, M., and Saadeghvaziri, M.A. (1997). "State of the art of concrete-filled steel tubular columns." *ACI Structural Journal*, 94(5), 558-571.

Shams, M., and Saadeghvaziri, M.A. (1999). "Nonlinear response of concrete-filled steel tubular columns under axial loading." *ACI Structural*

*Journal*, 96(6), 1009-1017.

Shan, J.H., Chen, R., Zhang, W.X., Xiao, Y., Yi, W.J., and Lu, F.Y. (2007). "Behavior of concrete filled tubes and confined concrete filled tubes under high speed impact." *Advances in Structural Engineering*, 10(2), 209-218.

Shanmugam, N.E., and Lakshmi, B. (2001). "State of the art report on steel-concrete composite columns." *Journal of Constructional Steel Research*, 57(10), 1041-1080.

Shen, Z.Y., and Lu, L.W. (1983). "Analysis of initially crooked, end restrained steel columns." *Journal of Constructional Steel Research*, 3(1), 10-18.

Shim, C.S., Chung, Y.S., and Han, J.H. (2008). "Cyclic response of concrete-encased composite columns with low steel ratio." *Proceedings of the Institution of Civil Engineers-Structures and Buildings*, 161(2), 77-89.

Sinha, B.P., Gerstle, K.H., and Tulin, L.G. (1964). "Stress-strain relations for concrete under cyclic loading." *ACI Structural Journal*, 61(2), 195-211.

Song, T.Y., Han, L.H., and Yu, H.X. (2010). "Concrete filled steel tube stub columns under combined temperature and loading." *Journal of Constructional Steel Research*, 66(3), 369-384.

Sugano, S., and Nagashima, T. (1992) "Seismic behavior of concrete-filled tubular steel columns." *Proceedings, Tenth Structures Congress*, San Antonio, Texas, 914-917.

Susantha, K.A.S., Aoki, T., and Hattori, M. (2008). "Seismic performance improvement of circular steel columns using precompressed concrete-filled steel tube." *Journal of Constructional Steel Research*, 64(1), 30-36.

Susantha, K.A.S., Aoki, T., and Kumano, T. (2006). "Strength and ductility evaluation of steel bridge piers with linearly tapered plates." *Journal of Constructional Steel Research*, 62(9), 906-916.

Susantha, K.A.S., Ge, H., and Usami, T. (2001). "Uniaxial stress-strain relationship of concrete confined by various shaped steel tubes." *Engineering Structures*, 23(10), 1331-1347.

Tang, J., Hino, S., Kuroda, I., and Ohta, T. (1996). "Modeling of stress-strain relationships for steel and concrete in concrete filled circular steel tubular columns." *Journal of Steel Construction JSSC*, 3(11), 35-46.

Tao, Z., Han, L.H., and Zhao, X.L. (2004). "Behaviour of concrete-filled double skin (CHS inner and CHS outer) steel tubular stub columns and beam-columns." *Journal of Constructional Steel Research*, 60(8), 1129-1158.

Tao, Z., Han, L.H., and Zhuang, J.P. (2007). "Axial loading behavior of CFRP strengthened concrete-filled steel tubular stub columns." *Advances in Structural Engineering*, 10(1), 37-46.

Teng, J.G. (1994). "Plastic collapse at lap joints in pressurized cyclinders under axial load." *Journal of Structural Engineering*, ASCE, 120(1), 23-45.

Teng, J.G., Chen, J.F., Smith, S.T., and Lam, L. (2002). *FRP-strengthened RC Structures*, John Wiley and Sons.

Teng, J.G., Chen, J.F., Smith, S.T., and Lam, L. (2003). "Behaviour and strength of FRP-strengthened RC structrues: a state-of-the-art review." *Proceedings of the Institution of Civil Engineers-Structures and Buildings*, 156(1), 51-62.

Teng, J.G., and Hu, Y.M. (2004) "Suppression of local buckling in steel tubes by

FRP jacketing." *Proceedings, Second International Conference on FRP Composites in Civil Engineering*, Adelaide, Australia, 8-10 December.

Teng, J.G., and Hu, Y.M. (2006) "Theoretical model for FRP-confined circular concrete-filled steel tubes under axial compression." *Proceedings, Third International Conference on FRP Composites in Civil Engineering*, Miami, Florida, USA, 13-15 December, 503-506.

Teng, J.G., Huang, Y.L., Lam, L., and Ye, L.P. (2007). "Theoretical model for fiber-reinforced polymer-confined concrete." *Journal of Composites for Construction*, ASCE, 11(2), 201-210.

Teng, J.G., Jiang, T., and Luo, Y.Z. (2009a). "Refinement of a design-oriented stress-strain model for FRP-confined concrete." *Journal of Composites for Construction*, ASCE, 13(4), 269-278.

Teng, J.G., and Lam, L. (2004). "Behavior and modeling of fiber reinforced polymer-confined concrete." *Journal of Structural Engineering*, ASCE 130(11), 1713-1723.

Teng, J.G., and Lin, X. (2005). "Fabrication of small models of large cylinders with extensive welding for buckling experiments." *Thin-Walled Structures*, 43(7), 1091-1114.

Teng, J.G., Yu, T., and Fernando, D. (2009b). "FRP composites in steel structures." *Proceedings, Third International Forum on Advances in Structural Engineering*, Shanghai, China, 13-14 November.

Tokgoz, S., and Dundar, C. (2010). "Experimental study on steel tubular columns in-filled with plain and steel fiber reinforced concrete." *Thin-Walled Structures*, 48(6), 414-422.

Tomii, M., and Sakino, K. (1979). "Elasto-plastic behavior of concrete filled square steel tubular beam columns." *Transactions of Architectural Institute of Japan*, 28, 111-120.

Toshiyuki, F., Noguchi, T., and Mori, O. (1996) "Evaluation for deformation capacity of concrete-filled steel tubular (CFT) beam-columns." *Proceedings, Third Joint Technical Coordinating Committee Meeting on Composite and Hybrid Structures*, Hong Kong, 1-15.

Tsuda, K., Matsui, C., and Mino, E. (1996). "Strength and behavior of slender concrete filled steel tubular columns." *Proceedings, Fifth International Colloquium on Structural Stability*.

Usami, T., and Ge, H.B. (1994). "Ductility of concrete-filled steel box columns under cyclic loading." *Journal of Structural Engineering*, ASCE, 120(7), 2021-2040.

Uy, B. (1998). "Concrete-filled fabricated steel box columns for multi-storey buildings." *Progress in Structural Engineering and Materials*, 1(2), 150-158.

Uy, B. (2000). "Strength of concrete filled steel box columns incorporating local buckling." *Journal of Structural Engineering*, ASCE, 126(3), 341-352.

Valipour, H.R., and Foster, S.J. (2010). "Nonlinear static and cyclic analysis of concrete-filled steel columns." *Journal of Constructional Steel Research*, 66(6), 793-802.

Varma, A.H., Sause, R., Ricles, J.M., and Li, Q.G. (2005). "Development and validation of fiber model for high-strength square concrete-filled steel tube beam-columns." *ACI Structural Journal*, 102(1), 73-84.

Wang, M.L., and Shah, S.P. (1987). "Reinforced-concrete hysteresis model based on the damage concept." *Earthquake Engineering and Structural*

*Dynamics*, 15(8), 993-1003.

Wang, Z.B., Tao, Z., and Han, L.H. (2008). "Performance of CFRP-strengthened concrete filled steel tubes under axial compression." Proceedings, Tenth International Symposium on Structural Engineering for Young Experts, Hunan University, Changsha, China,October 19-21, 689-694.

Wei, S., Mau, S.T., Vipulanandan, C., and Mantrala, S.K. (1995). "Performance of new sandwich tube under axial loading - experiment." *Journal of Structural Engineering*, ASCE, 121(12), 1806-1814.

Wheeler, A., and Bridge, R.Q. (2002) "Effect of concrete infill on non-compact tubes subjected to pure bending." *Proceedings*, *Advances in Steel structures*, Hong Kong, 479-486.

Williams, M., and Sexsmith, R.G. (1995). "Seismic damage indices for concrete structures: a state-of-art review." *Earthquake Spectra*, 11(2), 319-349.

Wu, G., Lu, Z.T., and Wu, Z.S. (2006a). "Strength and ductility of concrete cylinders confined with FRP composites." *Construction and Building Materials*, 20(3), 134-148.

Wu, Y.F., Liu, T., and Oehlers, D.J. (2006b). "Fundamental principles that govern retrofitting of reinforced concrete columns by steel and FRP jacketing." *Advances in Structural Engineering*, 9(4), 507-533.

Xiao, Q.G., Teng, J.G., and Yu, T. (2010). "Behavior and Modeling of concfined high-stregth concrete." *Journal of Composites for Construction*, ASCE, 14(3), 249-259.

Xiao, Y. (1989). *Experimental Study and Analytical Modeling of Triaxial Compressive Behaviour of Confined Concrete*, PhD thesis, Kyushu University, Fukuoka, Japan (in Japanese)

Xiao, Y. (2004). "Applications of FRP composites in concrete columns." *Advances in Structural Engineering*, 7(4), 335-343.

Xiao, Y., and Choi, K.K. (2010). "Analytical studies of concrete-filled circular steel tubes under axial compression." *Journal of structural Engineering*, ASCE, 136(5), 565-573.

Xiao, Y., He, W.H., and Choi, K.K. (2005). "Confined concrete-filled tubular columns." *Journal of Structural Engineering*, ASCE 131(3), 488-497.

Xiao, Y., and Wu, H. (2000). "Compressive behavior of concrete confined by carbon fiber composite jackets." *Journal of Materials in Civil Engineering*, 12(2), 139-146.

Yamao, T., Iwatsubo, K., Yamamuro, T., Ogushi, M., and Matsumura, S. (2002). "Steel bridge piers with inner cruciform plates under cyclic loading." *Thin-Walled Structures*, 40(2), 183-197.

Yu, X., Tao, Z., Han, L.H., and Uy, B. (2009). "Residual strength of concrete-filled double-skin steel tubular stub columns after exposure to fire." *Proceedings, Ninth International Conference on Steel-Concrete Composite and Hybrid Structures*, D. Lam, ed., Leeds, England, 08-10 July, 483-488.

Zhang, S.M., and Liu, J.P. (2007). "Seismic behavior and strength of square tube confined reinforced-concrete (STRC) columns." *Journal of Constructional Steel Research*, 63(9), 1194-1207.

Zhang, Y.C., Xu, C., and Lu, X.Z. (2007). "Experimental study of hysteretic behaviour for concrete-filled square thin-walled steel tubular columns." *Journal of Constructional Steel Research*, 63(3), 317-325.

Zhao, X.L., Grzebieta, R.H., Wong, P., and Lee, C. (1999). "Concrete filled cold-formed C450 RHS columns subjected to cyclic axial loading." *Proceedings, Advances in Steel Structures*, Hong Kong, China, 429-436.

Zhao, X.L., and Zhang, L. (2007). "State-of-the-art review on FRP strengthened steel structures." *Engineering Structures*, 29(8), 1808-1823.

Zhao, Y., and Teng, J.G. (2001). "Buckling experiments on cone-cylinder intersections under internal pressure." *Journal of Engineering Mechanics*, ASCE, 127(12), 1231-1239.

# APPENDIX

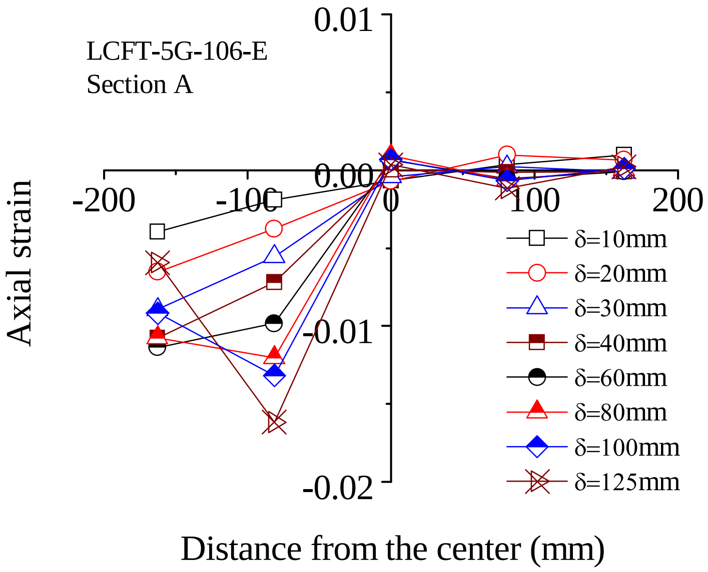


(a) Section A

Figure A.1 Axial strain distributions on examined sections of column LCFT-5G-106-E

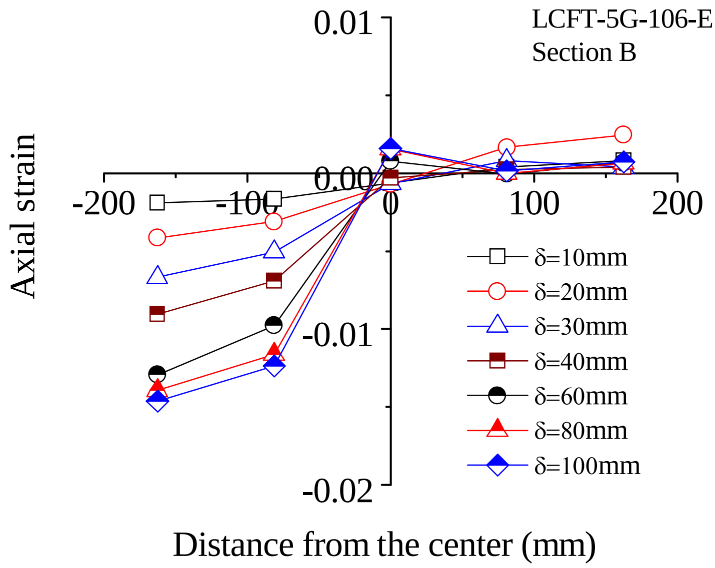


(b) Section B

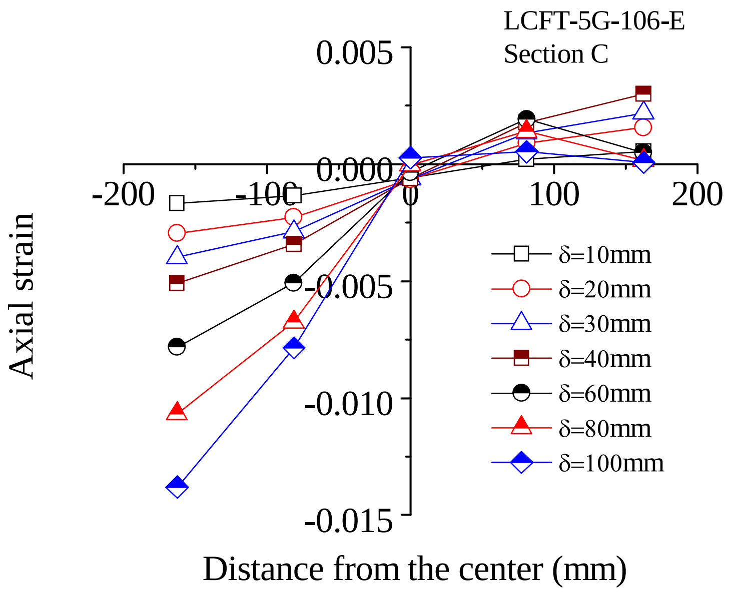


(c) Section C

Figure A.1 Axial strain distributions on examined sections of column LCFT-5G-106-E (continued)

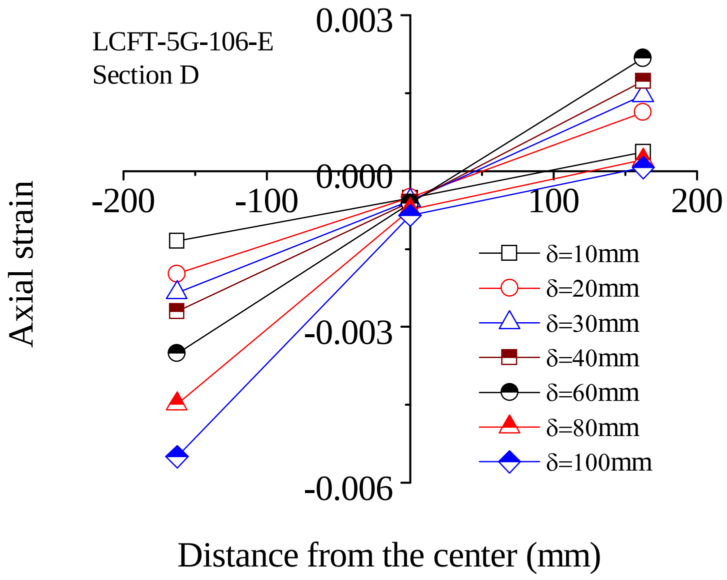


(d) Section D

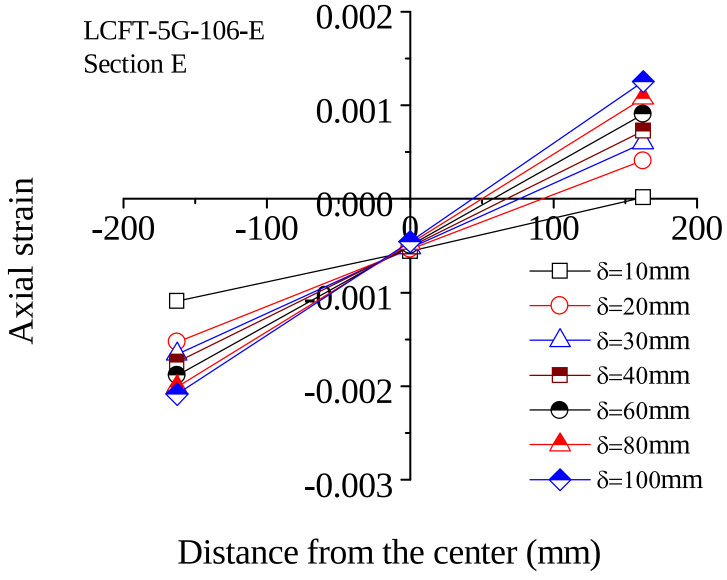


(e) Section E

Figure A.1 Axial strain distributions on examined sections of column LCFT-5G-106-E (continued)

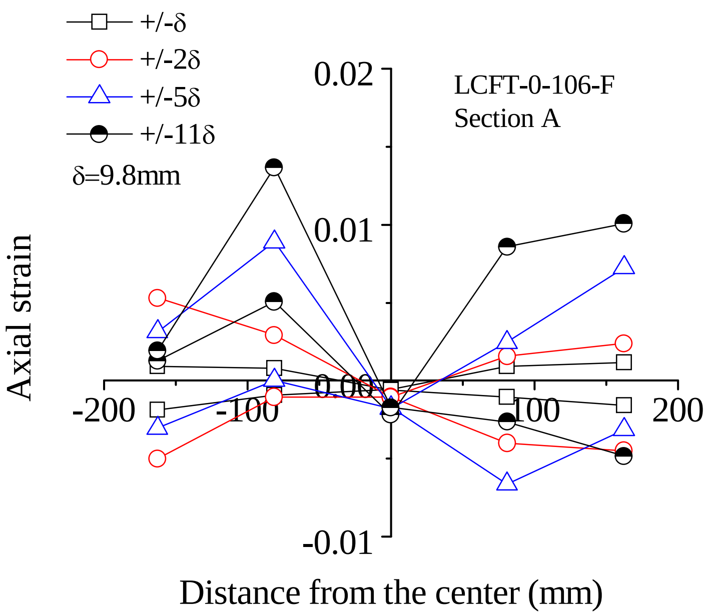


(a) Section A

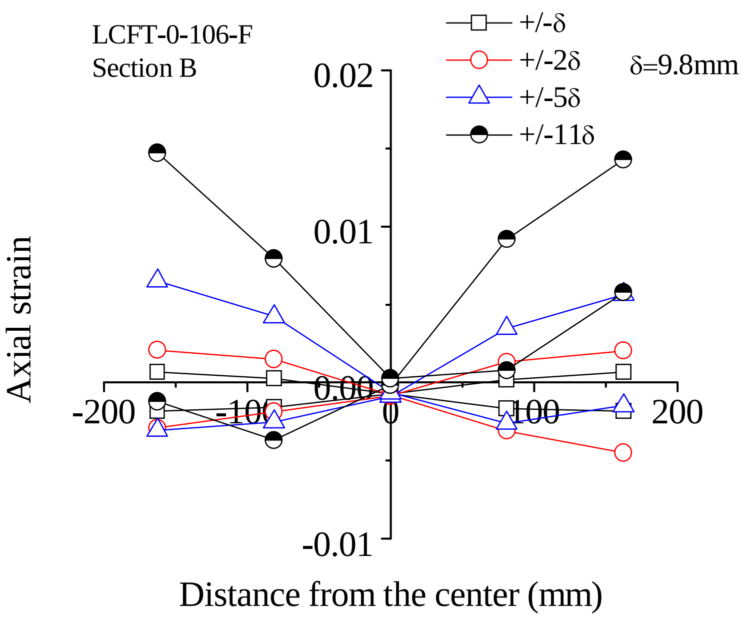


(b) Section B

Figure A.2 Axial strain distributions on examined sections of column LCFT-0-106-F

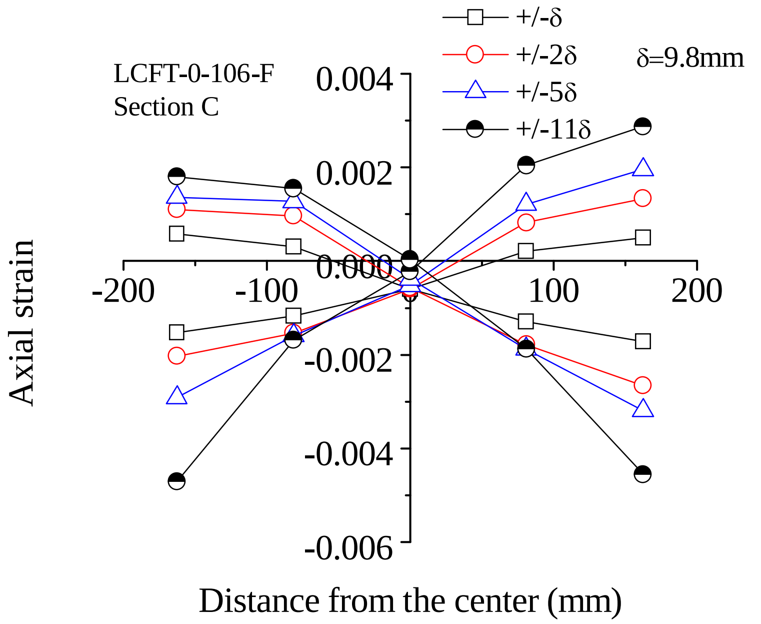


(c) Section C

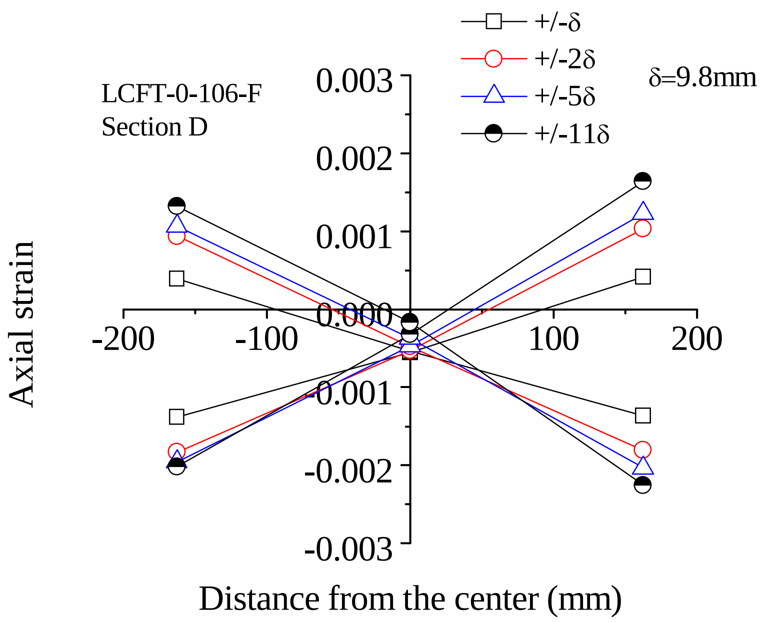


(d) Section D

Figure A.2 Axial strain distributions on examined sections of column LCFT-0-106-F (continued)

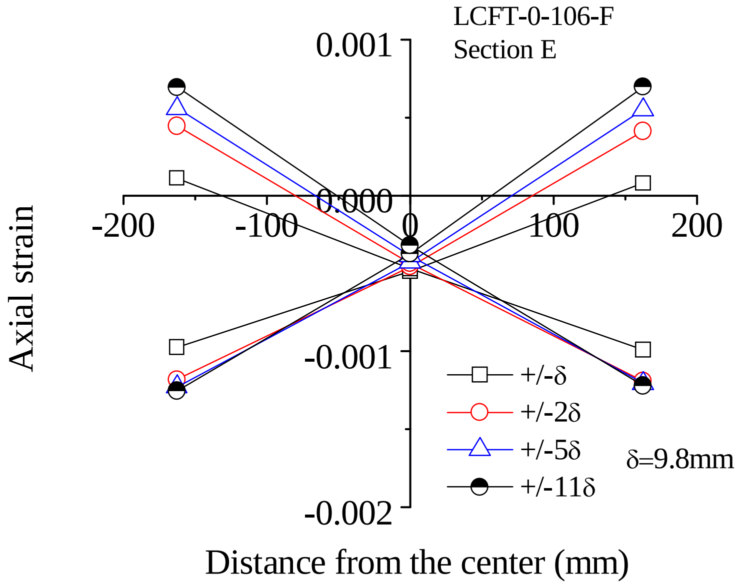


(e) Section E

Figure A.2 Axial strain distributions on examined sections of column LCFT-0-106-F (continued)

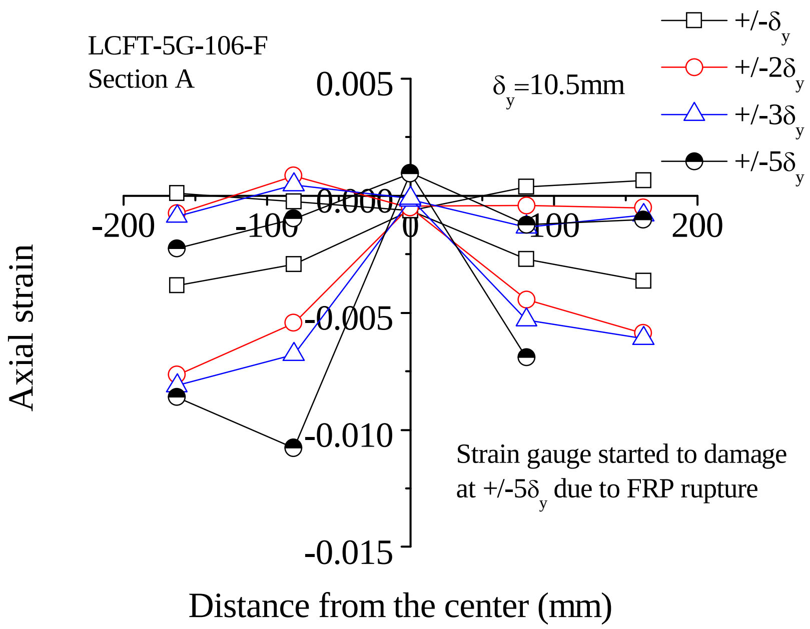


(a) Section A

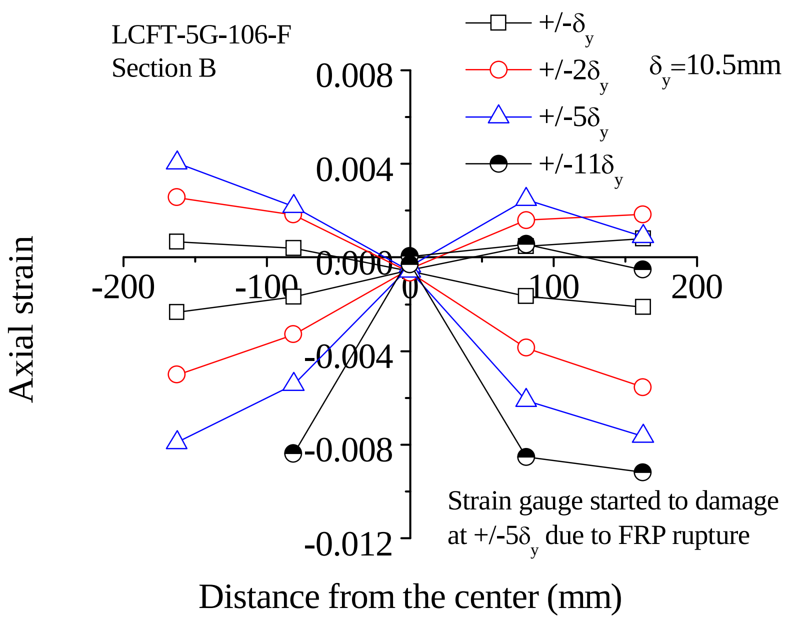


(b) Section B

Figure A.3 Axial strain distributions on examined sections of column LCFT-5G-106-F

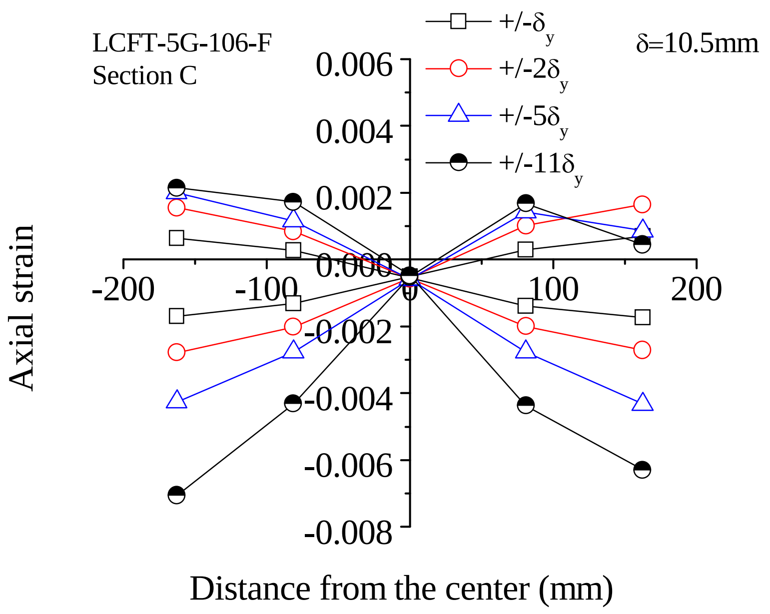


(c) Section C

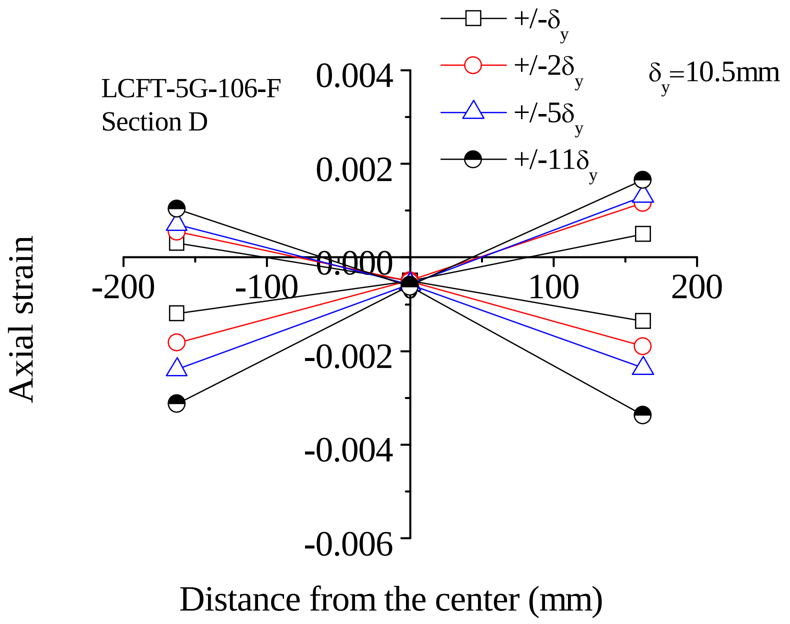


(d) Section D

Figure A.3 Axial strain distributions on examined sections of column LCFT-5G-106-F (continued)

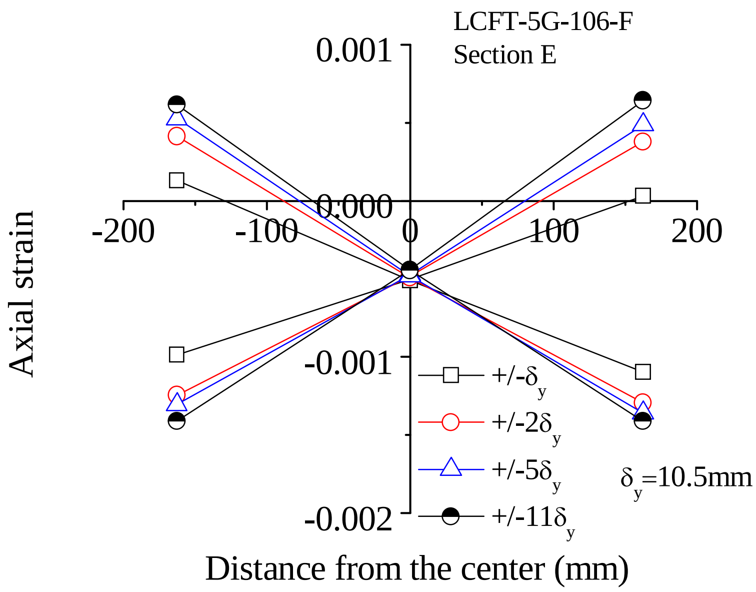


(e) Section E

Figure A.3 Axial strain distributions on examined sections of column LCFT-5G-106-F (continued)

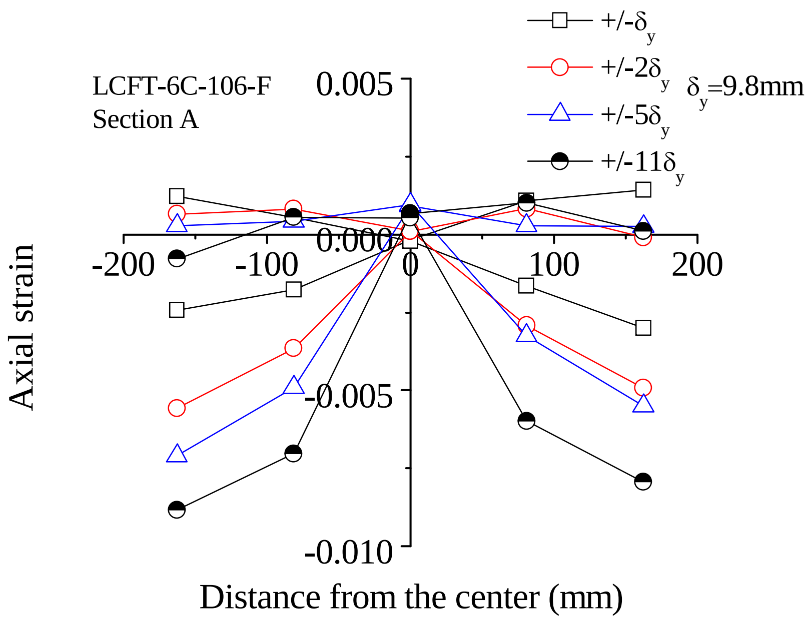


(a) Section A

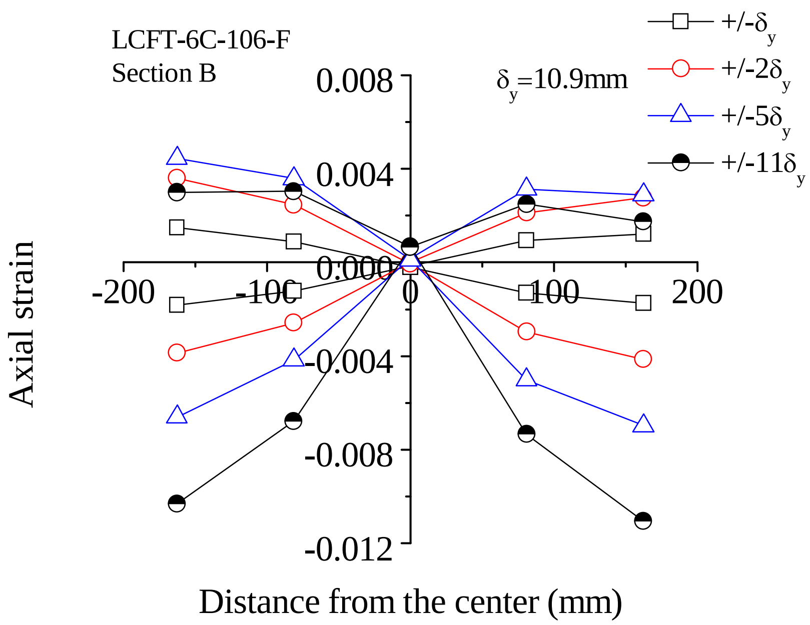


(b) Section B

Figure A.4 Axial strain distributions on examined sections of column LCFT-6C-106-F

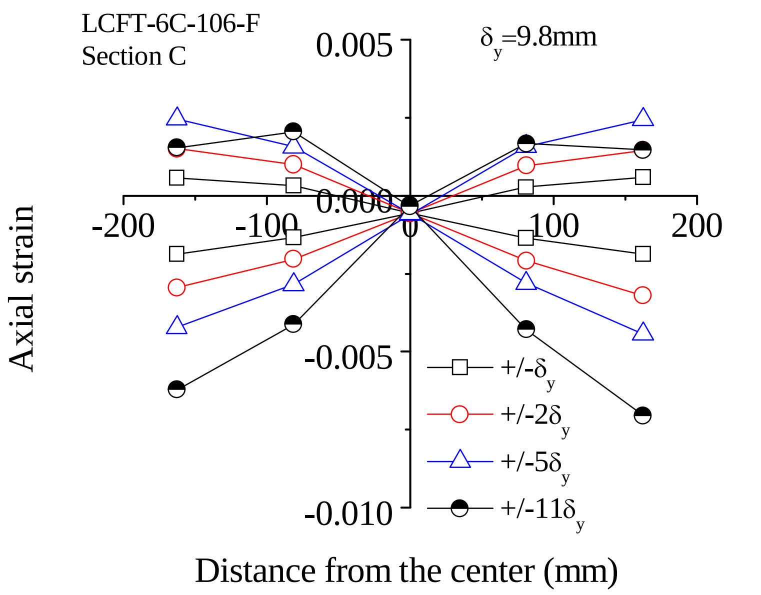


(c) Section C

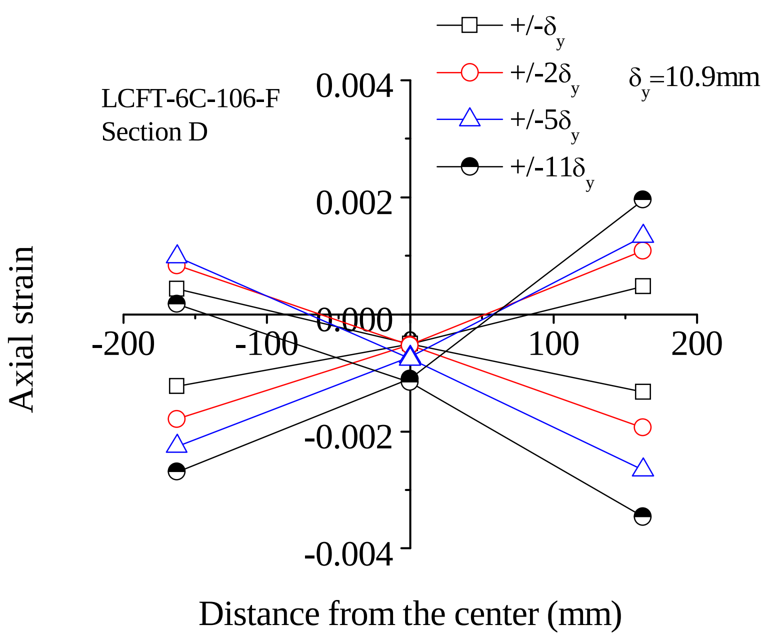


(d) Section D

Figure A.4 Axial strain distributions on examined sections of column LCFT-6C-106-F (continued)

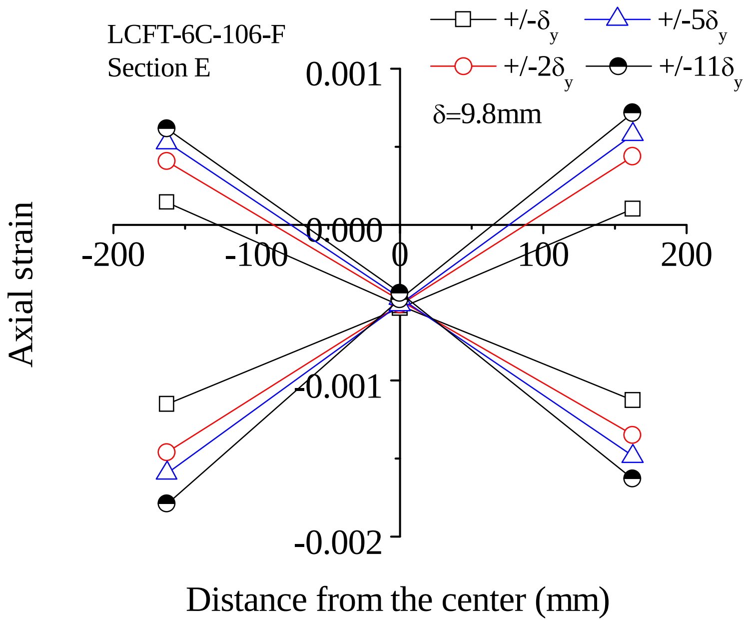


(e) Section E

Figure A.4 Axial strain distributions on examined sections of column LCFT-6C-106-F (continued)